REPORT DOCUMENTATION PAGE

1. AGENCY USE ONLY *(Leave blank)*	2. REPORT DATE	3. REPORT TYPE AND DATES COVERED
	17.May.02	DISSERTATION

4. TITLE AND SUBTITLE
AN INTEGRATED MICROSTRUCTURAL STUDY OF DRY SNOW
METAMORPHISM UNDER GENERALIZED THERMAL CONDITIONS

5. FUNDING NUMBERS

6. AUTHOR(S)
MAJ MILLER DANIEL A II

7. PERFORMING ORGANIZATION NAME(S) AND ADDRESS(ES)
MONTANA STATE UNIVERSITY

8. PERFORMING ORGANIZATION REPORT NUMBER

CI02-69

9. SPONSORING/MONITORING AGENCY NAME(S) AND ADDRESS(ES)
THE DEPARTMENT OF THE AIR FORCE
AFIT/CIA, BLDG 125
2950 P STREET
WPAFB OH 45433

10. SPONSORING/MONITORING AGENCY REPORT NUMBER

11. SUPPLEMENTARY NOTES

12a. DISTRIBUTION AVAILABILITY STATEMENT
Unlimited distribution
In Accordance With AFI 35-205/AFIT Sup 1

12b. DISTRIBUTION CODE

13. ABSTRACT *(Maximum 200 words)*

20020523 158

14. SUBJECT TERMS

15. NUMBER OF PAGES
244

16. PRICE CODE

17. SECURITY CLASSIFICATION OF REPORT	18. SECURITY CLASSIFICATION OF THIS PAGE	19. SECURITY CLASSIFICATION OF ABSTRACT	20. LIMITATION OF ABSTRACT

ABSTRACT

Snow microstructure significantly influences the mechanical, thermal, and electromagnetic properties of snow. The microstructure is constantly evolving from the time it is deposited on the surface until it sublimates or melts. The resulting time variant material properties make the study of snow metamorphism of fundamental importance to a wide variety of snow science disciplines. Dry snow metamorphism has traditionally been classified by the thermal gradient encountered in the snowpack. Snow experiencing a predominantly equi-temperature environment develops different microstructure than snow that is subjected to a temperature gradient. As such, previous research has evaluated snow metamorphism based upon select thermal gradient dependent processes, when in reality, there is a continuum of physical processes simultaneously contributing to metamorphism. In previous research, a discrete temperature gradient transition between the two thermal environments has been used to activate separate morphological analyses. The current research focuses on a unifying approach to dry snow metamorphism that is applicable to generalized thermal environments. The movement of heat and mass is not prescribed, but is allowed to develop naturally through modeling of physical processes. Heat conduction, mass conservation, and phase change equations are derived in a simplified two-dimensional approach. Each differential equation is non-linearly coupled to the others through phase change. The microstructural network is then discretized into elements and nodes. Finite difference equations are developed for the network, and numerically solved using iterative techniques. The finite difference model provides a unique platform to study the influence of numerous geometric and thermodynamic parameters relating to dry snow metamorphism. Numerical metamorphism studies in an equi-temperature environment agree well with established trends and published experimental results. A smooth transition between equi-temperature and temperature gradient environments is defined and influencing parameters are examined. In the temperature gradient environment, a dominant grain theory based on crystallographic orientation is postulated through numerical modeling, and is supported by experimental observation. Several specific metamorphism applications, ranging from avalanche debris sintering to model integration in a full scale snowpack, are presented. The microstructural model has proven to be capable of evaluating metamorphism for a broad range of geometric parameters and thermal environments, yet is flexible enough to accommodate additional scenarios.

Daniel August Miller II

Spring 2002 graduation

Advisor: Robert L. Brown

Title: AN INTEGRATED MICROSTRUCTURAL STUDY OF DRY SNOW
METAMORPHISM UNDER GENERALIZED THERMAL CONDITIONS

Keywords: snow metamorphism, equi-temperature, temperature gradient, kinetic growth,
depth hoar, sintering, metamorphism model, snow microstructure, avalanche debris
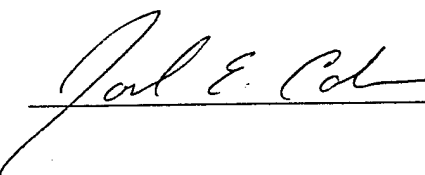
APPROVAL

of a dissertation submitted by

Daniel August Miller II

This dissertation has been read by each member of the dissertation committee and has been found to be satisfactory regarding content, English usage, format, citations, bibliographic style, and consistency, and is ready for submission to the College of Graduate Studies.

Robert L. Brown _____ 04/10/02
                                                          Date

Approved for the Department of Civil Engineering

Joel E. Cahoon _____ 4/10/02
                                                          Date

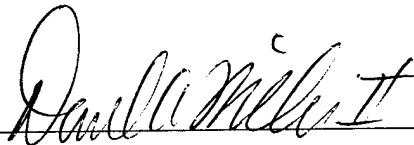Approved for the College of Graduate Studies

Bruce R. McLeod _____ 4-11-02
                                                          Date

STATEMENT OF PERMISSION TO USE

In presenting this dissertation in partial fulfillment of the requirements for a doctoral

degree at Montana State University, I agree that the Library shall make it available to

borrowers under the rules of the Library. I further agree that copying of this dissertation

is allowable only for scholarly purposes, consistent with "fair use" as prescribed in the

U.S. Copyright Law. Requests for extensive copying or reproduction of this dissertation

should be referred to Bell & Howell Information and Learning, 300 North Zeeb Road,

Ann Arbor, Michigan 48106, to whom I have granted "the exclusive right to reproduce

and distribute my dissertation in and from microform along with the non-exclusive right

to reproduce and distribute my abstract in any format in whole or in part."

Signature _____

Date _4/10/02_

TABLE OF CONTENTS

LIST OF TABLES

LIST OF FIGURES

ABSTRACT

Snow microstructure significantly influences the mechanical, thermal, and electromagnetic properties of snow. The microstructure is constantly evolving from the time it is deposited on the surface until it sublimates or melts. The resulting time variant material properties make the study of snow metamorphism of fundamental importance to a wide variety of snow science disciplines. Dry snow metamorphism has traditionally been classified by the thermal gradient encountered in the snowpack. Snow experiencing a predominantly equi-temperature environment develops different microstructure than snow that is subjected to a temperature gradient. As such, previous research has evaluated snow metamorphism based upon select thermal gradient dependent processes, when in reality, there is a continuum of physical processes simultaneously contributing to metamorphism. In previous research, a discrete temperature gradient transition between the two thermal environments has been used to activate separate morphological analyses. The current research focuses on a unifying approach to dry snow metamorphism that is applicable to generalized thermal environments. The movement of heat and mass is not prescribed, but is allowed to develop naturally through modeling of physical processes. Heat conduction, mass conservation, and phase change equations are derived in a simplified two-dimensional approach. Each differential equation is non-linearly coupled to the others through phase change. The microstructural network is then discretized into elements and nodes. Finite difference equations are developed for the network, and numerically solved using iterative techniques. The finite difference model provides a unique platform to study the influence of numerous geometric and thermodynamic parameters relating to dry snow metamorphism. Numerical metamorphism studies in an equi-temperature environment agree well with established trends and published experimental results. A smooth transition between equi-temperature and temperature gradient environments is defined and influencing parameters are examined. In the temperature gradient environment, a dominant grain theory based on crystallographic orientation is postulated through numerical modeling, and is supported by experimental observation. Several specific metamorphism applications, ranging from avalanche debris sintering to model integration in a full scale snowpack, are presented. The microstructural model has proven to be capable of evaluating metamorphism for a broad range of geometric parameters and thermal environments, yet is flexible enough to accommodate additional scenarios.

CHAPTER 1

BACKGROUND AND LITERATURE REVIEW

Introduction

The snow that perennially or annually blankets temperate and polar latitudes has a significant impact on our everyday lives. Snow is a substance of extremes: providing unique recreational opportunity and beauty, yet threatening the safety of individuals and communities. Snow can paralyze major geographic regions by restricting travel, causing property damage, and by creating life-threatening avalanche hazards. Snowcover can influence local as well as global climate changes (Berry,1981) due to interactions with the atmosphere through emissive, reflected, and absorbed radiation (Warren, 1982; Dozier et al., 1988). Snow also provides vital moisture reserves for the world. It is estimated that three-quarters of the world's terrestrial water resources are currently stored in snow and ice (Committee on Opportunities in the Hydrologic Sciences, 1991) and that snow supplies one third of the world's agricultural irrigation water (Stepphun, 1981). Snow's influence in vast and diverse areas of our world makes the study of snow mechanics a uniquely rewarding endeavor.

Microstructure Significance

The formal scientific study of snow dates back to the early 1800's (Colbeck, 1991). It was recognized early on that the response of snow to its environment depends upon its thermal, mechanical, and electromagnetic properties (Arons and Colbeck, 1995). Dry snow is composed of an ice network with interstitial pores filled with a mixture of air and water vapor. Wet snow includes a liquid phase of water that may occupy the bond areas or fill the pore spaces, depending upon the water content. This unique construction makes the microscopic details of the ice and pore spaces a major influence in snow's physical behavior. The microstructure of snow (defined as structures on the scale of individual ice grains, inter-granular bonds and pores) determines the mechanical (Yosida, 1963; Hobbs, 1965; Keeler, 1969; Yen, 1969; Kry, 1975; Gubler, 1978 a,b; Brown, 1980; Armstrong, 1980; St Lawrence and Lang, 1981; Adams and Brown, 1982a; Salm, 1982; Hansen and Brown, 1988; Brown and Edens, 1991; Edens and Brown, 1991; Mahajan and Brown, 1993; Shapiro, 1997; Johnson and Schneebeli, 1999), thermodynamic (Yosida, 1955, 1963; Colbeck 1980; Adams and Brown, 1990; Adams and Sato, 1993; Arons, 1994) and electromagnetic (Warren, 1982; McClung and Schaerer, 1993) properties of snow. The intergranular bonding of snow grains comprising a snowcover affects the strength, viscosity, creep, thermal, optical and electromagnetic properties (Adams et al., 2001).

Snow Metamorphism

Snow is a unique granular material. From the time it touches the earth until it either transitions to liquid (melts) or to vapor (sublimates), the snow microstructure is

continually changing in a process called metamorphism. The time-varying microstructural quantities result in nonlinear material responses, making the study, understanding, and prediction of snow metamorphism vital to nearly all areas of snow science. The critical dependence of snow properties on microstructure makes metamorphism an extremely important area of study. Microstructural changes were first described and documented in detail by Paulke (1934), although casual observations of snowpack metamorphism came much earlier (de Quervain, 1963). In recent times, efforts to understand the evolving microstructure in snow intensified. The combination of large crystal surface area to volume ratio and homologous temperature ($T/T_{melt} > 0.9$ generally) makes snow a very nonlinear and a highly temperature dependent material (Colbeck, 1983a). Because of the relatively warm temperatures in seasonal snow, water vapor is free to migrate and diffuse in the pore spaces of the ice matrix. Specific surface areas as large as 10,000 m^2/m^3 (Edens, 1997) result in snow continually trying to reduce that ratio, thereby reducing the overall surface free energy (de Quervain, 1963; Hobbs, 1965; Colbeck, 1980; Langham, 1981).

In general, we will consider two categories of metamorphism depending upon the thermal environment. In a snowpack where the temperature is nearly uniform, metamorphism is termed "equi-temperature". If a significant temperature gradient is applied (frequently found in alpine snow), then "temperature gradient" metamorphism results. Traditionally, each of these conditions has been treated as separate and distinct since each results in a unique microstructure (Sommerfeld and LaChapelle, 1970). Use of the temperature environment to describe the metamorphic process is not universally accepted. In fact, the categorization of metamorphism has resulted in heated discussion

and debate. Colbeck (1980, 1982, 1983a) used crystal forms and driving forces to describe metamorphism. The current research reported here does not require a distinction between the different types of metamorphism, rather it (as a preview) uses physical processes common to both. The resulting unified approach makes the discussion somewhat obsolete and irrelevant. But, in order to present past efforts in a logical manner, the equi-temperature and temperature gradient terminology will be used with no opinion offered on its validity.

Equi-temperature Environment. "Equi-temperature" or "radius-of-curvature" metamorphism results when only very small microscale temperature gradients exist in a snowpack. The characteristic microstructure resulting from this environment is smooth rounded grains connected by smooth reverse curvature necks. An example is given in figure 1 in chapter 2. The resulting snow tends to strengthen and densify with time. In the absence of a macroscopic temperature gradient, ice particles are observed to sinter by growing the bonds between the individual grains. This sintering process is commonly referred to as equi-temperature metamorphism. Colbeck (1980) correctly pointed out that truly equi-temperature metamorphism is impossible for any process involving phase change. Heat must flow in order for phase change to occur, thereby requiring microscopic temperature gradients. Colbeck (1980) introduced the term "radius-of-curvature" metamorphism (for reasons that will be obvious later). "Equi-temperature" metamorphism will be used here with the understanding that some (even though very small and highly localized) temperature gradients must exist for phase change metamorphic processes to take place.

There are several physical processes available for the movement of water molecules in snow metamorphism. Maeno and Eblnuma (1983) summarized six potential mechanisms that contribute simultaneously to the growth of necks between sintering ice particles: surface diffusion from a surface source (Kuczynski, 1949), volume diffusion from a surface source (Kuczynski, 1949), vapor transport from a surface source (Hobbs and Mason, 1964), boundary diffusion from a grain boundary source (Johnson, 1969; Colbeck, 1998; Adams et al., 2001), volume diffusion from a grain boundary source (Ashby, 1974), and volume diffusion from dislocation sources (Ashby, 1974). The question that arises is which (if any) are predominant and can any of these mechanisms be neglected? Several studies, theoretical and experimental, have addressed this issue.

Kingery (1960) showed ice particles brought together at subfreezing temperatures remain together even when the unifying force was removed. He claimed that surface diffusion from the grain surfaces to the newly formed bonds resulted in "regelation" of the particles. It was previously believed that pressure melting or a liquid-like surface layer was required for bonding, but Kingery disproved this. Kuroiwa (1961) conducted experiments similar to Kingery, but came to different conclusions on the mass transport mechanisms. Kuroiwa concluded that volume diffusion was dominant above -10°C with surface diffusion emerging and then dominating below -15°C. Hobbs and Mason (1964) and Hobbs (1974) also conducted ice sintering experiments with entirely different interpretation of results. They brought together several sizes of uniform spheres in a vapor-saturated environment. They then observed particles optically and measured bond sizes in time. Each mechanism was assumed to conform to the following law:

$$\left(\frac{r_b}{r_g}\right)^n = \frac{B(T)}{r_g^m}t$$

where t is time, B(T) is a temperature dependent function, r_g is the grain radius, r_b is the bond radius, m and n are integers that depend upon the mass transport mechanism. Hobbs and Mason (1964) claimed that it is impossible to experimentally distinguish (find independent m and n coefficients) between the sintering rates of vapor, surface, or volume diffusion. In fact, they show similar rate dependence for each case. Hobbs and Mason presented convincing arguments pointing to vapor diffusion as the dominant sintering mechanism (by four orders of magnitude) based on the size of the respective coefficients. Maeno and Eblnuma (1983) confirmed the vapor transport dominance except under certain temperature and geometric conditions where surface diffusion may be significant. The small bond size required for significant surface diffusion would be very short-lived since the sintering rates are so high with small bonds. As a consequence, experiments and analysis have focused on the vapor diffusion regime. Maeno and Eblnuma (1983) have shown (analytically) the significance of surface diffusion when $r_b/r_g < 0.06$, yet Hobbs and Mason (1964) didn't report measured ratios less than 0.1. The sintering progressed so quickly (a few minutes), that the very small bond to grain ratios were not visually captured. Until recently, the prevailing consensus, over at least the previous 20 years, is that vapor diffusion is the primary sintering mechanism during metamorphism of a macroscopically equi-temperature snow pack. Other mechanisms are probably at work, but at rates much lower than vapor diffusion. The only exception is the potential short-term contribution of surface diffusion under specific temperature and geometrical conditions.

Recently, grain boundary diffusion has been given more attention as a potential sintering mechanism. Grain boundary diffusion is a sintering process that occurs at the interface of two crystals, whereby mass migrates from the center of the contact to the surface of the bond. Sintering takes place when surface tension forces pull the grains together resulting in a stress gradient from the center to the surface of the bond. Colbeck (1998;1997) applied a grain boundary diffusion model (Zhang and Schneibel, 1995) to ice. His model assumed the presence of a grain boundary stress gradient producing molecular flux, which redistributes mass evenly onto spherical ice grain surfaces. Intergranular necks were not considered. Colbeck's analysis raised the question of grain boundary diffusion significance, but did not attempt to provide physical evidence of its existence. He recognized the need for better physical constants defining grain boundary molecular mobility before the significance of grain boundary diffusion can be evaluated. Adams et al. (2001) used a scanning electron microscope to examine bonds between sintering ice grains. They discovered a grain boundary "ridge" protruding into the pore at the grain boundary surface. This ridge is thought to result from the migration of molecules from the bond center to the surface, providing the first physical confirmation of grain boundary diffusion in ice. Adams et al. (2001) also presented a mass balance analysis which brought into question the validity of grain boundary physical parameters and, potentially, our understanding of sintering.

For the current effort, sintering due to vapor diffusion is the accepted dominant mechanism, conforming to current data. Colbeck (1980) suggested a process of vapor diffusion between surfaces of different radii of curvature. He derived the vapor pressure

over curved surfaces as a function of surface curvature through the chemical potential.

Vapor pressure over curved surfaces is given by the familiar form of Kelvin's equation:

$$P = P_0 \exp\left[f\left(\frac{1}{\rho_s}\right)\right],$$

where P is the equilibrium vapor pressure over the surface, P_0 is the equilibrium vapor

pressure over a flat surface at a reference temperature, and ρ_s is the average surface

curvature. ρ_s is defined by:

$$\frac{2}{\rho_s} = \frac{1}{r_1} + \frac{1}{r_2},$$

where r_1 and r_2 are radii of curvature measured in any two orthogonal planes on the

surface separating the phases (Colbeck, 1980). Vapor sintering takes place when vapor

sublimates from a high surface energy site (a convex grain), diffuses through the pore

space and then condenses on a lower surface energy site (concave bond). For convex

surfaces, radii are positive; conversely, radii are negative for concave surfaces. At a

given temperature, vapor pressures over convex surfaces are greater than vapor pressures

over concave surfaces. Molecules will sublimate from the convex surfaces, travel

through the vapor, and deposit on the concave neck between grains. This is also the

mechanism for the rapid decay of dendritic snow particles when they initially fall on the

snowpack. The sharp convex corners have very high vapor pressure compared to the

surrounding vapor and other surfaces. These sharp features decay quickly and rounded

forms develop. The same processes are responsible for the sintering of grains. This

process was described by Colbeck (1980) as "radius of curvature" metamorphism.

<u>Temperature Gradient Environment.</u> In seasonal snow, it is common for snowpack temperature gradients to develop, resulting in "temperature gradient" or "kinetic growth" metamorphism. The combination of heat stored in the ground over the summer months and geothermal warming keep the layer near the ground close to 0°C for most of the winter season (McClung and Schaerer, 1993), yet the upper surface of the snowpack is subjected to diurnal temperature fluctuations. Depending upon snow depth, surface thermal interaction and thermal penetration (both dependent upon microstructure), large temperature gradients can develop within the snowpack. Temperature differences produce water vapor concentration (density) gradients within the pore space. If a large enough pore space is present (as is generally the case for lower density snow), a substantial vapor flux from the warmer to colder regions develops.

Vapor can be transported through the pore by molecular diffusion or convection. Field studies (Trabant and Benson, 1972; Sturm, 1991; Sturm and Johnson, 1991) have shown that convection can be significant under certain extreme conditions. Trabant and Benson (1972) concluded convection was present because one-dimensional diffusive models failed to account for the total observed mass transport. Palm and Tveitereid (1979) examined thermal convection analytically and concluded convection only occurs in snow with strong temperature gradients and large air permiabilities. Follow-on diffusion models accounted for the increased flux (Sommerfeld, 1983; Colbeck, 1983a; Gubler, 1985), and authors have generally rejected convection contributions. Akitaya's (1974a, 1974b) experiments led him to the conclusion that natural convection occurred only when snow contained very large pore spaces. In fact, Akitaya found no convection in natural and sieved snow samples subjected to temperature gradients 170 – 200 °C/m.

While the issue of convection is not clearly settled or widely agreed upon, it clearly is not a significant transport mechanism in most commonly incurred temperature gradient scenarios. One exception may occur at the upper snow surface where very large temperature gradients in low density snow develop when conditions are favorable for surface hoar growth (Lang et al., 1984). General agreement remains for the dominance of diffusional vapor transport for seasonal snow conditions.

The diffusion of water vapor through the interstitial pore space changes the nature of metamorphism significantly. A temperature gradient (and resulting vapor pressure gradient) in the pore produces unique snow morphologies. As the temperature gradient increases, the snow microstructure can change from smooth rounded grains with smooth interconnections to large, highly faceted, angular crystals with large surrounding pore spaces and poor bonding. Even though research on the bonding of faceted crystals is sparse, the presence of these crystals has been attributed to lower material strength (Bradley et al., 1977a; Armstrong, 1980; Adams and Brown, 1982) and increased chance of avalanche release (Bradley et al., 1977b; Satyawali, 1998; McElwaine, 2000). These crystal forms are often referred to as facets, temperature gradient metamorphism forms, kinetic forms, recrystallized snow, and depth hoar.

The temperature gradient required to transition from a smooth and rounded microstructure to sharp and faceted forms is dependent upon density, grain size, pore size, and temperature (Colbeck, 1983b). Experimental observations generally show a temperature gradient transition between 10 and 20 °C/m (Akitaya, 1974a; Armstrong, 1980; Colbeck, 1983a, 1983b) or >25°C/m (Marbouty, 1980). There has been little theoretical research on the physical rationale for this transition. Below the transition

temperature gradient, Colbeck (1980,1983a) showed vapor transport due to temperature gradients quickly outpaces transport due to differences in curvature. As the temperature gradient increases, so does the growth rate of faceted crystals. The process has been conceptualized by Yosida el al. (1955) as "hand-to-hand" vapor transport. In this scenario, mass is transported by sublimation from the top of an ice grain, diffusion through the pore space, then condensation on the bottom of a neighboring grain. If the sublimation and condensation rates for a grain are not in balance, the grain grows or shrinks. In the early stages, angular grains with sharp edges appear. As metamorphism continues, the crystals can grow parallel to the temperature gradient and can develop large striated hollow structures. Depending upon crystal orientation, large hollow cups or columns may develop parallel to the temperature gradient. As these grains develop, they are commonly linked in large chains surrounded by elongated pore spaces, commonly referred to as macropores (Arons and Colbeck, 1995).

Larger crystals tend to grow in low density snow with large pore spaces (Akitaya, 1974a,b). For snow density exceeding approximately 350 kg/m^3, pore spaces are very small and the kinetic growth process is limited. "Hard" depth hoar develops (Akitaya, 1974a,b; Marbouty, 1980) under these conditions. Hard depth hoar crystals are comprised of sharp angular crystals, but are considerably smaller and stronger (due to higher degree of bonding) than classic depth hoar.

The increased avalanche danger posed by the development of depth hoar has stimulated extensive experimental research on temperature gradient metamorphism. Akitaya (1974a) conducted a series of depth hoar growth experiments in the laboratory with artificial snow and in the field with natural snow. He categorized crystals as

skeleton or solid type depth hoar. Solid type depth hoar grew under temperature gradients <25°C/m while skeleton type grew under larger temperature gradients when large air space was available. By examining thin sections, Akitaya identified linkages in the direction of the temperature gradient between the crystals. Marbouty's (1980) experiments quantified critical parameters in temperature gradient metamorphism. He found crystal growth rates increasing with temperature, temperature gradient (with a lower limit of 25 °C/m), and decreasing density (lower limit 150 kg/m^3, upper limit 350 kg/m^3). His experiments confirmed Akitaya's observations that lack of large pores results in hard depth hoar. The temperature gradients in Marbouty and Akitaya's experiments were less than 100 °C/m, yet temperature gradients near snow surfaces may be much greater. Fukuzawa and Akitaya (1993) conducted hoar crystal growth experiments with temperature gradients greater than 100 °C/m but less than 300 °C/m. These large temperature gradients can be found under a variety of conditions depending upon radiation balance conditions. They found linearly increasing crystal size with time at rates allowing rapid development of large crystals. Sturm and Benson (1997) presented an extensive study and analysis of depth hoar in the subarctic snow. They observed a grain size increase of a factor of 2-3 over the winter season. Initially, growth rates were high, but decreased by the end of the season. At season's end, the entire snowpack had metamorphosed through five different depth hoar textures. Sturm and Benson found layer-to-layer vapor fluxes to be ten times greater than inter-particle fluxes, potentially explaining field measurements of constant snow density during depth hoar formation. Kamata et al. (1999) quantified the effects of temperature and temperature gradient (size and direction) on crystal growth during low temperatures (-65 °C to –15

°C) and large temperature gradients (500 °C/m). Under these conditions, they concluded that crystal habit was primarily dependent upon temperature and secondarily upon temperature gradient.

Heat and Mass Modeling Efforts

Many researchers have studied snow transport modeling in the last 50 years. The complex nature of snow has resulted in many unique approaches including analytical as well as numerical solutions. From the perspective of snow metamorphism, an approach that not only accurately accounts for heat and mass distributions, but also includes the important influences of realistic microstructure and phase change is desired. In their review of snow heat and mass transfer research, Arons and Colbeck (1995) concluded that an integrated heat and mass transfer model using realistic geometry currently does not exist, but is needed. The following review of past efforts is presented to frame the importance and significance of the current research.

Bader (1939) developed a transport model between two parallel plates of ice. This is considered one of the first attempts to model temperature gradient or kinetic growth metamorphism. One-dimensional vapor diffusion and mass conservation between the plates made Bader's study an important first step in understanding the physical processes at work. Giddings and LaChapelle (1962) used a similar approach but inadvertently retained upward diffusing vapor at the next higher level (Sommerfeld, 1983). de Quervain (1963, 1973) incorporated three different ice structures when evaluating heat and mass flow. de Quervain's first structure was a series of cylindrical

pores in the ice running parallel to the temperature gradient. He then presented a set of parallel plates aligned perpendicular to the temperature gradient. His final structural model was a combination of the first two with cylindrical channels intersected by rectangular vapor "traps". These simplified geometries were clearly inadequate for actual snow, but provided a starting point for more advanced approaches.

The critical consideration of snow microstructure in any metamorphism research led to many studies in the early 1980's where differing assumptions and complexities led to several models. Perla (1978) recognized the importance of the granular nature of snow and incorporated a more realistic geometry in metamorphism models. Sommerfeld (1983) developed a temperature gradient metamorphism model based on the evolution of branch grains. A "branch" grain was defined as a grain poorly connected to the ice matrix making it favorable for phase change. Sommerfeld formalized a process envisioned by de Quervain (1973) whereby branch grains protruding into the warmer pore spaces will grow while those protruding into the colder spaces will shrink. Colbeck (1983a) developed an analytic metamorphism theory with a geometric "enhancement" factor between source and sink grains during hand-to-hand vapor transport. This was the first real step forward into meaningful microstructure modeling. He calculated diffusion using a potential field solution for electrostatically charged particles. Colbeck noted that as some grains grow faster than others and nearby sources disappear, new sources develop in warmer parts of the snowpack. This is a feedback mechanism whereby the grains that initially grow rapidly would continue to grow rapidly. He also noted that one-dimensional diffusion under predicts crystal growth rates, an observation previously attributed to the presence of convection (Trabant and Benson, 1972). The onset of kinetic

growth forms was noted from experimental data, but Colbeck's analysis did not provide insight into the value of the temperature gradient at kinetic growth onset. Gubler (1985) developed an analytic metamorphism model based on observed stereological interparticle structures (Gubler, 1978a). He defined chains, clusters, and end particles based on coordination number, but was forced to identify source and sink grains during the metamorphism process. Gubler used an electrostatic analog with a geometric factor, similar to Colbeck's (1983a), but used a more realistic, measurable, microstructural geometry. Adams and Brown (1982b, 1983) presented a crystal growth model in a temperature gradient environment accounting for pore size and crystal shape. They used excess vapor density, as a function of temperature and surface curvature, as the primary driving mechanism. While analytic models provide insight into physical phenomena, they can be limited in their utility for broad-based application to variable snow conditions.

Numerical models have been developed to explain and predict snow metamorphism. Christon et al. (1990) presented a 2-D finite element model with a deforming mesh. They developed coupled heat conduction for the ice and vapor diffusion for the pore. The three linear coupled differential equations resulting from energy balance, mass conservation, and phase change boundary conditions were solved using finite element techniques. Their results supported Yosida's (1955) hand-to-hand transfer analogy for temperature gradient metamorphism. Christon et al. (1994) extended their 2-D theory to three dimensions. They verified the existence of a diffusive geometric enhancement factor postulated by Colbeck (1983a) and Gubler (1985). The finite element solution did not include surface curvature effects, but in most temperature

gradient regimes, curvature may not be a significant factor (Colbeck, 1980). Christon's models did use a simplified geometry, but also explored the possibility of solving geometrically meaningful problems with coupled heat and mass transfer. Theoretically, one could explore realistic geometries using this approach, but it may be computationally burdensome as the number of degrees of freedom required can become large. Christon et al.(1994) considered 3-D periodic cell geometries to aid in simplicity and efficiency, yet their model still required 40,000-80,000 degrees of freedom. They found that the majority of computation time was spent solving the system of equations, followed by mesh movement, flux calculations, and coefficient matrix assembly calculations. By the nature of the studies and discussion presented, limited computational resources were clearly an issue for this finite element technique.

Several authors have used continuum mixture theory to describe various aspects of a phase changing snowpack. Morland et al. (1990) presented a four constituent continuum theory of mixtures to describe a three dimensional natural snowpack. They utilized four phases (ice, water, air and water vapor) and modeled their interactions through the mass, linear momentum, and energy conservation equations for the mixture. Constitutive relationships for each phase were presented and retained individual phase identity. Morland et al. (1990) related conservative law's partial variables with the constitutive law's intrinsic variables. Several reasonable simplifications resulted in seventeen partial differential equations in terms of fifty-three independent variables. Due to the complexity of the general problem presented, Morland et al. (1990) did not attempt to solve the set of equations. Simplified one-dimensional solutions were presented by Jordan (1991) and Bader and Weilenmann (1992). They reduced the three-dimensional

mixture theory by assuming lateral uniformity with only vertical gradients present, eliminating a number of independent variables. Bader and Weilenmann (1992) assumed zero gas (vapor and air) velocity and neglect sensible and latent heat contributions. Jordan (1991) also assumed no gas velocity but made provisions for heat exchanges during phase change. Gray and Morland (1994) improved the one-dimensional approach by including more complete gaseous phase modeling, but eliminated two phases by only considering ice and dry air. The mixture theories discussed so far do not consider any microstructural properties. Without even the most elemental microstructural properties such as grain, bond, or pore geometries, these approaches could not be used to predict the metamorphism of snow. They are useful (with various levels of success) in determining macroscopic temperature distributions. One significant strength to the rigor of mixture theory is the first principles approach and lack of empirical corrections.

Adams and Brown (1989, 1990) were the first to use the mathematical discipline of mixture theory, plus they included microstructural considerations. They developed three-dimensional conservation and constitutive relationships for immiscible phase changing snow consisting of ice and vapor as the major constituents. A consideration for spherical grains was included, but bonds or necks were not explicitly addressed. Adams and Brown (1989) analyzed ideal homogenous snow then extended the approach to a complex layered snowpack experiencing a thermal gradient (Adams and Brown, 1990). Heat and mass flux in a snowpack with layered stratigraphy were found by numerically solving the one-dimensional versions of their equations. Brown et al. (1999) developed a mixture theory for equi-temperature metamorphism with four constituents: ice grains, intergranular ice necks, air, and water vapor. Brown modeled snow as a distribution of

different sized particles with each size representing a separate phase. The theory predicted the sintering of spherical ice grains based largely on microstructural parameters. The ice constituents were defined by specific unique geometrical parameters such as grain radius, bond radius, and neck length. Geometric assumptions lead to other important parameters such as surface curvature. This approach directly linked microstructural parameters to mechanical and thermodynamic processes. Brown et al. (1999) were able to grow larger grains at the expense of smaller grains without explicitly designating source and sink grains. Intergranular necks grew at the expense of all grains, with decreasing growth rates as sintering progressed. The complicated mass transfer process was highly coupled to the microstructure, leading the authors to the conclusion that accurate textural descriptions are required in any sophisticated metamorphism modeling. This model has not been applied to a temperature gradient environment, but the development was not limited to equi-temperature conditions.

The need for accurate avalanche forecasting has led to the development of several snowcover models able to predict mountain snowpack evolution. Most of the research efforts described thus far were focused on scientific understanding of snow processes. The models used in avalanche forecasting have an "operational" focus. The goal of these models is the prediction of snowcover response to commonly available inputs, such as measurements from remote meteorological stations. SNTHRM (Jordan, 1991) was developed to find temperatures within the snowpack and particularly at the surface. The model incorporated snow layering and boundary conditions determined by meteorological instruments, but did not address snow microstructure in any detail. CROCUS (Brun et al., 1989) began as a mass and energy balance model able to predict

settlement, phase change, density, and temperature profiles. Early versions of CROCUS did not include detailed reference to microstructure. In later versions (Brun et al., 1992), empirical metamorphism laws were incorporated in CROCUS to calculate "dendricity" and "sphericity" of the snow. While the heat and mass balances were physically based, predictions of viscosity, thermal conductivity, settling, grain size, and grain shape remained largely empirical, potentially limiting the model's application. The Swiss Federal Institute for Snow and Avalanche Research developed one of the more sophisticated operational models, SNOWPACK. SNOWPACK used a lagrangian finite element approach to solve for heat and mass transfer, stresses and strains in snow (Lehning et al., 1999). Automated weather stations located at 45 points in the Swiss Alps provided SNOWPACK with upper surface boundary conditions (Brown et al., 2000) for finding temperatures and settling rates. Early versions of SNOWPACK used the same empirical metamorphism models as CROCUS, but recently, new physically based models have been added. The addition of Adams and Sato's (1993) microstructural effective conductivity model improved the heat conduction capability. Results from Brown et al. (1999) mixture theory were used to predict the metamorphism of equilibrium forms in an equi-temperature environment (Brown et al, 2000). This enhancement allowed SNOWPACK to calculate grain and bond growth rates during small temperature gradient conditions. The mixture theory calculations proved too burdensome to use in an operational program, so equations defining grain and bond growth as a function of grain size, bond size, density and temperature were generated from mixture theory and incorporated into SNOWPACK. When a significant temperature gradient ($>10°C/m$) was present, a microstructurally based heat and mass flux model was used (Satyawali, 1999;

Brown et al., 2000; Baunach et al., 2001) to calculate grain and bond growth rates. Each metamorphism model in SNOWPACK was applicable to different environments, and was completely different from the other. There was not a smooth or continuous transition between the two metamorphism models. Brown et al. (2000) commented "Future research should be directed at developing an all-encompassing theory that will work continuously from temperature gradients ranging from 0°C/m to higher than 100°C/m."

Lundy et al. (2000) gathered weather station information from the Bridger Range near Bozeman, Montana during a validation study of the Swiss SNOWPACK model. The weather station was established to provide boundary conditions for the model, as well as to provide temperature measurements through the snow depth. Weekly on-site observations of snowpack stratigraphy were performed. They found SNOWAPCK performed well for predicting internal temperatures, reasonably well for predicting density, and poorly at predicting grain size and shape. While some of the grain size error was attributed to the model, Lundy et al. (2000) pointed out the inherent accuracy issues associated with field observations, namely, that no standardized field observation technique currently exists.

Summary

Snow metamorphism modeling originated to explain the complicated time-varying snow structures found in natural snowpacks. Experimental investigations have provided some explanation as to when certain morphologies are present, but do not always answer the fundamental physical questions of why they happen. Early

investigations of heat and mass transfer utilized simple models to explain these complex processes with varying degrees of success. As the research matured, the importance of microstructure in nearly all aspects of snow performance became evident. As new studies are published, many point to the need for incorporating microstructure into any physical model.

Snow microstructure has been traditionally categorized by the temperature environment. Two major microstructural categories, with grains defined as smooth and rounded or sharp-edged and faceted, have been the focus of numerous experimental and theoretical studies. Past efforts have, in general, focused on grain structure with little discussion of the intergranular bonding. Theories have been developed that adequately explain the physics of snow sintering in an equi-temperature environment and faceted grain development in the presence of a temperature gradient. To date, no one has presented a unified theory of metamorphism that includes detailed microstructure yet is not restricted by the temperature environment. In fact, Arons and Colbeck (1995) comment "we still lack a model that integrates fundamental elements of geometry and the transfer of sensible and latent heat in a physically sound inductive model." Several of the studies allow insight into physical processes but do not lend themselves to inclusion in an operational model used for snowpack evolution calculations. A unifying conservation theory that accounts for the time varying microstructure yet is portable to snow prediction models is desired.

Research Objective

The objective of this research is to develop a unifying dry snow microstructure metamorphism theory that accounts for important physical parameters and processes yet is applicable in general thermal environments. The approach should be consistent with previous research and be supported by experimental data. The next chapter identifies the key parameters and processes and then proposes a numerical approach to examine snow metamorphism.

CHAPTER 2

THEORETICAL DEVELOPMENT

Basic Geometric Model

The metamorphism of dry snow involves complex interactions between the ice matrix and water vapor. Water vapor diffuses through air in the pore space, heat flows in the ice and in the pore space, and mass exchange between the pore vapor and ice matrix occurs. The nature of the phase change depends upon the ice and pore microstructural geometry, vapor environment, and temperatures. Because of these factors, the complex coupled characteristics of the physical processes and interactions have eluded previous models of these processes. In this chapter, an approach detailing important physical processes is developed. While several simplifying assumptions are presented, the theory retains key features previously not considered. The chapter starts with a geometric model definition, then key physical relationships are developed, and finally a numerical solution technique to the resulting non-linear coupled differential equations is presented.

The inclusion of detailed microstructural features is an important aspect to any effort hoping to accurately predict snow responses. Figure 1 is a scanning electron microscope image of typical snow that has not been subjected to significant temperature gradients.
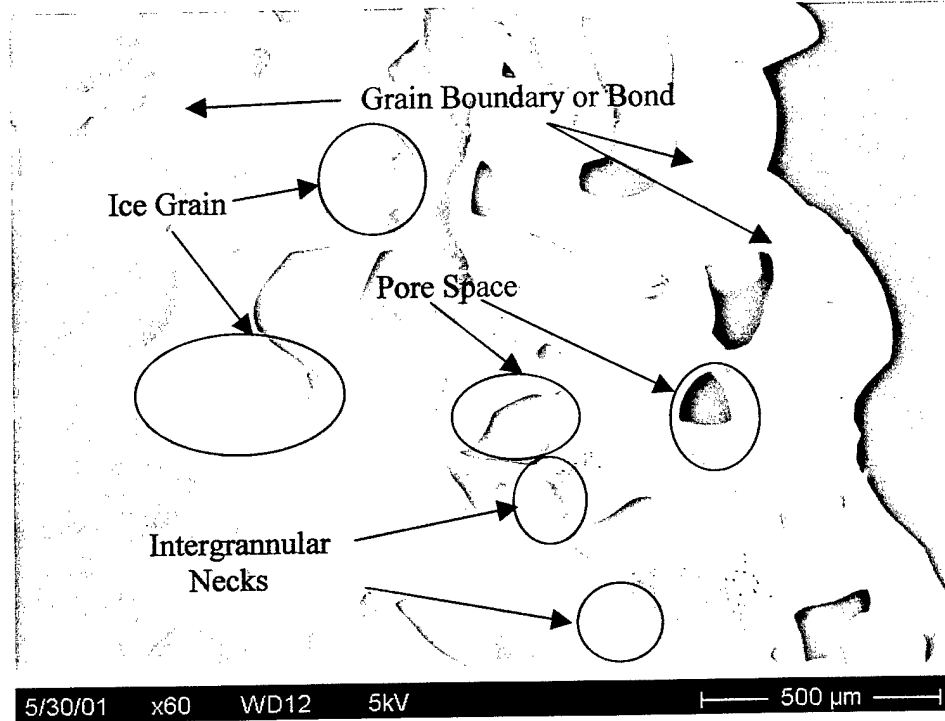
Figure 1. Scanning electron microscope image identifying typical microstructural features of snow that has been kept under macroscopically isothermal conditions.

The smooth and rounded features of the grains and interconnections are readily apparent. This morphology is commonly referred to as the equi-temperature (Sommerfeld and LaChapelle, 1970) or equilibrium form (Colbeck, 1983b). The grains are generally smooth convex structures with inter-connecting concave necks bonding neighboring grains. The pore space is clearly visible surrounding the grains and necks. Grain boundaries, also referred to as bonds, are visible at the center of the necks. To model the ice geometry, some simplifications are made. First, the grains for this morphology are assumed to be spherical. There may be several different sized grains, but the equilibrium forms are assumed perfectly round. A universally accepted intergranular neck definition does not exist. Therefore, smooth concave necks spanning either side of

crystal bonds are assumed to make the interparticle connections. Edens (1997) developed a stereological approach defining the grain-neck transition where the surface curvature changes sign. Geometric definitions used here are similar to Brown et al. (1999).
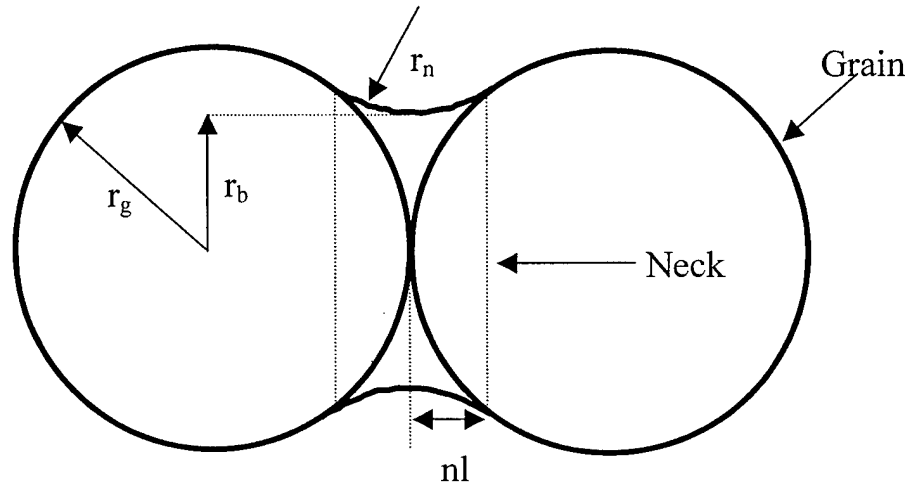
Figure 2. Basic equilibrium form grain and neck geometry

Figure 2 illustrates the basic equilibrium form of grain and neck definitions. The spherical grain radius is denoted by r_g, the bond radius is r_b, the concave neck surface radius of curvature is r_n, and the neck half length is given by nl. The convex to concave surface transition separates necks and grains. Important relationships can be obtained from simple geometric relationships from figure 2. The grain radius and bond radius, a measure of bond maturity, will be assumed to be known initial conditions. It is then desirable to represent other geometric quantities in terms of grain and bond radii. From figure 2

$$r_g^2 + \left(r_n + r_b\right)^2 = \left(r_g + r_n\right)^2.$$

(1)

The neck surface radius is then given by

$$r_n = \frac{r_b^2}{2(r_g - r_b)}.$$ (2)

The neck length is related to bond and grain radii by

$$nl = \frac{r_g r_b^2}{r_b^2 + 2r_g^2 - 2r_b r_g}.$$ (3)

The neck surface mean radius of curvature, ρ_s, is given by (Colbeck, 1980)

$$\frac{2}{\rho_s} = \frac{1}{r_b} - \frac{1}{r_n}.$$ (4)

In equations (1)-(4), all the values of radii of curvature are assumed numerically positive. Later, when calculating vapor densities over curved surfaces, concave radii of curvature will be numerically negative. It is interesting to note that when $r_b = r_n$, the curvature terms cancel out and the neck surface is equivalent to a flat surface. Using equation (2), it can be shown that this happens when $r_b/r_g = 2/3$. For two equally sized grains of this geometry, as the bond to grain radius ratio approaches 2/3, the neck surface curvature approaches zero.

With individual grains and their interconnecting necks defined, a macroscopic geometric model is required. The complex structure of snow makes the development of a realistic geometric model with general application difficult. For snow in an isothermal environment, it is assumed that the material is macroscopically isotropic, ie, the microstructure does not depend upon the observation direction. When a temperature gradient is applied, metamorphism can result in directionally oriented microstructure. During long exposure to significant temperature gradients, channels or mesopores

develop parallel to the temperature gradient. Ice chains may also develop with large, striated, faceted grains appearing. For depth hoar crystals and pore channels to develop, the temperature gradient must be large (>10°C/m), the density below 350 kg/m^3, and sufficient pore space available for vapor transport and grain growth (Akitaya, 1974a; Marbouty, 1980), although channel development has been observed in higher density snow (Adams et al, 1994). Due to this preferred orientation, it is assumed that the snow geometric properties are symmetric with respect to an axis of rotation about the temperature gradient direction, making the problem transversely isotropic. Symmetry is assumed in any plane perpendicular to the temperature gradient. To model equi-temperature and temperature gradient environments, a microscopic geometry is used by linking a large number of ice spheres and necks together with the geometry specified in figure 2. The geometry shown in figure 1 is modeled by arranging the grains, bonds, and pore spaces into a vertical configuration with symmetry assumed in the transverse directions. The differential equations defining the metamorphic processes of interest will be developed later in this chapter, but as a preview, a finite difference solution will be presented. As a result, a microstructural definition of elements and nodes is desired. The element discretized ice and pore geometry is shown in figure 3, nodal definitions will be presented when required by the numerical solution.
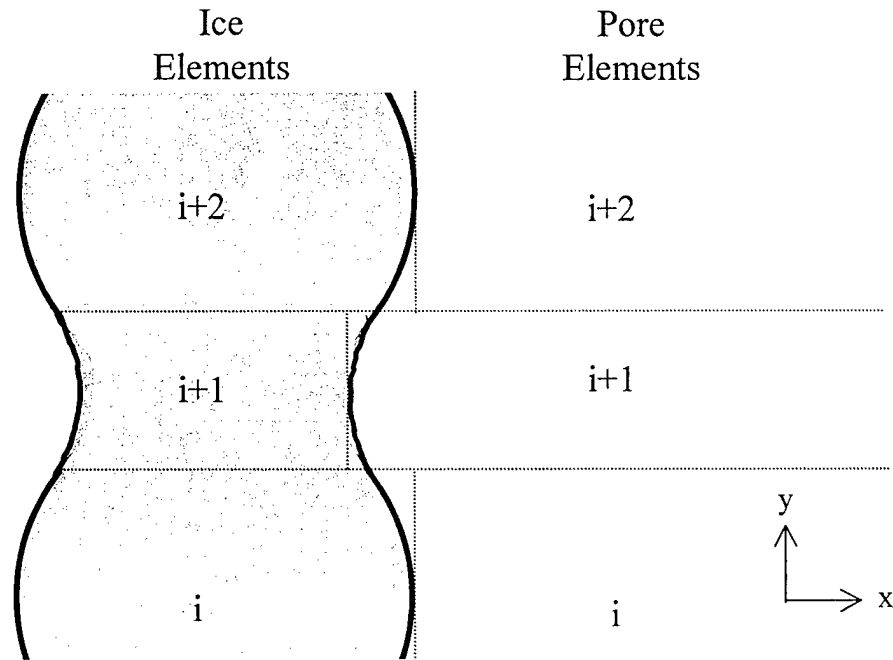
Figure 3. Grain, neck, and pore discretized elements.

In figure 3, element boundaries are defined at the transition between spherical grains and concave necks. Pore elements are defined by rotating the rectangular crossection in figure 3 about the ice centroidal axis leaving cylindrical pore. Each grain and neck represents an individual ice element. The pore is divided into similar elements having the same vertical dimension as each ice element. Element vertical dimensions are given by grain radii and neck lengths defined in figure 2. The ice and pore elements are numbered sequentially in the y direction. The number of grains and necks must be odd since a neck unconnected to a grain is not allowed. The microstructure discretization in figure 3 may be stacked vertically to any desired dimension. For equi-temperature conditions, this model represents a "straightened-out" configuration of grains, necks and

pore spaces identified in figure 1. If temperature gradient conditions prevail, this geometry provides the base ice network for the growth of faceted grains and bonds. The temperature gradient will be applied parallel to the y direction in the geometric model. Satyawali (1999) presented a similar geometry for simulating bond growth in a temperature gradient environment. He defined cells consisting of two grains connected by one neck with a vertical pore separating each cell. No cell connections extended in the direction of the temperature gradient. The ice geometry is well defined at this point, but only one dimension of each pore element has been defined. While the height of each pore is defined by grain radius and neck length, the other dimensions still remain undefined.
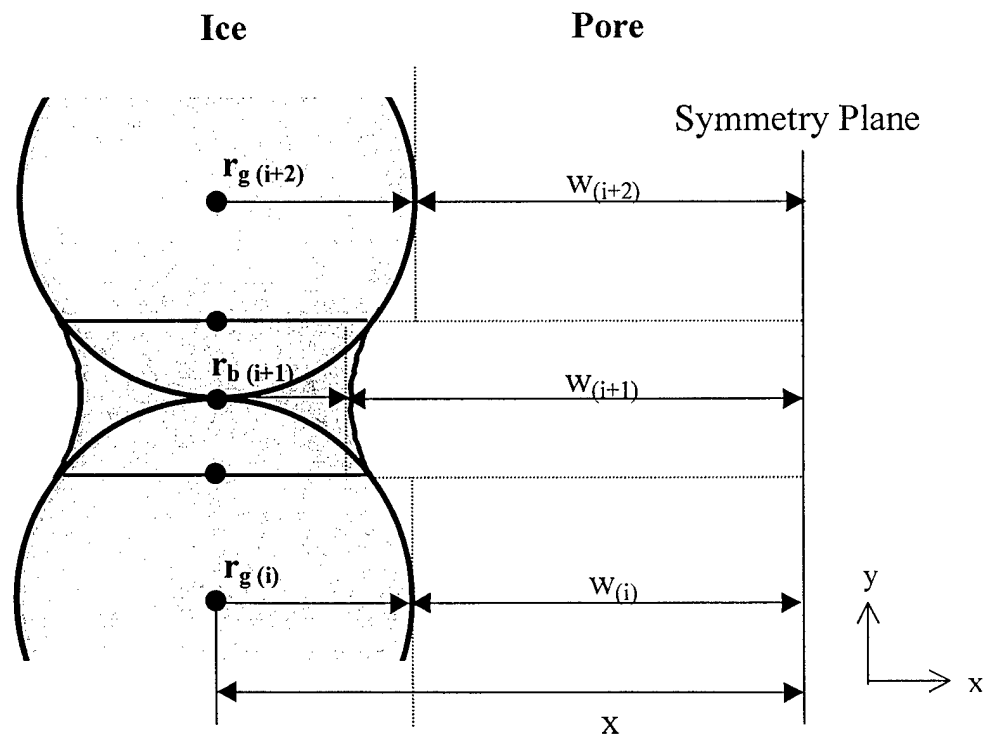
Figure 4. Pore dimensions.

Since the problem has been assumed isotropic or transversely isotropic (depending upon thermal environment), the model in figure 3 has symmetry about the vertical y axis. Figure 4 represents one model used to calculate pore dimensions.

The distance from the ice center to the symmetry plane is x. The symmtery plane is defined to empahsize that these model elements may be repeated indefinately. Each pore element is then assigned a width, $w_{(i)}$, based on the distance from the ice surface to the symmetry plane. If the ice geometry is known, the total pore volume is given by the snow density. The snow density and pore, ice volumes can be related by

$$\rho_{snow} = \rho_{ice} \frac{V_{ice}}{V_{total}} = \rho_{ice} \left(1 - \frac{V_{pore}}{V_{total}} \right), \tag{5}$$

where ρ_{snow} is the snow density, ρ_{ice} is ice density, V_{ice} is the total ice volume in the model, V_{pore} is the total pore volume in the model, and V_{total} is the sum of ice and pore volumes. For dry snow considered here, any liquid volume is neglected. Since the snow density and ice geometry are known, the total volume of pore and ice is given by

$$V_{total} = \frac{\rho_{ice}}{\rho_{snow}} V_{ice}. \tag{6}$$

The total pore volume is now given by

$$V_{pore} = V_{total} - V_{ice}. \tag{7}$$

Equation (7) gives the total pore volume for a sample with known density and ice microstructure. It is now required to apportion the pore volume to individual pore elements of the geometric model. The assumed pore shape is a rectangular cross section revolved about the y axis centered in the ice. 3-D "washer" shaped pore elements result. The total pore volume is given by the sum of all the pore element volumes

$$V_{pore} = 2\pi \sum_{odd\,i}\left(\frac{r_{g(i)}+x}{2}\right)\left(2r_{g(i)}\right)\left(x-r_{g(i)}\right) + 2\pi \sum_{even\,i}\left(\frac{r_{b(i)}+x}{2}\right)\left(2\,nl_{(i)}\right)\left(x-r_{b(i)}\right). \tag{8}$$

The odd numbered elements represent grains and the even numbered elements represent necks. Equation (8) was developed so individual pore elements may be defined for each grain and neck. While other pore models exist, they do not lend themselves to the microscopic approach proposed here. In equation (8), it is assumed that $r_{g(i)} \gg nl_{(i)}$, the reduction of $r_{g(i)}$ by $nl_{(i)}$ is neglected. For a large bond to grain ratio of 0.5, equation (3) gives a neck length that is 1/5 the size of the grain radius. Of course, the relative size of the neck to the grain will decrease with smaller bonds. The location of the symmetry plane, x, is now

$$x = \left[\frac{V_{pore} + 2\pi\left(\sum_{odd\,i} r_{g(i)}^3 + \sum_{even\,i} r_{b(i)}^2 nl_{(i)}\right)}{2\pi\left(\sum_{odd\,i} r_{g(i)} + \sum_{even\,i} nl_{(i)}\right)}\right]^{1/2}. \tag{9}$$

With the symmetric distance known, each pore width is found by

$$w_i = x - r_{g(i)} \text{ for grains or } w_i = x - r_{b(i)} \text{ for necks.} \tag{10}$$

Each individual pore volume can now be calculated based on the ice geometry and w_i, using relationships found in equation (8).

An alternative method for finding pore volume can be achieved by weighting the individual pore volume based on the relative size of the grains and necks. After finding the total pore volume using equations (5)-(7), the individual pore volume can be calculated by

$$V_{pore(i)} = \frac{r_i}{\sum r_i} V_{pore} , \tag{11}$$

where r_i is the grain radius for odd i and is the neck length for even i. Both methods are implemented in the research, and yield similar results. The first approach is more rigorous and is therefore preferred. The equilibrium form ice and pore geometries are now fully defined for a discretized model. Pore elements associated with ice grain and neck elements are also fully defined.

Governing Equations

The physical processes of snow metamorphism are very complex. Heat and mass move through the pore space while heat moves through the ice network. These processes are coupled by latent heat transfer and mass transport associated with phase change. To begin the development of a physical model, several simplifying assumptions are required. These assumptions are not all inclusive for the problem (others will be presented later), but are introduced here to begin the development.

Initial Assumptions

1. *Heat conduction in the pore space can be neglected, so that only heat flow through the ice network is considered.* This is a common assumption given the fact that the thermal conductivity of saturated vapor at cold temperatures is two orders of magnitude smaller than the thermal conductivity of pure ice (Incropera and DeWitt,1985).

2. *Saturated vapor, for a given temperature, exists everywhere in the pore spaces.* Even though no measurements of relative humidity in pore spaces have been published, this is a classic assumption given the large surface area of the ice available to interact with the pore.

3. *The vapor saturated pore may be treated as an ideal gas.* This is a common thermodynamic assumption for low pressure water vapor applications. The snowpack absolute pressure should be very close to atmospheric.

4. *The primary mass transport mechanism is vapor diffusion through the pore.* As discussed in chapter 1, substantial research has shown convection to be a significant mass transport mechanism under very select conditions. In general, convection is neglected for metamorphism modeling. Other diffusion mechanisms associated with the ice, such as lattice, surface, and grain boundary, are considered small and neglected in the primary development.

5. *Liquid water in the snow is not considered.* Solid ice and water vapor are the only phases of water considered for dry snow.

Heat and Mass Fluxes Considered

Figure 5 shows graphically the heat and mass fluxes available given the geometry and assumptions discussed. Mass can diffuse vertically through the pore spaces as well as to and from the ice surface during phase changes. Heat can flow vertically through the ice network as well as to or from the ice surface due to the latent heat exchange associated with phase change. The details of the phase change are addressed in a later section of this chapter, but for now, we assume these processes are present.
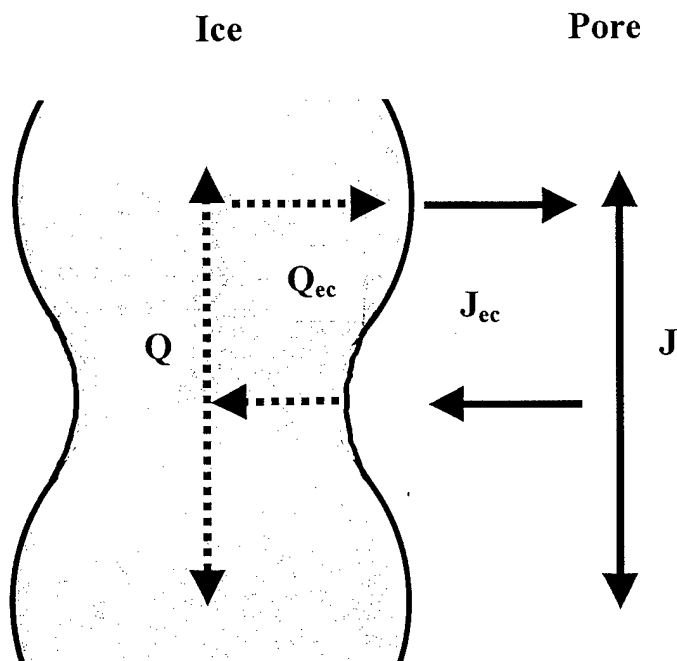
Figure5. Heat and mass flows during metamorphism. Q represents the heat flow through the ice network, Q_{ec} is the heat flow from evaporation or condensation, J is the mass flow in the pore, J_{ec} is the mass flow from evaporation or condensation.

Movement of Vapor in the Pore Spaces

The diffusion of water vapor in the pore space is governed by density (concentration) gradients as described by Fick's Law,

$$\underline{J} = -D\vec{\nabla}\rho, \tag{12}$$

where J is the molecular flux vector ($kg/(sm^2)$), D is the water vapor diffusion coefficient in air (m^2/s), and ρ is the vapor density (kg/m^3). Using the ideal gas relationship for the vapor, equation (12) becomes:

$$\underline{J} = -D\left(\frac{1}{RT}\vec{\nabla}P - \frac{P}{RT^2}\vec{\nabla}T\right), \tag{13}$$

where R is the water vapor gas constant (J/(kgK)), T is the pore temperature (K), and P is the pore pressure (Pa). For pressure, P(T(x,y,z)), the chain rule yields

$$\underline{\bar{\nabla}} P(T(x,y,z)) = \frac{\partial P}{\partial T} \underline{\bar{\nabla}} T \ . \tag{14}$$

The equilibrium vapor pressure temperature dependence is given by the Clausius-Clapeyron relationship, with the differential form (eg, Weast, 1985)

$$\frac{\partial P}{\partial T} = \frac{PL}{RT^2} \ , \tag{15}$$

where L is the water latent heat of sublimation (J/kg). Substituting equations (14) and (15) into (13) gives

$$\underline{J} = -D \frac{P}{RT^2} \left(\frac{L}{RT} - 1 \right) \underline{\bar{\nabla}} T \ . \tag{16}$$

Since L/(RT) >> 1, equation (16) can be approximated as

$$\underline{J} = -D \frac{PL}{R^2 T^3} \underline{\bar{\nabla}} T = \frac{-D}{RT} \underline{\bar{\nabla}} P \ . \tag{17}$$

Equation (17) is a commonly used form of Fick's Law for low pressure water vapor treated as an ideal gas.

Water vapor will flow in the pore due to concentration gradients, but phase changes resulting in the addition or removal of water vapor in the pore are also important. Mass conservation for a flow with mass sources and sinks is given by

$$\frac{\partial \rho}{\partial t} + \underline{\vec{\nabla}} \cdot (\rho \underline{V}) = MS \ , \tag{18}$$

where V is the vapor flow velocity (m/s), t is time (s), and MS is the mass supply or sink from phase change (kg/m³s). MS is identical to phase interaction from mixture theory, except here, only one gaseous and one solid phase is considered. The mass interactions

are restricted to the solid and gas phases. The mass supply term is coupled to the ice phase through flux resulting from phase change (J_{cc}). The sign convention used here is that mass added to the pore results in a numerically positive MS term.

Next, the spatial dimension of the problem is reduced. Recalling the discussion of equi-temperature and temperature gradient environments, isotropy is assumed to exist in the horizontal plane. In addition, only mass flux in the horizontal plane from mass exchanges during phase change (figure 5) is considered. The ability for mass to enter the pore, diffuse to another area vertically in the microstructure, and then redeposit on the ice is critical. To account for the two dimensional nature of the problem, diffusion due to phase change will be included in the mass source term. As vapor enters the pore due to sublimation from the ice, vapor flux is included in equation (18) as a mass source. If vapor is leaving the pore due to condensation on the ice, a mass sink is present in equation (18). This approach reduces the right hand side of equation (18) to one dimension, but the process is still considered quasi-two dimensional due to the phase change interactions. Considering one dimensional diffusion (vertical y direction) and mass sources and sinks due to phase change, equation (17) becomes

$$J = \frac{-DPL}{R^2 T^3} \frac{\partial T}{\partial y}.$$

(19)

For one dimensional flow

$$\rho V = J,$$

(20)

equation (18) becomes

$$\frac{\partial \rho}{\partial t} + \frac{\partial}{\partial y}\left(\frac{-DPL}{R^2 T^3} \frac{\partial T}{\partial y}\right) = MS.$$

(21)

The unsteady term in equation (21) may be expressed as

$$\frac{\partial \rho}{\partial t} = \frac{\partial \rho}{\partial T} \frac{\partial T}{\partial t}.$$ (22)

Using the ideal gas relationship and neglecting a small term (as was done for a similar term in equation (16)), equation (22) becomes

$$\frac{\partial \rho}{\partial t} = \frac{1}{RT} \frac{\partial P}{\partial t},$$ (23)

but,

$$\frac{\partial P}{\partial t} = \frac{\partial P}{\partial T} \frac{\partial T}{\partial t}.$$ (24)

Using equations (24) and (15) in (23) leaves

$$\frac{\partial \rho}{\partial t} = \frac{PL}{R^2 T^3} \frac{\partial T}{\partial t}.$$ (25)

After expanding equation (21) and substituting equation (25) into (21), the complete form of the mass conservation relationship becomes

$$\frac{PL}{R^2 T^3} \frac{\partial T}{\partial t} - \frac{DPL}{R^2 T^3} \left[\frac{\partial^2 T}{\partial y^2} + \frac{L}{RT^2} \left(\frac{\partial T}{\partial y} \right)^2 - \frac{3}{T} \frac{\partial T}{\partial y} \right] = MS.$$ (26)

At this point, another simplifying assumption is made. The process of mass diffusion is assumed to be quasi-steady, neglecting the local derivative in equation (26). Christon et al. (1990, 1994) calculated temperature gradient mass storage time constants on the order of milliseconds, while the process of temperature gradient metamorphism is on the order of several minutes (at least). Neglecting storage terms is consistent with Kuroiwa's (1974) observation that temperature gradient metamorphism is a quasi-steady process. The temperature distribution, ice and pore geometry, and solid/vapor interfaces

will still change in time making the problem quasi-steady. It is assumed that the time constant associated with equi-temperature metamorphism is much longer than for temperature gradient metamorphism since it is generally a much slower process. The numerical solution in the current study will allow for environment and response changes in time, but neglect storage terms during each time increment. During each time increment, the vapor flows are assumed steady. Pore temperature may then be considered strictly a function of vertical position. Equation (26) was developed in full form for completeness, but with a quasi-steady assumption it may be simplified to

$$\frac{-DPL}{R^2 T^3}\left(\frac{d^2 T}{dy^2} + \frac{L}{RT^2}\left(\frac{dT}{dy}\right)^2 - \frac{3}{T}\frac{dT}{dy}\right) = MS. \tag{27}$$

The pore mass continuity equation (27) is a non-linear, second order, ordinary differential equation that is coupled to the ice phase through an interaction term. While no mathematical definition of the mass source term has yet been presented, the left hand side of equation (27) is a function of pore temperature only. As such, when the description of MS is presented, the goal will be to include the pore temperature distribution as a dependent variable. Of course, properties of the ice will be included in the interaction term, creating the desired coupling during metamorphism.

Heat Transfer in the Ice Network

Heat conduction through the solid ice phase is now considered. Heat is allowed to flow vertically (y direction) through the ice network, and horizontally (x direction) to accommodate phase change. As with the vapor derivation, a quasi-two dimensional approach is used. Vertical heat flow proceeds while heat enters or leaves the ice through

phase changes at the lateral ice surface taken in the horizontal plane. A differential ice element is shown in figure 6, displaying the main heat flow in the ice network (Q_y) and heat flow due to phase change (dQ_{ec}).
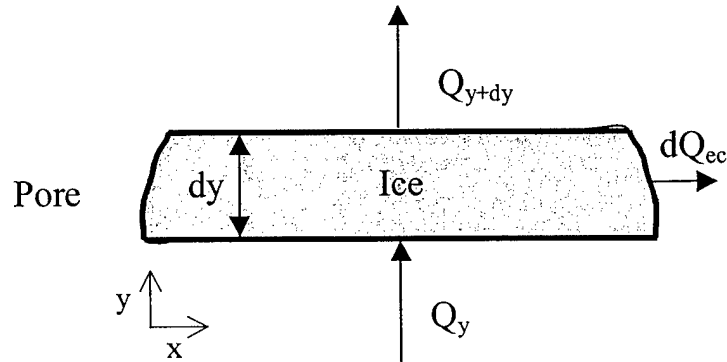
Figure 6. Differential Ice Element. Q_y and Q_{y+dy} are heat fluxes in the y direction, dQ_{ec} is the differential heat flow from evaporation or condensation.

Heat due to phase change enters or leaves the ice depending upon whether it is condensing or sublimating. If water vapor is sublimating from the ice to the pore, latent heat is leaving the ice. The sign convention used here is consistent with the vapor source previously defined, i.e., sublimation is considered positive as heat leaves the ice. A truncated Taylor series approximation for heat flux is given by

$$Q_{y+dy} = Q_y + \frac{\partial Q_y}{\partial y} dy, \tag{28}$$

where Q is the total conduction heat flow (W) for an area, A. Fourier's heat conduction law is

$$Q_y = -kA \frac{d\theta}{dy}, \tag{29}$$

where k is the ice thermal conductivity (W/mK), A is the cross sectional area for heat diffusion (m^2), and θ is the ice temperature (K). Conservation of energy for the differential element in figure 6 yields

$$Q_y = Q_{y+dy} + dQ_{ec} + \rho_{ice} C \frac{\partial \theta}{\partial t} dVol_{ice}, \qquad (30)$$

where dQ_{ec} is the differential heat flow from sublimation or condensation (W), ρ_{ice} is the density of ice (kg/m^3), C is the ice specific heat (J/kgK), and $dVol_{ice}$ is differential element volume (m^3). Using equation (29), equation (30) becomes

$$\frac{\partial}{\partial y}\left(kA \frac{\partial \theta}{\partial y} \right) dy = dQ_{ec} + \rho_{ice} C \frac{\partial \theta}{\partial t} dVol_{ice}. \qquad (31)$$

A quasi-steady assumption is now made, similar to the vapor development. Lock (1990) finds this limitation acceptable. He applies the quasi-steady Stefan (1891) problem to a wide class of ice problems involving phase change. Lock (1990) terms this problem "quasi-steady" because a moving phase change boundary must be accounted for, even though the storage term in the energy equation is neglected. Neglecting the ice heat capacity, and expanding equation (31) leaves

$$\left(kA \frac{\partial^2 \theta}{\partial y^2} + k \frac{\partial A}{\partial y} \frac{\partial \theta}{\partial y} \right) dy = dQ_{ec}. \qquad (32)$$

Equation (32) is very similar to a variable fin geometry heat transfer problem (Incropera and DeWitt, 1985), except it contains a phase change heat sink in place of radiation or convection terms from a fin. The differential phase change term may be expressed in terms of the vapor flux leaving the surface, J_{ec}, the latent heat of sublimation, L, and a differential surface area available for phase change, dA_{ec},

$$dQ_{ec} = L\left(J_{ec} dA_{ec}\right). \tag{33}$$

It is important to notice that two area terms have been presented in this section, and these areas are quite different. A(y) is the ice cross sectional area, perpendicular to the y axis, available for heat flow, while dA_{ec} is the differential surface area of the ice available for phase change. Assuming ice temperature, θ, is a function of y only, the energy balance now becomes

$$kA\frac{d^2\theta}{dy^2} + k\frac{dA}{dy}\frac{d\theta}{dy} = LJ_{ec}\frac{dA_{ec}}{dy}. \tag{34}$$

In the vapor conservation equation, we defined a vapor/ice interaction term in the form of a mass source to and from the vapor during phase change. In keeping with the same approach, a heat source is now defined,

$$HS = J_{ec}L\frac{dA_{ec}}{dy}, \tag{35}$$

where HS is a heat source term that is coupled to the pore through the phase change at the boundary. While not explicitly required, HS is defined here to show the heat conservation analogy to the MS term in the vapor conservation relationship. As will be seen later, HS and MS are related by the mass flux, J_{ec}, to and from the phase change boundary. J_{ec} will be a nonlinear function of ice and pore parameters, providing the desired coupling between the solid and vapor phases. The final form of the ice conservation relationship becomes

$$\frac{d^2\theta}{dy^2} + \frac{1}{A}\frac{dA}{dy}\frac{d\theta}{dy} = \frac{HS}{kA}. \tag{36}$$

At this point, the heat and mass interaction terms need to be defined in detail. They each will depend upon the size and direction of the phase change flux which is dependent upon the microstructural geometry and current environmental conditions. The equi-temperature and temperature gradient environments result in different microstructural geometries, therefore, the heat and mass interaction terms will be derived separately for each condition.

Mass and Heat Source Interactions from Phase Change for Equilibrium Forms

Equations (27) and (36) contain mass and heat interaction terms (respectively). The mass interaction, MS, is a mass supply to the pore from phase changes at the ice-pore interface. The heat interaction, HS, is a heat sink from the ice due to phase changes at the ice-pore interface. The phase change vapor flux in the horizontal direction, J_{ec} (undefined up to this point) is the coupling lynch pin between HS and MS. The vapor flux leaving the surface is dependent upon the physical processes and environmental factors in both the pore and the ice. In this section, the physics of phase change with a smooth rounded (equilibrium form (Colbeck, 1983b)) microstructural geometry is presented. The equilibrium form of the microstructure is the primary limiting factor; no assumptions are required relative to temperature gradient environment. In a following section, heat and mass interaction terms will be derived for kinetic growth forms.

The metamorphism of smooth, rounded microstructure has been termed "equi-temperature" (Sommerfeld and LaChapelle, 1970) because of its appearance in a macroscopically isothermal environment. Colbeck (1980) developed expressions for metamorphism due to surface curvature alone. He derived surface curvature relationships

for this metamorphism, but found temperature gradients quickly overcome geometric constraints. At a given temperature, the vapor pressure over a convex surface is greater than over a flat surface. Conversely, concave surfaces have a lower vapor pressure than for a flat surface at the same temperature. Metamorphism can take place as water vapor sublimates from rounded ice grains, travels by vapor diffusion through the pore, and condenses on the concave intergranular necks. Of course, for phase change and diffusion to take place, temperature gradients must exist (even if very small), creating the controversy surrounding the term "equi-temperature" metamorphism. The term "radius-of-curvature" metamorphism has been used to describe geometrically driven processes (Colbeck, 1980) which may more precisely describe this process than the term "equi-temperature" metamorphism.

Colbeck (1980) presented a rigorous thermodynamic derivation of Kelvin's equation given by

$$P_{ice} = P' \exp\left(\frac{2\sigma}{\rho_{ice}RT'\rho_s}\right), \tag{37}$$

where P_{ice} is the saturation vapor pressure (Pa) over the curved ice surface at a temperature T' (K), P' is the saturation vapor pressure (Pa) over a flat ice surface at a temperature T', R is the water vapor gas constant (J/kgK), σ is the ice surface tension (N/m), ρ_{ice} is the density of ice (kg/m³), and ρ_s is the mean ice surface radius of curvature (m) as defined in equation (4). Kelvin's equation describes the saturation vapor pressure over curved surfaces. For convex surfaces, ρ_s is positive, and is negative for concave surfaces. The integrated form of the Clausius-Clapeyron equation (15) defines saturation vapor pressure, P, as a function of temperature, T,

$$P = P_0 \exp\left[\frac{L}{R}\left(\frac{1}{T_0} - \frac{1}{T}\right)\right], \tag{38}$$

where P_0 is a reference vapor pressure (Pa) at reference temperature T_0 (K). We now have an expression for saturation vapor pressure as a function of surface geometry and another as a function of temperature. The combined metamorphic effects of temperature and geometry are vital to any realistic model. Equations (37) and (38) may be combined to get saturation vapor pressure over a curved ice surface at some arbitrary temperature T, giving (Adams and Brown, 1983; Gubler, 1985)

$$P_{ice} = P_o \exp\left(\frac{2\sigma}{\rho_{ice}RT_o\rho_s}\right)\exp\left(\frac{L}{R}\left(\frac{1}{T_o} - \frac{1}{T_s}\right)\right), \tag{39}$$

where T_s is the phase change temperature (K). The phase change is assumed to take place at a constant temperature, requiring solid and vapor very close to the phase change boundary to be at the same temperature, T_s. The derivation of surface and phase change temperatures is presented in a later section of this chapter. The temperature of phase change must account for the heat and mass flux possible given the surrounding conditions. Since metamorphism takes place at all sub-freezing temperatures, no single phase change temperature exists (unlike melt/freeze processes).

With temperature and geometric relationships for the vapor pressure of saturated vapor, the flux due to phase change can be developed. The vapor flux from phase change due to vapor pressure differences between the ice surface and surrounding pore is given by Fick's law in the one dimensional form of equation (17)

$$Jec = \frac{-D}{RT}\frac{dP_v}{dx}. \tag{40}$$

The vapor pressure differential in equation (40) is between the ice surface and surrounding pore. The ice surface vapor pressure is represented by equation (39), and the pore vapor pressure is given by equation (38). Flux is assumed positive as it enters the pore (pore mass source). Equation (40) may then be approximated by

$$J_{ec} = \frac{-DP_0}{RT\Delta x}\left(\exp\left(\frac{2\sigma}{\rho_{ice}RT_o\rho_s}\right)\exp\left(\frac{L}{R}\left(\frac{1}{T_o}-\frac{1}{T_s}\right)\right) - \exp\left(\frac{L}{R}\left(\frac{1}{T_0}-\frac{1}{T}\right)\right)\right), \quad (41)$$

where Δx is the diffusion distance (m) between the ice surface and pore. The flux due to phase change can now be related to the mass and heat terms previously developed.

The mass source term, MS, in equation (27) represents the mass flow per unit volume entering the pore. Since this interaction term is from phase change, it is related to J_{ec} by

$$MS = J_{ec}\frac{A_{ec}}{V_{pore}}, \quad (42)$$

where V_{pore} is the volume of the pore (m^3). Recall, the flux due to phase change is mass flow per unit area of phase change, so the ice surface area undergoing phase change is required for the pore mass balance. Using equations (41) and (42) in (27), the highly coupled nature of the problem becomes evident. The ice physical constants, surface geometry, temperature, and phase change temperature all appear in the pore mass conservation relationship. After substituting equations (41) and (42) in (27) and simplifying, the pore mass conservation (with equilibrium form interactions) equation results

$$\frac{L\exp\left(\frac{L}{R}\left(\frac{1}{T_0}-\frac{1}{T}\right)\right)}{RT^2}\left[\frac{d^2T}{dy^2}+\frac{L}{RT^2}\left(\frac{dT}{dy}\right)^2-\frac{3}{T}\frac{dT}{dy}\right]+$$

$$\frac{A_{ec}}{\Delta x V_{pore}}\left[\exp\left(\frac{2\sigma}{\rho_{ice}RT_o\rho_s}\right)\exp\left(\frac{L}{R}\left(\frac{1}{T_o}-\frac{1}{T_s}\right)\right)-\exp\left(\frac{L}{R}\left(\frac{1}{T_0}-\frac{1}{T}\right)\right)\right]=0. \qquad (43)$$

The heat source term, HS, in equation (36) also results from phase change and is related to J_{ec}. The amount of heat lost from the ice during phase sublimation is related to the phase change flux through equation (35). The latent heat of sublimation, L, couples the ice thermal conservation equation to the pore. The heat conduction (with equilibrium form interactions) equation becomes

$$\frac{d^2\theta}{dy^2}+\frac{1}{A}\frac{dA}{dy}\frac{d\theta}{dy}=$$

$$\frac{-DP_0L}{kART\Delta x}\frac{dA_{ec}}{dy}\left(\exp\left(\frac{2\sigma}{\rho_{ice}RT_o\rho_s}\right)\exp\left(\frac{L}{R}\left(\frac{1}{T_o}-\frac{1}{T_s}\right)\right)-\exp\left(\frac{L}{R}\left(\frac{1}{T_0}-\frac{1}{T}\right)\right)\right). \qquad (44)$$

As with the pore equation, heat conservation results in non-linear coupling to pore physical parameters and temperatures. Equations (43) and (44) contain microstructural ice and pore parameters, physical constants, ice and pore temperatures, and phase change temperature. Given a particular microstructure, the ice and pore temperatures are the primary unknowns. The phase change temperature, T_s, can be expressed in terms of the ice and pore temperatures.

Phase Change and Phase Change Temperature
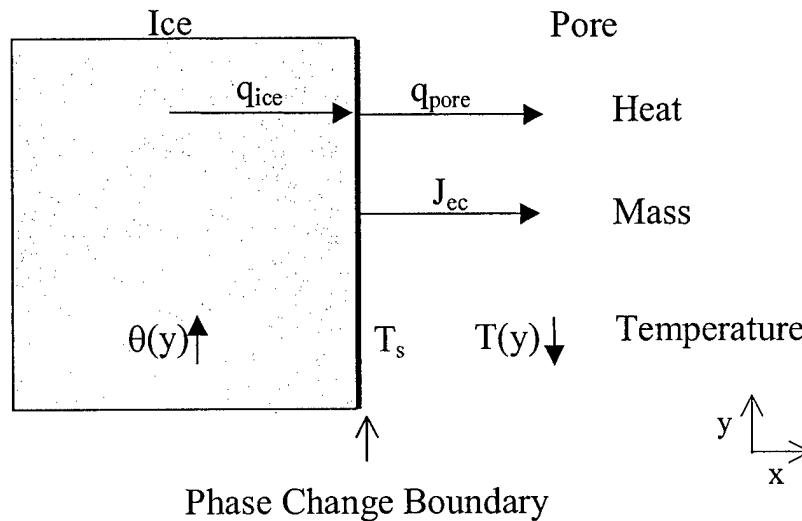
Figure 7. Heat, mass and temperature relationships between the ice and pore during sublimation.

To determine the temperature during the phase change process, the thermodynamics of phase change must be examined. Figure 7 shows the relationships of heat, mass and temperature during sublimation near a flat ice surface. q_{ice} is the heat flux for phase change in the ice (W/m^2), q_{pore} is the heat flux for phase change in the pore (W/m^2), J_{ec} is the vapor flux (kg/sm^2) leaving the surface, $\theta(y)$ is the ice temperature (K) away from the surface, $T(y)$ is the pore temperature (K) away from the surface, and T_s is the surface temperature. Sublimation commences as the required latent heat is brought to the surface by conduction. In order for heat conduction to the surface to commence, thermal gradients must exist from the ice and pore to the surface. For sublimation shown in figure 7, warmer ice temperatures and cooler pore temperatures result in heat

conduction to the surface. An energy balance at the surface yields (Lunardini, 1988; Lock, 1990)

$$q_{ice} - q_{pore} = q_L,$$
(45)

where q_L is the latent heat flux (W/m^2) for sublimation. q_L is positive during sublimation and negative during condensation. One dimensional heat conduction for phase change gives

$$\left(-k_{ice}\frac{d\theta}{dx} + k_{pore}\frac{dT}{dx}\right)A = \dot{m}L,$$
(46)

where k_{ice} and k_{pore} are thermal conductivities (W/mK), A is a conduction area (m^2), $\dot{m}$ is the mass flow from phase change (kg/s), L is the latent heat of sublimation (J/kg), θ is the ice temperature (K), and T is the pore temperature. In the previous sections, it was assumed ice and pore temperatures were a function of y only, but here, the thermal gradient from the ice or pore interior to the surface is included. The ice and pore temperatures will be assumed fixed allowing the calculation of a surface or phase change temperature as the primary variable. Since the solid and vapor phases at the ice/pore interface are at the same temperature, thermal gradients for both the ice and pore will include phase change temperature, T_s. If the phase change and conduction areas are equal at the surface (Colbeck, 1980; Lock, 1990), equation (46) becomes

$$-k_{ice}\frac{d\theta}{dx} + k_{pore}\frac{dT}{dx} = \frac{\dot{m}}{A}L,$$
(47)

but

$$J_{ec} = \frac{\dot{m}}{A}.$$
(48)

Substituting equation (40) for the phase change flux into (48) and (47) leaves,

$$-k_{ice}\frac{d\theta}{dx} + k_{pore}\frac{dT}{dx} = \frac{-DL}{RT\Delta x}\left(P_{pore} - P_{ice}\right).$$ (49)

If the expressions for pore and ice surface vapor pressure from equations (38) and (39) are used in (49), the fully coupled form of the surface/phase change temperature differential equation is

$$-k_{ice}\frac{d\theta}{dx} + k_{pore}\frac{dT}{dx} -$$

$$\frac{DP_0L}{RT\Delta x}\left[\exp\left(\frac{2\sigma}{\rho_{ice}RT_o\rho_s}\right)\exp\left(\frac{L}{R}\left(\frac{1}{T_o} - \frac{1}{T_s}\right)\right) - \exp\left(\frac{L}{R}\left(\frac{1}{T_0} - \frac{1}{T}\right)\right)\right] = 0.$$ (50)

The phase change conduction problem is coupled to the ice and pore through the ice and pore temperatures, ice and pore geometries, and physical constants.

Heat and Mass Interactions from Phase Change for Kinetic Growth Forms

The differential equations developed so far make no distinction between equi-temperature and temperature gradient thermal environments. Certain restrictions on the ice and pore geometry were presented in the first section of this chapter. The ice geometry described so far has been the smooth rounded equilibrium form common in an equi-temperature environment. At this point, it is appropriate to extend the theory to include other geometric forms. When significant temperature gradients exists, it has been observed that large faceted crystals may develop quickly in the snowpack. The presence of these crystals has been attributed to lower material strength (Bradley et al., 1977a;

Armstrong, 1980; Adams and Brown, 1982) and increased chance of avalanche release (Bradley et al., 1977b; Satyawali, 1998; McElwaine, 2000). These crystal forms are often referred to as facets, temperature gradient metamorphism forms, kinetic forms, recrystallized snow, and depth hoar. As such, it is important for a reasonably accurate metamorphism model to include such morphologies.

Faceted Geometry. The hexagonal crystal structure of ice gives it unique characteristics when grown from vapor at high rates. While a detailed review of ice crystal mechanics is not presented here, there are several sources available for the reader to review if desired (Hobbs, 1974; Lock, 1990; Petrenko and Whitworth, 1999). Ice has a hexagonal crystallographic structure, which is defined by three a-axes orientated at 120° to one another on the "basal plane" with a c-axis defined as normal to that plane. Perpendicular to the basal plane (parallel to the c-axis) are the six "prism faces". The basal and prism planes have been shown to be the dominant growth features, therefore, their relative growth rates determine the primary geometric habit of the faceted crystal (Lock, 1990). If c-axis growth dominates, prism-like structures appear. Conversely, plate-like structures form when a-axis growth is dominant. For growth rates nearly equal, striated "cups" may develop. Early experiments by Nakaya et al.(1938) showed that crystal habit varied with temperature and humidity. While specific environmental and crystal habit relationships were not developed, his experiments indicated that basic crystal habit was primarily determined by temperature. Several authors have determined the effects of supersaturation and temperature on the growth of ice from the vapor, but Kobayashi's (1957; 1961) experiments rigorously confirmed primary crystal habit

dependence on temperature with secondary features determined by vapor supersaturation.

Lamb and Hobbs (1971) experimentally investigated linear facial growth velocity as a

function of temperature at constant supersaturation. Their results are given in figure 8.
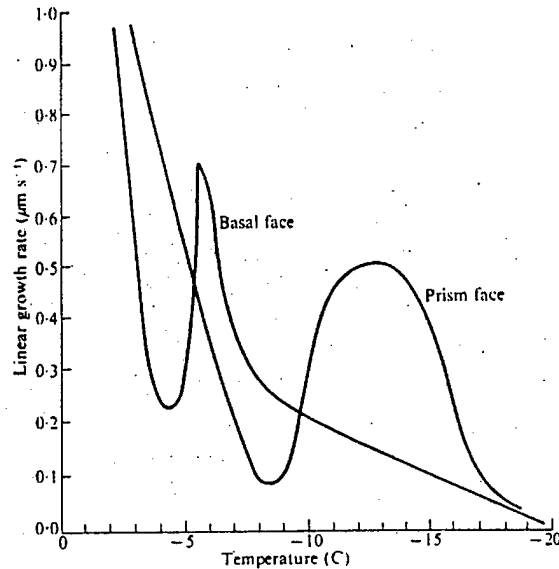
Figure 8. Best fit curves to experimental measurements of the linear (normal) growth rates on the basal and prism faces, at a constant excess vapor pressure of 1.3×10^{-5} bar, as a function of temperature (from Lamb and Hobbs (1971) with changes Hobbs (1974)).

A simple representation of facet crystal geometry is now presented. While the

very complex features of many crystal habits with complex secondary features would be

difficult to model, primary crystal habit can be incorporated. The faceted crystals are

considered to nucleate and grow on the rounded equilibrium form "parent" grains. The

rounded form provides the base to grow the kinetic growth morphologies.

Figure 9 shows the proposed facet geometry to include crystal habit. In figure 9a,

the basal plane showing the characteristic prism length, l, is illustrated. The c-axis is

perpendicular to the basal plane. While a complete hexagon is represented, the current

theory allows for one to six faces.
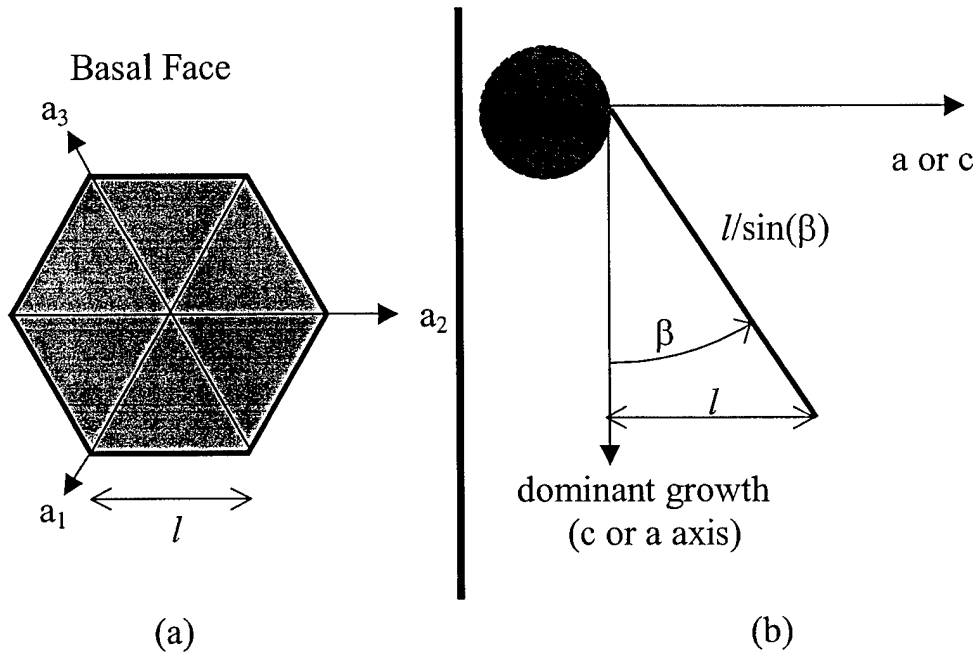
Figure 9. Facet crystal geometry showing basal plane and growth from
exisitng equilibrium form crystal.

In figure 9b, a faceted crystal is shown growing from a rounded parent grain. The

angle from the dominant growth direction to the crystal is defined by β, which is

determined by the relative growth velocity of the two crystallographic directions. Since β

is measured from the dominant growth axis, it is never greater than 45°. If the relative

growth velocities are known, β can be found by

$$\tan(\beta) = \frac{V_a}{V_c} \tag{51}$$

for c-axis dominant growth, and

$$\tan(\beta) = \frac{V_c}{V_a} \qquad\qquad (52)$$

for a-axis dominant growth, where V_c and V_a are, respectively, linear growth velocities (μm/s) of the c and a-axes. The actual growth velocities in figure 8 are not used directly, but the relative facial velocities are used to determine crystal habit as a function of ice temperature. Lamb and Hobbs (1971) growth curves in figure 8 are approximated by a series of five straight lines for each curve (basal or prism). The facial growth velocities are found by:

basal face:

-3.6<θ<0, $\qquad V_c = 0.5\theta + 2.05$;

-5<θ<-3.6, $\qquad V_c = 0.26$;

-5.7<θ<-5, $\qquad V_c = -0.5833\theta - 2.6165$; $\qquad\qquad (53)$

-7.5<θ<-5.7, $\qquad V_c = 0.2388\theta + 2.06$;

θ<-7.5 $\qquad V_c = 0.02108\theta + 0.4216$:

prism face:

-7.6<θ<0, $\qquad V_a = 0.17555\theta + 1.444$;

-9.2<θ<-7.6, $\qquad V_a = 0.11$;

-11<θ<-9.2, $\qquad V_a = -0.2\theta - 1.72$; $\qquad\qquad (54)$

-14.3<θ<-11, $\qquad V_a = 0.48$;

θ<-14.3, $\qquad V_a = 0.1433\theta + 2.529$.

Using the linear growth rate data from Lamb and Hobbs (1971) as approximated

by equations (53) and (54), the crystal habit or angle β can be calculated using equations

(51) or (52) depending upon dominant growth axis and temperature. The actual growth

velocities in figure 8 are for specific test situations, but it is assumed that the relative size

of prism and basal growth velocities are applicable in a wide range of environments.

Once a crystal habit has been established, the actual growth velocity of the

dominant axis can be calculated. Spiral defect propagation theory offers one explanation

of the kinetic growth of ice crystals. Burton et al. (1951) developed an extensive model

for step propagation enabling the calculation of crystallographic face growth velocity.

Hobbs (1974) and Lock (1990) interpret Burton et al (1951) with the following

relationship for facial velocity,

$$V_I = \frac{\alpha}{\rho_{ice}} \left(\frac{m}{2\pi K \theta} \right)^{\frac{1}{2}} \frac{\Delta P^2}{\Delta P_1} \tanh\left(\frac{\Delta P_1}{\Delta P} \right), \tag{55}$$

where V_I is the facial velocity (m/s), I is either c or a-axis (depending on which is

dominant), α is the absorption coefficient, m is the molecular mass (kg), K is

Boltzmann's constant (J/Kmole), ρ_{ice} is ice density (kg/m^3), and ΔP is the excess vapor

pressure (Pa). ΔP_1 is a critical excess vapor pressure given by

$$\Delta P_1 = 2\sqrt{2} \frac{\eta \pi a_0^2 P_0}{K X_s \theta}, \tag{56}$$

where η is the ledge energy per unit step length (J/m), a_0 is the lattice parameter (m)

(different for a vs c-axis growth), X_s is the mean absorption migration distance (m), and

P_0 is the equilibrium vapor pressure (Pa). For $\Delta P_1 \gg \Delta P$, $V_I \propto \Delta P^2$, and for $\Delta P_1 \ll \Delta P$,

$V_I \propto \Delta P$. Such behavior has been noted in laboratory studies. If $\Delta P < 0$, then the growth

velocity is set to zero. Sublimation is not allowed under the kinetic growth regime. With the dominant growth velocity, the overall crystal growth rate is easily obtained from simple geometric relationships.

Heat and Mass Source Terms for Kinetic Growth. With the crystal habit and the dominant crystal growth velocity established, the heat and mass source terms used in the conservation equations need to be developed for kinetic growth. To establish source terms, the mass flow from the vapor to the ice during kinetic growth is required. Even though detailed geometry of faceted crystals has been studied little, some geometric parameters have been measured. Sturm and Benson (1997) conducted extensive experimental research in Alaska on depth hoar. They collected numerous depth hoar samples for mass and size characterization. Using mass fraction techniques in various sized sieves, Sturm and Benson (1997) established a polynomial fit of sieve size and grain mass as

$$\overline{m}_j = \psi \left(\frac{\overline{D}_{j,j+1}}{2} \right)^3 , \tag{57}$$

where $\overline{m}_j$ is the grain mass average for the sieve, ψ is a fit constant (126.6 kg/m^3), and $\overline{D}_{j,j+1}$ is the average size of the j and j+1th sieves (m). This mass to grain size approximation is useful in determining how much mass is added as the crystal grows. For the current problem, it is assumed the average sieve size, $\overline{D}_{j,j+1}$, is the largest dimension of the crystal (ref figure 9b). While a narrow, yet long crystal may fit through

a sieve smaller than the largest dimension, the relatively planar characteristics of these crystals makes the largest dimension approximation reasonable. Equation (57) becomes

$$\overline{m}_j = \psi \left(\frac{l}{2\sin(\beta)} \right)^3 .$$

(58)

The faceted grain surface is composed of a number of triangular elements (ref figure 9a on basal face). The total surface area, A_{facet} (m^2), of a particular grain is given by

$$A_{facet} = NS \frac{l^2}{2\sin(\beta)},$$

(59)

where NS is the number of facet surfaces present (1-6). If the crystal is uniform thickness, δ (m), then the crystal volume is given by

$$Vol_{facet} = NS \frac{\delta l^2}{2\sin(\beta)}.$$

(60)

Comparing the volume given by equation (60) and the volume given by equation (58) (after dividing by the density of ice), the crystal thickness becomes

$$\delta = \frac{\psi l}{4\rho_{ice} NS \sin^2(\beta)}.$$

(61)

The crystal is assumed to grow from the exposed tips during kinetic growth, consistent with the theory of growth by spiral steps. As such, the surface area available for phase change is the rectangular end of each crystal with dimension l by δ.

$$A_{phase\ change} = NS\delta l ,$$

(62)

where $A_{phase\ change}$ is the area (m^2) at the crystal tips available for step growth. Substituting equation (61) into (62) and simplifying leaves

$$A_{phase\ change} = \frac{\psi l^2}{4\rho_{ice}\sin^2(\beta)}.$$ (63)

With the facial growth velocity in equation (55), the growth area in equation (63), the mass flow can be calculated

$$\dot{m} = V_{crystal}A_{phase\ change}\rho_{ice},$$ (64)

where $V_{crystal}$ is the velocity (m/s) of the crystal growth, which is geometrically related to the facial growth velocity in equation (55). Recall the mass source terms in the vapor mass conservation equation were mass flow from phase change per unit pore volume. The mass source for facet growth is then

$$MS_{facet} = -\frac{\psi V_l l^2}{4V_{pore}\sin^2(\beta)\cos(\beta)}.$$ (65)

The negative sign for the facet mass source terms is needed because mass can only condense from the vapor phase; sublimation is not allowed here. The expression for facet growth mass sources can now be properly substituted into equation (43), mass conservation.

The heat source term for facet growth proceeds in a similar manner. The HS term was the latent energy exchange per unit length from sublimation during phase change. Using the mass flow in equation (64), the facet heat source becomes

$$HS_{facet} = -\frac{LV_l\psi l}{4\sin(\beta)\cos(\beta)}.$$ (66)

Summary of Equations

58

The development now includes heat and mass interactions between the pore and ice for an equilibrium geometry form and a kinetic form. The final form of the pore mass conservation equation becomes

$$\frac{L\exp\left(\frac{L}{R}\left(\frac{1}{T_0}-\frac{1}{T}\right)\right)}{RT^2}\left[\frac{d^2T}{dy^2}+\frac{L}{RT^2}\left(\frac{dT}{dy}\right)^2-\frac{3}{T}\frac{dT}{dy}\right]+$$

$$\underbrace{\frac{A_{ec}}{\Delta x V_{pore}}\left[\exp\left(\frac{2\sigma}{\rho_{ice}RT_o\rho_s}\right)\exp\left(\frac{L}{R}\left(\frac{1}{T_o}-\frac{1}{T_s}\right)\right)-\exp\left(\frac{L}{R}\left(\frac{1}{T_0}-\frac{1}{T}\right)\right)\right]}_{\text{from equilibrium form mass interactions}}+ \tag{67}$$

$$\underbrace{\frac{\psi V_l l^2 RT}{4DP_0V_{pore}\sin^2(\beta)\cos(\beta)}}_{\text{from kinetic form mass interactions}}=0.$$

Recall, the phase change temperature, T_s, in equation (67) is found in

$$-k_{ice}\frac{d\theta}{dx}+k_{pore}\frac{dT}{dx}-$$

$$\underbrace{\frac{DP_0L}{RT\Delta x}\left[\exp\left(\frac{2\sigma}{\rho_{ice}RT_o\rho_s}\right)\exp\left(\frac{L}{R}\left(\frac{1}{T_o}-\frac{1}{T_s}\right)\right)-\exp\left(\frac{L}{R}\left(\frac{1}{T_0}-\frac{1}{T}\right)\right)\right]}_{\text{heat interaction at phase change interface}}=0. \tag{50}$$

The final form of the ice heat conduction equation becomes

$$\frac{d^2\theta}{dy^2} + \frac{1}{A}\frac{dA}{dy}\frac{d\theta}{dy} =$$

$$\underbrace{\frac{-DP_0L}{kART\Delta x}\frac{dA_{ec}}{dy}\left(\exp\left(\frac{2\sigma}{\rho_{ice}RT_o\rho_s}\right)\exp\left(\frac{L}{R}\left(\frac{1}{T_o}-\frac{1}{T_s}\right)\right)-\exp\left(\frac{L}{R}\left(\frac{1}{T_0}-\frac{1}{T}\right)\right)\right)}_{\text{from equilibrium form heat interactions}} - \qquad (68)$$

$$\underbrace{\frac{LV_l\psi l}{4kA\sin(\beta)\cos(\beta)}}_{\text{from kinetic form heat interactions}}.$$

These equations represent a quasi-two dimensional heat and mass flow in a phase changing dry snowpack. They are very nonlinear and very coupled.

Numerical Solution Techniques

The governing equations (50), (67), and (68) do not lend themselves to closed form analytic solutions. The phase change coupling creates a very complicated interaction of temperature and geometry with heat and mass. Having already divided the geometry into elements, a finite difference solution will be developed requiring the definition of nodes within the elements. The resulting discretization utilizes finite differences for unequal sized mesh, since grain, neck, and bond sizes vary. The proper equations are developed for each node, resulting in three nonlinear systems of equations. Iterative Newton's techniques for nonlinear equations are used on two of the systems, and a direct technique is used on the third. The systems of equations are solved sequentially.

The solution is repeated until convergence of the phase interaction terms is achieved. After finding the steady state condition, the problem is incremented in time, new metamorphosed geometry defined, and the iterative solution begins again. The solution process is presented in figure 10, the details in each solution step are then presented in separate sections. Time integration does not increment until stable solutions for all three equations and their interactions are established. The time incremental geometry and temperatures provide the desired time variable metamorphism simulation.

Initial conditions

solve surface temperature
(iterative)

solve pore mass conservation
(iterative)

solve ice conduction
(direct)

integrate in time

no   convergence of
phase interaction?

yes

update geometry
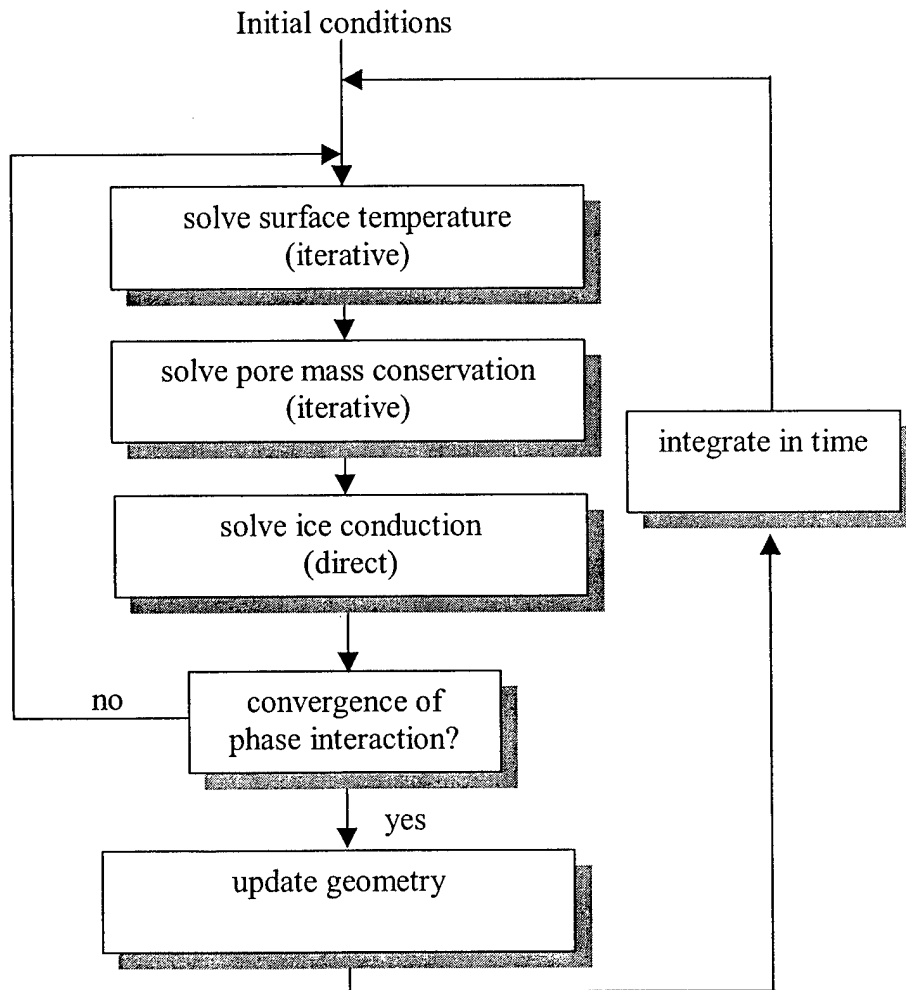
Figure 10. Problem solution methodology

Nodal Definitions

The nodal definitions to accompany ice and pore elements are presented in figure 11. Two categories of nodes are prescribed for the ice and pore elements. Nodes placed at the geometric center of ice and pore elements are called "central" nodes, while nodes placed at the interface between elements are called "boundary" nodes. Recall the ice element boundaries were defined at the transition from grains to necks, with pore elements corresponding to the ice geometry. Each element (pore or ice) has a unique center node and two boundary nodes that are shared with neighboring elements.
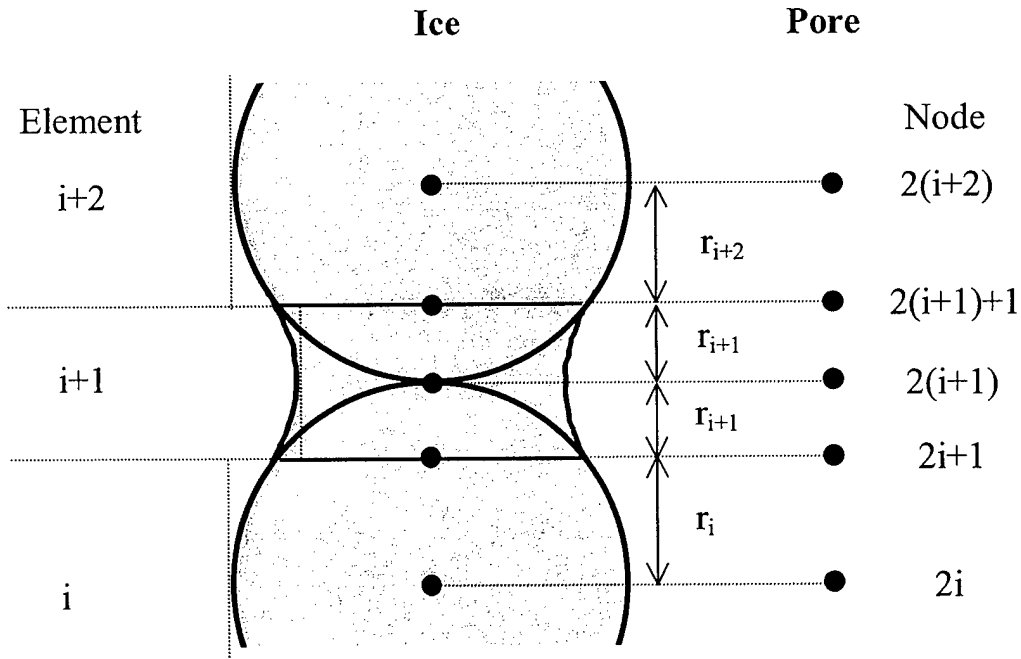
Figure 11. Finite difference node definitions with previously defined elements

For n elements (n must be odd), there will be 2n+1 pore nodes and 2n+1 ice nodes. As with the element numbering, nodal numbering is sequential. The central node for the ith element is numbered 2i (even). Boundary nodes are defined either side of

central nodes and are odd numbered. In anticipation of a finite difference solution, each ice and pore element is assigned a nodal dimension, r_i, such that

$$r_i = r_{g(i)} \text{ for odd i (grains) and,}$$

$$r_i = nl_{(i)} \text{ for even i (necks).} \tag{69}$$

r_i is the spacing from the center to boundary nodes in both the ice and pore ith element. This is an approximation that assumes $r_{g(i)} >> nl_{(i)}$, the reduction of $r_{g(i)}$ by $nl_{(i)}$ is neglected. As discussed earlier in this chapter, this is an acceptable approximation for realistic geometries.

Finite Difference Definitions

The node and element discretization in figure 10 resulted in unequal spacing between the two central nodes surrounding each boundary node. Several finite difference schemes were examined for solving the equations, but as one might expect, a central difference proved most reliable in terms of convergence and accuracy. The details of other difference techniques are not presented. Rather, central difference methods are used throughout. For any particular quantity, φ, located at a central node, j (even), the first and second derivatives are the familiar forms for equally spaced nodes

$$\frac{d\varphi}{dy} = \frac{\varphi_{j+1} - \varphi_{j-1}}{2r_{j/2}}, \quad \text{and} \tag{70}$$

$$\frac{d^2\varphi}{dy^2} = \frac{\varphi_{j-1} - 2\varphi_i + \varphi_{j+1}}{r_{j/2}^2}. \tag{71}$$

These central difference equations are order r^2 accurate (Burden and Faires, 1993) approximations. At a boundary node, j (odd), the spacing to neighboring nodes differs

requiring modified difference equations. The development of unequally spaced nodes is straight forward, but is not presented here. For boundary nodes, the difference equations become (Tannehill et al, 1997)

$$\frac{d\varphi}{dy} = \frac{\varphi_{j+1} - \varphi_{j-1}}{r_{(j-1)/2} + r_{(j+1)/2}}, \text{ and} \tag{72}$$

$$\frac{d^2\varphi}{dy^2} = \frac{2\left(r_{(j-1)/2}\left(\varphi_{j+1} - \varphi_j\right) + r_{(j+1)/2}\left(\varphi_{j-1} - \varphi_j\right)\right)}{\left(r_{(j-1)/2} + r_{(j+1)/2}\right)r_{(j-1)/2}r_{(j+1)/2}}. \tag{73}$$

Equation (72) is order r^2 accurate while equation (73) is order r accurate (Lindfield and Penny, 1995). Of course, if the mesh becomes uniform, equations (72) and (73) reduce to equations (70) and (71) respectively.

Boundary and Initial Conditions

For the second order differential equations (67) and (68), flux, temperature, or mixed boundary conditions may be used. For the current problem, temperature boundary conditions are specified. As discussed in chapter 1, operational models used in snowpack prediction have proven reliable at predicting averaged macroscopic temperatures. As such, boundary temperatures T_1, θ_1, θ_{2n+1}, and T_{2n+1} are specified, where n is the number of elements. There may be conditions, such as impermeable crusts or dry ground, where vapor or heat boundary conditions could be specified, but that solution is not developed here.

To begin the first iteration, initial temperatures are required. If no temperature gradient is applied, all the nodal temperatures (pore and ice) are set to the boundary temperature. If a temperature gradient is applied, a spatially linear temperature

distribution is assumed. This provides no restriction on the final solution, but does provide a first estimate for iterative techniques.

Pore Mass Conservation Solution

Pore mass conservation equation (67) is now expressed in finite difference form at each node. At this point, a simplifying assumption is made. Based on the nodal distribution in figure 11, mass interaction terms will be considered at central nodes only. The phase change mass source terms associated with grains and necks will be lumped at each central node. The interaction terms at boundary nodes are set to zero. The interaction terms could be distributed between the boundary and central nodes but are not in order to achieve additional simplicity. Using equations (70) and (71) for the ith (even) central node, equation (67) becomes

$$
f_i = \frac{L\exp\left(\frac{L}{R}\left(\frac{1}{T_0} - \frac{1}{T_i}\right)\right)}{Rr_{i/2}^2}\left[\frac{T_{i-1}}{T_i^2} - \frac{2}{T_i} + \frac{T_{i+1}}{T_i^2} + \frac{L}{4RT_i^4}\left(T_{i+1}^2 - 2T_{i+1}T_{i-1} + T_{i-1}^2\right) - \right.
$$

$$
\left(T_{i+1} - T_{i-1}\right)\frac{3r_{i/2}}{2T_i^3}\right] + \frac{Aec_{i/2}}{\Delta x_{i/2}Vpore_{i/2}}\left[\exp\left(\frac{L}{R}\left(\frac{1}{T_0} - \frac{1}{Ts_{i/2}}\right) + \frac{2\sigma}{\rho_{ice}RTs_{i/2}\rho_{s\,i/2}}\right) - \right. \tag{74}
$$

$$
\left.\exp\left(\frac{L}{R}\left(\frac{1}{T_0} - \frac{1}{T_i}\right)\right)\right] - \frac{\psi V_{I\,i/2}l_{i/2}^2 RT_i}{4DP_0Vpore_{i/2}\sin^2\left(\beta_{i/2}\right)\cos\left(\beta_{i/2}\right)} = 0.
$$

In equation (74), the surface area for phase change, A_{ec}, diffusion distance, Δx, phase change temperature, T_s, and surface curvature, ρ_s, are assigned to the respective ice element and used for the center node equation in that element. In addition, V_{pore} for each pore element is used in the appropriate center node equation.

For boundary nodes, no source terms are considered. Using equations (72) and (73) for the ith (odd) boundary node, equation (67) becomes

$$
f_i = \frac{L\exp\left(\dfrac{L}{R}\left(\dfrac{1}{T_0}-\dfrac{1}{T_i}\right)\right)}{R\left(r_{(i+1)/2}+r_{(i-1)/2}\right)}\left[\frac{2T_{i+1}}{r_{(i+1)/2}T_i^2}-\frac{2}{r_{(i+1)/2}T_i}+\frac{2T_{i-1}}{r_{(i-1)/2}T_i^2}\right.
$$

$$
\left.-\frac{2}{r_{(i-1)/2}T_i}+\frac{L\left(T_{i+1}^2-2T_{i+1}T_{i-1}+T_{i-1}^2\right)}{T_i^4 R\left(r_{(i+1)/2}+r_{(i-1)/2}\right)}-\frac{3\left(T_{i+1}-T_{i-1}\right)}{T_i^3}\right]=0 \tag{75}
$$

<u>Vapor System of Non-Linear Equations</u>. After applying the appropriate finite difference equation ((74) or (75)) to each interior node and assigning temperature boundary conditions, a set of non-linear equations with nodal pore temperature degrees of freedom emerge

$$
\underline{F}\left(f_i\left(T_{i-1},T_i,T_{i+1}\right)\right)=\underline{0}\qquad i=2,\ldots,2n. \tag{76}
$$

Direct solution techniques of the system did not yield consistently convgergent results. Several attempts were made to manipulate the form of (76) to find solutions directly, but the highly non-linear nature of the equations generally resulted in divergent solutions. The details of failed numerical attempts are not presented. Rather, the one technique that provided stable convergent solutions is now discussed. Newton's method for non-linear systems yielded convergent solutions to the system of equations in (76). Newton's method is an iterative technique where increments in nodal degrees of freedom, ΔT_i, are found by

$$
\underline{J}\left(f_i\left(T_{i-1},T_i,T_{i+1}\right)\right)\underline{\Delta T}=\underline{F}\left(f_i\left(T_{i-1},T_i,T_{i+1}\right)\right), \tag{77}
$$

where J is the Jacobian defined by

$$\underline{J}\left(f_i\left(T_i\right)\right) = \begin{bmatrix} \dfrac{\partial f_2}{\partial T_2} & \dfrac{\partial f_2}{\partial T_3} & \cdots & \dfrac{\partial f_2}{\partial T_{2n}} \\[2mm] \dfrac{\partial f_3}{\partial T_2} & \dfrac{\partial f_3}{\partial T_3} & \cdots & \dfrac{\partial f_3}{\partial T_{2n}} \\[2mm] \vdots & \vdots & & \vdots \\[2mm] \dfrac{\partial f_{2n}}{\partial T_2} & \dfrac{\partial f_{2n}}{\partial T_3} & \cdots & \dfrac{\partial f_{2n}}{\partial T_{2n}} \end{bmatrix}. \tag{78}$$

Nodal temperatures are then updated after solving (77) by

$$T_i^{new} = T_i^{old} + \Delta T_{i-1}. \tag{79}$$

The process of forming $\underline{F}$, forming $\underline{J}$, solving for $\underline{\Delta T}$, and updating $\underline{T}$ is continued until the increments in nodal temperatures become small. Once converged, new pore temperatures are known and are then used in the surface temperature and ice temperature calculations.

For the current problem, $\underline{F}$ is a vector with elements given by equations (74) or (75) depending upon if the node is central or boundary. It is noted that each f_i is a function of the ith node and its two immediate neighbors, i-1 and i+1, only. The Jacobian entries for central (even numbered) nodes are then given by

$$\frac{\partial f_i}{\partial T_{i-1}} = JB_i = \frac{L \exp\left(\dfrac{L}{R}\left(\dfrac{1}{T_0} - \dfrac{1}{T_i}\right)\right)}{R r_{i/2}^2}\left[\frac{1}{T_i^2} + \frac{LT_{i-1}}{2RT_i^4} - \frac{LT_{i+1}}{2RT_i^4} + \frac{3r_{i/2}}{2T_i^3}\right], \tag{80}$$

$$\frac{\partial f_i}{\partial T_i} = JA_i = \frac{L^2 \exp\left(\dfrac{L}{R}\left(\dfrac{1}{T_0} - \dfrac{1}{T_i}\right)\right)}{R^2 r_{i/2}^2 T_i^2}\left[\frac{T_{i-1}}{T_i^2} - \frac{2}{T_i} + \frac{T_{i+1}}{T_i^2} + \frac{L\left(T_{i+1}^2 - 2T_{i+1}T_{i-1} + T_{i-1}^2\right)}{4RT_i^4} - \right.$$

$$\frac{3r_{i/2}}{2T_i^3}\left(T_{i+1}-T_{i-1}\right)\Bigg] + \frac{L\exp\left(\dfrac{L}{R}\left(\dfrac{1}{T_0}-\dfrac{1}{T_i}\right)\right)}{Rr_{i/2}^2}\left[\frac{-2T_{i-1}}{T_i^3}+\frac{2}{T_i^2}-\frac{2T_{i+1}}{T_i^3}-\right. \qquad (81)$$

$$\frac{L\left(T_{i+1}^2-2T_{i+1}T_{i-1}+T_{i-1}^2\right)}{RT_i^5}+\frac{9r_{i/2}\left(T_{i+1}-T_{i-1}\right)}{2T_i^4}\Bigg]-\frac{Aec_{i/2}}{\Delta x_{i/2}Vpore_{i/2}}\left[\frac{L\exp\left(\dfrac{L}{R}\left(\dfrac{1}{T_0}-\dfrac{1}{T_i}\right)\right)}{RT_i^2}\right]-$$

$$\frac{\psi V_{1\,i/2}l_{i/2}{}^2 R}{4DP_0 Vpore_{i/2}\sin^2\left(\beta_{i/2}\right)\cos\left(\beta_{i/2}\right)},$$

$$\frac{\partial f_i}{\partial T_{i+1}}=JF_i=\frac{L\exp\left(\dfrac{L}{R}\left(\dfrac{1}{T_0}-\dfrac{1}{T_i}\right)\right)}{Rr_{i/2}^2}\left[\frac{1}{T_i^2}+\frac{LT_{i+1}}{2RT_i^4}-\frac{LT_{i-1}}{2RT_i^4}-\frac{3r_{i/2}}{2T_i^3}\right]. \qquad (82)$$

Similar expressions for the boundary nodes (odd numbered) are achieved using equation (75), the Jacobian terms become

$$\frac{\partial f_i}{\partial T_{i-1}}=JB_i=\frac{L\exp\left(\dfrac{L}{R}\left(\dfrac{1}{T_0}-\dfrac{1}{T_i}\right)\right)}{R\left(r_{(i+1)/2}+r_{(i-1)/2}\right)}\left[\frac{2}{r_{(i-1)/2}T_i^2}+\frac{2LT_{i-1}}{R\left(r_{(i+1)/2}+r_{(i-1)/2}\right)T_i^4}-\right.$$

$$\frac{2LT_{i+1}}{R\left(r_{(i+1)/2}+r_{(i-1)/2}\right)T_i^4}+\frac{3}{T_i^3}\Bigg], \qquad (83)$$

$$\frac{\partial f_i}{\partial T_i}=JA_i=\frac{L^2\exp\left(\dfrac{L}{R}\left(\dfrac{1}{T_0}-\dfrac{1}{T_i}\right)\right)}{R^2 T_i^2\left(r_{(i+1)/2}+r_{(i-1)/2}\right)}\left[\frac{2T_{i+1}}{r_{(i+1)/2}T_i^2}-\frac{2}{r_{(i+1)/2}T_i}+\right.$$

$$\frac{2T_{i-1}}{r_{(i-1)/2}T_i^2}-\frac{2}{r_{(i-1)/2}T_i}+\frac{L\left(T_{i+1}^2-2T_{i+1}T_{i-1}+T_{i-1}^2\right)}{R\left(r_{(i+1)/2}+r_{(i-1)/2}\right)T_i^4}- \qquad (84)$$

$$\left.\frac{3(T_{i+1}-T_{i-1})}{T_i^3}\right] + \frac{L\exp\left(\dfrac{L}{R}\left(\dfrac{1}{T_0}-\dfrac{1}{T_i}\right)\right)}{\left(r_{(i+1)/2}+r_{(i-1)/2}\right)}\left[\frac{-4T_{i+1}}{r_{(i+1)/2}}+\frac{2}{r_{(i+1)/2}T_i^2}\right.$$

$$\left.-\frac{4T_{i-1}}{r_{(i-1)/2}T_i^3}+\frac{2}{r_{(i-1)/2}T_i^2}-\frac{4L\left(T_{i+1}^2-2T_{i+1}T_{i-1}+T_{i-1}^2\right)}{R\left(r_{(i+1)/2}+r_{(i-1)/2}\right)T_i^5}+\frac{9(T_{i+1}-T_{i-1})}{T_i^4}\right],$$

$$\frac{\partial f_i}{\partial T_{i+1}}=JF_i=\frac{L\exp\left(\dfrac{L}{R}\left(\dfrac{1}{T_0}-\dfrac{1}{T_i}\right)\right)}{R\left(r_{(i+1)/2}+r_{(i-1)/2}\right)}\left[\frac{2}{r_{(i-1)/2}T_i^2}+\frac{2LT_{i+1}}{R\left(r_{(i+1)/2}+r_{(i-1)/2}\right)T_i^4}-\right.$$

$$\left.\frac{2LT_{i-1}}{R\left(r_{(i+1)/2}+r_{(i-1)/2}\right)T_i^4}-\frac{3}{T_i^3}\right]. \tag{85}$$

The Jacobian for the pore problem then becomes a square 2n-1 matrix,

$$\underline{J}=\begin{bmatrix} JA_2 & JF_2 & 0 & 0 & 0 & \cdots & 0 \\ JB_3 & JA_3 & JF_3 & 0 & 0 & \cdots & 0 \\ 0 & JB_4 & JA_4 & JF_4 & 0 & \cdots & 0 \\ \vdots & & \ddots & \ddots & \ddots & & \vdots \\ 0 & \cdots & 0 & JB_{2n-2} & JA_{2n-2} & JF_{2n-2} & 0 \\ 0 & \cdots & 0 & 0 & JB_{2n-1} & JA_{2n-1} & JF_{2n-1} \\ 0 & \cdots & 0 & 0 & 0 & JB_{2n} & JA_{2n} \end{bmatrix}. \tag{86}$$

By forming $\underline{J}$ and $\underline{F}$ with the current values of $\underline{T}$, then inverting $\underline{J}$ in equation (77), the temperature increment is found, and new temperatures calculated. This process continues until $\underline{\Delta T}$ becomes small. Since the number of nodes is variable, the convergence tolerance must account for the model size. The L_2 norm of the temperature change is

$$\left\|\underline{\Delta T}\right\| = \sqrt{\sum \Delta T_i^2} \ . \tag{87}$$

If the average temperature change at convergence is assigned a tolerance, tol, then when

$$\left\|\underline{\Delta T}\right\| \le tol\sqrt{2n+1} , \tag{88}$$

Newton's method has converged. The tolerance used was very small (<1e-9) since the temperature changes are expected to be very small. The technique is quadratically convergent (Burden and Faires, 1993), but a rather large Jacobian matrix is formed and inverted at each iteration. Most studies in upcoming chapters converged in six iterations or less. On average, it is estimated that three iterations were required for convergence.

Ice Heat Conservation Solution

The solution to the ice heat conservation equation (68) proceeds in a similar manner as the pore equation, except a direct solution technique produces acceptable results. Similar to the pore equation, heat source terms are only considered at central nodes of grain and necks. Phase change interaction terms are not included at the boundary nodes between grains and necks. The temperature boundary conditions are, with n elements defined, θ_1 and θ_{2n+1} prescribed. Heat flux boundary conditions are not prescribed. Using the finite difference formulation for central nodes (equations (70) and (71)), equation (68) becomes

$$\left(\frac{1}{r_{i/2}^2}+\frac{A_{i-1}-A_{i+1}}{4A_ir_{i/2}^2}\right)\theta_{i-1}-\frac{2}{r_{i/2}^2}\theta_i+\left(\frac{1}{r_{i/2}^2}+\frac{A_{i+1}-A_{i-1}}{4A_ir_{i/2}^2}\right)\theta_{i-1}=\frac{HS_{i/2}}{KA_i}, \tag{89}$$

where $HS_{i/2}$ is the sum of heat source terms defined in equations (35) and (66). For boundary nodes, using equations (72) and (73) in (68) yields

$$\left(\frac{2}{\left(r_{(i+1)/2}+r_{(i-1)/2}\right)r_{(i-1)/2}}+\frac{A_{i-1}-A_{i+1}}{A_i\left(r_{(i+1)/2}+r_{(i-1)/2}\right)^2}\right)\theta_{i-1}-\left(\frac{2}{\left(r_{(i+1)/2}+r_{(i-1)/2}\right)}\right)\theta_i$$

$$+\left(\frac{2}{\left(r_{(i+1)/2}+r_{(i-1)/2}\right)r_{(i+1)/2}}+\frac{A_{i+1}-A_{i-1}}{A_i\left(r_{(i+1)/2}+r_{(i-1)/2}\right)^2}\right)\theta_{i+1}=0. \tag{90}$$

After making some convenient coefficient definitions, equations (89) and (90) may be represented as

$$HH_i\theta_{i-1}+II_i\theta_i+JJ_i\theta_{i+1}=KK_i, \tag{91}$$

for central nodes and,

$$LL_i\theta_{i-1}+MM_i\theta_i+NN_i\theta_{i+1}=0, \tag{92}$$

for boundary nodes. The coefficients in equations (91) and (92) can be determined from equations (89) and (90). After writing the appropriate difference equations for all interior nodes, the system of equations becomes

$$
\begin{bmatrix}
II_2 & JJ_2 & 0 & 0 & 0 & 0 & \cdots & 0 \\
LL_3 & MM_3 & NN_3 & 0 & 0 & 0 & \cdots & 0 \\
0 & HH_4 & II_4 & JJ_4 & 0 & 0 & \cdots & 0 \\
0 & 0 & LL_5 & MM_5 & NN_5 & 0 & \cdots & 0 \\
\vdots & \vdots & \vdots & \ddots & \ddots & \ddots & \cdots & 0 \\
0 & 0 & 0 & 0 & HH_{2n-2} & II_{2n-2} & JJ_{2n-2} & 0 \\
0 & 0 & 0 & 0 & 0 & LL_{2n-1} & MM_{2n-1} & NN_{2n-1} \\
0 & 0 & 0 & 0 & 0 & 0 & HH_{2n} & II_{2n}
\end{bmatrix}
\begin{bmatrix}
\theta_2 \\ \theta_3 \\ \theta_4 \\ \theta_5 \\ \vdots \\ \theta_{2n-2} \\ \theta_{2n-1} \\ \theta_{2n}
\end{bmatrix}
=
$$

$$
\begin{bmatrix}
KK_2 - HH_2\theta_1 \\
0 \\
KK_4 \\
0 \\
\vdots \\
KK_{2n-2} \\
0 \\
KK_{2n} - JJ_{2n}\theta_{2n+1}
\end{bmatrix}.
\qquad (93)
$$

The coefficient matrix in equation (93) does not contain any temperature degrees of freedom. The KK_i terms on the right hand side are the non-linear coupling to the pore through phase change. Referring to figure 10, the ice, pore, and surface temperature solutions will be solved iteratively until the interaction terms converge. As such, the interaction terms are considered constant here, and equation (93) may be solved by simply inverting the coefficient matrix and multiplying by the right hand side. Within the ice conduction problem, a direct solution technique avoided computationally costly iterative techniques. The only non-linearity came from the heat source interaction terms, making heat conservation much simpler to solve than the pore mass conservation problem.

Phase Change Temperature Solution

The mass and heat conduction problems each contained the phase change temperature described in equation (50). Recalling the geometry at the phase change boundary from figure 7, the phase change temperature equation may be differenced for each element, i, as

$$-k_{ice}\frac{Ts_i-\theta_{2i}}{r_i}+k_{pore}\frac{T_{2i}-Ts_i}{w_i}+\frac{DL}{RT_{2i}\Delta x_i}\left(Ppore_i-Pice_i\right)=0 \tag{94}$$

Since the pore temperatures, T, and ice temperatures, θ, are known, a simple version of Newton's method can be used to solve the non-linear equation at each element. If the ice and pore vapor pressures are substituted into equation (94), then

$$f=k_{ice}\frac{Ts_i-\theta_{2i}}{r_i}+k_{pore}\frac{Ts_i-T_{2i}}{w_i}+$$

$$\frac{DLP_0}{RT_{2i}\Delta x_i}\left[\exp\left(\frac{2\sigma}{\rho_{ice}RT_0\rho_{si}}\right)\exp\left(\frac{L}{R}\left(\frac{1}{T_o}-\frac{1}{Ts_i}\right)\right)-\exp\left(\frac{L}{R}\left(\frac{1}{T_0}-\frac{1}{T_{2i}}\right)\right)\right]. \tag{95}$$

Then,

$$\frac{\partial f}{\partial Ts_i}=\frac{k_{ice}}{r_i}+\frac{k_{pore}}{w_i}+\frac{DL^2P_0}{R^2T_{2i}Ts_i^2\Delta x_i}\left[\exp\left(\frac{2\sigma}{\rho_{ice}RT_0\rho_{si}}\right)\exp\left(\frac{L}{R}\left(\frac{1}{T_o}-\frac{1}{Ts_i}\right)\right)\right]. \tag{96}$$

New approximations at the phase change temperature at each node, Ts_i, may be found by using Newton's method,

$$Ts_{new}=Ts_{old}-\frac{f(Ts_{old})}{\dfrac{\partial f(Ts_{old})}{\partial Ts_i}}. \tag{97}$$

New approximations are calculated until the change in Ts_{new} from Ts_{old} is less than an assigned tolerance. A convergence tolerance of 1e-8 worked well for phase change temperatures, smaller values could be used if required.

Update Geometry

After the steady state solution to the pore, heat, and phase change problems has converged, time integration may commence. The equilibrium and kinetic forms considered change uniquely with time and are considered separately.

Equilibrium Form Geometry Changes.

With the pore, ice, and surface temperatures known, the phase change flux, J_{ec}, is easily calculated using equation (41) for each element. Since each ice element has a unique phase change area, A_{ec}, the volumetric rate of change of each ice element is given by

$$\dot{V} = -\frac{J_{ec} A_{ec}}{\rho_{ice}}.$$

(98)

For spherical grains, the radius rate of change is given by

$$\dot{r}_g = \frac{\dot{V}}{4\pi r_g^2}.$$

(99)

Hobbs (1974) shows the volume for the necks described in figure 2 is

$$V_{neck} = \frac{\pi^2 r_b^4}{4r_g}.$$

(100)

The growth of the bond is then given by

$$\dot{r}_b = \frac{\dot{V} r_g}{\pi^2 r_b^3}.$$

(101)

Once the rate of change of each grain or bond radius is known, new values are simply found with small increments in time. The remainder of the physical parameters are easily updated. For the grains,

$$\rho_s = r_g,$$

$$A = \pi r_g^2,$$

(102)

and $A_{ec} = 4\pi r_g^2.$

The neck volume is given in equation (100), neck length in equation (3), surface curvature in equations (2) and (4), and

$$A = \pi r_b^2,$$

and $A_{ec} = 4\pi r_b r_g.$

(103)

With the newly defined ice geometry, the pore dimensions can be calculated. Assuming the symmetry distance, x, in figure 4 remains constant, new pore widths next to grains are found by

$$w_{new} = w_{old} - \dot{r}_g \Delta t,$$

(104)

and for pores next to bonds,

$$w_{new} = w_{old} - \dot{r}_b \Delta t,$$

(105)

where Δt is the time increment (s). New snow density is easily calculated.

Kinetic Form Geometry Changes. The faceted crystal characteristic length, l, rate of growth is found by

$$\dot{l} = V_I \tan(\beta).$$

(106)

Once the new characteristic length is calculated, crystal mass, surface area, volume, thickness, and phase change area can be updated using equations (58)-(63).

Time Step. After geometrical rates of change are found, new values are calculated by taking small time steps. The size of the time step has a significant impact on the accuracy of the geometric metamorphism. When intergranular necks are small, growth rates are very large, so small time steps, on the order of minutes, are required. As bonds get larger, the time step can be increased to several hours. As faceted crystals grow, they reach deeper into warmer vapor spaces, increasing the growth rate. As the growth rate increases, the time step must decrease to keep the kinetic growth process stable. Again, a time step on the order of minutes may be required for large crystals.

CHAPTER 3

NUMERICAL STUDIES

Introduction

In this chapter, numerous numerical studies are presented. Several well-known snow metamorphism trends are examined. Some studies are designed to evaluate the current approach's ability to predict these trends, while other studies demonstrate the model's inherent flexibility in evaluating the influence of several parameters on snow metamorphism. The relative significance of factors such as ice grain geometry, bonding, density, temperature, crystal orientation, etc may be examined in any thermal environment.

The theory developed in chapter 2 was implemented using MATLAB V6 (2000). The details of the programming are not discussed here, but the code listing is found in appendix B. MATLAB was chosen for its superior numerical computational features. This allowed increased focus on solving new physical problems and alleviated tedious programming for mathematical manipulations.

Macroscopically isothermal snow is examined first. It was observed that under these conditions, small microstructural temperature gradients must develop in order for metamorphism to commence. A definition for the onset of temperature gradient

metamorphism is then presented, and the resulting studies discussed. After the onset of a kinetic growth regime, the development of faceted crystals is presented with some interesting results relative to crystal orientation and bonding. Finally, the ability of the model to predict published experimental results is evaluated. Metamorphism data from both equi-temperature and temperature gradient environments are simulated with good correlation to known trends and published results.

Equi-temperature Environment

Equal Sized Grains

In its most idealized and simplest form, dry seasonal snow may be thought of as a group of equally sized spheres with intergranular necks and bonds (Kingery, 1960; Kuroiwa, 1961; Hobbs and Mason, 1964; Colbeck, 1980; Maeno and Eblnuma, 1983; Adams and Brown, 1989; Brown et al., 1999). In reality, snow is composed of various sized structures which may influence metamorphism. Colbeck (2001) shows that at neighboring grain radii ratios exceeding 1.57, the resulting curved grain boundary does not leave sufficient exposed area for the smaller grain to bond in a "chain". His theory potentially explains the difficulty of inter-layer bonding in some snow but the lack of bonding between unequally sized grains gives credence to examining metamorphism of nearly equal sized grains.

During snow metamorphism, several microstructural parameters are important. Traditionally, grain size has been the primary time varying parameter. Grains are the most readily visible structure when examining snow. In addition to grain size, the

interconnecting neck size has recently been recognized as an equally important feature. As with grains, bonds and necks influence nearly all physical attributes such as strength, stability, thermal properties, optical properties, elastic response, inelastic response etc. The broad influence of grains and their interconnections requires that their interactions be included in any reasonable metamorphism theory. In the current research, bonds, necks, and grains have been described and are an integral part of the theory. While the absolute sizes of grains and bonds are important, their relative size is commonly used to describe the level of bonding or maturity of metamorphism. The bond to grain ratio is given by

$$ratio = {r_b}/{r_g} . \tag{107}$$

As metamorphism progresses in an equi-temperature environment, the ratio may grow due to vapor sublimating off of convex grains and then depositing onto concave necks.

During the metamorphism of equal sized grains in an equi-temperature environment, several parameters such as grain geometry, intergranular neck geometry, pore geometry, density, and temperature influence the rate and nature of metamorphism. Demonstration values used to examine the development are offered in table 1.

Grain Sizes	r_g=0.125, 0.5, 1.0 mm
Ratio	0.4
Snow Density	150 kg/m^3
Temperature	-5°C

Table 1. Equal sized grain equi-temperature metamorphism study parameters

Bond to grain radii ratio, density and temperature are each individually varied for all three grain sizes. Figure 12 pictorially represents the vapor flux path that results from

79

this analysis. Small vapor pressure gradients between nodes result in vapor flux from the convex surfaces, to the pore, through the pore, and onto the concave necks. The local temperature gradient in the pore was only on the order of 0.05 °C/m to commence and maintain the metamorphism. While this temperature gradient appears very small, metamorphism in a macroscopically isothermal environment could not take place without it.
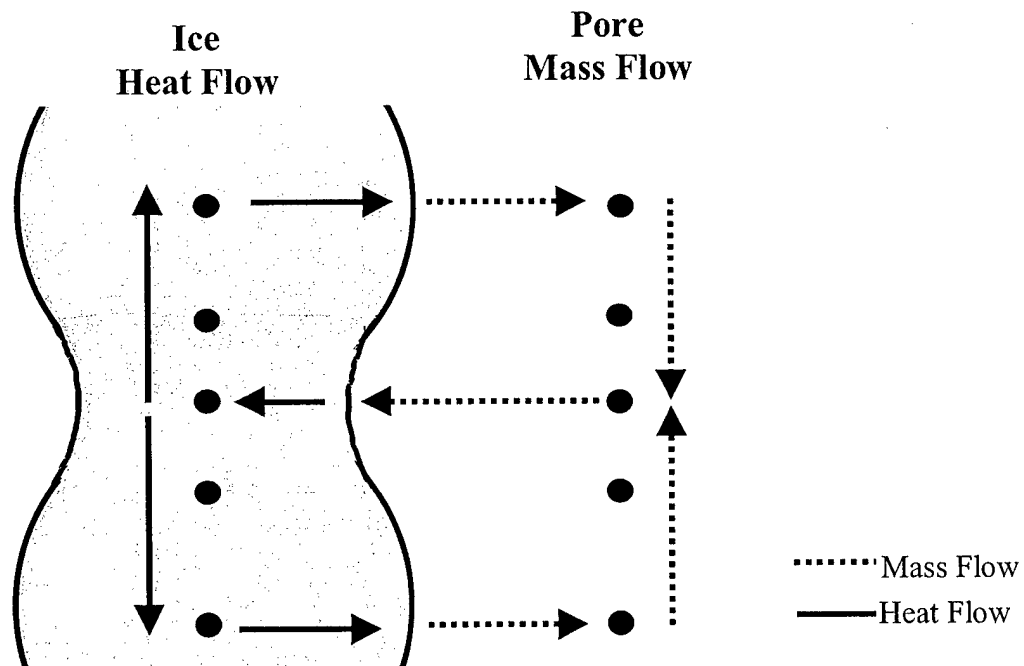
Figure 12. Generic heat and mass flows between nodes during equi-temperature metamorphism.

The vapor and heat flow depicted in figure 12 result from the following process. The convex grain surface curvature creates a vapor pressure gradient between the surface and central pore node. Vapor sublimates from the surface and becomes a vapor source, causing vapor to diffuse to the central pore node. As vapor is added at the node, the

temperature increases slightly, creating a gradient to the neighboring boundary and central nodes. Vapor diffuses in the pore toward the necks thereby increasing the vapor pressure at this node. A vapor pressure gradient therefore develops between the pore node and the concave neck surface, causing vapor to diffuse toward the neck. Vapor is allowed to condense and release the associated latent heat to the ice neck's central node. This slightly raises the neck nodal temperature resulting in heat conduction to the neighboring boundary and central nodes. At the grain central node, heat is removed thereby providing the latent heat of sublimation required, and the cycle is complete. The geometry is updated as time integration proceeds by adding or removing mass from ice elements. Even though heat and mass are conserved globally, there are no physical constraints to ensure a heat and mass balance between individual grains and necks, since heat and vapor are allowed to cross element boundaries. Recall temperature boundary conditions were applied, not heat or mass flux limitations. It would seem prudent to believe that the vast majority of the vapor used in the equi-temperature sintering process would originate at the grain and terminate at the neck. This is discussed in an upcoming section of this chapter.

Metamorphism as a Function of Bond to Grain Ratio. Figure 13 shows the variation of grain decay and bond growth with bond to grain radii ratio. As the bond to grain ratio increases from 0.2 to 0.6, the bond growth rate decreases by two orders of magnitude for each grain size. The reduction in surface curvature, increase in neck length, neck surface area, and neck volume during metamorphism combine to reduce the growth rate with increasing bond size. An analogous process is taking place during grain

radius reduction. The sintering rate decreases dramatically with increased bonding, a simple well understood yet important result (Hobbs and Mason, 1964; Maeno and Eblnuma, 1983). Observations have shown that snow sinters very rapidly initially, then decreases dramatically in time. As the bonds grow, the vapor pressure gradient decreases as the neck radius of curvature decreases. It is evident from figure 13 why very large bond ratios are rarely, if ever, observed in seasonal snow.

The conditions described in table 1 can be integrated in time to show this grain size and ratio dependence during metamorphism. Figure 14 shows the bond to grain radii ratio time integrated for 24 hours. The smaller grained snow sinters rapidly when compared to the larger grained snow. Again, this is due to a combination of factors that include the higher energy state of the smaller grains as well as the smaller grain and neck volume associated with smaller grains. As predicted in figure 13, figure 14 demonstrates the decrease in bond growth rate with time (and ratio) for the 1/8 mm grains. To see the same effect for the larger grains, the problem is extended in figure 15 from 24 hours to 30 days. Again, the decrease in bonding rate in time is evident for the larger grained snow. The selection of a time step for integration requires some preplanning. For very small bonds, the growth rate is very large requiring small time steps to prevent over predicting bond growth rates. In figures 14 and 15, a final time step was obtained by varying the time step from large to small until the growth rates converged to the same values at the same total time. If an excessively large time step is chosen, the growth rates will decrease as the time step decreases. For figure 14, a time step of 600 seconds (10 minutes) provided convergent results. For figure 15, a time step of 14400 seconds (4 hours) was used. In each case, if the initial bond to grain ratio was smaller than 0.2, a

shorter time step would have been required early in the analysis. Since the time to reach a bond to grain radii ratio of 0.2 is very short (minutes), it was used as a reasonable starting point.

Metamorphism as a Function of Temperature. Using the parameters in table 1 but now varying temperature, figure 16 shows the grain decay rate and bond growth rate for snow comprised of equally sized grains in an equi-temperature environment. As expected, metamorphism is sensitive to temperature. The bond growth rate decreases by a factor of approximately 8 for all three grain sizes as the temperature is lowered from 0 to −20 °C, confirming another well established experimental metamorphic trend (Hobbs and Mason, 1964). As previously discussed, microstructural temperature gradients do develop in the pore and ice, but here the boundary temperature is varied. Initially, the entire sample is set to the boundary temperature, then microstructural temperature gradients develop during the iterative solution. Recall the iterative solution stops when steady state conditions are achieved.

As with the previous solution, time integration for particular temperatures could be accomplished. Similar trends would emerge with metamorphism commencing at higher rates for warmer temperatures. As with bond and grain size, temperature is a very significant factor in equi-temperature snow metamorphism. For the sake of brevity, the time integration results are not presented.
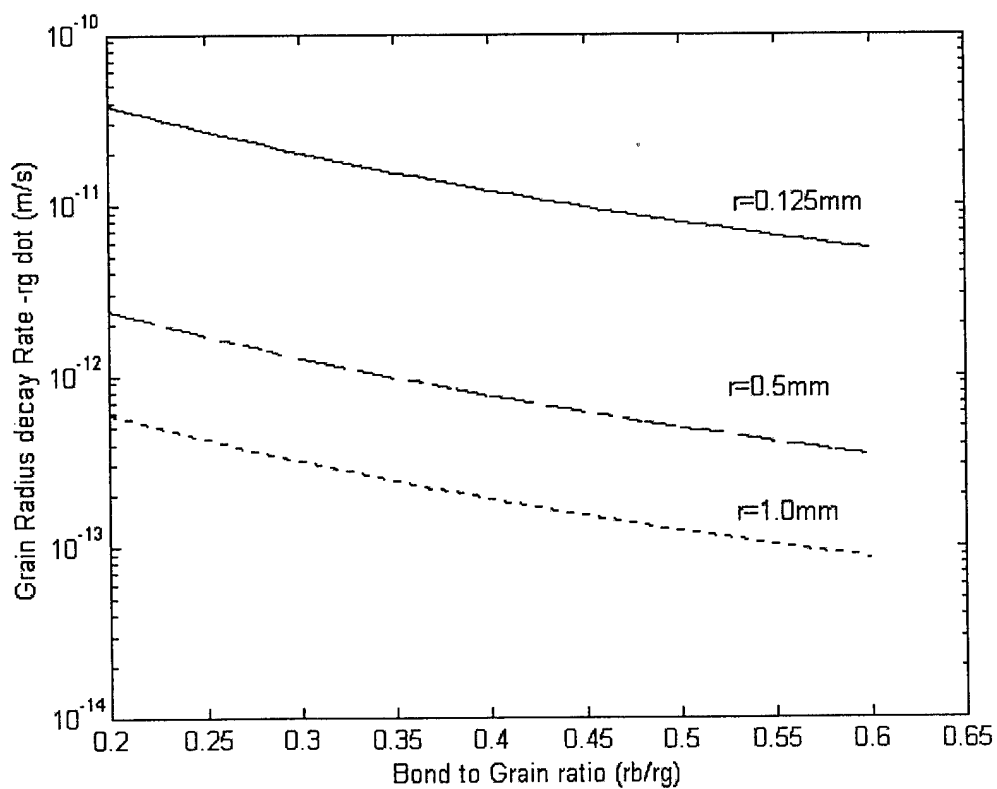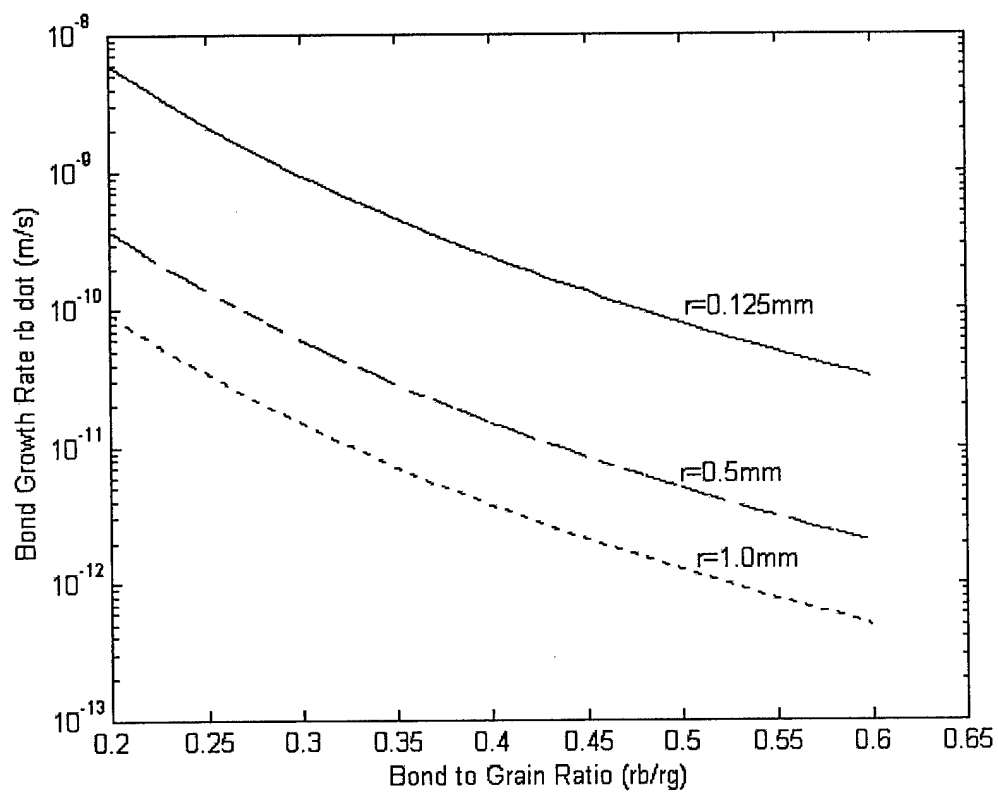
Figure 13. Bond growth rate and grain decay rate vs bond to grain ratio. T=-5°C, ρ=150 kg/m³

ABSTRACT

Knowledge of the effects of a combined cardiovascular and leg-strengthening program and their effects on sub-maximal cycle ergometry scores on USAF active duty males age 18 to 50 are of noteworthy clinical impact. The purpose of this 12-week study is to compare and identify the percent change in sub-maximal cardiovascular cycle ergometry scores between a more traditional cardiovascular and resistance training regimen and a non-traditional cardiovascular and resistance training regimen that incorporates intensive leg training emphasis. Anthropometric measures (waist and hip circumferences) and body weight will be taken to identify any relative relationships between these measures and cycle ergometry scores. The research hypothesis is twofold: (1) the leg resistive training group may enhance cycling economy (requiring oxygen use for the given amount of work performed) and (2) reduce leg strain during the cycle ergometry test due to increased leg strength and a more efficient heart rate response to leg work. It is postulated some USAF active duty enrolled in this training program may also experience a greater benefit in weight loss, due to the doubling of post-exercise caloric burn with the double workouts. Pre- and post-test data will be analyzed by a dependent correlated t-test ($p \geq 0.05$) to determine if there is any significant change in VO_2 scores after 12 weeks of training. A Pearson Product Moment Correlation Coefficient will be used to determine the statistical relationship between WHR and BMI and cycle ergometry scores.

AN INTEGRATED MICROSTRUCTURAL STUDY OF DRY SNOW

METAMORPHISM UNDER GENERALIZED THERMAL CONDITIONS

by

Daniel August Miller II

A dissertation submitted in partial fulfillment
of the requirements for the degree

of

Doctor of Philosophy

in

Engineering

MONTANA STATE UNIVERSITY
Bozeman, Montana

April 2002
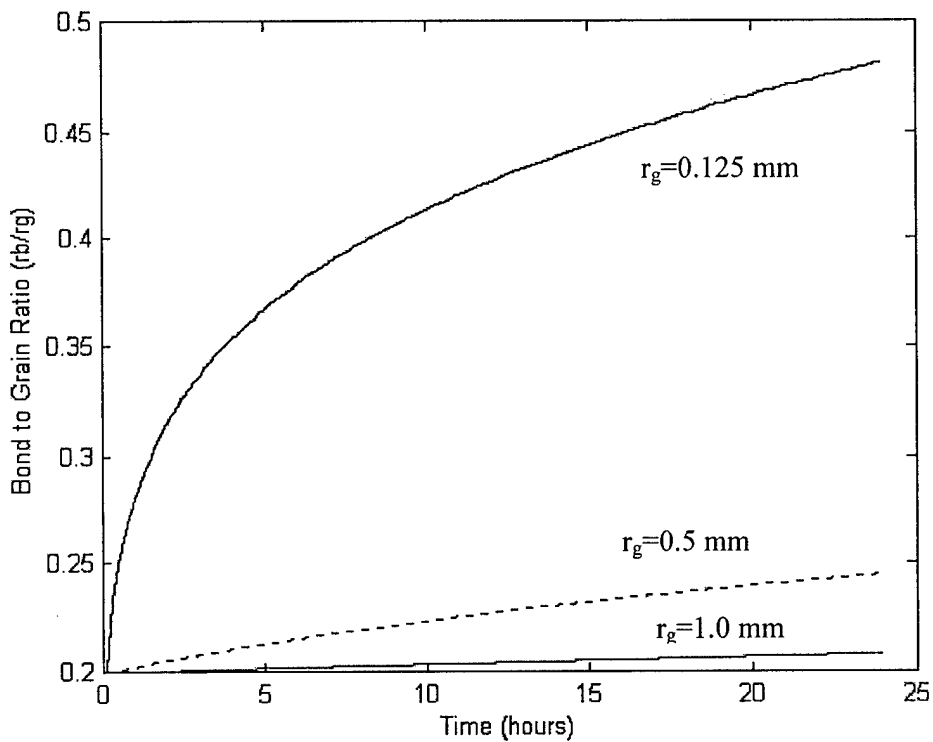
Figure 14. 24 hour time integration of grain to bond radii ratio.
T=-5°C, ρ=150kg/m³
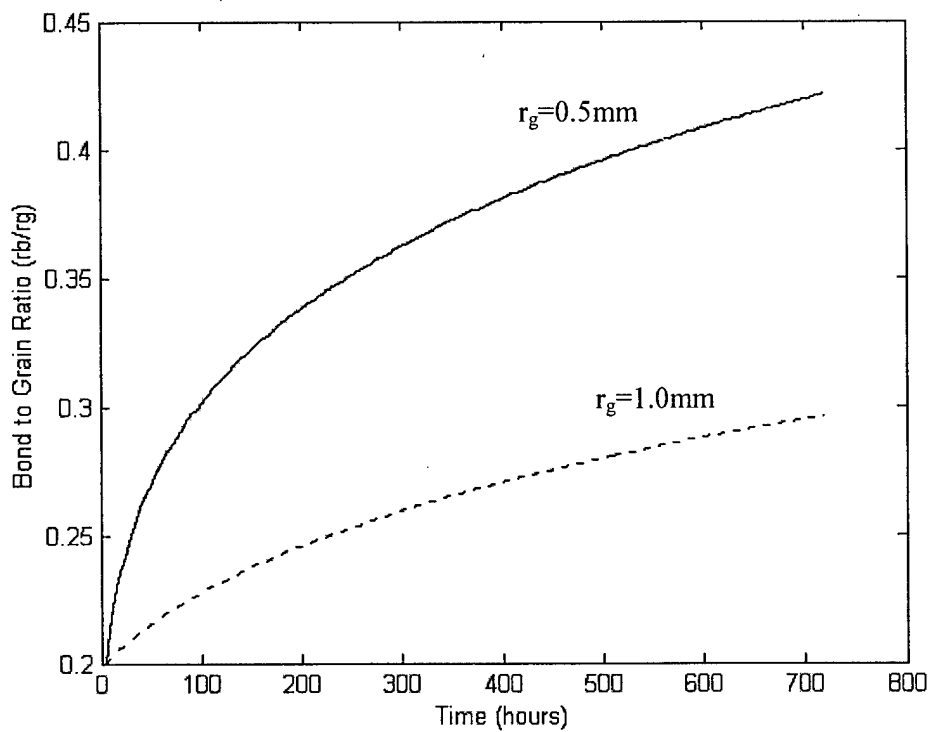
Figure 15. 30 day time integration of bond to grain radii ratio.
T=-5°C, ρ=150kg/m³
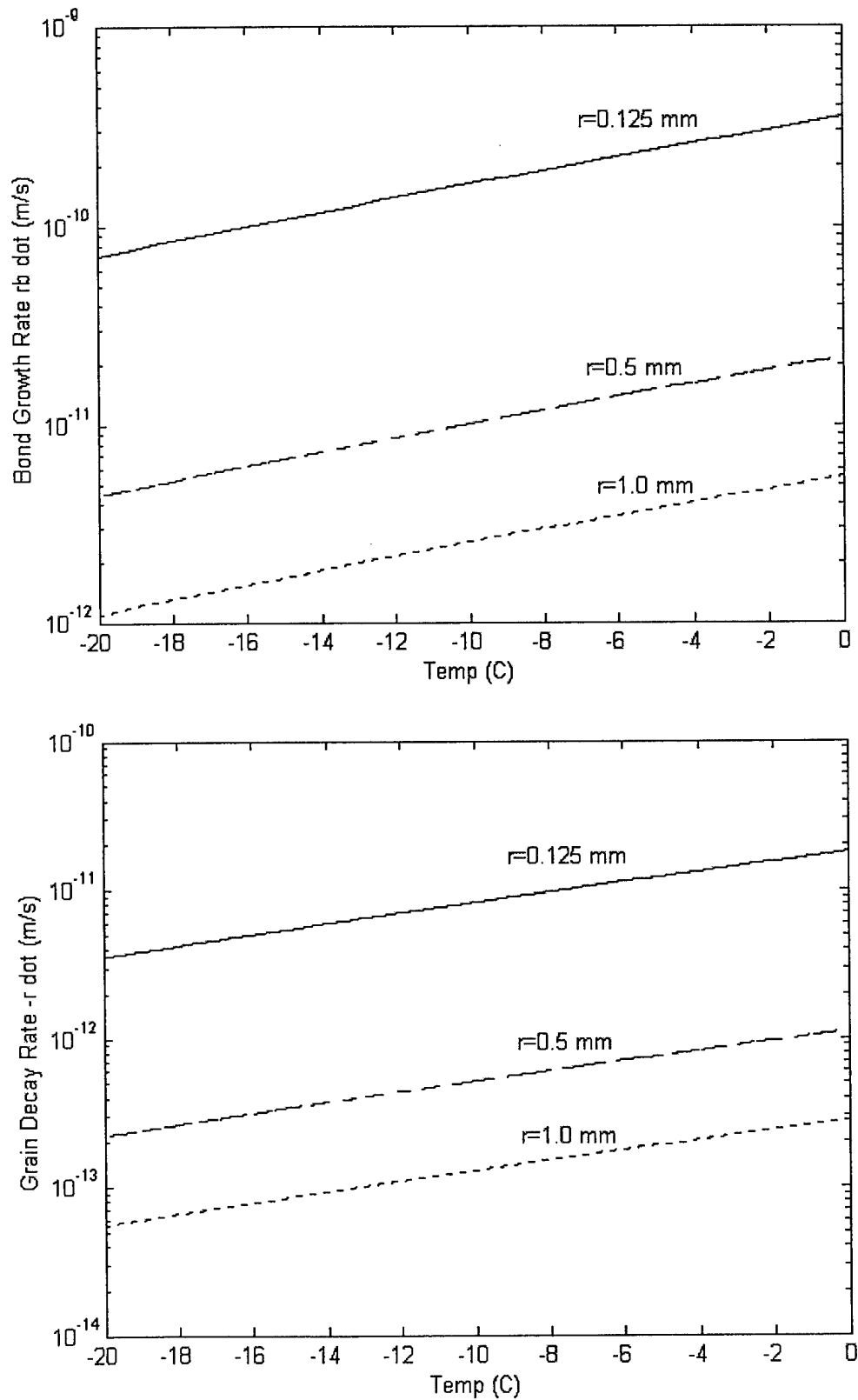
Figure 16. Bond growth rate and grain decay rate vs
temperature. ρ=150 kg/m^3, r_b/r_g=0.4

Metamorphism as a Function of Density. The snow density in table 1 is varied while holding the temperature and bond ratio fixed for all three grain sizes. The ice geometry is fixed for a particular problem and the pore sizes are varied with density as described in chapter 2. As the density increases, the size of the pore space for vapor movement decreases. Figure 17 shows the variation of bond growth rate and grain decay rate with density. Metamorphism in an equi-temperature environment appears to be relatively insensitive to variations in density. The bond growth rate changes are generally less than 20% over a large range of densities. Grain decay rate changes with density are slightly larger, but still small compared to bond size and temperature affects.

This result was surprising at first, but upon further thought and investigation, is logical. During vapor metamorphism in an equi-temperature environment, it is believed that vapor moves the very short distance from grains to neighboring necks (Kingery, 1960; Hobbs and Mason, 1964; Maeno and Eblnuma, 1983). As the vapor leaves the grain surface, diffuses through the pore, and condenses on the neck, the size of the pore is not a limiting parameter due to the local vapor movement. Given a specific ice geometry, the diffusion distance between grains and necks does not vary substantially with density, only the pore size changes. Since the pore size decreases with increased density, the pore's vapor storage capability decreases, slightly decreasing the metamorphic rate. The size of the pore is not the critical factor in this metamorphic regime. In the extremely dense snow where the pore becomes very small, pore size could become a limiting factor. For common snow densities less than 450 kg/m^3, density is not limiting local vapor transfer between grains and necks.
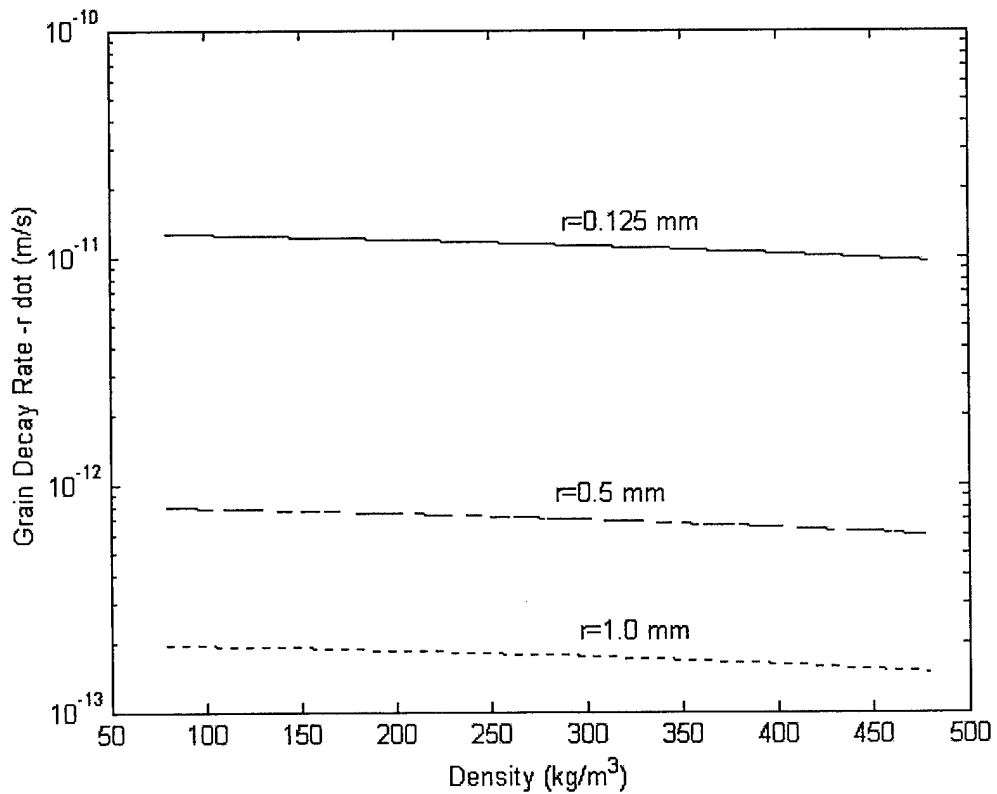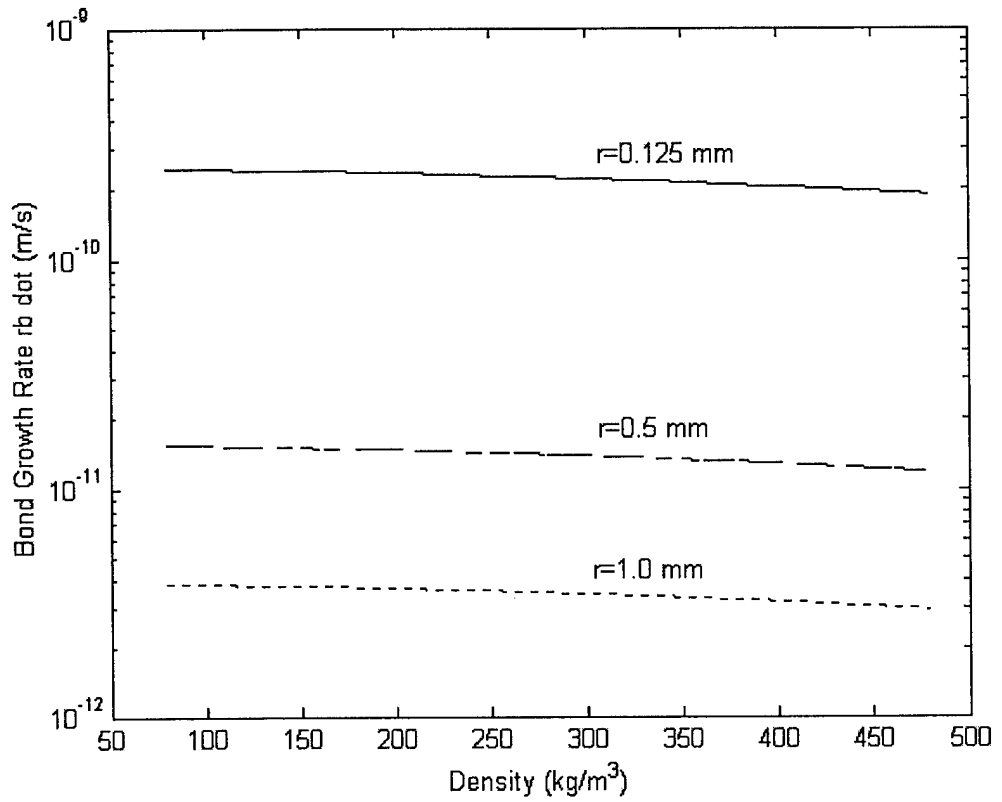
Figure 17. Bond growth rate and grain decay rate vs density. T=-5°C, r_b/r_g=0.4

In order for this result to be valid, most of the vapor leaving a grain should deposit on neighboring necks. If this were not the case, the pore would either supply vapor or remove vapor locally through diffusion. If significant diffusion to or away from neck and grain localities existed, the pore size would influence metamorphic rates. When a temperature gradient is applied, the density (pore size) will become a significant factor. The mass leaving the grains and the mass arriving at the necks were compared to see if a mass balance exists. Figure 18 gives the ratio of mass leaving the grain to mass arriving on the neck. The conservation of mass is very good between the necks and grains. As the density decreases, the pores get larger and vapor is allowed to move more readily away from grains and necks. Figure 18 shows slightly more vapor leaving the grains than attaching to the necks. For lower density snow, the larger pore is able to diffuse the excess vapor away. For higher density snow, the vapor is unable to diffuse through the smaller pore and the sintering rate is attenuated slightly. This explains why some previous studies (Hobbs and Mason, 1964; Maeno and Eblnuma, 1983) have been successful at modeling sintering by considering only the ice surface energies and not accounting for snow density or pore sizes in an equi-temperature environment.

Unequally Sized Grains

Most snow is not comprised of equally sized grains. Grain size distributions certainly occur throughout the snowpack. During the early phases of metamorphism, large grain size distributions may exist. As time progresses, bigger grains grow at the expense of smaller grains resulting in a decrease in the dispersion of grain
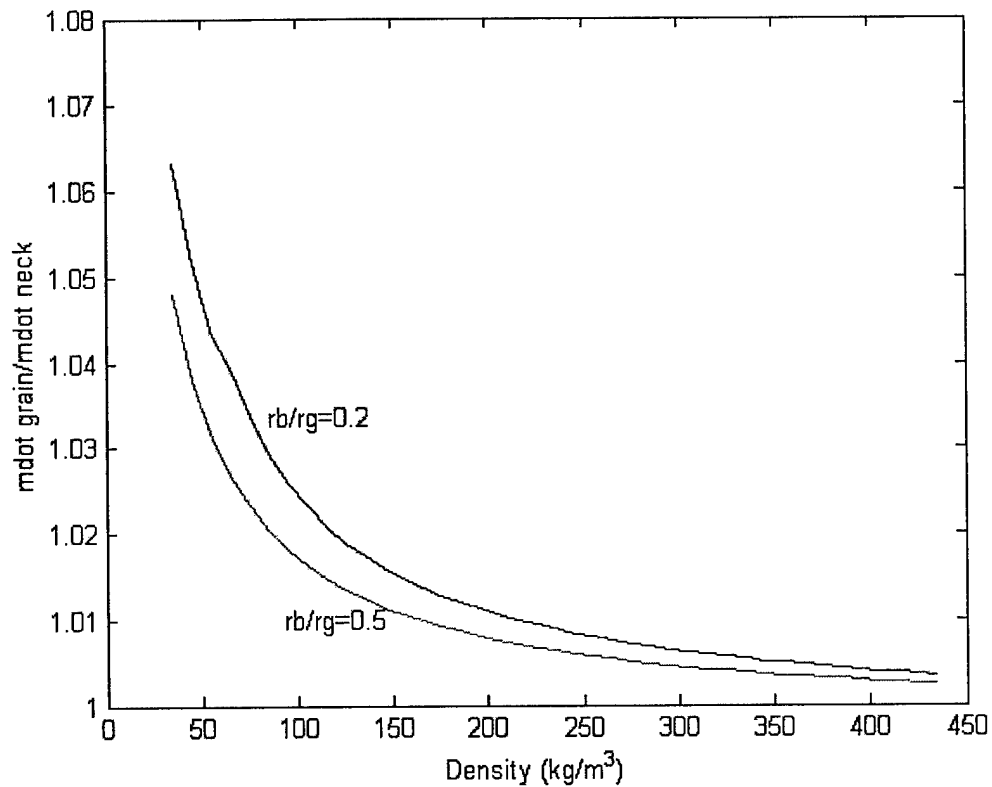
Figure 18. Ratio of mass leaving grain to mass attaching to neck vs density.
T=-5°C, all grain sizes

sizes. The growth of large grains at the expense of small grains has been explained by

surface curvature differences in an equi-temperature environment (Colbeck, 1980). The

decomposition of new dendritic crystals into smooth equilibrium forms is thought to

progress in a similar manner. The very sharp convex surfaces of dendrite tips cause rapid

sublimation and mass transfer to concave regions of the crystal. This process continues

until smooth rounded forms appear and the previously described sintering process

commences. While the current theory does not specifically address dendritic decay, the

physical principles involved in such a process are included.

The inclusion of multiple grain sizes in long-term metamorphism modeling is of questionable value since most seasonal snow layers rapidly become reasonably uniform, typically in a matter of minutes or hours (Tremper, 2001). Figure 1 is a classic example of snow transforming in an equi-temperature environment. While varying grain sizes are evident, the differences are not large.

On the other hand, during the early phases of metamorphism, modeling multiple grain sizes may be of value. As the crystal dendritic decay progresses, several sizes of grains inevitably result. The very small grains have been observed to disappear with the larger grains surviving. The current theory can provide a platform to evaluate this process and what parameters may influence it.
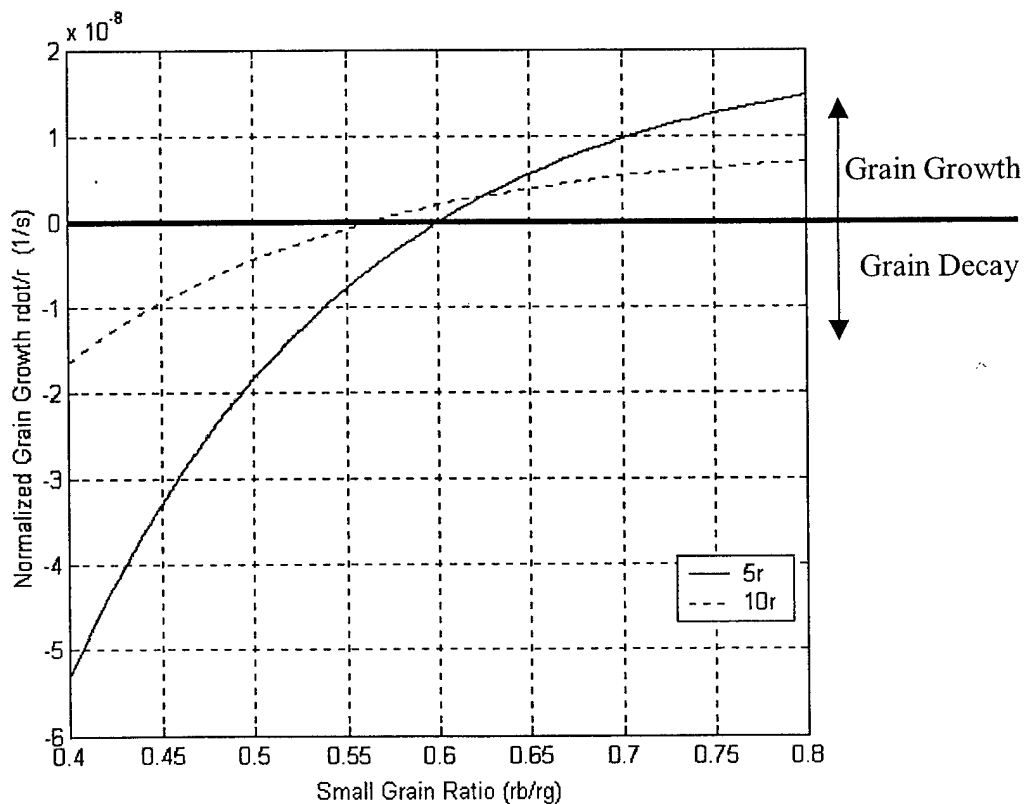
Figure 19. Normalized grain growth for large grain surrounded by small grains. $r_{g\,small}=1/32mm$, $\rho=150kg/m^3$, $T=-3°C$.

In the first study, a single large grain is surrounded by numerous smaller grains. Smaller diameter grains (1/16 mm) surround two different large grain sizes. Figure 19 shows the normalized grain growth rate as a function of bond to grain radii ratio for two different large grains. The bond to grain radii ratio is based on the smaller grain sizes. At lower bonding levels, the necks demand so much vapor that both the large and small grains give off vapor and therefore decay. As the bonds grow, their demand for vapor decreases, and the larger grains are now able to grow at the expense of the smaller grains. Throughout the simulation, the smaller grains continually decayed while the larger grains transition from decay to growth due to their lower surface energy. Figure 20 shows a similar result, but does so in terms of mass flow from the grain. Recall that the sign convention used has positive mass flow during sublimation, negative during condensation. The bigger grains transition sooner than the smaller ones, in fact, the large grain with a radius of $2r_g$ does not grow at the expense of the smaller grains for a wide range of bond to grain radii ratios.

In the next analysis, a simple distribution of grain sizes is defined to examine the model's ability to handle grain size variations. Fifty percent of the grains are assigned a diameter of 1/16 mm, while the other fifty percent are ten times larger (5/8 mm). In figure 21, the mass flow leaving the ice grains as a function bond to grain ratio is presented for the large and small grains. For comparison, a model of average sized grains is presented. For half the grains with radii of r_g, and the other half with grain radii of $10r_g$, the grain radius based on averaging the number of grains is $5.5r_g$. If an average based on grain volume is used, the grain radius would be $7.9r_g$. For the average radius results, the grains always decay since all the grains are of equal size. In the distributed

grain size case, the large grains grow at the expense of small grains when the bond to

grain ratio becomes sufficient.
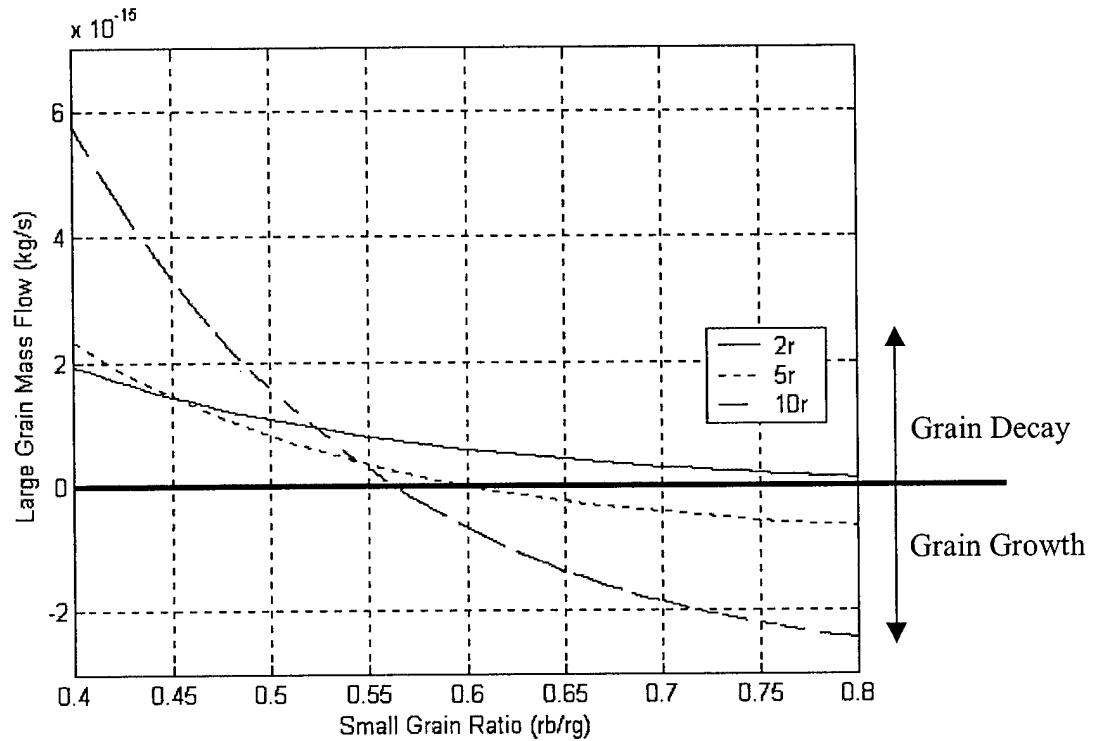
Figure 20. Mass flow for large grain vs small grain bond ratio.
$r_{g\,small}$=1/32mm, ρ=150 kg/m^3, T=-3°C.

With size variations, it is unlikely that the mass leaving individual grains will

arrive at a single neck as they did in the equally sized grains. To evaluate the mass

contributions that may or may not be required by the pore, a mass fraction is defined such

that

$$Mass\ Fraction = \frac{mass\ flow\ residual}{total\ mass\ flow} = \frac{\sum \dot{m}}{\sum \|\dot{m}\|}. \tag{108}$$

Equation (108) gives a relative indication of how much mass is being supplied by or being diffused away from the pore to support metamorphism. Figure 22 shows the mass fraction as a function of bond to grain radii ratio (based on the small grains). When the bonds are small, up to 20% of the total vapor for metamorphism is provided through diffusion by the pore. In this case, significant diffusion is made possible by the pore spaces associated with the large grains. This was not the case for equally sized grains. As bonding develops, the pore diffuses away excess vapor coming off the small grains that cannot be accepted by the bonds or large grains. Again, the large pore spaces associated with large grains make this process possible.
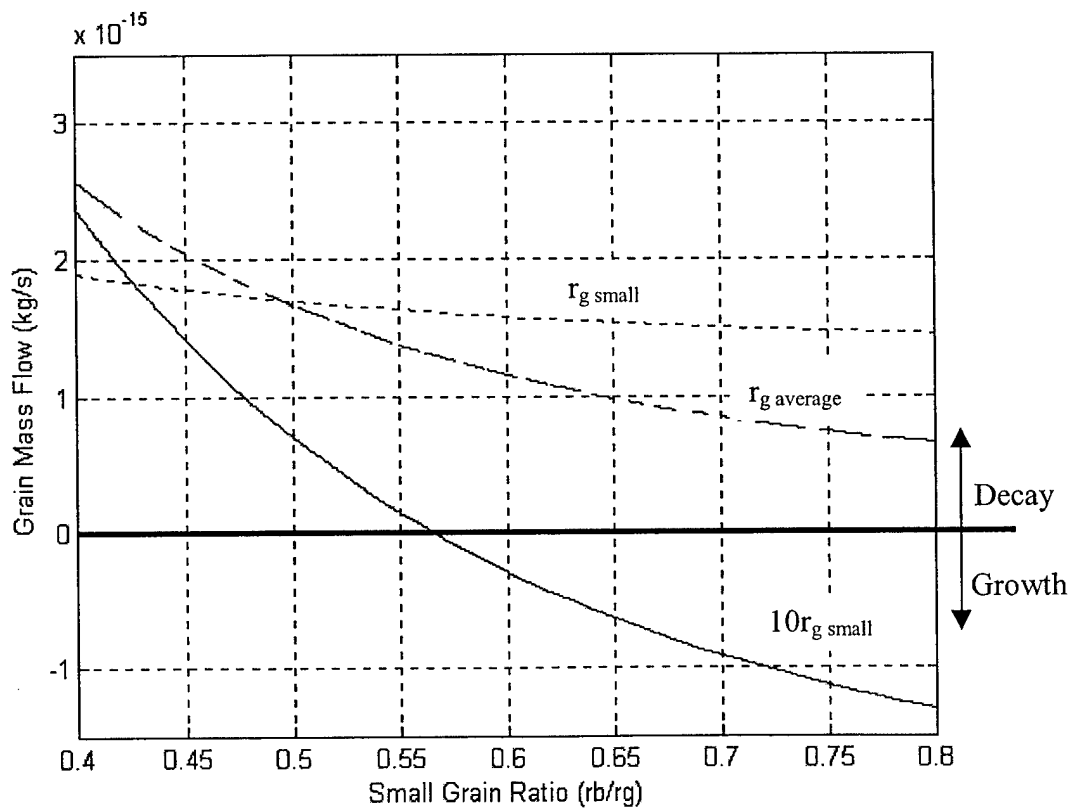
Figure 21. Grain mass flow vs small grain bond ratio for mixed and averaged grain sizes. $\rho=150$ kg/m^3, T=-3°C.

The preceding two studies demonstrate the model's ability to handle multiple grain sizes. Trends in growth and decay appear correct, but the importance of large size dispersions is questionable (Colbeck, 2001). The analysis does point to a potential future expansion for the theory, describing dendritic decay during early metamorphism. While the current model does not handle such a situation, the trends suggest the approach may be modified for such an application.
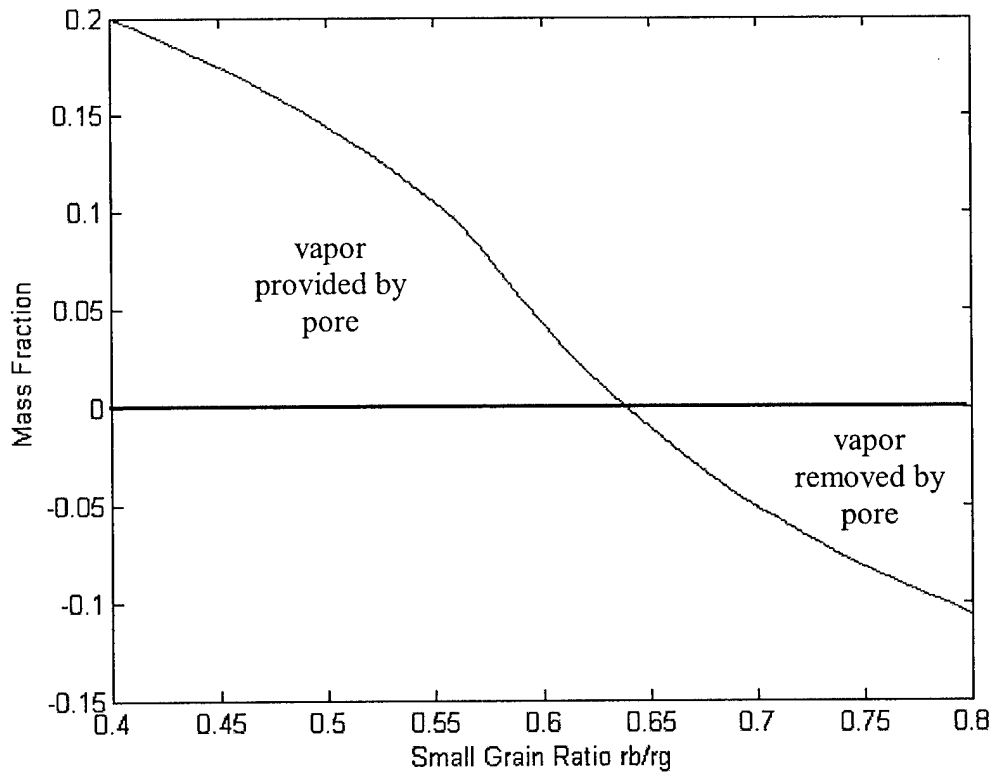
Figure 22. Mass fraction vs bond ratio for 50% small and 50% large grain sizes. ρ=150kg/m^3, T=-3°C.

Summary of Equi-temperature Metamorphism Analysis

The current approach and resulting model demonstrated the ability to examine numerous microstructural parameters and evaluate their influence on equi-temperature snow metamorphism. The small microstructural temperature gradients that have been previously speculated (Colbeck, 1980) to exist were evident. These gradients developed naturally in the model resulting in the well known metamorphic process whereby vapor sublimates from the grains, travels through the pore, and deposits on the necks. Several equi-temperature metamorphic trends were predicted. The model clearly demonstrated strong metamorphic dependence on grain size, bond size, and temperature with weak dependence on snow density. Bond growth rates decreased (significantly) with increasing bond size, increasing grain size, and increasing time. The effect of grain size was evident. Smaller grains sintered rapidly due to high surface energy, small neck volume, and short diffusion distances. As the grain size increases, sintering rates decreased dramatically. The sintering rate was also a strong function of temperature. As temperature decreased, so did the metamorphic rate. While metamorphism is a function of density, density was shown to be secondary to other parameters. It is believed that the very local nature of vapor flow between grains and necks is not heavily influenced by pore size. A mass balance showing the vast majority of vapor leaving an individual grain arrived at neighboring necks supported this theory. While no restrictions on local vapor travel were made, the commonly held thoughts on mass conservation during equi-temperature metamorphism were supported. Two studies of unequal sized grains demonstrated the model's ability to predict the growth of large grains at the expense of smaller ones. The evaluation size requirements for this growth/decay scenario were

complicated by other factors such as bond size and grain distribution. Overall, the model

followed many well established trends in snow metamorphism.

Onset of Kinetic Growth Metamorphism

Introduction

The transition between the smooth rounded growth forms common in an equi-

temperature environment and the sharp faceted forms found in a temperature gradient

environment has not been studied extensively. Most research surrounding this transition

is experimental. It is commonly believed that the critical temperature gradient for faceted

growth is around 10-20°C/m (Akitaya, 1974a; Armstrong, 1980; Colbeck, 1983a, 1983b)

or greater than 25°C/m (Marbouty, 1980). It is recognized that this transition is a

function of density, pore size, grain size, and temperature (Colbeck, 1983b), but little

analytical work has been done to show the relative importance of each. It is recognized

that low density snow transitions at a lower temperature gradient than higher density

snow, but microstructurally based analytical approaches explaining this phenomenon are

lacking. The current approach may be used to study this transition and various

parameters influencing the transition. First, a definition of kinetic growth transition

temperature gradient is required.

Definition of the Onset of Kinetic Growth Metamorphism

There is clearly no agreed upon point where equilibrium forms dominate and then

suddenly faceted forms appear. A smooth transition based on physical constraints is

desired instead of relying on incomplete empirical data. The transition temperature gradient required to "turn on" the kinetic growth model was described in chapter 2, requiring no phenomenological modifications. Grains cannot grow in a kinetic form when they are decaying, as is the case in an equi-temperature environment. When a temperature gradient is applied, vapor diffuses in the pore, and heat conducts through the ice. As the temperature gradient increases, the grain decay rate decreases, and the neck growth rate increases due to the excess vapor pressure of the pore. Kinetic growth processes are allowed to begin when the temperature gradient is sufficient to transition the grains from decay to growth.

The temperature gradient where a "majority" of the grains start to grow is defined as the onset or transition temperature gradient for kinetic growth. It is in fact somewhat arbitrary, but has a logical justification. One can think of the equi-temperature and temperature gradient processes commencing simultaneously in both environments, but which is predominant when? In an equi-temperature environment, the excess vapor pressure in equation (55) is negative resulting in a negative kinetic growth velocity. Since a negative growth velocity in a screw dislocation model has no meaning, that process is inactive when the grain is decaying, resulting in no kinetic growth. The smooth rounded forms are allowed to develop as previously described. As the temperature gradient increases to the point where grains begin to grow, this is the first opportunity for kinetic growth. Near the transition temperature gradient, the smooth and faceted forms may be equally viable, resulting in combined morphologies. Mixed rounded and kinetic forms are rare, but have been observed (Colbeck, 1982; 1983a). As the temperature gradient continues to increase, the grain growth due to kinetic

98

metamorphism becomes predominant. The model includes both, and allows each to commence as required. Figure 23 gives a pictorial representation of this process and the definition of the transition temperature gradient. As the temperature gradient increases, the flux leaving the grains decreases. At the transition temperature gradient, the grains begin to grow.
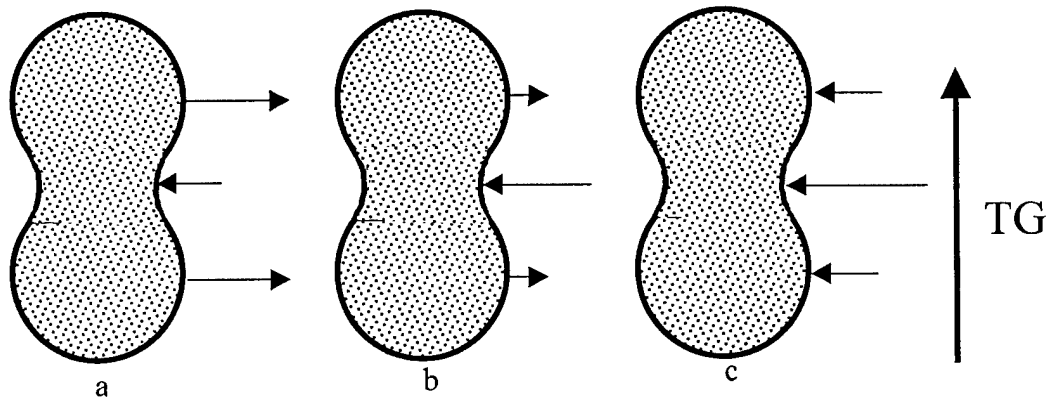
Figure 23. Vapor flux definition of temperature gradient at onset of kinetic growth. (a) TG=0, Equi-temperature vapor fluxes. (b) TG>0, TG less than onset of kinetic growth. (c) TG>0, TG at onset of kinetic growth

Numerical Studies for Kinetic Growth Onset

With the onset of kinetic growth defined, the model may be used to examine various parametric dependencies. The first study examines the grain growth rate in snow as the temperature gradient increases. A smooth transition from grain decay to growth is presented. The onset of kinetic growth is then studied as a function of density. Finally, the kinetic growth transition is examined as a function of temperature and grain to bond radii ratio.

Grain Growth Transition. The transition from grain decay to grain growth is shown for three grain sizes as a function of the applied temperature gradient in figure 24. As the temperature gradient increases, the grain growth rate increases. The onset of kinetic growth is clearly visible as the grain radial growth rate transitions from negative to positive. Throughout the temperature gradient range, the changes are smooth and continuous. Previous models required a discrete transition as new physical models were required. Also, kinetic growth transitions have generally been based on the 10°C/m criteria, with little or no regard to any physical parameters that may effect that value. Since the temperature gradient shown did not exceed 25°C/m, the 0.5mm grains did not yet reach their kinetic growth transition. The bond grow growth rate is also represented in figure 24. As expected, the bond growth rate is always positive and increasing with temperature gradient. Unlike the equi-temperature simulations, in a temperature gradient environment, the vapor diffusing from the pore is critical. This is apparent as the grains begin to grow while necks continue to grow, requiring a vapor supply from elsewhere. The pore is supplying this vapor where the pore only transported vapor from the grains to the necks in the equi-temperature model. Therefore, the transition temperature gradient to kinetic growth should be dependent upon the snow density. An upcoming result confirms this.
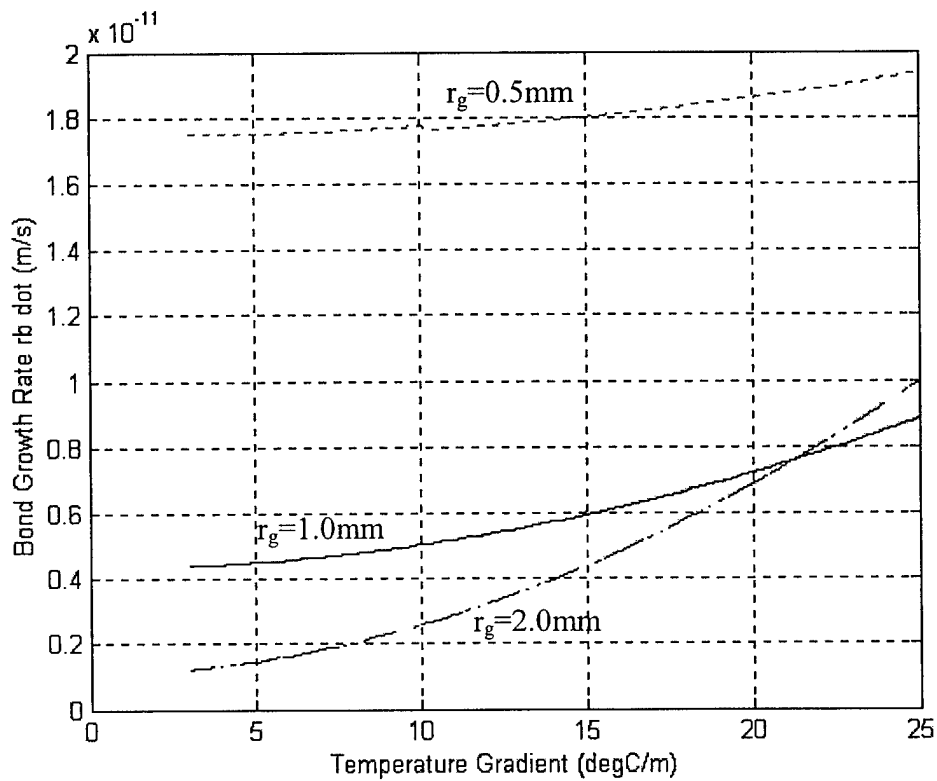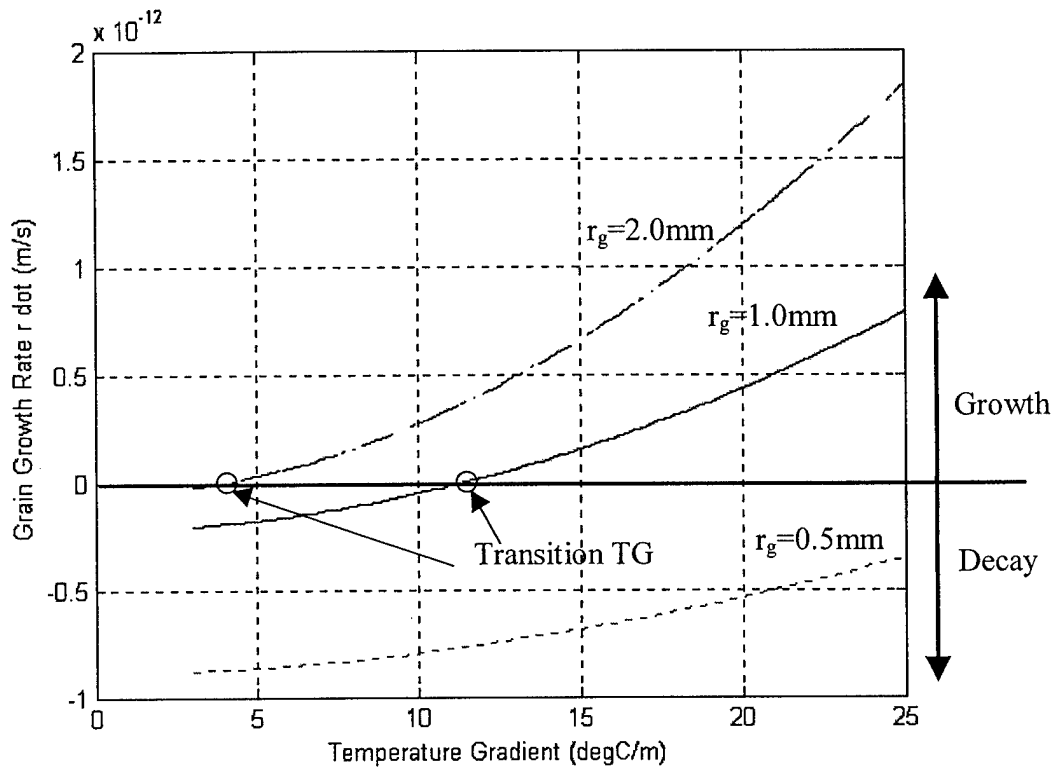
Figure 24. Grain and bond growth rate vs temperature gradient, equally sized grains. T=-3°C, ρ=150 kg/m^3, r_b/r_g=0.4.

<u>Onset of Kinetic Growth as a Function of Density and Grain Size.</u> With the smooth transition from grain decay to growth with increasing temperature gradient established, the onset of kinetic growth can be examined. In a temperature gradient environment, the size of the pore spaces, and therefore the density, should be a major factor in the onset of kinetic growth. It is commonly accepted that lower density snow (larger pore spaces) is much more likely to show kinetic growth with a smaller temperature gradient. In addition to the pore size for vapor transport, large faceted crystals need sufficient space to grow. Marbouty (1980) showed an increase in the grain size with decreasing density when subjected to a temperature gradient sufficient for kinetic growth. He also showed a kinetic growth upper limit density of 350 kg/m^3, above which kinetic growth was not observed even under large temperature gradients. In higher density snow, Marbouty found the lack of pore space obstructs crystal growth. The crystals became sharp, but failed to grow appreciably in size. These crystals formed under large temperature gradients and dense conditions were referred to as "hard" depth hoar (Akitaya, 1974a).

Figures 25 and 26 show the kinetic growth transition temperature gradient as a function of density for three grain sizes. In figure 25, the bond to grain radii ratio is 0.5, whereas it is only 0.2 in figure 26. As expected, the onset of kinetic growth is a strong function of density. As the density decreases, the larger pore spaces allow for easier vapor movement, resulting in a lower onset temperature gradient. Notice the bond to grain radii ratio influences the onset temperature gradient. Smaller necks demand more vapor, leaving less available for the grains resulting in a higher temperature gradient for kinetic growth. The small bonds in figure 26 remain for only a short time and are found

in newly deposited snow, while figure 25 is representative of snow that has sintered for many hours or days. As expected by the definition, grain size has a strong influence on the onset of kinetic growth. Larger grains require a lower vapor pressure to overcome their convex shape, resulting in a lower temperature gradient required for kinetic growth. It is interesting to note that for very commonly observed grain sizes and densities, the accepted range of 10-25°C/m is supported by the analysis. In addition to establishing this onset in a mathematical context, the model enables the study of important parameters that may influence the onset of kinetic growth. Other important parameters (in addition to grain size and density) such as temperature and bond size are now examined in further detail.
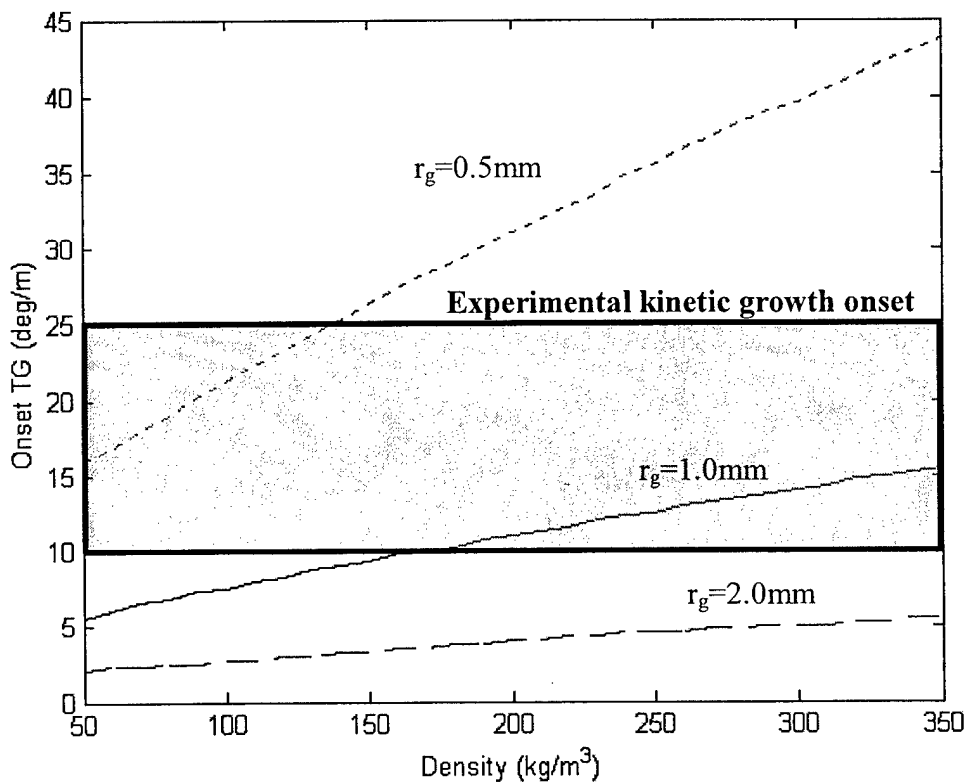
Figure 25. Onset temperature gradient for kinetic growth vs density, T=-3°C, r_b/r_g=0.5. Boxed region represents experimental temperature gradient required for kinetic growth.
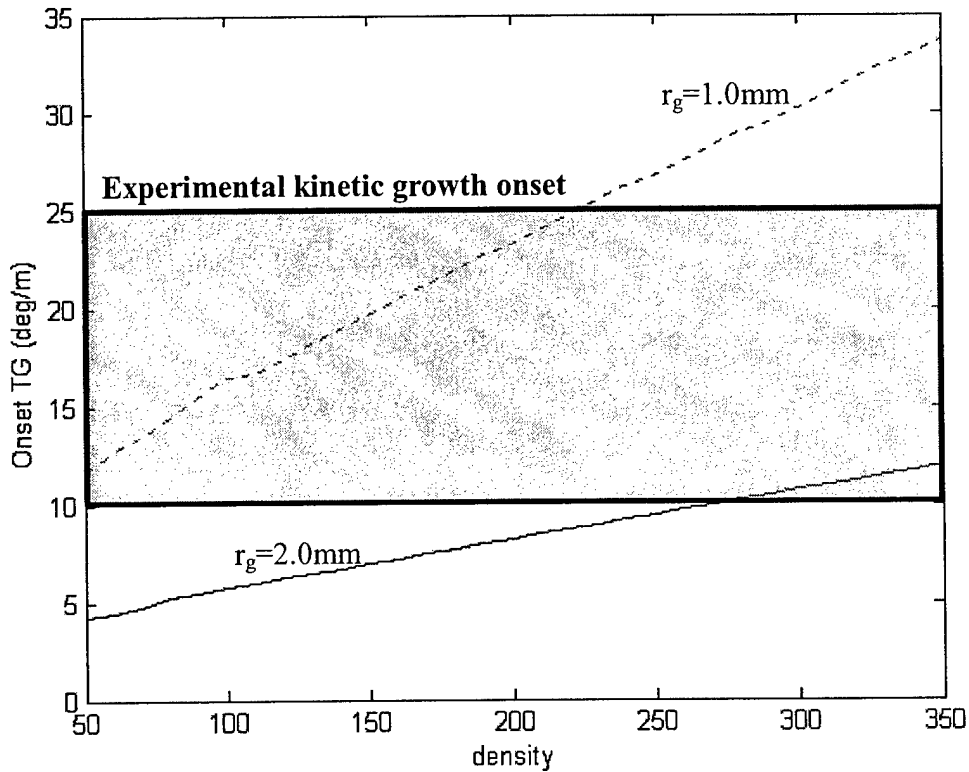
Figure 26. Onset temperature gradient for kinetic growth vs density,
$T=-3°C$, $r_b/r_g=0.2$. Boxed region represents experimental temperature
gradient required for kinetic growth.

<u>Onset of Kinetic Growth as a Function of Pore Temperature.</u> The influence of

temperature on the temperature gradient required for kinetic growth is examined next.

The grain geometry of figure 26 is used, except a density of 100 kg/m^3 is fixed as the

pore temperature is varied. In figure 27, it is evident that the temperature gradient at the

onset of kinetic growth is relatively insensitive to temperature. While the onset of kinetic

growth may not be sensitive to temperature, clearly the metamorphic rates should be, as

was the case for the equi-temperature environment. Figure 28 shows the variation of

bond growth rate at the onset of kinetic grain growth as a function of pore temperature.

The decrease in bond growth rate with decreasing temperature is evident. So while the

onset of kinetic growth is not a strong function of temperature, the metamorphic process

rates are.
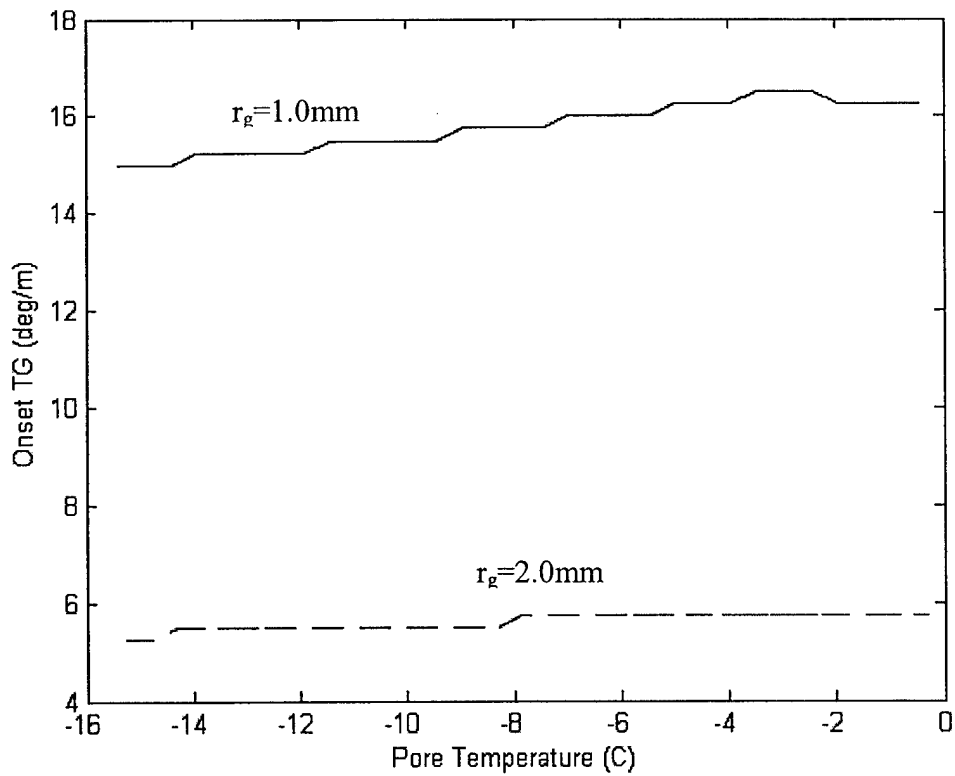
Figure 27. Onset temperature gradient for kinetic growth vs pore temperature. $\rho=100\text{kg/m}^3$, $r_b/r_g=0.2$.
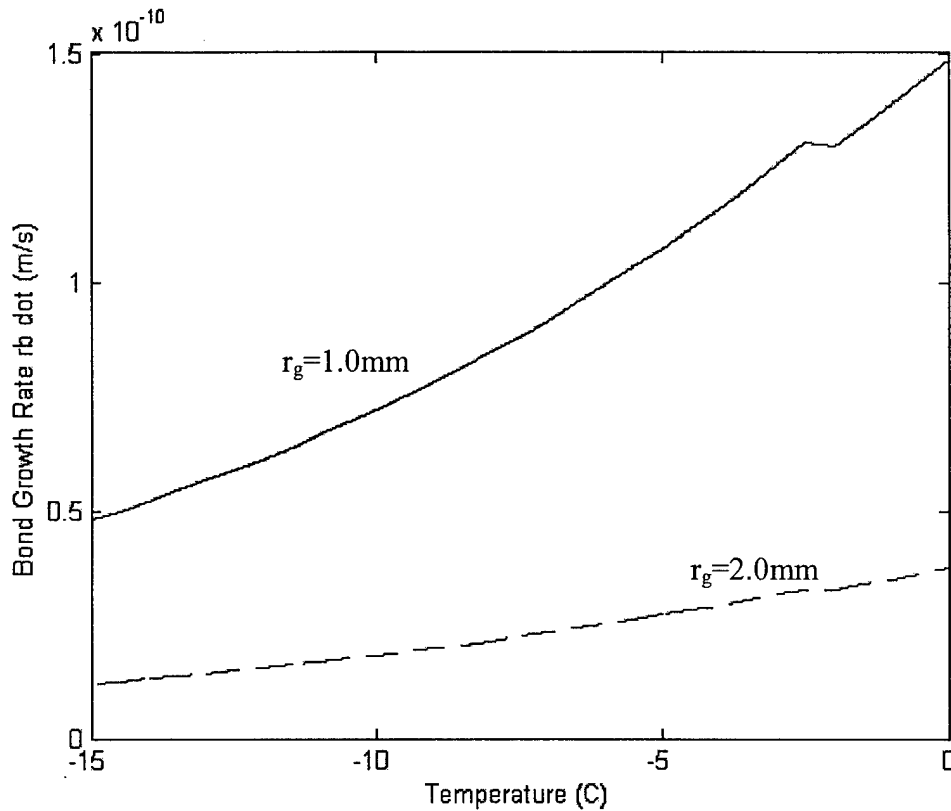
Figure 28. Bond growth at the onset of kinetic growth vs temperature.
$\rho=100$ kg/m^3, $r_b/r_g=0.2$.

Onset of Kinetic Growth as a Function of Bond to Grain Radii Ratio. As

observed in figures 25 and 26, the relative size of grains and bonds, in part, determines

the vapor demand for bond growth. As a result, the temperature gradient at the onset of

kinetic growth in influenced by the bonding maturity. Figure 29 shows the sensitivity of

onset temperature gradient to bond to grain radii ratio. The onset can vary by a factor of

two or three between small and large bonds. The implications of this result may be

significant to the prediction of depth hoar development. As freshly fallen snow begins to

decompose to other forms, the intergranular bonds are small, but develop quickly. If subjected to a temperature gradient at this time, kinetic growth may not commence until sufficient vapor is available to satisfy new vapor hungry necks and grain growth. If the newly fallen snow is allowed to sinter under equi-temperature for several hours or days before a temperature gradient is applied, the neck vapor demands are lower and kinetic growth may commence sooner. Of course this analysis does not account for density changes due to snow settlement, which could be large for young snow. The increase in onset caused by increased density may offset the decrease in onset for highly bonded snow.
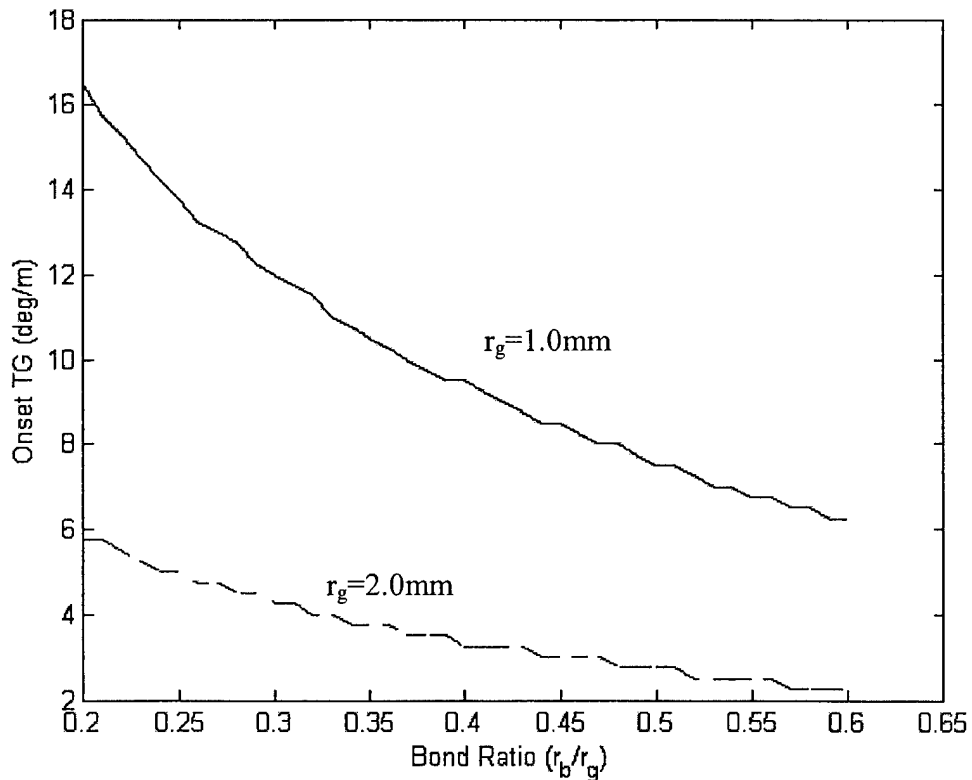
Figure 29. Onset temperature gradient for kinetic growth vs bond to grain radii ratio. T=-3°C, ρ=100kg/m^3.

<u>Onset of Kinetic Growth for Unequally Sized Grains.</u> The studies presented so far for the onset of kinetic growth have been for snow comprised of equally sized grains. The onset of kinetic growth was examined using the three grain sizes of 0.5, 1.0, and 2.0 mm. In this section, the onset of kinetic growth for snow comprised of mixed grain sizes is examined. For the first case, half of the grains had 0.5mm radius and the other half of the grains had a 1.0mm radius. The second case used 0.5mm and 2.0mm grains in equal numbers. The definition of kinetic growth onset for this study was when the smaller grains transitioned from decay to growth. The resulting temperature gradients required for grain growth are presented in Table 2.

| | Onset TG(°C/m) | | |
	0.5mm	1.0mm	2.0mm
Equally Sized Grains	57	20	7
Half 0.5mm, Half 1.0mm	61	54	n/a
Half 0.5mm, Half 2.0mm	36	n/a	33

Table 2. Onset of kinetic growth comparison for snow comprised of equally sized grains and mixed sized grains.

The mixed grain sizes are clearly influenced by the smaller grains. In both mixed grain examples, the large grain transition temperature gradient increases toward the smaller grain transition. In fact, the 1mm grains transition at nearly the same temperature gradient as the equally sized 0.5mm grains alone. In one case, the small grain transition temperature gradient increased slightly when mixed with 1mm grains. In the other case,

the small grain transition temperature gradient decreased significantly. In both cases, it is clear that the transition temperature is heavily influenced by the smaller grains. As expected, the size of the pore is significant where the majority of the grains influence the transition. For the 1.0/0.5mm mixture, the pore appears to be limited by the smaller grains since the transition is close to the 0.5mm grains alone. When an even larger grain size difference is applied in the 2.0/0.5mm mixture, the pore space associated with the 2.0mm grains helps alleviate the vapor flow limitations of the 0.5mm grains. Overall, the size of the pore spaces, whether controlled by density or grain size, will be a major factor determining when kinetic growth may commence.

Summary of Onset of Kinetic Growth Metamorphism

In this section, a new physical definition for the onset of kinetic is proposed. The transition of grain decay to growth with increasing temperature gradient is smooth and continuous. The onset temperature gradient is examined in light of several microstructural parameters, with the size of the pore space and grains emerging as the premier factors determining when kinetic growth may occur. The pore space can be changed through density or grain size variations, making the onset a strong function of both grain size and density. For high density snow, the smaller pore space limits vapor travel. For larger grains, the transition happens sooner due to larger pore spaces and smaller surface curvature. While the onset of kinetic growth is not a strong function of temperature, the overall metamorphic rates are. Bond size influences the kinetic growth transition. For new snow with small bonds, the vapor demand of the necks holds off the transition to larger temperature gradients. This seems to imply that older, highly bonded

low density snow will transition sooner, but snow densification associated with settling may offset this affect. This process was not modeled here. Finally, with mixed grain sizes, a large number of small grains may fill the pore spaces, limiting vapor travel and resulting in a greater transition temperature gradient.

<center>Kinetic Growth Metamorphism</center>

Introduction

With the transition to the kinetic growth regime defined, the kinetic model presented in chapter 2 may be implemented. Recall the primary faceted crystal habit was determined from temperature, (figure 8 from Lamb and Hobbs, 1971). The angle from the dominant growth direction to the crystal, β, fixed the crystal habit by defining relative c and a axis growth (figure 9). While the crystal habit and growth from parent grains were discussed, the relationship between the crystal and the temperature gradient was not addressed. In this section, the variation in parent grain crystal orientation is simulated and included in the model. Faceted crystal development is then modeled for various scenarios. The resulting model predicts a grain size distribution, depending upon crystal orientation. This leads to a discussion of a dominant grain theory for kinetic growth and potential bonding mechanisms.

Crystal Orientation and Dominant Grain Theory

In chapter 2, a mathematical model of kinetic growth was developed using research from several authors combined with some original development. It was

proposed that faceted crystals nucleate on existing or parent grains, but what crystallographic orientation do these faceted growth forms acquire? It seemed logical to assume that vapor nucleating on existing grains would develop with the same orientation as the parent grain, but no direct evidence exists in the literature to support this. It is well established that ice crystals grown from the liquid phase will tend to take on the crystallographic orientation of the primary structure onto which they develop, but is the same true for vapor growth? A laboratory experiment was conducted where ice crystals were formed from vapor on existing ice with known crystallographic orientation (Adams and Miller, 2002). The details of this experiment are provided in chapter 4, but the results clearly show ice crystals grown from the vapor on existing ice substrates acquire the same crystallographic orientation as the substrate.

Even though the primary crystal habit is established by temperature, all grains have the potential to grow as facets. Certain crystal orientations (relative to the temperature gradient) may be preferentially oriented for enhanced growth. In light of this, a hypothesis about some morphologic processes in a snowpack is now presented.

Atmospherically formed snow crystals will in general be deposited onto the ground in a random crystallographic orientation. When subjected to a temperature gradient, the "new" crystals will pick up the orientation of the parent (primary/nucleate) snow grains onto which they accrete. Because the primary crystal habit is determined by temperature, a particular kinetic growth crystal is at an advantage due to parent crystal orientation, since it is better positioned to quickly grow deeper into warmer vapor (if it is not restricted by the proximity of other grains). This will produce a larger temperature gradient and faster growth at the tip of the crystal. New crystals that are favorably

oriented could crowd out other less optimally oriented crystals. Since crystals grow with the same orientation as the parent grain, and observed depth hoar crystal morphologies are similar amongst grains in the same snowpack location (Akitaya, 1974a), this dominant grain theory seems plausible. An analogous situation exists in the growth of ice from the liquid phase. Ice covers grown under quiescent conditions on lakes will tend toward a c-axis vertical orientation. The nomenclature on lake ice growth describes this as S1 ice, where the S represents a secondary growth pattern, which follows the primary, P, formation (Michel and Ramseier, 1971). However, ice developing from the liquid phase has a higher growth rate parallel to the basal plane, due to differences in thermal conductivity (Lock, 1990). Therefore, given opportunistic conditions, a vertically oriented basal plane will grow more deeply into the liquid phase than an adjacent c-axis vertical crystal. As this process progresses, vertically oriented basal planes advance deeper into the warmer liquid, enhancing the temperature gradient at the tip and further benefiting its natural growth advantage. Basal plane growth dominance results in crowding out c-axis vertical crystals and the ice sheet may develop into a c-axis horizontal preference, referred to as S2 ice.

To study the dominant grain growth scenario, the variation of crystal orientation relative to the temperature gradient must be established. In figure 9, the crystal habit was defined by the angle β from the dominant growth axis to the crystal. The habit was determined using the relative crystal growth data as a function of temperature (figure 8 from Lamb and Hobbs, 1971). Now, the angle from the temperature gradient to the dominant growth direction is defined by γ. Figure 30 shows the relationships between the

crystal, crystallographic axes, and temperature gradient. Given a distribution of crystal

orientations, γ, certain crystals may have a more advantageous orientation for growth.
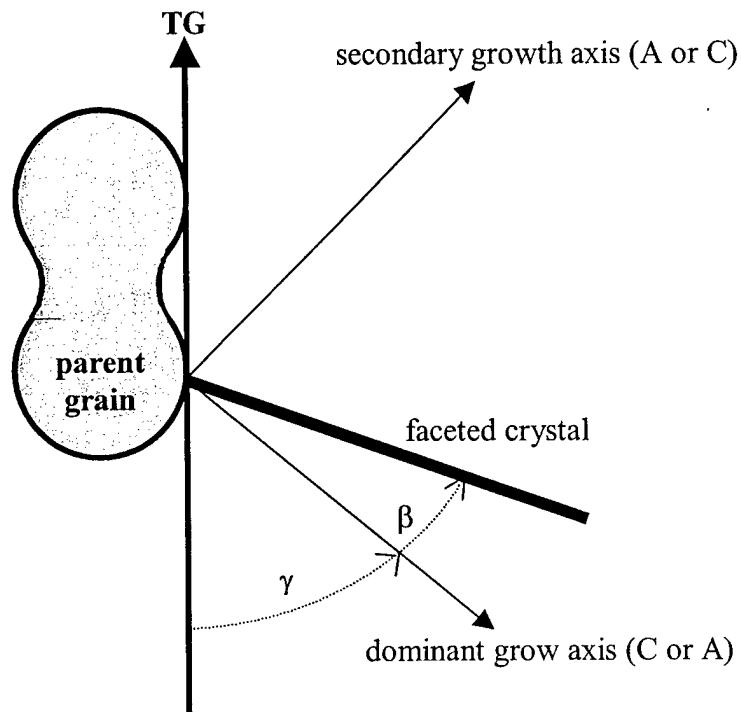
Figure 30. Relationship between crystal habit (β), crystal orientation relative to temperature gradient (γ).

Numerical Considerations

Before numerical calculations may commence, some approximations are required.

The crystal growth velocity described in equation (55) requires excess vapor pressure

over the ice surface. For this analysis, the excess vapor pressure is found from the

difference of vapor pressure in the pore near the tip of the crystal (growth end) and the

vapor pressure over the ice surface itself. Since a facet is essentially flat, the Clausius-Clapeyron equation (38) is used to find vapor pressure over the ice and the vapor pressure in the pore. Since a finite difference solution is used, what is the proper temperature of the ice and pore to use in vapor pressure calculations? As the crystal grows, its tip may travel through several pore elements. To establish the vapor pressure of the pore near the tip, the current crystal tip location and corresponding pore element is found. If the tip is in an element associated with a grain, a spatial linear interpolation between neighboring nodes is then accomplished to establish the pore vapor pressure. If the tip is in an element associated with a neck, the average value of all three element nodal pressures is used. Since the neck lengths are generally very small when compared to the grain radii, the approximation of constant vapor pressure in an element near a neck is reasonable. As will be shown later, the faceted crystal growth rates are such that the transition through neck associated elements is relatively rapid, most of the growth takes place in pore spaces associated with the grains. If the crystal tip points up into a cooler part of the vapor, the excess vapor pressure is negative and clearly the kinetic growth velocity is zero. The ice surface temperature is simply taken as the nodal temperature of the crystal attachment (central ice grain nodal temperature). Since the thermal conductivity of ice is nearly two orders of magnitude larger than the vapor, this approximation seems reasonable. In reality, the ice tip would be slightly warmer than the crystal root to allow for latent heat dissipation. Coupled with the theory and assumptions presented here, the kinetic growth theory described in chapter 2 may be solved numerically.

Kinetic Growth Simulations

As the temperature gradient increases, the transition to kinetic growth has now been established. Rounded grains are then allowed to grow kinetically with a specific crystal habit (based on temperature) and orientation relative to the temperature gradient. The influence of temperature on the growth of faceted crystals is examined, followed by the influence of crystal orientation.

Facet Growth as a Function of Temperature. The change in facet growth rate as function of temperature is not a simple result. In addition to the temperature dependence of metamorphic processes due to molecular mobility, the dominant crystal habit changes as the temperature changes (figure 8). The growth rates of the a and c-axes are not the same under identical conditions. The critical excess vapor pressure in equation (56) is greater for c-axis growth due to a larger lattice parameter, a_0 (Petrenko and Whitworth, 1999). As a result, under a-axis dominant growth, the crystal grows faster than if the c-axis dominated under the same conditions. The growth velocity of the dominant axis is calculated using equation (55). The combination of these affects on growth velocity is presented in figure 31. For ease of comparison, the angle from the crystal to the temperature gradient was fixed at 20° (the combination of crystal habit and crystal orientation). The overall growth rate does decrease with decreasing temperature. In addition, the transitions between a and c-axis dominant growth are evident, and take place at temperatures indicated in figure 8. The increased a-axis growth rate is apparent.
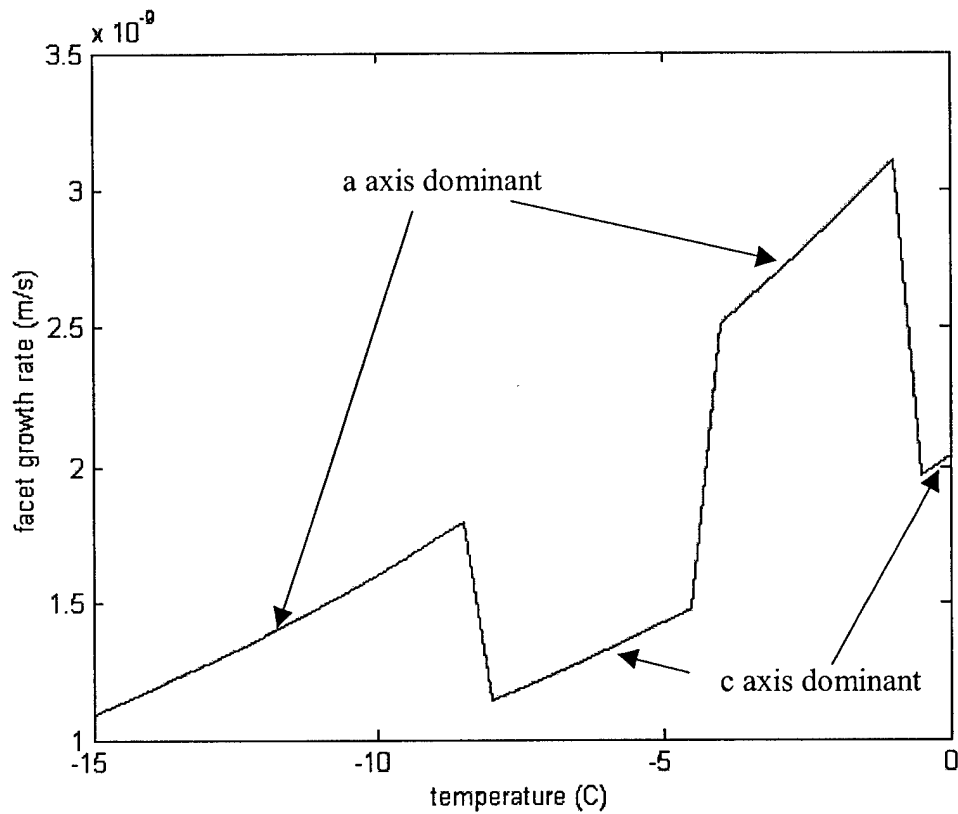
Figure 31. Facet growth vs temperature. $\gamma+\beta=20°$, $\rho=150$ kg/m^3, TG=45°C/m, base grain $r_g=0.5$mm, $r_b/r_g=0.6$, facet length=0.75mm

Facet Growth as a Function of Crystal Orientation. Figure 32 shows the variation in the facet growth velocity with dominant growth axis orientation to the temperature gradient, γ. A grain 25% larger than the parent grain was used to show the growth in the pore element associated with the neighboring neck. Recall that a constant average vapor pressure was assumed in the pores associated with necks resulting in a nearly constant growth rate. As the crystal is rotated counterclockwise away from the temperature gradient, the tip enters the pore associated with the grain. Here, the vapor pressure is

spatially linearly interpolated resulting in a decreasing growth rate as the dominant crystal growth axis diverges from the temperature gradient direction. As the crystal is oriented perpendicular to the temperature gradient, the excess vapor pressure becomes negative and growth ceases. If the crystal is smaller than the parent grain, the pore next to a neck is not encountered by the tip, making the decrease in growth rate smooth and continuous. If the crystal is large, several grain and neck associated pores may be encountered resulting in a "stepped" decrease in growth rate with increasing γ.
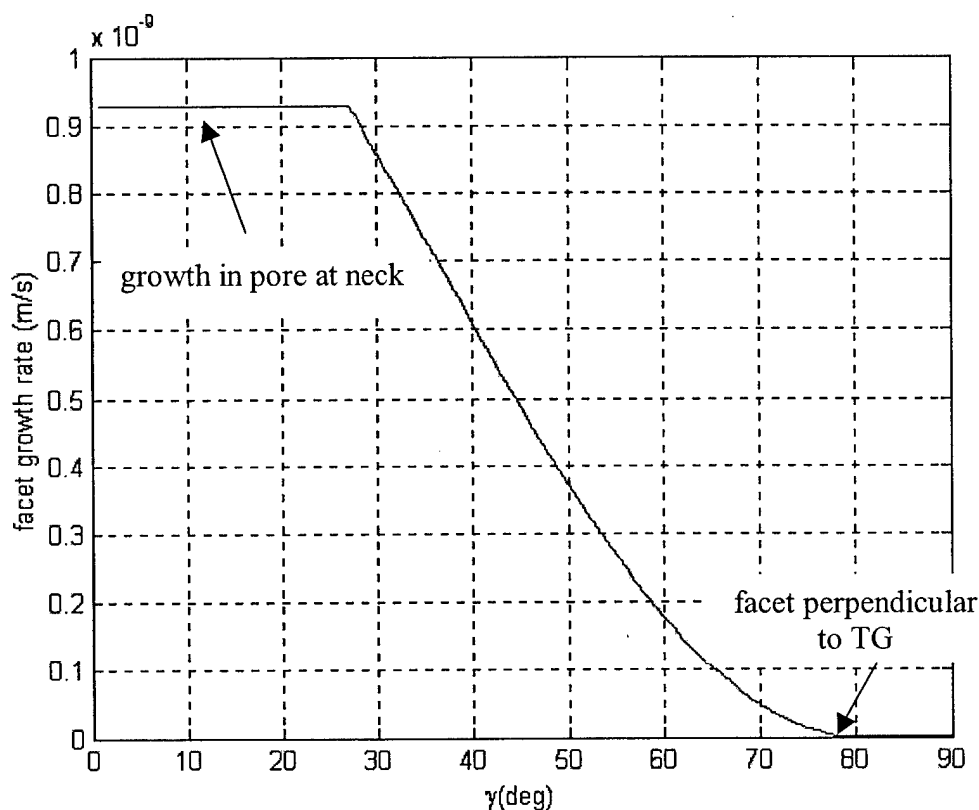
Figure 32. Facet growth rate vs crystal orientation, γ. A axis dominant with β=9.5°, TG=25°C/m, base grain r_g=0.5mm, r_b/r_g=0.6, facet length=0.625mm, ρ=150kg/m^3

Facet Time Integration for Various Crystal Orientations. The faceted crystal growth problem may be integrated in time using the geometric parameters and mass terms described in chapter 2. For this study, four values of the crystal orientation angle, γ, are used to evaluate the significance of crystal orientation on growth. Figure 33 shows the crystal size during 350 hour time integration. As expected, crystals more aligned with the temperature gradient grow quickly. As the crystals grow, the preferentially oriented crystals are able to reach deeper into warmer vapor sooner than other crystals. Preferentially oriented crystals grow rapidly due to the larger excess vapor pressure created as the tip reaches warmer vapor.
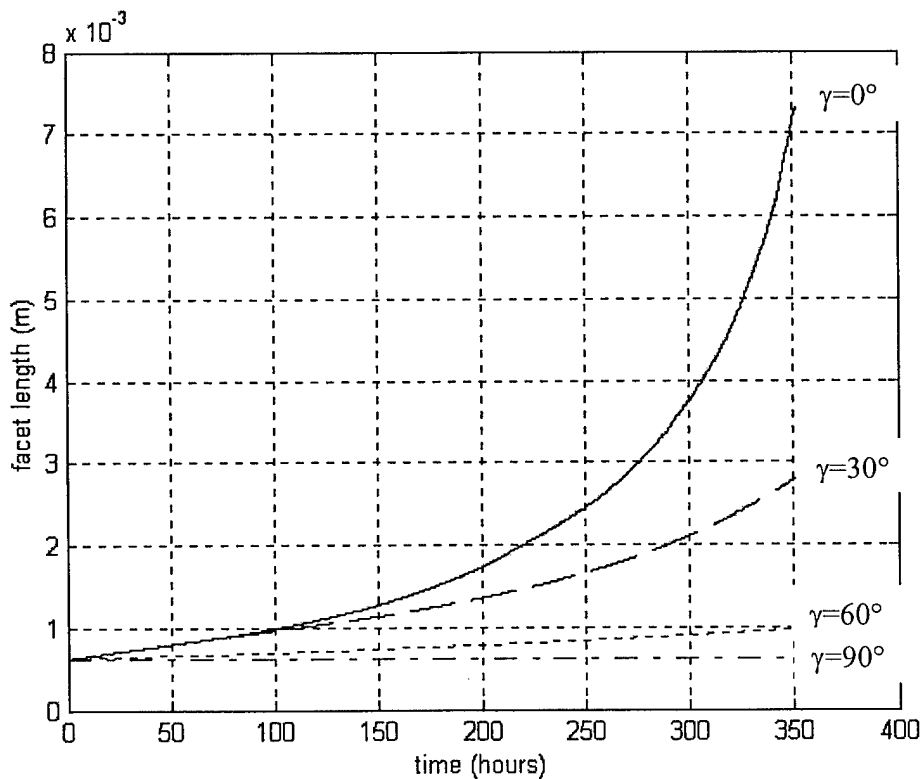
Figure 33. Facet size vs time for different crystal orientations. β=9.5°, TG=25°C/m, base grain r_g=0.5mm, r_b/r_g=0.6, initial facet length=0.625mm, ρ=150kg/m^3

Figure 34. Facet growth rate vs time for different crystal orientations. $\beta=9.5°$, TG=25°C/m, base grain $r_g=0.5$mm, $r_b/r_g=0.6$, initial facet length=0.625mm, $\rho=150$kg/m³

In addition to the facet size, the facet growth rate was examined during the same 350 hour time period with the results in figure 34. The increasing growth rate for a preferentially oriented crystal is evident. The crystal growth rate in pore spaces associated with grains increases in time while the growth rate in pore spaces near necks is constant. This is from the interpolation scheme discussed previously. By examining the crystals with $\gamma=0°$, the increase in growth velocity is evident not only in the slope, but by the contraction of transition time between neck and grain pores. It is evident that crystal orientation is an important factor, critical to determining which crystal may survive at the

expense of other grains. To further align the crystal with the temperature gradient, negative values of the crystal orientation angle, γ, are examined next.

Up to this point, the crystal habit angle, β, has been fixed and only positive values of γ have been evaluated. Since β is always positive and less than 45°, negative values of γ may better align the crystal with the temperature gradient (figure 30). The total angle from the crystal to the temperature gradient, α, is given by

$$\alpha = \beta + \gamma .$$ (109)

α combines the effects of crystal orientation and crystal habit by locating the crystal relative to the temperature gradient. Figure 35 demonstrates that the location of the crystal relative to the temperature gradient is a primary factor in determining which crystals will dominate and survive. For the problem in figure 35, the crystal habit was determined using equations (51)-(54) for each faceted grain. The values of β varied from 42.3°-44.7° depending on the crystal temperature which is a function of crystal location in the model. Various crystal orientations were then analyzed. As previously speculated, the smaller the absolute angle from the crystal to the temperature gradient, the faster the growth rate. While only a few select orientations were evaluated, any grain orientation distribution could be implemented. If further research found grain orientations that were not random, the model could be easily modified to analyze any distribution.
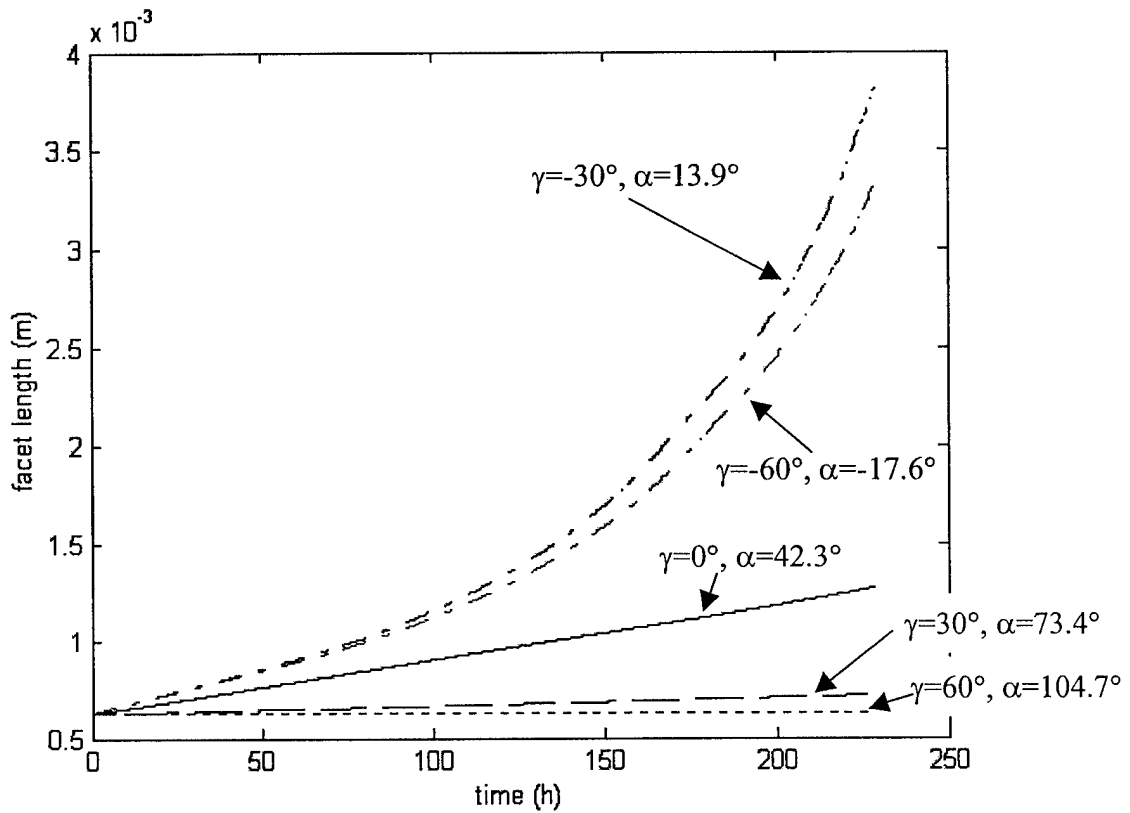
Figure 35. Facet size vs time. TG=25°C/m, base grain r_g=0.5mm, r_b/r_g=0.6, initial facet length=0.625mm, ρ=150kg/m^3

Numerical Issues. While the case studies presented in figures 31 – 35 provide excellent trend data, numerical problems were encountered. As certain crystals get large, the heat and mass source terms for those crystals also get large. When the big crystals reach deeper into the warmer pore and their growth rate is enhanced, a numerical imbalance develops between heat and mass source terms of other crystals. This imbalance can create convergence problems in the numerical solution. When evaluating metamorphism in an equi-temperature environment, this problem does not exist since there are not large disparities in the values of heat and mass flux between various elements.

The grains were generally able to grow eight to ten times their original size before convergence problems were encountered. Crystals were numerically grown up to 0.5 – 0.9 cm in length depending upon temperature gradient and crystal orientation. For smaller temperature gradients, larger crystals were obtainable since the growth rate was lower. As the growth rates on certain grains become large, establishing a smaller time step did temporarily postpone numerical problems, but even they would eventually fail.

This is not a significant limitation in the model's ability to predict kinetic growth metamorphism. Akitaya (1974a) and Marbouty (1980) both experimentally found the size of the pore space to be a major limiting factor in determining the final size of faceted crystals. In dense snow with small pore spaces under large temperature gradients, they found crystal growth was space limited (even though faceted grains did appear). The current model is able to predict growth through many pore elements, increasing the likelihood of interference with other grains. In addition, research has seldom (if ever), reported excessively large grains grown in actual snow. Strum and Benson (1997) observed subarctic snow for an entire season where the snow rarely experienced temperature gradients less than 10°C/m, with an average growth rate that was much larger. After more than 120 days, they found average grain sizes less than 5mm in diameter (using surface section techniques). Fukuzawa and Akitaya (1993) examined snow subject to very large temperature gradients (100 – 300°C/m) for tens of hours and found average grain sizes less than 4mm. Marbouty's (1980) experiments on depth hoar showed similar trends with a maximum grain size of 8mm for snow subjected to 66°C/m for nearly a month. Given these conditions, it appears the size limitations in the current model are reasonable and not considered severe. There may be actual extreme conditions

where the model will not be able to grow sufficiently large crystals. In this case, some crude approximations will allow growth to continue.

If the crystal size limitations are deemed unacceptable, the troublesome heat and mass source terms may be reduced or eliminated, allowing the model to execute with no numerical instability. When mass source terms are eliminated, the mass leaving the pore and condensing on the ice is neglected in the mass balance. In a similar way, when heat source terms are neglected, the dissipation of latent heat associated with phase change is eliminated from the heat balance. This technique is viable but not advised since it neglects much of the fundamental physics deemed important. It is envisioned that the current theory is sufficient for most natural snow conditions.

While not really a numerical problem, another issue arises when some crystals become large. Grains exist on each end of the geometric boundary. If grains near the boundary are allowed to grow kinetically, they can rapidly outgrow the physical boundaries of the model, creating a catastrophic error. This problem is avoided simply by making a sufficiently large model (hundreds of grains), and not allowing grains near the boundary to grow kinetically. Provisions for this are simple and included in the code.

Summary of Kinetic Growth Metamorphism

The kinetic growth theory developed in chapter 2 was expanded to include crystallographic orientation relative to the temperature gradient. Further numerical approximations were discussed to accommodate crystals as they grew through several pore elements. Crystal orientation coupled with the crystal habit resulted in grains that

may grow in a preferential orientation, analogous to lake ice. This led to a dominant grain growth theory that may explain the perceived reduction in the number of crystals while exposed to a kinetic growth environment. The dependence of growth on temperature/crystal habit (unavoidably linked) and crystallographic orientation were demonstrated. Time integration studies were also presented, further supporting a decrease in growth rate as crystals misalign with the temperature gradient. Finally, some numerical problems and limitations were discussed.

Comparisons and Validation

The numerical studies presented so far have focused on trends and parametric sensitivities, but with the exception of the onset of kinetic growth, no comparison has been made with measured data to validate metamorphic values. Important trends have been examined with excellent correlation. While, in theory, comparisons with experimental data should be straightforward, there are several issues complicating direct comparisons of model and experimental parameters. In chapter 2, grain, neck, and bond geometries were defined for use in this model to describe snow metamorphism. The geometry used here is common, but not universally accepted. As a result, it is sometimes unclear what measured "size" represents in a particular study. This, coupled with the fact that most metamorphic experiments have been phenomenological in nature and not focused on detailed microstructural properties, make finding suitable comparisons in the literature challenging. Grain size is the main parameter measured experimentally, but as previously discussed, maturity of bonding is emerging as an important snow

metamorphism parameter. After reviewing many studies, two were selected for their rigor of observation and experimental discipline. One of the studies examined sintering of rounded grains in an equi-temperature environment while the other reports on kinetic growth subjected to large temperature gradients.

Equi-temperature Environment Comparison

Hobbs and Mason (1964) studied ice sintering by measuring neck growth rates on ice spheres 50 – 700 μm in diameter in temperatures -3 - -20°C. They generated uniformly sized spheres and brought them into contact in a temperature controlled, vapor saturated environment. The dimensions of intergranular necks were observed and measured optically during growth. They assumed neck geometry very similar to that presented in chapter 2 and used in the current model. The focus of Hobbs and Mason's (1964) study was not to simply collect sintering growth rate data under controlled conditions, but to show that vapor diffusion was the predominant sintering mechanism in an equi-temperature environment. Earlier experiments and theoretical work had been incomplete and misinterpreted, leading to the incorrect conclusion that either volume or surface diffusion control ice sintering (Kuroiwa, 1961; Kingery, 1960). Hobbs and Mason (1964) very meticulously shattered this belief and proposed vapor diffusion as the dominant mechanism. This hypothesis is still widely accepted today. The current model was used to simulate their experiment and compare the results with their measured sintering data. The measured data points were carefully extracted from logarithmic graphs within their paper, and although no systematic bias is anticipated, extracting data

from the log graphs was difficult and some errors are inevitable. The experiment was simulated at two different temperatures for a total of six grain sizes.

The data and analysis comparison of bond growth vs time is presented in figure 36. Due to the nonlinear nature of ice sintering, Hobbs and Mason presented their data on logarithmic plots. While conducting their experiment, Hobbs and Mason did not make their first measurements until several minutes after the ice spheres were brought together, giving different initial times for each experiment. In fact, they state "spheres were usually in contact for some unknown time before the first measurement was made." Therefore, the first measurements from their experiment were used as the initial conditions for the model analysis.

The analysis compares very well for the T=-3°C experiment and reasonably well for the T=-10°C experiment. In both cases, experimental trend data is captured by the model. Hobbs and Mason developed a vapor diffusion theory to simulate the experimental results. Their solution is of the form

$$\left(\frac{r_b}{r_g}\right)^n = \frac{B(T)}{r_g^3}t \qquad (110)$$

where t is time, n is an integer, and B(T) is a temperature dependent function. Hobbs and Mason determined n analytically and experimentally. Equation (110) implies a linear relationship (with a slope of 1/n) on a logarithmic scale, but clearly the data shown in figure 36 is not truely linear. Hobbs and Mason determined experimental slopes and values of n ranging from 4.2 – 6.2, where the analytic value is 5. They also recognized
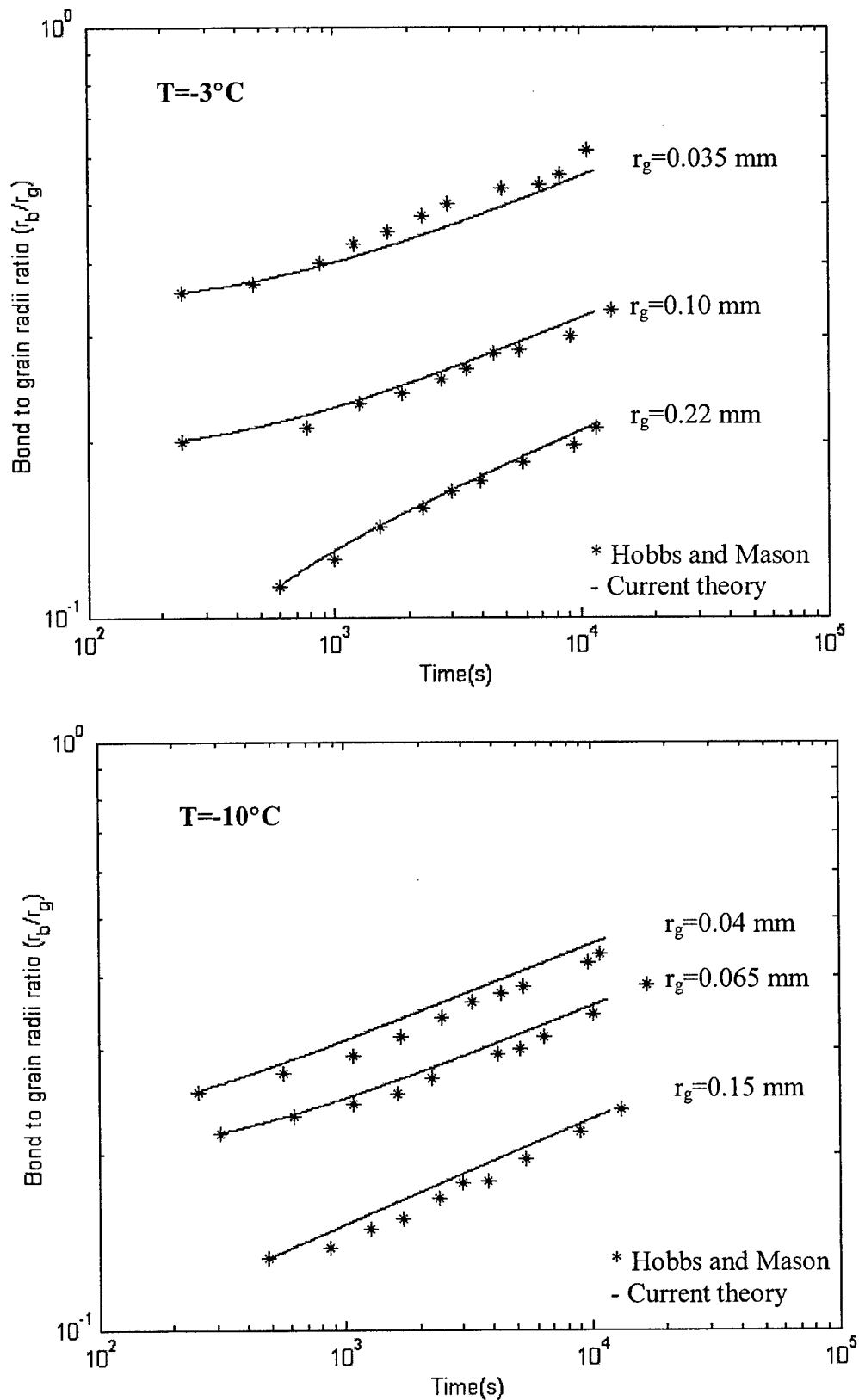
Figure 36. Comparison of Hobbs and Mason (1964) tests with current theory.

the linearity discrepancy between their theory and data, but attributed it to uncertainty in their initial conditions. The current model predicts some of this observed nonlinearly. The analytical curves in figure 36 are not strictly linear, but may have been so if proper initial conditions were known. Hobbs and Mason evaluated a transfer coefficient for vapor sintering and found observed and computed values agreed to a factor of five. They found this difference acceptable given their approximations and experimental error. While a transfer coefficient was not examined here directly, the model results in figure 36 suggest better correlation than the previous theory. Hobbs and Mason do recognize the presence of experimental error, but they do not comment on the size of the error.

The -10°C analysis does not compare as favorably with experimental data as the -3°C analysis. One potential explanation is proposed. The current theory assumes a constant diffusion coefficient, D, of water vapor through air, but in reality, diffusivity decreases with decreasing temperature. In fact, the water vapor diffusion coefficient at -10°C is 6.5% smaller than the value for 0°C. Since a temperature dependent coefficient is not used in the model, slight over prediction of sintering at lower temperatures is possible. Implementation of a temperature dependent diffusion coefficient in the model would be simple, and is envisioned for future versions. Even in colder experiments, the model does an excellent job predicting the highly nonlinear growth of the bonds between the grains. Overall, the current theory does an excellent job predicting the sintering in Hobbs and Mason's (1964) experiments.

Kinetic Growth Comparison

Fukuzawa and Akitaya (1993) developed kinetic crystals in the laboratory by exposing snow to very high temperature gradients. Their experiment simulated the growth of faceted crystals near the surface of low density snow on clear cold nights. To further understand the relationship between temperature gradient and crystal growth, they exposed snow to gradients ranging from 100- 300 °C/m for up to 50 hours. Previous studies (Marbouty, 1980) had examined kinetic growth features, but at much smaller temperature gradients. This study was singled out for comparison because the authors were very meticulous in their experimental setup, conduct, and data collection. In addition, the large temperature gradients create rapid growth rates which are deemed challenging for the current model.

As previously mentioned, there are no standardized methods to quantitatively describe the geometry of kinetic growth crystals. With rounded crystals, grain radii are generally used as the primary measure of size, but complex kinetic growth crystals do not lend themselves to such obvious parameters. In chapter 2, the crystal's length, measured from the grain root to its tip, was proposed as a size measure. Some experimenters use sieves to determine size, while others analyze images using various geometric parameters. As a result, attempting to compare grain sizes between several studies is difficult. Fukuzawa and Akitaya (1993) took photographs of their samples and used an image analyzer to determine grain size. They designated grain size as the diameter of a circle with the same projected surface area as the grain itself. This measure is similar to, but not identical to the length definition in chapter 2. For simple structures such as a hexagonal plate, the two size measures should be alike, but as grains get highly ornate or

cupped, the measurement methods diverge. In addition to grain size, Fukuzawa and Akitaya calculated one standard deviation for grain size distributions. This measurement is rarely reported, yet is highly informative. As the grains grew in their experiments, the size variation increased. The increased size variations may be predicted when variable crystal orientations are considered. As already shown, variations in crystal orientation create larger size distributions as preferentially oriented grains outpace their neighbors.

Even though each project utilized a different crystal size definition, the current model was used to simulate Fukuzawa and Akitaya's experiments. For all experiments, they reported an initial grain size of 0.12mm which was used to generate a model "base" of round grains. Facets with various crystal orientations were then allowed to grow from the base grains. For the test temperature of -16°C, the crystal habit was a-axis dominant with β=19.5-20.5° (depending upon location in the temperature gradient). In order to "jump start" the growth of kinetic crystals, the facets were given an initial length of $1.25r_g$ - $1.5r_g$. The current model places the facet root at the center node of the parent grain (figure 30), but nucleation may take place elsewhere on the grain or necks. As a result, some nucleation sites may be preferentially located for superior growth, analogous to preferential crystal orientation. Since several nucleation sites on the same grain are not currently considered, the initial facet size was selected to allow some crystal edges to initially extend just beyond the base grain, as would be the case for nucleation on a warmer part of the grain or neck. Size increases on the order of 25% – 50% worked well, but the selection was primarily subjective, based on comparisons with the test data.

Figures 37 and 38 present the model and experimental data comparisons. Fukuzawa and Akitaya's observed average size and one standard deviation (represented

by the vertical bars) are presented in each of the graphs. Temperature gradients of 200 and 250 °C/m for an initial crystal size of $1.25r_g$ are in figure 37, and temperature gradients of 150 and 159 °C/m for an initial crystal size of $1.5r_g$ are in figure 38. In all cases, the model initial grain size falls within the standard deviation of the measured grains.

In figure 37 for the 200°C/m experiment, the model accurately predicts the observed grain size and distribution. The increase in grain size differences result from varying crystal orientations, providing some physical explanation for size variation increases. As the temperature gradient increases to 250°C/m, the model does not track the experiment as accurately. In the initial stages (first 24 hours), the model predicts the experimental results reasonably well, but starts to diverge from the experiment as the grain size increases. In all four experiments analyzed, the one standard deviation maximum size never exceeded 0.55mm, even under very large temperature gradients. It seems logical to expect some interference between grains growing and contacting neighboring grains, especially when they become large. The current model does not account for growth limitations created by finite pores, potentially accounting for the overestimation of growth. Figure 38 presents the results of two more experiments. The model's correlation with experimental data is good, but appears to be under predicting growth as grains get larger.
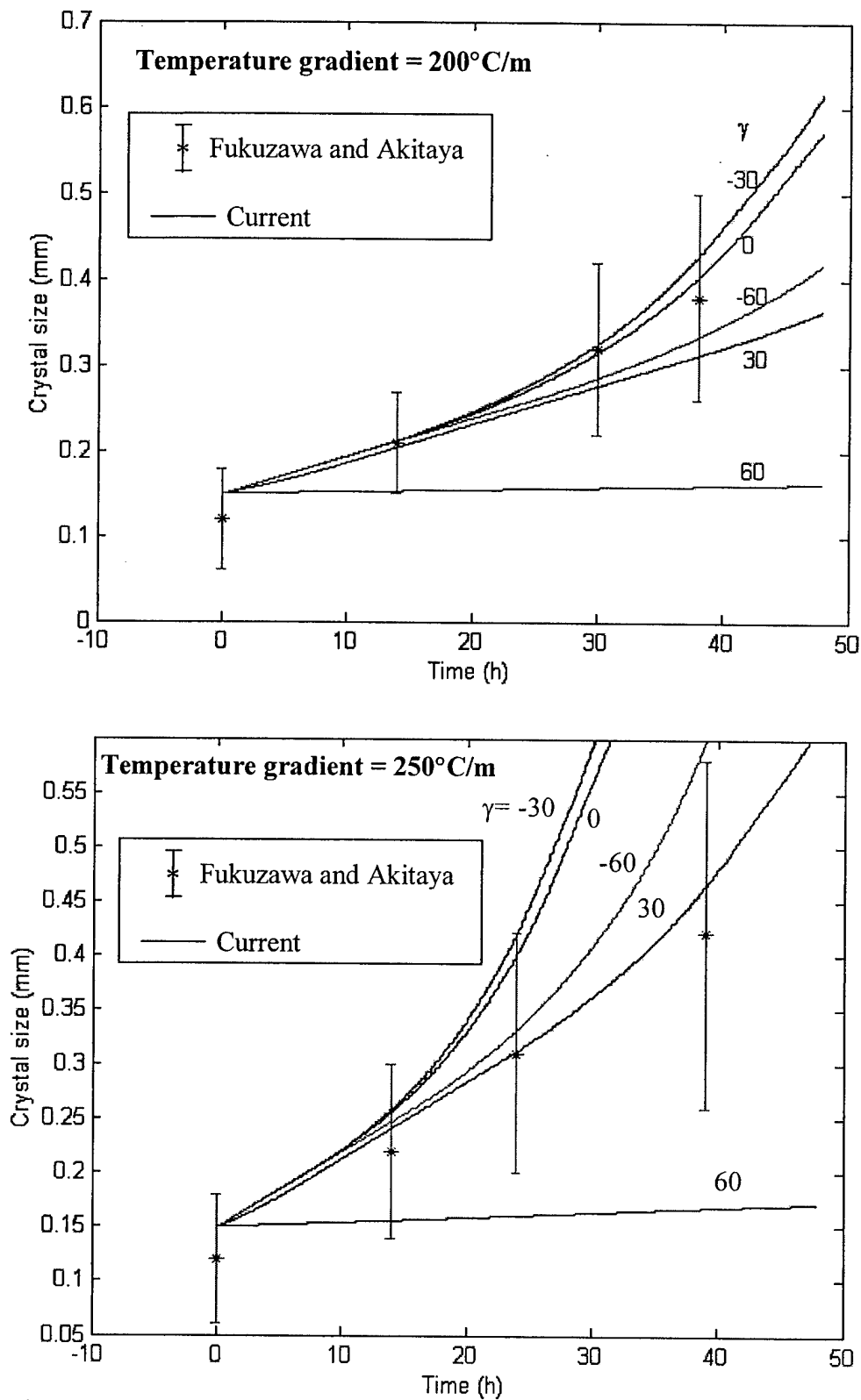
Figure 37. Kinetic growth validation, TG= 200, 250°C/m, initial size1.25r_g.
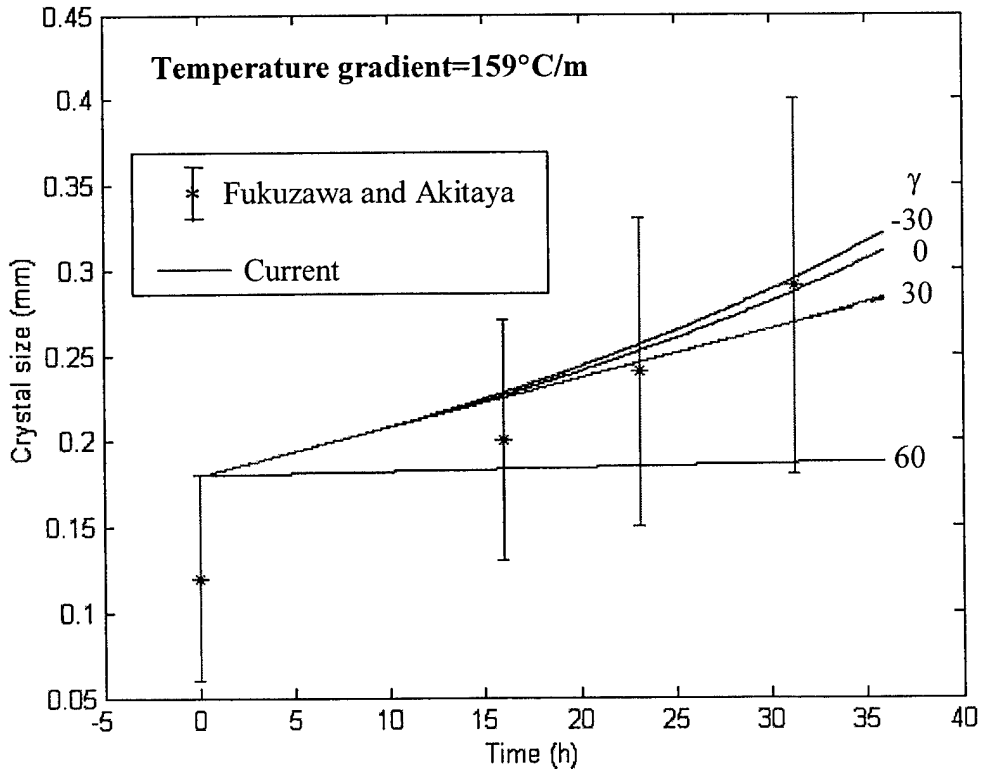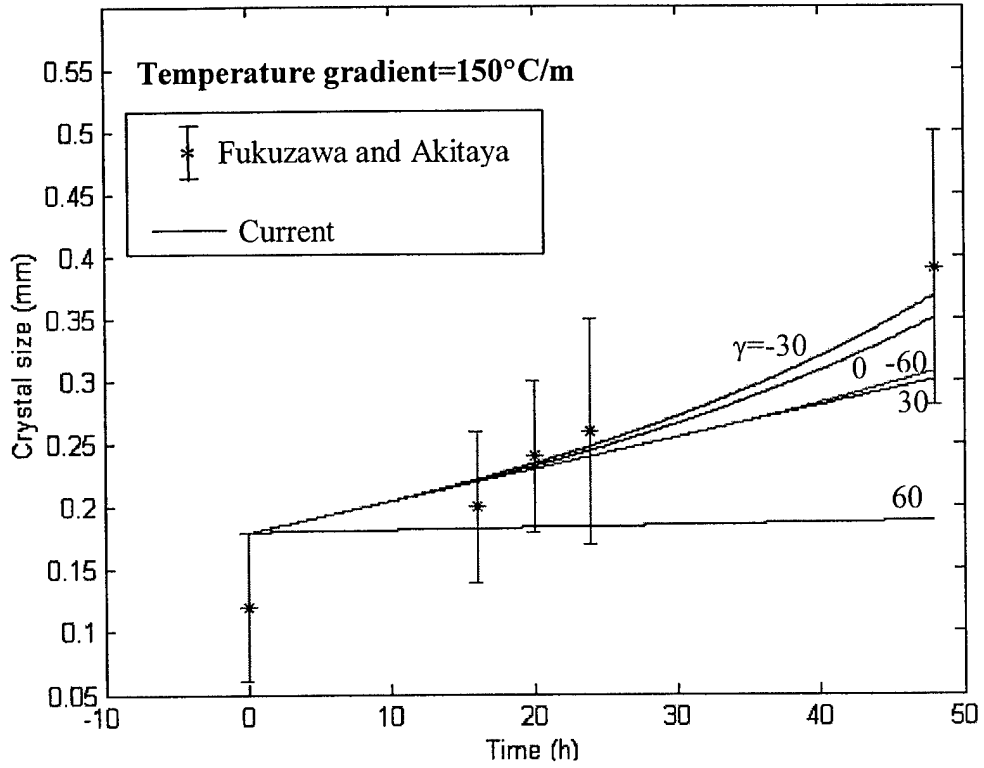
Figure 38. Kinetic growth validation, TG= 150, 159°C/m, initial size1.5r$_g$.

133

Summary of Numerical Studies

Numerous numerical studies were presented in this chapter to demonstrate the versatility and accuracy of the theory and model proposed in chapter 2. The numerical model has proven useful in studying various parameters and their influence on dry snow metamorphism subjected to a variety of thermal environments. Several microstructural and environmental applications were used to show the model's ability to predict many well known trends.

In an equi-temperature environment, metamorphism of equally sized grains was examined as a function grain size, temperature, density, and bond size. Microstructural temperature gradients developed, resulting in heat and mass flow driving mass from the grains to the necks through the vapor. Rapid sintering resulted from small grains, smaller bonds, and higher temperatures. Density did not have a large influence on metamorphism in an equi-temperature environment. Mass was generally conserved between individual grains and necks, reinforcing the insignificance of density due to local vapor movement. Comparisons with experimental sintering data showed excellent correlation in trends as well as measured growth rates. Analysis of unequally sized grains showed large grains growing at the expense of very small grains, but the rate and required size differences varied with bond size.

A definition for the onset of kinetic growth was proposed. The influences of grain size, density, bond size, and temperature were examined. Unlike equi-temperature studies, density emerged as a major parameter determining when kinetic growth may

begin. As expected from the onset definition, smaller grains delayed the onset of kinetic growth. The onset of kinetic growth did support widely accepted limits, but also provided further insight into how and why the transition happens.

Prior to kinetic growth studies, a crystal orientation scenario was introduced and added to the numerical model. Kinetic growth was analyzed as a function of temperature and crystal orientation. The resulting grain size distributions increased as the growth process was allowed to progress. Some grains were preferentially oriented for superior growth while others grew at lower rates. The model did a reasonable job at predicting several laboratory experiments from the literature where snow was subjected to very large temperature gradients.

Overall, the model predicts many previously experimentally observed snow metamorphism trends. It is also capable of studying many parameters and their influence in metamorphism simultaneously. The possible combinations of microstructural and environmental scenarios that may be investigated are endless.

CHAPTER 4

EXPERIMENTS AND METHODS

Introduction

In this chapter, several experiments and corresponding techniques are presented. Since the current research has focused on microstructure in a snow metamorphism model, the experiments will also emphasize microstructure. Before any experiments are presented, snow microstructural preservation and observation techniques are discussed. Optical, scanning electron microscope (SEM), and computed tomography (CT) imaging of snow microstructure are presented so that the reader can understand their applications when utilized in the actual experiments.

Several experiments are then proposed and their results presented. These experiments provide insight into certain aspects of snow metamorphism that have not been previously published. The experiments are designed to support assumptions used in the model development, observe and confirm the existence of microstructural features elucidated by the model, and to provide some realistic applications of snow metamorphism.

Preserving Snow Microstructure

When snow is collected from a field or laboratory environment, it is desirable to halt all metamorphic processes in order that the existing microstructure may be examined in detail at a later date. The most common technique for stopping metamorphism involves placing a substance in the pore spaces thereby removing the water vapor that contributes to metamorphism. This method does not stop all metamorphic processes since lattice, grain boundary, and surface diffusion may still be active. As discussed in chapters 1 and 2, vapor diffusion is considered dominant, while all others transport mechanisms are assumed insignificant. As such, pore filling is the common method for long term preservation of microstructure.

Two materials are commonly used to fill pore spaces. Perla (1982) used dimethal phthalate to stop sintering and preserve snow. Dimethal phthalate is a relatively benign material with a freezing point of -10°C. The material may be kept below 0°C yet above its freezing temperature and poured into snow samples to fill the spaces. If the sample is cooled below -10°C, the dimethal phthalate freezes making the entire sample solid. The microstructure may then be examined at a later date by surface sectioning or nondestructive techniques. While dimethal phthalate has been used extensively, there are several issues that make its use challenging and frustrating. Maintaining dimethal phthalate in liquid state at sub-zero temperatures is difficult. Also, dimethal phthalate is relatively viscous at low temperatures, resulting in incomplete pore filling on many types of snow samples (high density samples in particular). Some nondestructive inspection techniques, such as CT imaging, measure density differences to get accurate images of each material. The solid phases of dimethal phthalate and water have very similar

densities, creating difficulty in obtaining high contrast CT images. After considering this information, an alternative to dimethal phthalate was investigated.

Brun and Pahaut (1991) used isooctane (2,2,4 – trimethyl pentane) to preserve detailed snow microstructure for several months. Isooctane is a common gasoline additive that is readily available and reasonably priced (~ \$35/gal). It has a very low viscosity at the low temperatures (0 - -20°C) for suitable pore filling. Since isooctane has a freezing point of -108°C, the ice microstructure is surrounded by liquid isooctane for the vast majority of snow storage conditions. The difference in ice and isooctane densities is enough to allow CT imaging of snow samples with isooctane filled pores. Brun and Pahaut (1991) placed disaggregated snow grains from the field in subfreezing isooctane, transported them to the laboratory, and stored them for several months. Their study showed excellent retention of detailed microstructure, even of very high energy surface features. They suggest the use of isooctane in any situation where microstructure investigation must take place at a different location or time.

A simple laboratory demonstration was conducted to verify the microstructure preservation capabilities of isooctane. A sample of well developed faceted snow was carefully disaggregated with some grains placed in isooctane while other grains were left in an enclosed air environment. The grains were examined optically under a microscope at the end of three months of storage. The grains stored in the air showed significant rounding and degradation of sharp high energy features while the grains held in isooctane appeared sharp and ornate. In fact, no change in the grains placed in isooctane was discernable. Since this simple demonstration essentially verifies Brun and Pahaut's experiments, the resulting images are not presented here. While Brun and Pahaut did not

use isooctane to preserve in situ samples, the simple extension to use isooctane as a pore filler is assumed reasonable. Several snow samples were placed in a 30 ml plastic Nalgene container and saturated with isooctane. A syringe was used to inject the chemical from the bottom to allow the air and water vapor to escape. For low density samples having large pore spaces, the isooctane completely filled the pores. In higher density snow (>400 kg/m^3), some small voids were periodically visible, but tended to fill when left overnight. Isooctane was used to stop metamorphism and preserve all snow samples in this study. With snow samples indefinitely preserved, the methods used to examine the detailed microstructure of snow are presented next.

Visible Optical Techniques Used for Observing Snow Microstructure

Visible observation is the most commonly used technique for examining snow microstructure. Due to the small size of most snow grains, optical magnification is usually required. In the field, hand held loupes with magnifications of 10 – 25x are common. In the laboratory, microscopes with camera penetrations allow researchers to vary magnification and record results. While visual observation is the most common, easy, and simple technique, significant difficulties can hinder its scientific use for some applications. In situ examination of snow under a microscope is very difficult. Disaggregation is usually required, although small areas may be examined with little disturbance. The visible transparency of ice makes simultaneous imaging of several neighboring features difficult. As magnification increases, the optical depth of field decreases. The three-dimensional nature of snow prohibits all features from existing in

the same focal plane. As a result, it can be difficult to get all the interesting features in focus for a single image. The shallow depth of field places practical limits of magnification to less than 100x (author's opinion). On the positive side, optical microscopic imaging of snow exposes the very dominant features of the microstructure in a way humans are used to seeing them. Grain structure and crystal habit are readily apparent under the microscope.

A Wild M5A trinocular microscope was used for all the visible optical microstructural images presented in this dissertation. This microscope has variable magnification of 15 – 75x with binocular viewing and camera port. The system has transmitted incandescent and reflected fiber optic lighting systems. The fiber optic light ensured minimum heat transmission to the samples during illumination. Figure 39 shows four examples of different snow morphologies and lighting conditions captured using this system. The grain characteristics are obvious, emphasizing the utility of this technique. The shallow depth of field is especially apparent in (d) of figure 39. All images were taken with 35mm transparency film (Fuji Velvia, ISO 64) and then digitized.
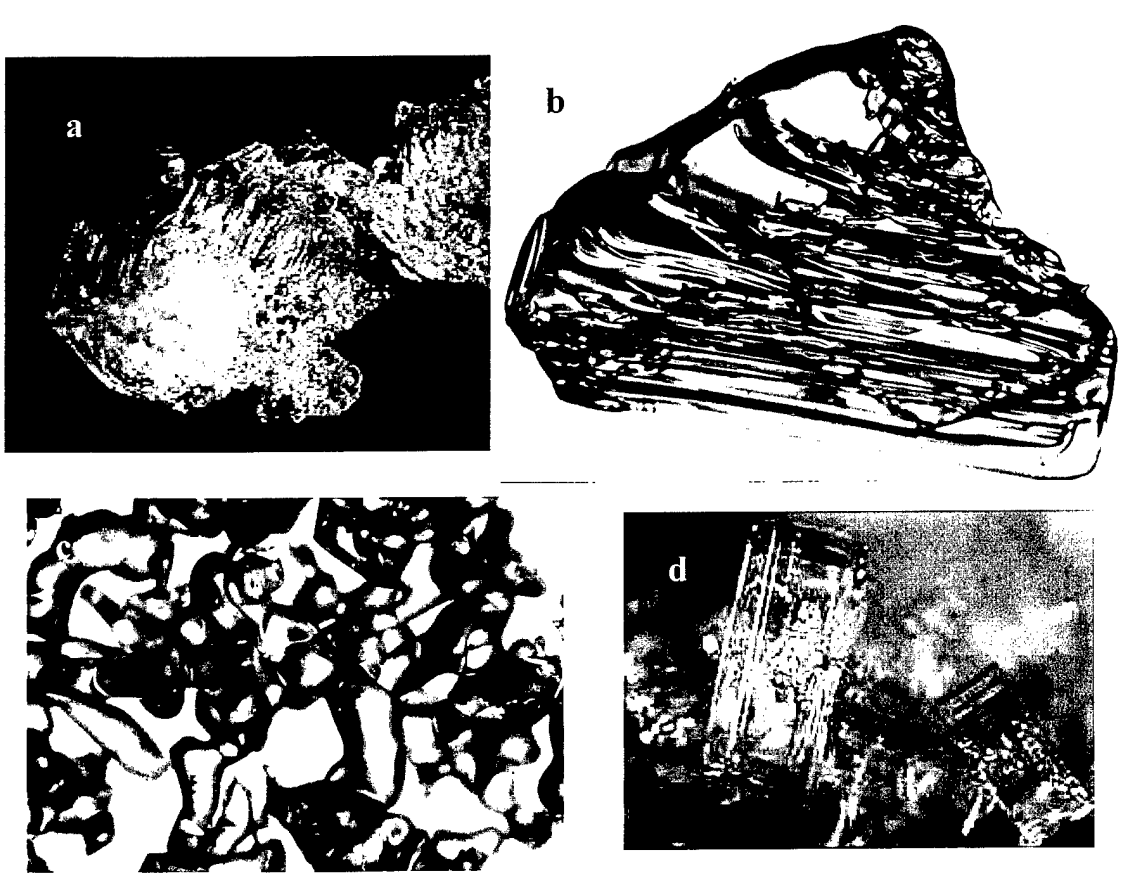
Figure 39. Examples of optical microscope imaging. (a) Depth hoar, top reflected light. (b) Depth hoar, transmitted light. (c) Equilibrium form, transmitted light. (d) Columns, side reflected light.

Low Temperature Scanning Electron Microscope Imaging of Snow Microstructure

In order to achieve high magnification, increased depth of field, and to view detailed surface features (masked in optical images due to ice transparency), snow was examined in a low temperature scanning electron microscope (SEM). A JOEL 6100

SEM with cryogenic chamber (-170°C capability) was used to examine surface details. Wergin et al (1996) developed techniques for collection and storage of remotely collected samples that were imaged on a low temperature SEM. Wergin et al (1996) mounted samples to SEM palettes with Tissue-Tek® then plunged collected samples into lN_2 for transport and storage. Their procedures were initially adopted, but later modified. While detailed procedures are not described here, some important issues are discussed. The boiling of the lN_2 greatly agitated samples, creating damage and frequent sample loss prior to imaging. An alternative technique was developed where the samples were kept cold, yet not immersed in lN_2. Short sublimation was normally required to remove any surface condensation that occurred during handling and preparation. Sublimation occurred between -80 and -110°C until the accumulated surface condensation disappeared. Samples were imaged with either a thin (<9 Å) coating of Au or with no coating at all. Due to the porous nature of snow, poor electrical connections made imaging difficult, even when gold coated. Frequent sample charging was generally avoided by using lower accelerating voltages and magnifications.

Figure 40 shows four examples of typical snow SEM images. The high magnification capabilities are evident in the grain boundary ridge image (b). Magnifications in excess of 30000x were demonstrated. While not discussed in detail here, the discovery of grain boundary ridges was a direct result of the SEM imaging capabilities. Grain boundary ridges provided physical evidence of grain boundary diffusion between crystals (Adams et al., 2001). Figure 40 (c) and (d) demonstrate the capability of the SEM to capture detailed and complex surface features. In optical

142

microscopy, many of these details are masked by ice transparency and shallow depth of field.

While providing some excellent results, the low temperature SEM imaging of snow was not a simple task and involved significant trial and error. Operating the SEM with cryogenic stage was very expensive ($60/hr), making frequent trials costly and frustrating. Even though sample in situ imaging is not possible, exposure of detailed surface features and/or high magnification capability make low temperature SEM a powerful surface imaging choice.
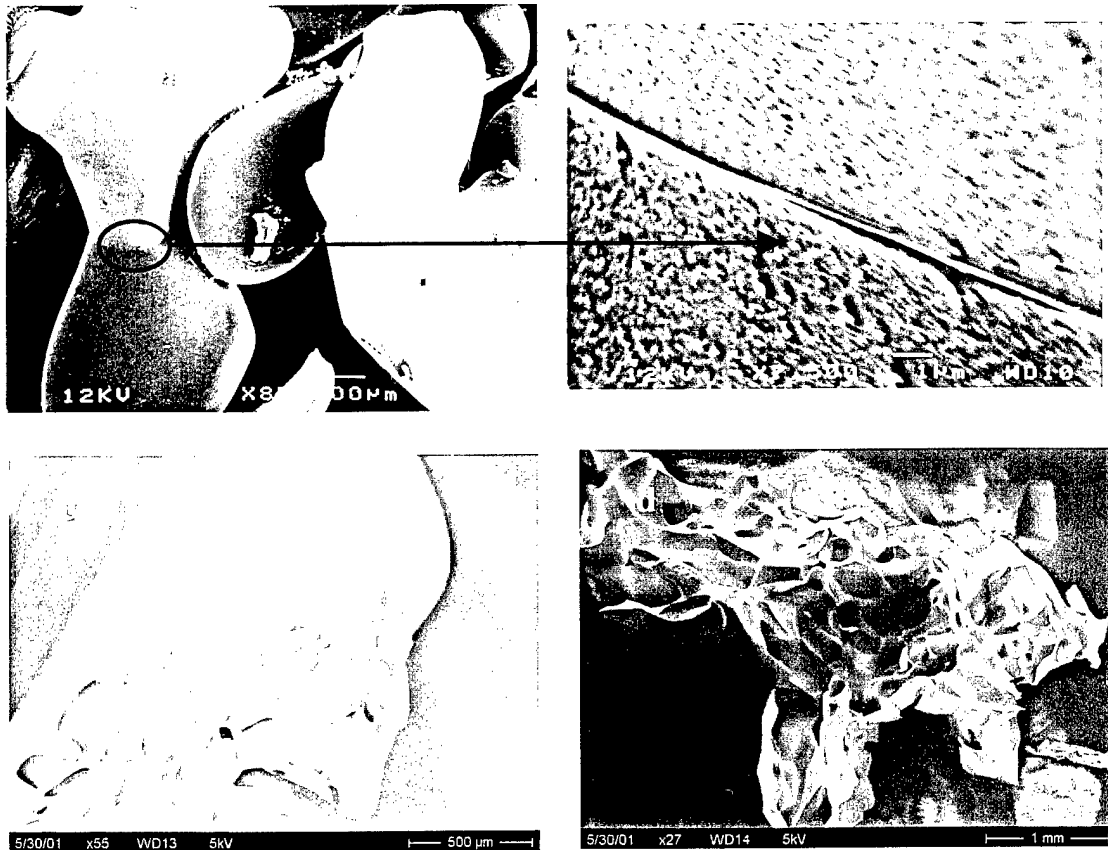
Figure 40. Examples of scanning electron microscope imaging. (a) Equilibrium form snow, low magnification. (b) Increased magnification of area indicated in (a) showing grain boundary ridge. (c) Transition between faceted grain and bond. (d) Bond between faceted grains.

X-ray Computed Tomography Imaging of Snow Microstructure

In computed tomography (CT) imaging, the internal structure of snow may be nondestructively examined. Samples may be prepared such that little or no disturbance of internal structure occurs, approximating the in situ configuration. Important geometric properties of snow microstructure may be examined. Due to the nondestructive nature of CT imaging, snow metamorphism may be progressively studied by periodic scanning of the same snow sample (Lundy, 2000). This provides a very powerful tool in understanding time varying metamorphic parameters.

In CT imaging, a collimated x-ray beam is transmitted through a sample to a phosphor fluorescent screen. Due to differences in x-ray absorption of dissimilar materials, the screen fluoresces with variable intensity, which is recorded by a digital camera. After each image is recorded, the sample is rotated about a fixed vertical axis through a preset angular increment and imaged again. This is repeated until the sample has rotated through 360°. The total number of images is dictated by the angle between subsequent images. With smaller angles, higher quality images are produced, but longer scan times result. The series of images are then "reassembled" to produce a grayscale planar image of the x-ray's path through the sample. If multiple serial planar images are obtained, three-dimensional reconstructions are possible.

The Montana State University, Department of Civil Engineering CT scanner system was custom designed and built by Synergistic Detector Designs. The x-ray source was manufactured by Seifert X-Ray Corporation.

CT Scanner Set Up

Sample Container and Cold Chamber. To simplify scanning activities, all experiments requiring CT scanning used the same sample container. Thirty ml Nalgene polycarbonate wide-mouth sample jars housed all CT samples. Polypropylene containers were examined, but were rejected due to their inability to retain isooctane for long periods of time. To keep the samples cold during imaging, a special chamber was built to hold both the sample and dry ice. The chamber consisted of a 2 foot section of 3 in diameter PVC with sample and coolant areas built inside. Dry ice was packed above and below the sample leaving a large surrounding air space in the plane of the x-ray for clear imaging. Chamber temperature was monitored with a T-type thermocouple to ensure that subfreezing temperatures were maintained during imaging.

X-ray Source Position	505mm
Sample Position	86mm
Optical Lens Position	190mm
CCD Position	325mm
Resolution	40.588 μm/pixel
X-ray Voltage	160 kv
Exposure time	4.5s
Scan Angle Increments	0.5°

Table 3. X-ray CT scanner settings.

<u>CT Scanner Configuration</u>. The CT image resolution is determined by the relative positions of the sample, x-ray source, and camera. For the sample container described above, the parameters given in Table 3 yielded a resolution of 40.588 μm/pixel.

Image Processing

The x-ray CT process results in 16 bit (65,536 shades of gray) 1024 x 1024 pixel images where higher density materials appear lighter and lower density materials are darker. The grayscale images expose the internal detail and gradual transitions between materials. To study internal geometry, established stereological software was applied to the scans. Edens and Brown (1994) presented a very comprehensive approach to measuring and evaluating microstructural features from digitized surface section images. They developed a detailed stereological approach to quantify three-dimensional features from two-dimensional binary images. In order to extract the binary images required for the stereology software, the raw gray scale CT images were processed to precisely differentiate between ice and pore structures.

The raw CT images required smoothing to eliminate scan noise. This smoothing process was somewhat subjective, and great care was taken to ensure that noise, not data, was eliminated during the smoothing process. After evaluating several smoothing techniques, a gaussian blur method was selected. In a gaussian blur, a gaussian weighted value is applied in a user defined pixel region. A simple experiment was designed to determine the size of the smoothing region. A snow sample was scanned with no pore filler. On the resulting image, the transition from ice to pore was very obvious, but as usual, the image was somewhat noisy as evidenced by single pixel discontinuities

surrounded by relatively continuous values. The gaussian blur pixel radius was increased until the majority of the image noise (discontinuities) was eliminated. While this was a subjective determination, the large density difference of ice and air made the transition obvious. This image was used as a control to determine the proper pixel radius smoothing for samples filled with isooctane. Since isooctane and ice densities differ by only 25%, the smoothing cut off was not as crisp as it was for ice and air. The same snow sample was then filled with isooctane, and scanned again. The gaussian blur area was increased (to 2.5 pixels) until the image with isooctane and ice looked like the image with air and ice. A 2.5 pixel gaussian blur was then used on all CT images of snow filled with isooctane.

After the images were smoothed, grayscale images were converted to binary for use in the stereology software. A square image was extracted from the circular sample. This was done to eliminate the container from any binary cut off calculations and for input to image processing software. The density of each sample was measured prior to isooctane insertion. Since the actual density of each sample was known, the area fraction of snow and ice is also known. Using this information, the pixel value for binary cutoff was increased until the proper area fractions between ice and pore were established. This iterative calculation was programmed in a macro language provided with Scion Image, an image processing software package. The resulting binary image was then used in the stereology software to evaluate snow microstructure.

Figure 41 shows examples of a raw CT image (a), the square area selected for evaluation (b), a smoothed grayscale image (c), and binary image resulting from threshold iteration (d). In the raw and smoothed images ((a),(b), and (c)), the ice
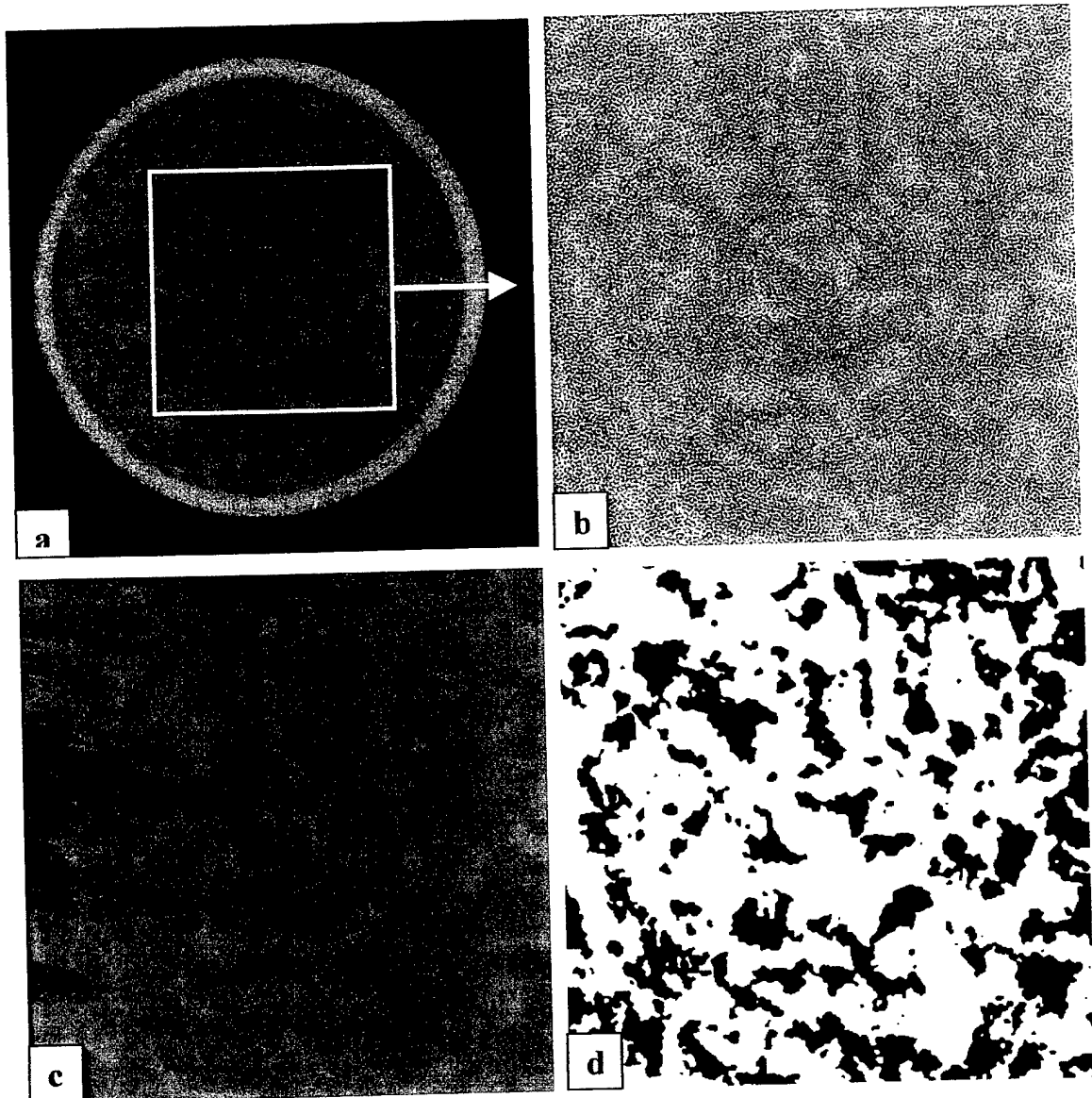
Figure 41. X-ray CT image processing. (a) Raw CT image. (b) Raw CT image with square area selected. (c) CT image smoothed with 2.5 pixel gaussian blur. (d) Binary image based on sample density.

148

network appears lighter in color while the ice is black in the binary image. In the raw image, the hole made by the syringe that injected the isooctane is evident in the upper left region. The smoothed image in figure 41(c) was then used to iterate the binary cut off threshold until the proper area ratio was obtained, resulting in the binary image in figure 41(d). A qualitative examination of the images shows that the primary features of the raw image are visible in the final binary image. While some data is clearly lost in the smoothing and binary thresholding operations, the error appears small as major features are retained throughout the process. The images in figure 41 are much clearer and crisper in digital form than in the printed form of this report. Printer resolution and shading limitations reduce the hard copy accuracy. The printed representation is really not important since image processing was conducted on the digital representations.

Orientation of Crystals Grown from the Vapor Phase on Existing Ice Substrates

Experiment Background and Objective

In chapter 3, a detailed model was developed for kinetic growth based on crystal orientation. It was postulated that certain crystal arrangements are preferentially oriented for superior growth. The hypothesis was based on the assumption that crystals grown from the vapor on existing ice would acquire the same crystallographic orientation as the parent grain. While this has been demonstrated for ice grown from the liquid phase, no direct evidence supports an analogous situation when crystals are grown on existing ice from the vapor. A laboratory study was designed to verify the supposition that heterogeneous nucleation and growth from the vapor phase will result in crystals with the

same crystallographic orientation as a large crystal ice substrate (Adams and Miller, 2002).

Methodology

Large ice crystals, with known crystallographic orientation, were used as "parent" grains on which new crystals would nucleate and grow from the vapor phase. By optical examination of the new crystals, it can be determined if crystals grown from the vapor phase retain the parent grain orientation.

An ice core sample taken from Lake Bonney, located in the McMurdo Dry Valleys, Antarctica, was used as substrate for the crystal growth experiment. Lake Bonney has about 4 m of ice cover composed, (at least in the lower regions) of S1 ice (Adams et al., 1996). As described in chapter 3, S1 is the secondary growth pattern with the c-axis vertically oriented ice, as is the case with lake ice grown under quiescent conditions. A universal stage for ice (Langway, 1958) was employed to determine the crystallographic orientation and to verify the S1 structure of a sample from 2.4 m below the lake ice surface. Utilizing the fact that the c-axis is the optic axis in ice, the instrument uses a four-axis universal stage onto which is placed a thin sample of ice. This is positioned and manipulated between cross-polarized plates, which provide a means to determine the spatial orientation of the optic axis. From the S1 ice, two thin (approximately 2 mm thick) plates were cut from the 8 cm diameter core. One of the ice coupons was cut so that the c-axis was contained in the thin plane of the sample while the other coupon had the c-axis perpendicular to the thin dimension. The ice samples were then mounted to a plexiglas plate. Once attached to the plexiglas, the samples were

slightly melted by simultaneously placing the exposed faces of both ice samples in contact with a "warm" aluminum plate. This provided a smooth surface as well as a uniform thickness for both ice coupons. The very thin liquid layer resulting from this melt adopted the crystal orientation of the substrate upon freezing, as was verified using cross polarization. The experiment was also executed when the ice surface was prepared using a razor blade.

A small, insulated box, shown in figure 42, was constructed in which the plexiglas plate was used as a top seal. Snow was placed in the box with a ~3 cm gap between the snow and the ice samples. The package was placed on a -1 C° plate in a -17 C° cold laboratory to establish a temperature gradient and thus a supersaturated environment at the ice coupon. One ice sample's c-axis was parallel to the temperature gradient (vertical) and the other ice sample's c-axis perpendicular to the temperature gradient (horizontal). The ice temperature, measured by placing a T-type thermocouple in contact with the ice, remained near -12 C° throughout the experiment. The resulting temperature gradient created a vapor flow from the snow to the ice coupon surfaces where new crystals nucleated and grew.

Crystal development under the conditions described was examined by daily removing the plexiglas plate with the attached ice coupons from the insulated box. Crystals were photographed using the Wild M5A trinocular optical microscope with photographic mount. The experiment was repeated several times with each test lasting between seven and ten days.

Ice Coupons

Plexiglass Top

3cm

12cm

C ⟶

C

T=-12°C

Vapor Flow

SNOW VAPOR SOURCE

T=-1°C
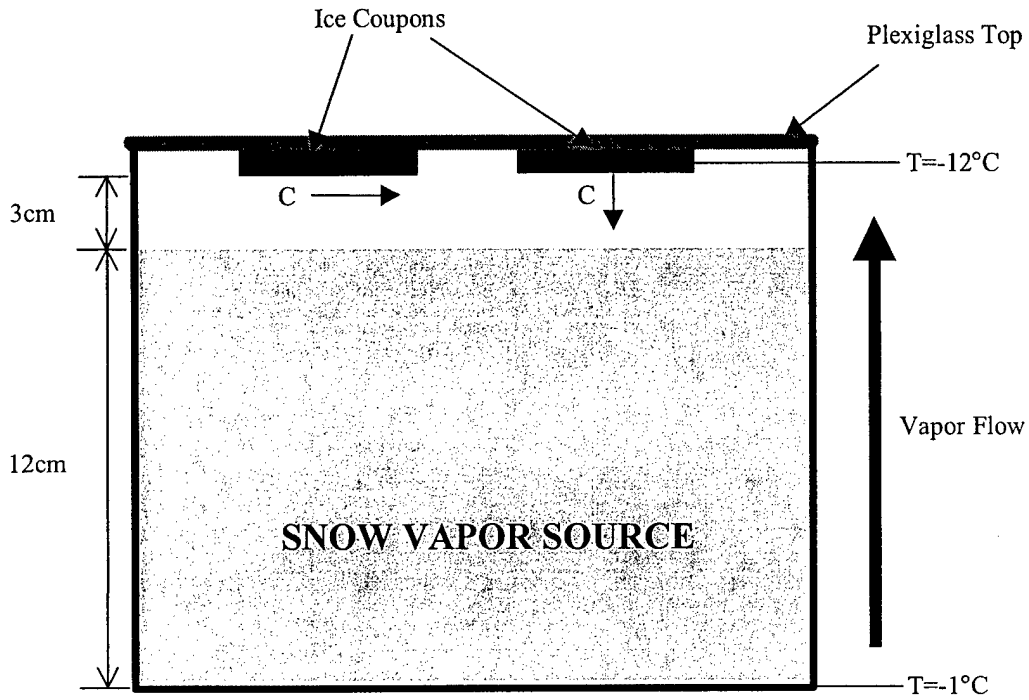
Figure 42. Experimental configuration for crystal growth on existing ice from the vapor phase.

Results and Discussion

Examination of the substrate coupons after a few days revealed multiple individual crystals on each of the flat surfaces of the large c-axis vertical and horizontal crystal surfaces. These crystals developed in the same orientation as the large substrate crystals in both crystal configurations (c-axis horizontal and vertical). The in situ crystals are shown in figure 43. In the c-axis horizontal sample (figure 43 (c),(d)), the crystal c-axes are also parallel, which is analogous to S3 ice grown from the liquid. S3 ice is

defined as the c-axis being parallel as well as horizontal. The hexagonal orientations of the c-axis vertical crystals (figure 43 (a),(b)) are also uniformly oriented with regard to the six prism faces. Hollow hopper type crystals were well developed on both the basal and prism faces (figure 43 (b),(d)). It should be noted that scratches, corners and imperfections all showed enhanced growth rates. In fact, the well developed prism face crystal seen in figure 43 (c) developed on an edge of the c-axis horizontal ice coupon. Even across the flat relatively uniform substrate surfaces, there was a variation in growth rates. Off the ice plates, on the plexiglas substrate, crystals also developed but no preferential orientation could be discerned. Well-developed cup shapes were not apparent on the plexiglas growth, although partial cups and columns were evident.

This experiment clearly demonstrated that crystals grown from the vapor phase on large existing crystals obtain the same orientation as the parent grain. Even though this experiment was limited to large parent grains, it is assumed that the same process would result as vapor condenses on small ice grains in a snowpack during kinetic growth. This experiment validates the assumption used in chapter 3 for the development of kinetic crystals.
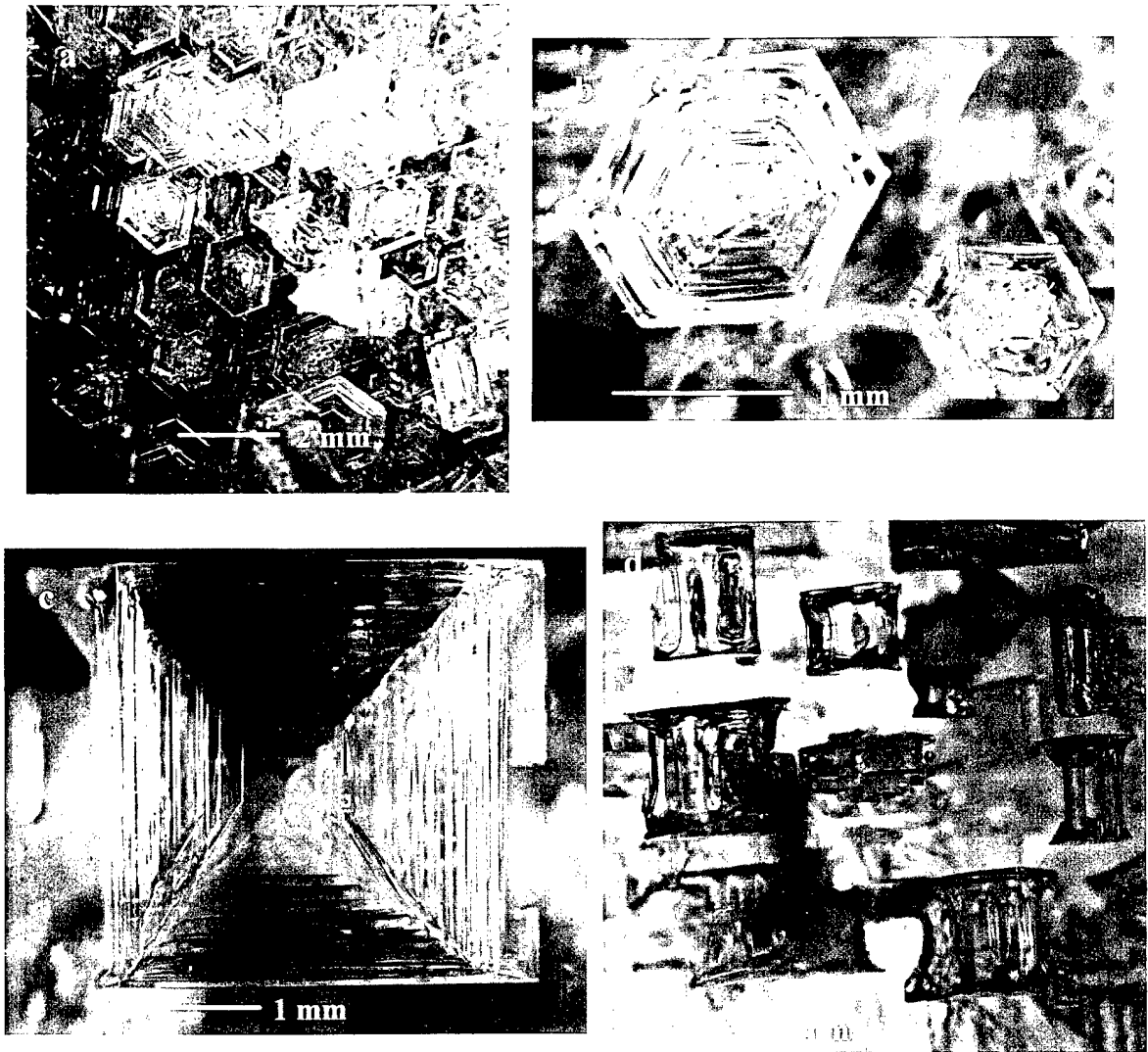
Figure 43. Ice crystals grown from vapor phase onto existing ice substrates. (a) and (b) formed on crystals with c axis parallel to the temperature gradient. (c) and (d) formed on crystals with the c axis perpendicular to the temperature gradient.

Kinetic Growth Experiment

Experiment Background and Objectives

To gain further insight into the development, growth, and progression of kinetic growth forms, an experiment was designed to examine the microstructure of snow

subjected to a temperature gradient. Initially, the objective was to further validate the kinetic growth section of the model by providing time domain microstructural data in a kinetic growth environment. As will be discussed later, the stereology software had difficulty measuring the transversely isotropic microstructure, leaving a weak validation. Another objective was to gain further qualitative understanding of the kinetic growth process in snow. The third objective was to produce mature depth hoar so that intergranular connections could be examined.

Methodology

To examine the detailed microstructural features and development of faceted snow types, depth hoar was grown in a laboratory setting. Natural snow was collected from the Bridger Range, MT and transported to the laboratory. The collected snow had fallen approximately 36 hours prior to collection. The snow was placed in a 0.5m cubic box with insulated sides and open top and bottom. The box was lined with plastic to minimize any vapor loss to the environment. The box was placed in a -17°C cold room on a heated plate. The hot plate maintained the bottom temperature at between 0 and -1°C. T-type thermocouples were placed in the snow at 10 cm intervals and temperatures were recorded every fifteen minutes. The box had a removable side panel that allowed access to the snow profile for examination and sample collection. The experiment was allowed to run for 41 days.

Periodically, the removable panel was separated from the box, exposing the snow vertical section. Samples were collected in the 30 ml Nalgene containers at 5 and 20 cm above the hot plate located at the bottom of the snow sample. The sample containers

were pressed into the snow wall until they were filled and then were carefully excavated. The samples were then filled with isooctane to halt metamorphism and preserve the microstructure. The box panel was replaced, and any resulting voids were filled with snow. Subsequent samples were collected in areas untouched by previous collections.

With the samples preserved, they could be imaged in the CT scanner. Using the techniques described earlier in this chapter, each sample was scanned, the resulting image smoothed, and finally a binary image was produced based on the snow's density. The experimental configuration, sample collection technique, and imaging process yielded an image in the plane of the temperature gradient. Previous efforts used the CT scanner to examine microstructure in a plane perpendicular to the temperature gradient (Lundy, 2000). The binary images were then evaluated using stereology software (Edens and Brown, 1994).

Results

Table 4 summarizes the elapsed time, location, grain size, density, and general characteristics of the snow samples collected from the temperature gradient experiment. Densities were measured with the known volume container. Grain type and size were somewhat subjective and based on personal observation using a 25x hand lens. Grain size is based on largest dimension of the crystal, such as diameter for rounded forms.

Elapsed time (day)	Height (cm)	Size (mm)	Density (kg/m³)	Comments
0	5,20	0.5 – 0.75	245	Initial sample. Decomposing, partially rounded particles
8	5	0.75 – 1.25	222	Small facets forming
8	20	0.5 – 0.75	241	Rounded grains
19	5	1.5 – 2.0	253	Mature facets, striations visible
19	20	0.75 – 1.0	258	Rounded with facets visible and forming
29	5	1.5 – 2.5	289	Long chains visible
29	20	1.0 – 1.5	305	Mature facets, striations visible
41	5	not measured	311	Starting to hollow out due to mass loss, last sample
41	20	not measured	311	Mature facets, striations visible. Chains developing

Table 4. Sample observations from kinetic growth experiment.

Binary Images. After CT scanning and image smoothing, binary images were obtained for all the samples. The binary images for samples collected at 5 cm are given in figure 44. Figure 44 shows the development of large faceted crystals as time progresses, and in the later stages of the experiment, large mesopores or pore channels are evident parallel to the temperature gradient. The crystals became oriented in long ornate chains. Similar images were obtained for the samples collected at 20 cm, but growth and development was slower due to the lower temperature gradient (~35°C/m).
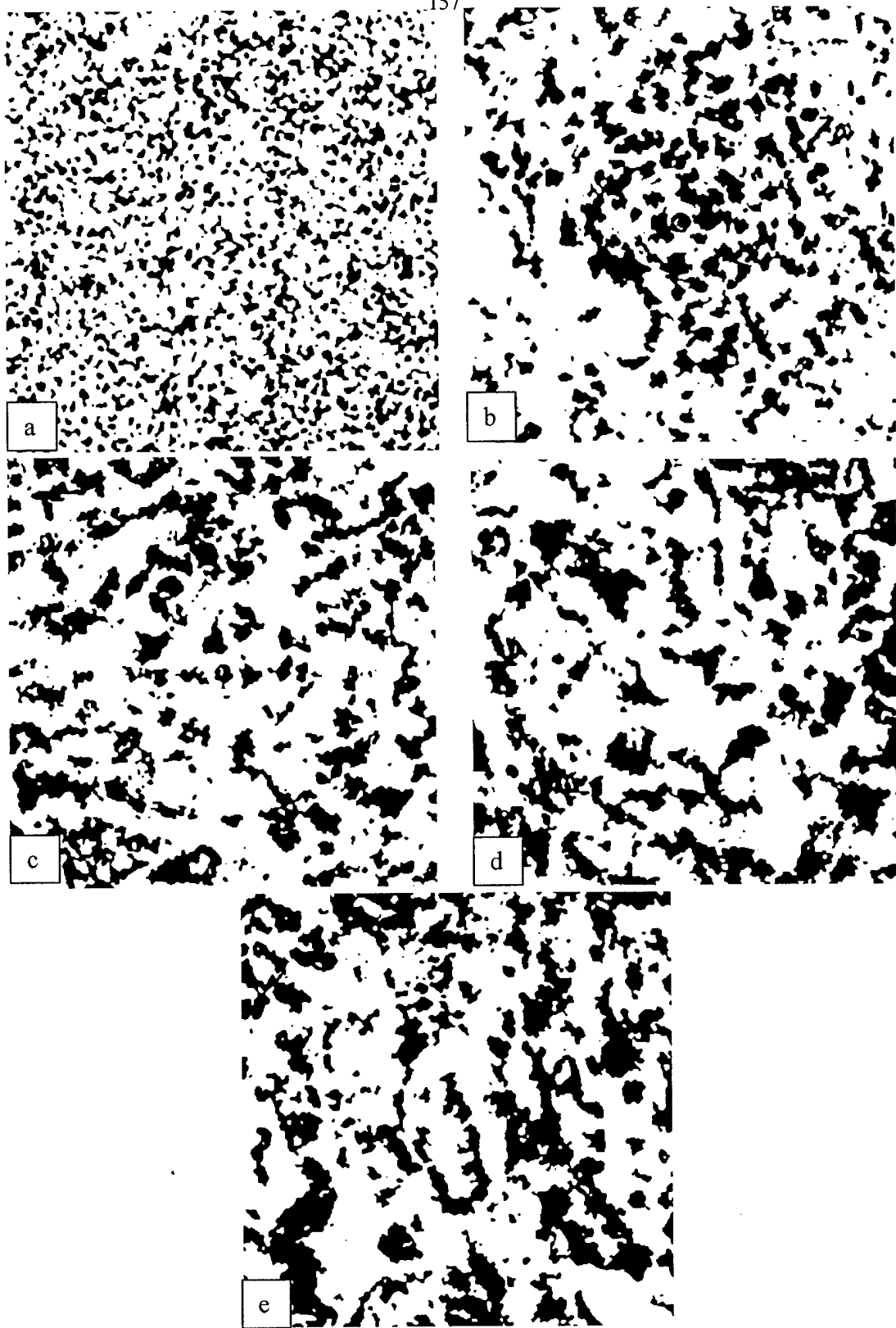
Figure 44. Binary images of snow 5 cm from bottom in kinetic growth experiment. (a) 0 hours, (b) 8 days, (c) 19 days, (d) 29 days, (e) 41 days. Average temperature gradient 61 °C/m.

Model Simulation of Kinetic Growth Experiment. The first objective of this experiment was to provide further validation of the kinetic growth model by comparison to experimental data. Originally, the experimental microstructural parameters were to be measured using Eden's (1994) stereology software from binary CT images. The highly transversely isotropic nature of the resulting snow proved very challenging for the software. Since the stereology package was designed to find three-dimensional parameters from two-dimensional images, an isotropic microstructure with spherical grains was assumed in its development. After bonds, necks and grains are defined, the largest diameter circle that fits within each grain is calculated. This diameter is used to find the grain radius. Because the CT scans were taken in the plane of the temperature gradient, long, narrow grains were evident in the images. As a result, the grain radius calculated by the software was excessively small and deemed unreliable. This is not a reflection on the quality of the stereology package since these transversely isotropic samples were well outside the program's designed capability. In order to capture some useful data from the scans, a different parameter was used as a crude measure of grain size. After bonds were defined, the average grain "size" was taken as the ice mean intercept length from the binary image. Since the crystal size defined in chapter 2 involved the length of facets, the mean intercept length is considered to be a better size definition than the grain radius given by the software, although this too is considered to be a crude approximation and a significant underestimation of size. With the image representing a planar slice only, it is unlikely that entire grains are contained in the image. Any small out of plane tilt results in only a portion of the grain being imaged. As

such, the ice mean intercept length is considered a lower limit on grain size. On the other hand, the size observations in table 4 are considered an upper limit on size. These sizes were based on optical observation of grains placed on a meshed grid. It is commonly believed that this technique over predicts size since the human eye may be drawn naturally to larger features. In any case, it too is a crude, inaccurate technique, but is included as an upper bound on grain size. For the initial sample, composed primarily of rounded grains, the optical grain sizes and software stereology grain sizes agreed, as expected for rounded forms. This initial grain size was used to begin the numerical simulation of the experiment. Grain orientations and an average temperature gradient were then applied. The experiment and simulation grain growth results are given in figure 45.

The dominant crystal orientations from the model fall in between the lower bound CT observations and upper bound optical observations. This result is useful in considering model validity, but really points to the need for standardized definitions and measurement techniques for kinetic growth forms. It is hard to evaluate the adequacy of a modeling approach when measures of actual snow structure are uncertain. Clearly, some trends are predicted by the model while others are not. In the model, crystals continue to grow in the large temperature gradient while the experimental grains seem to reach a maximum size after an extended period. There are two reasons why the actual grain growth appeared to cease. First, as grains get larger, the chances of interference from other grains increases. If a grain contacts other ice structures in a warmer (lower) part of the snow, a thermal short circuit develops and growth rates decrease. Currently, the model does not account for limited growth space and thermal shorts. Secondly, in the

laboratory experiment, the boundary at the hot plate does not supply vapor to the flow. As a result, as vapor diffuses from warmer to cooler sections of the snow, undersaturated conditions must develop in the pore near the hot plate. This requires the sublimation of snow in lower sections to supply the upper reaches of the experiment. The actual impact of this on growth rates is unknown, but it is believed that the growth rate transitions from negative to positive over some region above the hot plate, as dictated by saturation conditions. Since the model utilized temperature boundary conditions and assumed saturated conditions in the vapor everywhere (Clausius-Clapeyron equation), this variable growth rate is not predicted. A hollow area that developed near the hot plate after approximately four weeks provided evidence to mass redistribution. Lundy's (2000) experiment experienced the same phenomena.

The experimental analysis, as presented in figure 45, provided some additional validation, but given the uncertainties in measuring the actual microstructure, did not provide the detailed evaluation originally envisioned. The kinetic growth validation presented in chapter 3 was more rigorous. While the quantitative results were disappointing, the qualitative aspects of the experiment were very valuable.

The experiment did provide well developed depth hoar samples suitable for further qualitative analysis. The transition from smooth, rounded forms to sharp faceted kinetic forms was evident as the experiment progressed. The regions with larger temperature gradients developed facets sooner and they grew at a higher rate. This progression was successfully documented with the CT scanner. As the growth matured, large ornate oriented crystals developed. While the crystal development was interesting, the crystals themselves have been the focus of substantial past research. The bonds that

were observed between the grains gave insight and encouragement to the dominant grain

theory.
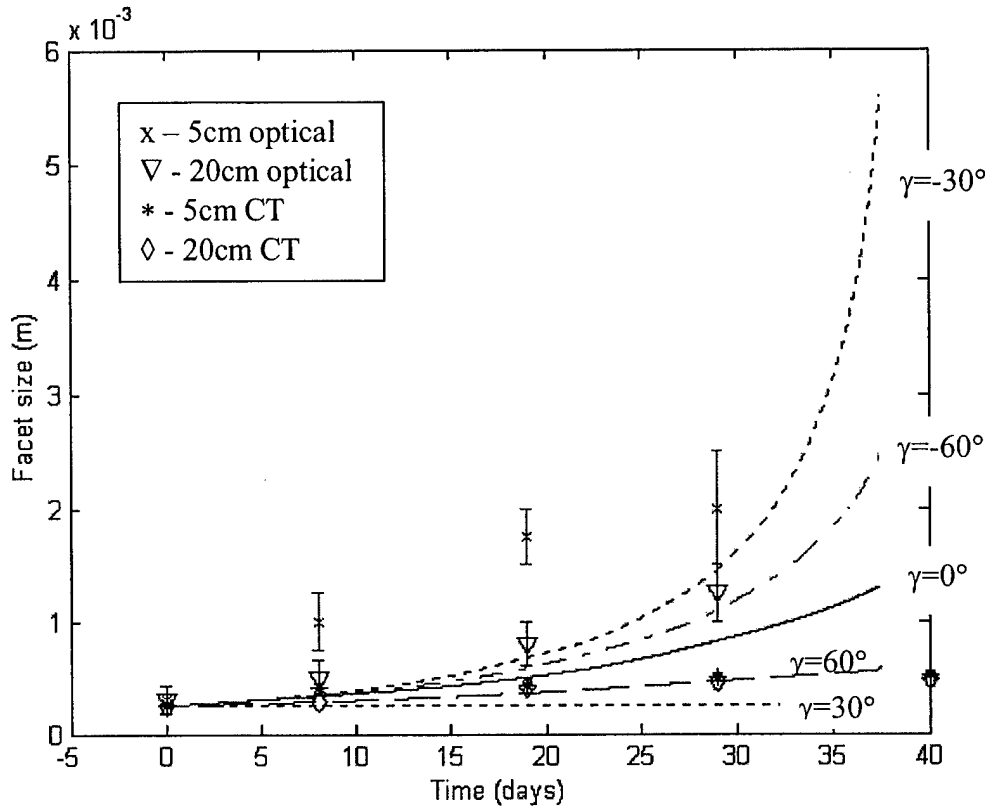
Figure 45. Comparison of model and measured grain facet sizes in kinetic growth environment for various crystal orientations.

Examination of Kinetic Growth Bonds. The SEM images in figure 46 clearly

reveal several cleanly fractured bonds of equilibrium form snow. In all SEM imaging,

failures and fractures of the snow microstructure were observed in the bond region.

Snow strength should be a strong function of the relative bond to grain radii ratio and

grain coordination number. Similarly, the interconnections between depth hoar grains

may provide insight into the strength and stability of snow composed of these faceted

crystals.
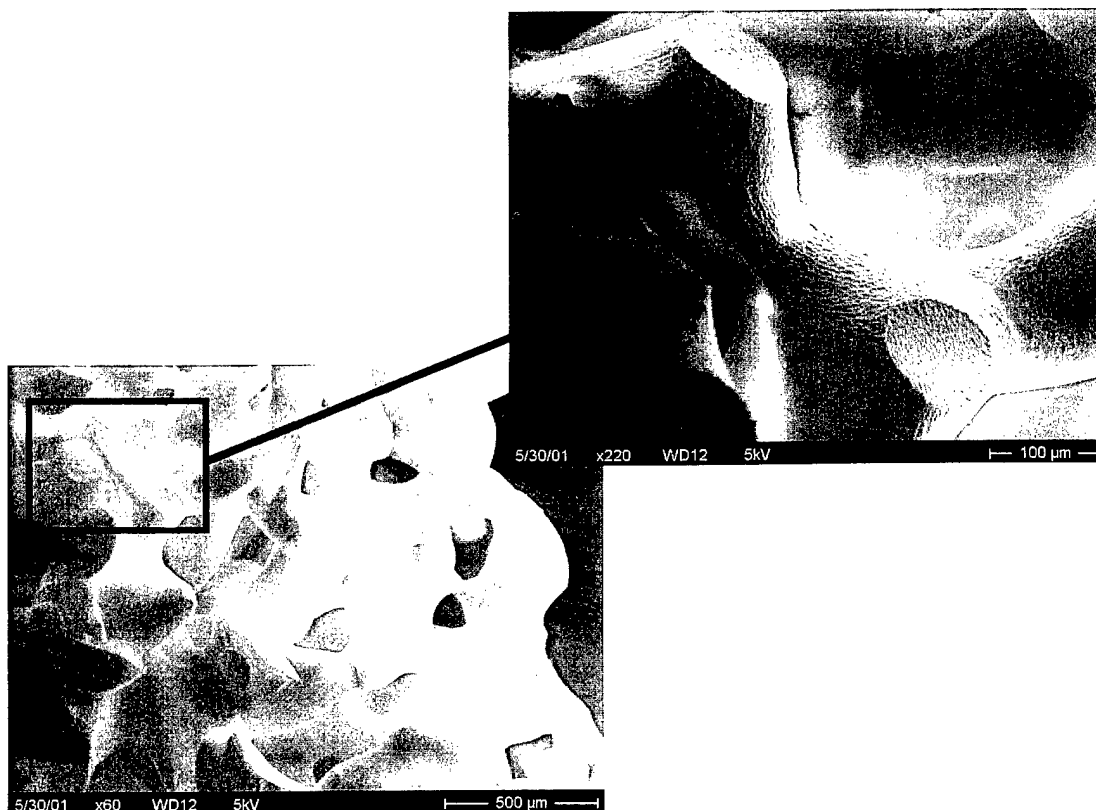
Figure 46. Scanning electron microscope of typical equilibrium form snow. Enlarged image showing fractured bonds.

The dominant grain theory developed and analyzed in chapter 3 focused on

faceted grains only. While certain crystallographic orientations were identified as having

very low growth rates, there was no mention of what happened to those crystals as the

optimally oriented grains out-pace them. As previously mentioned, faceted crystals

within a localized region exhibit similar morphologies (Akitaya, 1974). This, coupled

with the results of the crystal orientation experiment and model, supported the postulated

dominant grain theory. During kinetic growth, it has been reported that the number of grains decreased (Sturm and Benson, 1997), but is this really the case? Could this numeric crystal reduction be attributed to observation of only large dominant grains? Examination of the intergranular connections or bonds between large faceted crystals provided insight into the disposition of less optimally oriented grains. The temperature gradient experiment provided excellent samples to examine these grain connection regions. The SEM images in figure 47 display the bond region for kinetic growth crystals. These images serve to further support the dominant grain growth theory hypothesized.

In the presence of a sufficiently large temperature gradient and, therefore, mass flux, numerous heterogeneous nucleations may activate on each grain, inheriting that orientation, as was demonstrated in the study on the large crystallographicly oriented substrates (figure 43). When a locally preferred crystal growth environment dominates, less ideally oriented crystals will have their advance curtailed. In a supersaturated vapor environment, many of the original grains likely remain, ensconced under the conglomeration of truncated kinetic growth crystals. Multiple abridged crystals may manifest themselves at the "attachment" locations or bonds of depth hoar crystals, as seen in figure 47.

It is important to note that these kinetic growth bonds are not small relative to the bonds of the equilibrium form. The transition from the faceted grain to these attachments or bonds is clearly visible in figure 47 where the striated grain is contrasted to the geometrically complex bonds. Even though these connections appear relatively large, they may be weak since they are not continuous, and the irregular structure will induce stress concentrations. In addition, the bond to grain size ratio may be much less than for

the equilibrium form and the grain coordination number will also likely be smaller as the structure will tend to metamorphose into a transversely isotropic arrangement composed of ice crystal chains and channeled pores (Trabant and Benson, 1972; Akitaya, 1974; Adams et al, 1996).
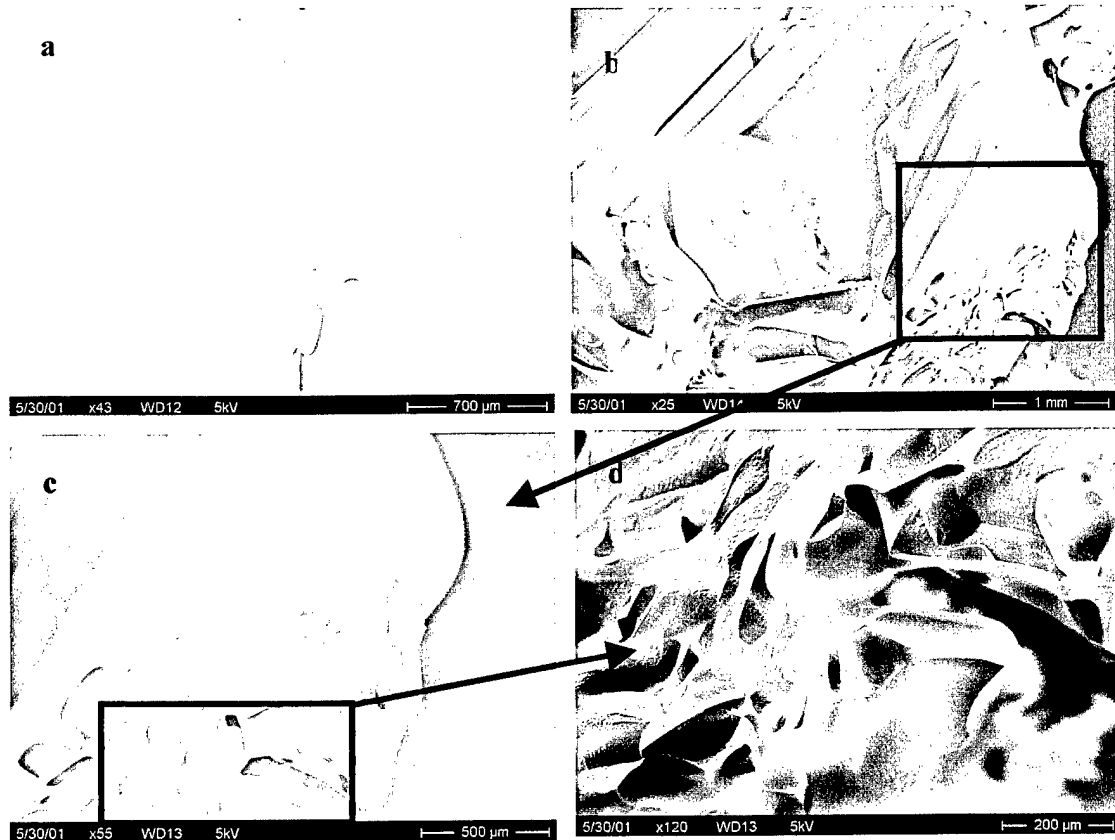
Figure 47. Scanning electron microscope images of intergranular connections in depth hoar. b - d show successive magnifications of the kinetic growth bonds. In b the striations of the depth hoar crystal are apparent and finally d shows what may be truncated kinetic growth nucleations.

In light of these observations and indications given by the numerical model, the hypothesized kinetic growth process may be summarized. In regard to the morphology of a snowcover subjected to a temperature gradient, there is a potential for a preferred

structure to develop that is analogous to what is often seen in lake and sea ice, whereby the ice cover has a distinct crystallographic orientation. A fresh deposit of snow, or snow metamorphosed to the equilibrium form, will be composed of randomly oriented crystal grains. However, when such a configuration is subjected to a large temperature gradient, the ensuing supersaturation will induce the nucleation of numerous crystals onto the existing ice grain network. Depending on temperature and level of supersaturation, a particular crystal habit grown from the vapor will be preferential. Some of these developing crystals within a region of the snowpack will be more optimally situated (relative to the temperature gradient) due to the orientation of the substrate or parent crystal. This, when coupled with an ice grain/pore configuration that will afford space in the preferred grow direction, results in some of the crystals being at a developmental advantage. As the optimally sited growing crystals progress, others will have their development arrested in the competition with the preferred configuration crystals. This leads to a perceived reduction in the number of grains as well as a (locally) crystallographicly oriented snow cover.

Microscopic observations of the regions near the attachment points of depth hoar crystals may provide evidence of the truncated faceted crystals described. These highly irregular bonds are prone to stress concentrations and may provide a relatively small bond to grain ratio when compared to microscopic observations of the smooth bonds apparent in the equilibrium metamorphic form. This provides some insight into the relative strengths of these snow types.

Avalanche Debris Experiment

One of the real dangers associated with avalanches is the burial of victims in avalanche debris. Avalanche deposits become very strong and hard in a short period of time, necessitating the use of metallic probes and strong shovels to retrieve a burial victim. It has been reported that this rapid set or strengthening of avalanche debris is the result of frictional heating during the event. McClung and Schaerer (1993) describe a thin liquid layer on the grain surface that develops from frictional heating during the avalanche, although direct evidence is not presented. Once the debris halts, this small liquid layer rapidly freezes creating nearly instantaneous bonds. Of course, the amount of frictional heating is dependent upon the size and duration of the avalanche. In large avalanches, debris fields have been observed to be nearly isothermal at 0°C, making the melt-freeze scenario likely (Tremper, 2001). But in smaller avalanches (much more common), is there enough energy to consistently raise the temperature to melting? Also, after grains and clusters violently interact, what affect does the sintering process have on debris hardening? An avalanche debris experiment was designed to examine these questions and to provide another application for the metamorphism model.

Methodology

During the 2000-2001 season, debris was collected from avalanche experiments conducted at the Montana State University Avalanche Research Site located in the Bridger Range, MT. The objective was to collect and preserve avalanche debris at

various time intervals starting immediately after an avalanche. In order to evaluate the significance of frictional heating, two sets of temperature measurements were desired. Snow temperatures in the flowing avalanche, as well as avalanche debris temperatures, helped determine what was happening during and after an avalanche. Temperature and temperature changes in the flow gave an indication to the amount of frictional heating during the avalanche while debris temperatures measured the snow's thermal state when it came to rest. Snow samples were collected before and after the avalanche for laboratory microstructural evaluation.

At the Revolving Door avalanche path in the Bridger Range, MSU has an avalanche research site consisting of a small shed and infrastructure to make various measurements during an avalanche. The site received extensive modification during the course of this study, but due to space limitations, only instrumentation used in this particular study is discussed. Five T-type thermocouples, spaced at approximately 7m intervals, were placed along the avalanche running surface to measure macroscopic temperatures of the flowing snow. To capture avalanche debris, a pit measuring approximately 1.5 x 1.0m was placed in the avalanche path. As the avalanche passed by, the pit filled completely with avalanche debris. Snow temperature was also monitored with four T-type thermocouples through the debris pit depth during the study period. The debris was then sampled and preserved as soon as possible after the test. Sampling was repeated several times, up to 68 hours after the test. Samples were collected in the 30 ml Nalgene containers, preserved with isooctane, and transported to the lab on dry ice. Once in the cold laboratory, binary images were created from CT scanner images. The images were then analyzed using Edens and Brown's (1994) stereology software. The samples

were evaluated using the current model to quantify the affects of sintering in avalanche debris.

Results

Field. Three avalanche tests were conducted during the 00-01 winter season. Drought conditions in southwest Montana precluded a larger number of experiments. Due to several unfortunate circumstances and a painful learning curve, reliable temperatures at the base of the flow were recorded on only one occasion. Temperatures were successfully measured in the avalanche debris pit for all three tests. Table 5 gives the pre-test and avalanche debris snow densities as well as the average temperature of the debris immediately following the avalanche. Pre-test samples were collected in the avalanche release zone prior to the test; unfortunately, snow temperature profiles were not measured there prior to the avalanche test. Notice in table 5 that none of the debris temperatures approached the melting temperature. While this does not preclude surface melting, as this temperature measurement is macroscopic, it does show that the entire debris pile did not become isothermal at 0°C. In large avalanches with long run outs, excessive frictional heating could raise the snow temperature to the melting point. Since the snow in these tests did not approach the melting point, it seems unlikely that all of the observed debris strengthening can be attributed to the freezing of liquid water on the grain surfaces. This does not imply that fictional heating is of no consequence. In the 19 Feb 01 avalanche test, temperatures were recorded along the base of the avalanche flow at the specified 7m interval. Figure 48 shows the snow's increase in temperature (from an initial temperature) along the avalanche test track. Since the initial temperature

measured on the track prior to the test was probably different than the initial temperature

of the avalanching snow, the absolute increase in temperature of the flowing snow is

unknown. To minimize this error, each thermocouple was covered with snow prior to the

test, but the temperatures of snow on different parts of the slope are not likely identical.

In figure 48, the time-phased nature of the flow is evident as the temperature changes

occur later for thermocouples further down the slope. It also appears that the temperature

change tends to increase the farther the avalanche has run. Figure 49 shows the actual

temperatures along the track. In general, as the avalanche progressed down the slope, the

absolute temperature appeared to increase. It is unresolved why the thermocouple at the

top of the test section consistently recorded higher temperatures. From figure 48, it is

clear that the temperature increase experienced by this thermocouple is generally smaller

than for the others. Since temperature profiles of the pre-test snow were not collected, it

is impossible to tell if the higher temperature at the top of the track is from actual snow

originating in a warmer section of the release zone or if it is an instrumentation problem.

These temperature results of a running avalanche are very preliminary, but hold promise

for further research now that the infrastructure and procedures are in place. At this time,

there is not enough repeatable data to make significant conclusions, but the trends in this

one test are logical and promising.
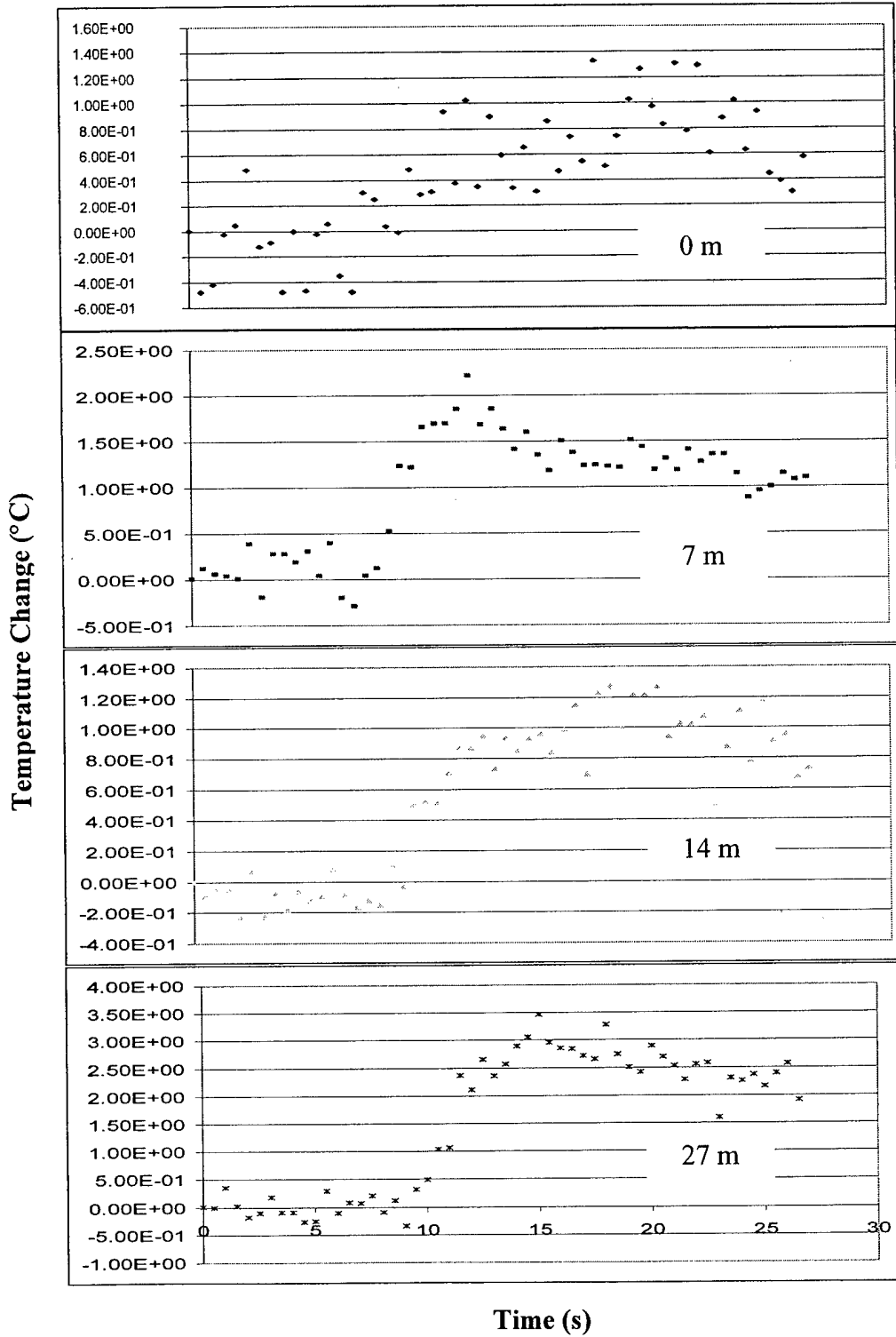
Figure 48. Temperature change at the base of 19 Feb 01 avalanche flow. Distance from upper end of track indicated.
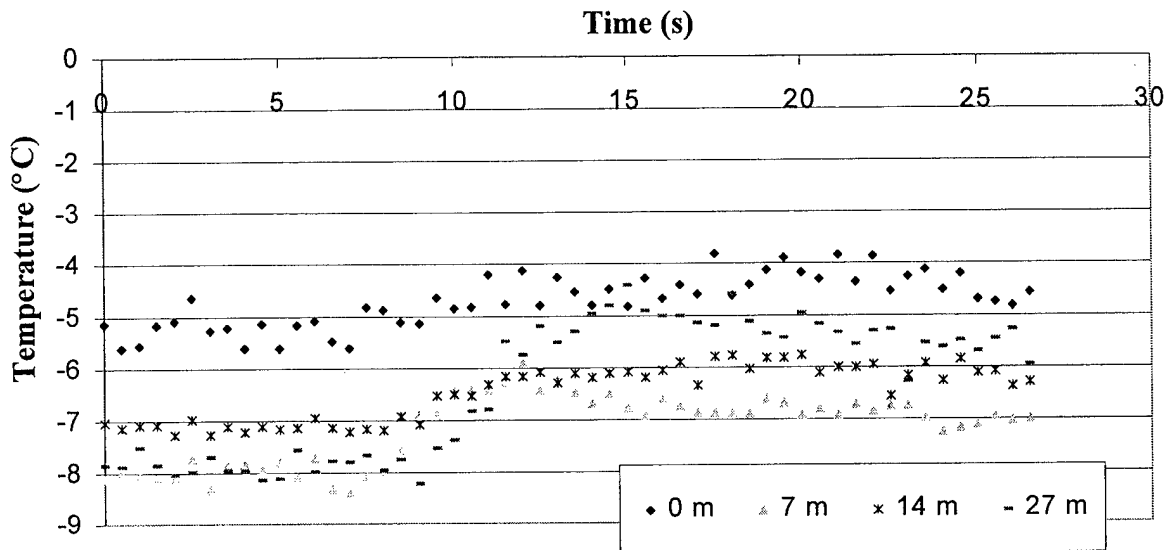
Figure 49. Temperatures at the base of 19 Feb 01 avalanche flow.

Date	Pre-test Density (kg/m^3)	Debris Density (kg/m^3)	Debris Temperature (°C)
19 Feb 01	260	450	-5.5
15 Mar 01	117	407	-4.6
31 Mar 01	230	420	-1.2

Table 5. Density of pre and post avalanche snow with debris temperatures.

Laboratory and Numerical. After the preserved samples were transported to the

laboratory, they were CT scanned and processed, as described earlier in this chapter, to

obtain binary images. It was originally envisioned that the grain and bond data from the

stereological evaluation of the binary images would be compared to the numerical

evaluation of the sintering process. Accurate bond data was not obtained from the

images primarily due to limitations of the CT scanner. Obtaining high contrast and

resolution images of the high density debris samples filled with isooctane proved very

challenging for the CT scanner. The CT scanner was operated at its maximum power and exposure time in an attempt to record details of the microstructure, but the resulting images were noisy and lacking in contrast. In some high density cases, the overall image intensity varied from the center of the image to its edges. As a result, bond measurements were deemed unreliable as the details of these small features were the first features lost. On the other hand, the grain measurements appeared consistent and similar to field observations. Since grains are much larger than the bonds, they were less affected by noise and contrast issues.

The stereological analysis produced two-dimensional coordination numbers from the binary images. The coordination number is a measure of the average number of bonds per grain. The stereology package measured the number of grains (as a percentage) for each coordination number. This parameter is particularly useful since the strength of the snow should increase as the number of bonds per grain increases. Even though the details of the bonds were not accurately captured, the number of connections between grains seemed reasonable. The density increases shown in table 5 should accompany an increase in the coordination numbers as the snow is consolidated during an avalanche. Figure 50 shows an overall increase in the number of bonds per grain from before and after the avalanche. As expected, the number of bonds increased significantly in the avalanche debris. Bond growth is examined next using the numerical metamorphism model.
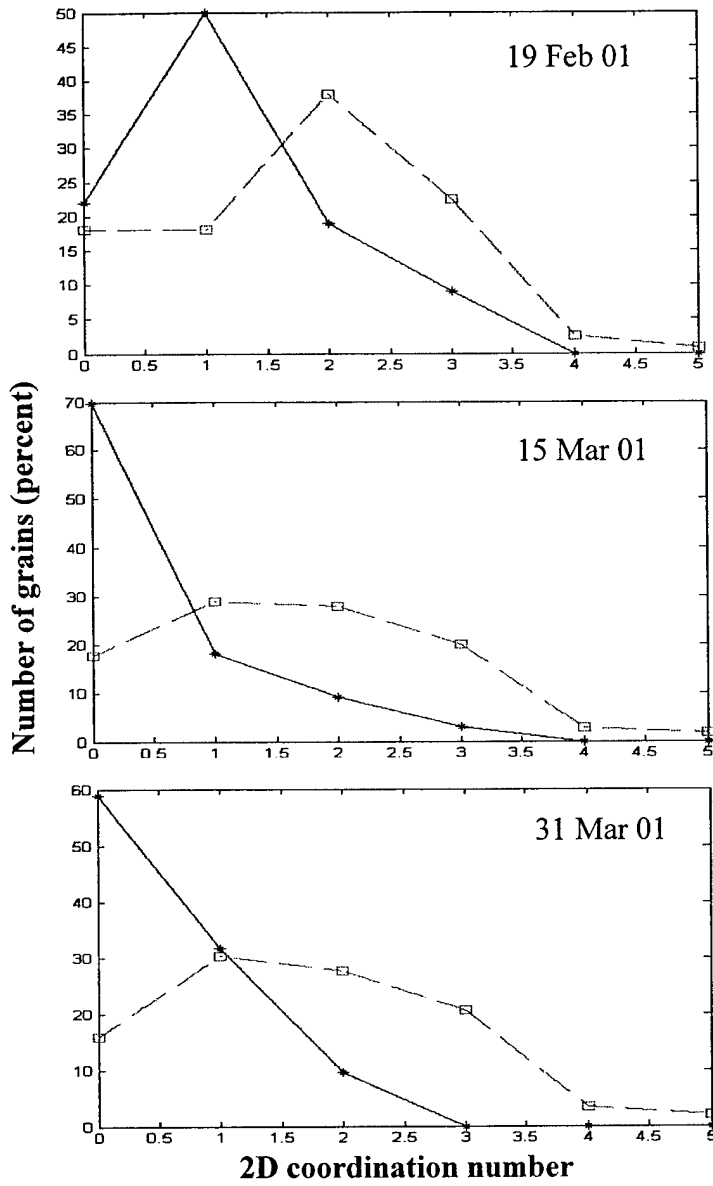
Figure 50. 2D grain coordination number frequency from avalanche tests.
* - pre-test, □ - avalanche debris.
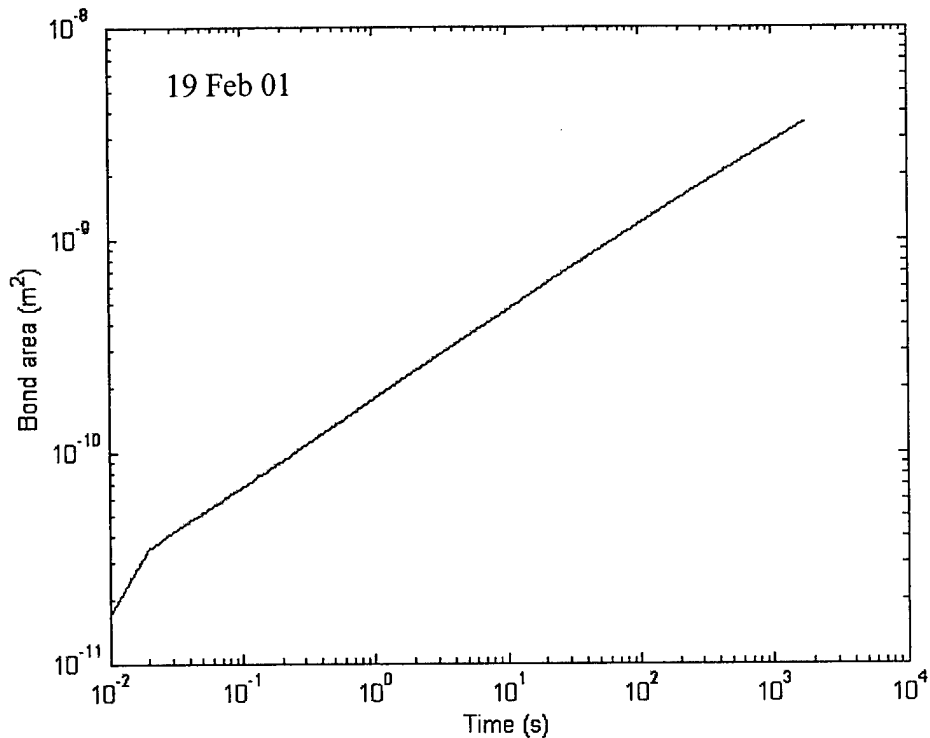
Figure 51. Bond area growth starting immediately after an avalanche.

With the increase in the number of bonds evident in avalanche debris, what is the growth rate of these bonds after an avalanche event? Since the CT scanner failed to give reliable bond data, bonds were evaluated using the numerical sintering model. It was assumed that the bonds were broken during the avalanche and began to grow again in the debris pile. The modeled microstructure was defined by the CT grain size in the debris pile, initial bond to grain radii ratios of 1%, and density and temperature from the field recorded values. Sintering was allowed to progress with these parameters. As already discussed, the amount of intergranular bonding is a measure of snow strength. In figure 51, the increase in bond area is calculated for the first 30 minutes following the 19 Feb 01 avalanche. During the first 30 minutes, the bond area within the avalanche debris

increased over 200 times, significantly strengthening the debris. The rapid increase in bond area coupled with the increase in bonds per grain present an alternative to the melt freeze explanation for the hardening of avalanche debris. Considerable research potential still exists on avalanche debris, but the avalanche debris sintering problem provided an excellent application of the current model.

Summary

In this chapter, several experiments and procedures were presented. The use of isooctane to preserve and store snow samples was discussed. Procedures for optical, SEM and CT microstructural imaging were established, and the advantages and disadvantages of each technique were discussed. These imaging techniques were subsequently used in lab and field experiments wherever they were deemed appropriate and capable of providing viable data.

The first experiment demonstrated that crystals grown from the vapor phase on existing ice acquire the same crystallographic orientation as the substrate. This result supported the postulated dominant kinetic grain growth theory described in chapter 3.

Next, a laboratory depth hoar experiment was presented. While the experiment did provide some additional validation of the kinetic growth model, its real value was in providing samples for examining bonds between faceted grains.

The final experiment examined the metamorphism of avalanche debris. Limited temperature data indicated that temperatures in small avalanches do not always approach the melting temperature. A sintering analysis using measured debris parameters found

that rapid growth of bonds, in the absence of liquid water, may be a major contributor to

the hardening of avalanche debris.

CHAPTER 5

APPLICATION OF THE MICROSTRUCTURAL MODEL IN LARGE SNOWPACKS

The current research has intentionally focused on small detailed microstructural snow parameters. Several other recent efforts recognized the importance of microstructure in determining snow physical characteristics such as thermal conductivity, radiation interaction, and mechanical behavior. Existing large scale models, such as SNOWPACK (Lehning et al, 1999), fail to accurately predict microstructural metamorphism over a wide range of environmental conditions (Lundy, 2000). Enhanced metamorphic capabilities would benefit these models, as many of the required macroscopic responses are tightly coupled to microstructure. While the current research does not address large scale snowpack modeling directly, it is important to establish a conceptual connection between the snow microstructure and the snowpack's macroscopic response. This chapter presents examples utilizing the current model in a full sized snowpack to predict metamorphism. A simple steady state snow conduction model was developed with time varying temperatures applied at the snow surface. The conduction model, represented in figure 52, is not intended to be an accurate snowpack simulation. Instead, it is presented to show how the microstructural model may interface with a more sophisticated approach. Metamorphism of internal snow layers was analyzed for various

snowpack and environmental scenarios. While the approach is very simple, its value lies in the conceptual application of the current research to a broader snow prediction effort.

Snowpack Thermal Simulation

The current model requires defined temperature boundary conditions and microstructural parameters. So far, the source of those boundary conditions has not been discussed in detail. Ideally, actual snowpack temperatures would be used for specific layers in a metamorphism simulation. In reality, real time temperature measurements in all regions of interest is not possible. As a result, numerical models are routinely utilized to simulate the field conditions. To demonstrate how a microstructural model may interface with a larger scale snowpack simulation, a very simple heat conduction model was developed. The microstructural model was used to evaluate the metamorphism of specific layers within a larger snowpack. As the microstructure evolves, feedback to larger scale models dependent upon microstructure enhances the accuracy of predictions.

A three-layer steady state conduction model is shown in figure 52. The basal temperature was maintained at 0°C while the surface temperature was variable. To simulate diurnal temperature fluctuations, a 24 hour period sinusoidal surface temperature with selectable average and peak temperatures was used. Since a steady state assumption was used, temperature gradient reversals due to transient effects were not included. Within each layer, the effective thermal conductivity was assumed constant and given by Yen's(1981) empirical relationship,

$$k_{eff} = 2.22326\rho_s^{1.885},$$

(111)

where k_{eff} is the layer's effective thermal conductivity (W/(mK)), and ρ_s is the snow density (Mg/m^3). While equation (111) is applicable for a wide range of densities, this simple relationship accounts for density only. Adams and Sato (1993) presented an advanced microstructurally based formulation for effective conductivity. Even though their approach was not used here, it is considered superior, further emphasizing the importance of microstructure. SNOWPACK utilizes the Adams and Sato approach, yet cannot capitalize on all its features due to metamorphic modeling limitations.

In figure 52, each layer was given an independent density (therefore thermal conductivity), microstructural parameters, and thickness. Temperatures at the interfaces between layers were then calculated using a very simple steady state Fourier heat conduction model with finite difference techniques. The details of that development are omitted primarily due to space limitations and the very simple nature of the conduction model. The resulting temperature gradient within each layer is linear. A conceptual representation of temperature distributions through the three layers is also shown in figure 52. The thermodynamic conditions in each layer were passed to the metamorphism model at each time step. It is envisioned that the current microstructural model will be integrated into sophisticated snowpack models in the future. To further demonstrate the utility of the current research, several common snowpack scenarios were evaluated using the conduction and microstructural models.
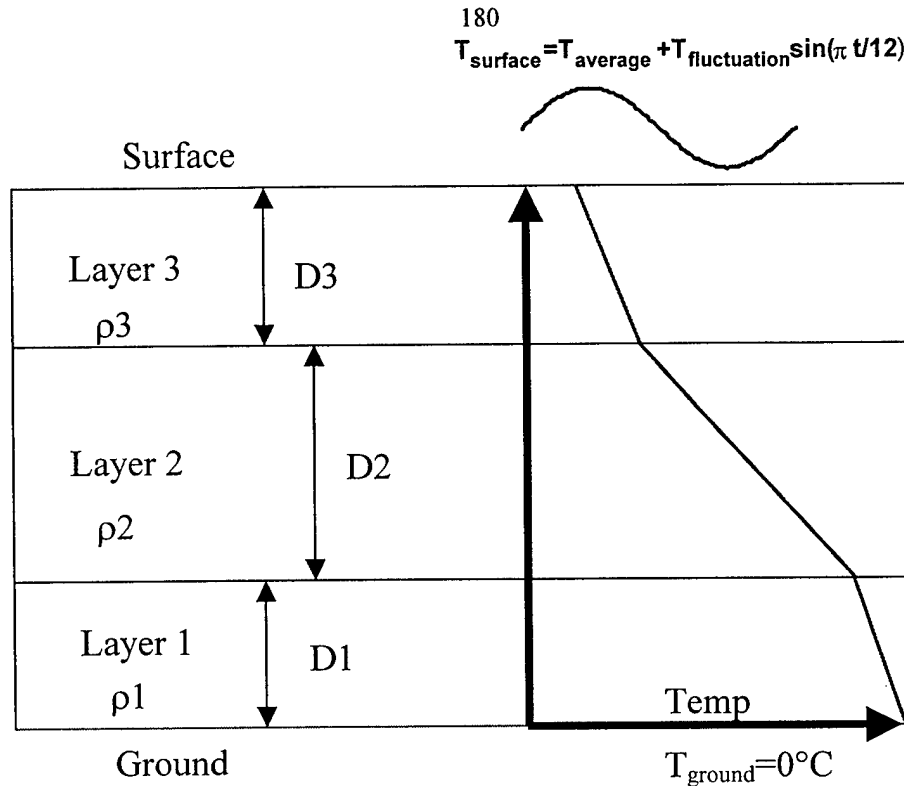
Figure 52. Three layer snow conduction model. The temperature boundary conditions and representative temperature distributions are shown on the right. $T_{surface}$ represents diurnal temperature cycles. t is in hours.

Case Studies Using Conduction and Microstructural Models

In table 6, four common snowpack scenarios are described and presented as examples of the snowpack technique. Each scenario was designed to demonstrate a particular capability of the microstructural model in common snowpack environments. Using the model described above, the temperature distributions, based on the average surface temperature, are given in figure 53.

Scenario	Density (kg/m^3)	Layer Thickness (m)	Surface Temp (C)	Comments
Case 1 – Layer 1	200	0.33	-6±5°C	Uniform snow with warm surface
Layer 2	200	0.33		
Layer 3	200	0.33		
Case 2 – Layer 1	450	0.25	-6±5°C	Layered snow with warm surface
Layer 2	250	0.25		
Layer 3	150	0.5		
Case 3 – Layer 1	150	0.2	-20±5°C	Thin, layered snow with cold surface
Layer 2	150	0.2		
Layer 3	200	0.2		
Case 4 – Layer 1	350	0.5	-20±5°C	Low density snow on top with cold surface
Layer 2	350	0.5		
Layer 3	150	0.2		

Table 6. Snowpack conditions for the heat conduction model.

The temperature distributions in figure 53 show relatively small temperature gradients for the first two cases and larger gradients for cases 3 and 4. Since the layer densities and thicknesses were identical for case 1, the temperature gradients were uniform through the entire depth. The variable layer densities and thicknesses in case 2 resulted in different temperature gradients in each layer. Case 4 had a large temperature gradient in the surface layer while case 3 had large temperature gradients below the surface layer.
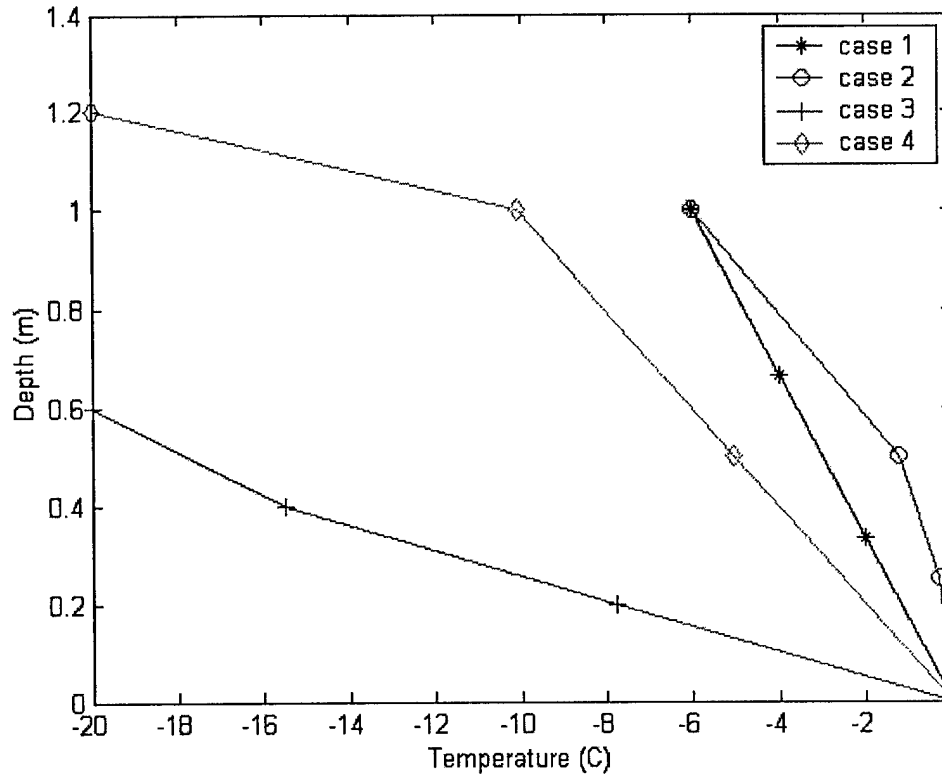
Figure 53. Snowpack temperature distributions for four example cases. The distribution is based on the average surface temperature used in the simulations.

Case 1: Equilibrium Form Metamorphism with a Uniform Snowpack

The first case simulates a very simple uniform snowpack with small surface temperature fluctuations. The variable surface temperature was applied, and the microstructure metamorphism for each layer was evaluated for a 24 hour period. The resulting temperature gradient was not sufficient for kinetic growth but did enhance the equilibrium form sintering with increased vapor pressure gradients. The temperature distribution, temperature gradients, and bond growth rates are given in figure 54.
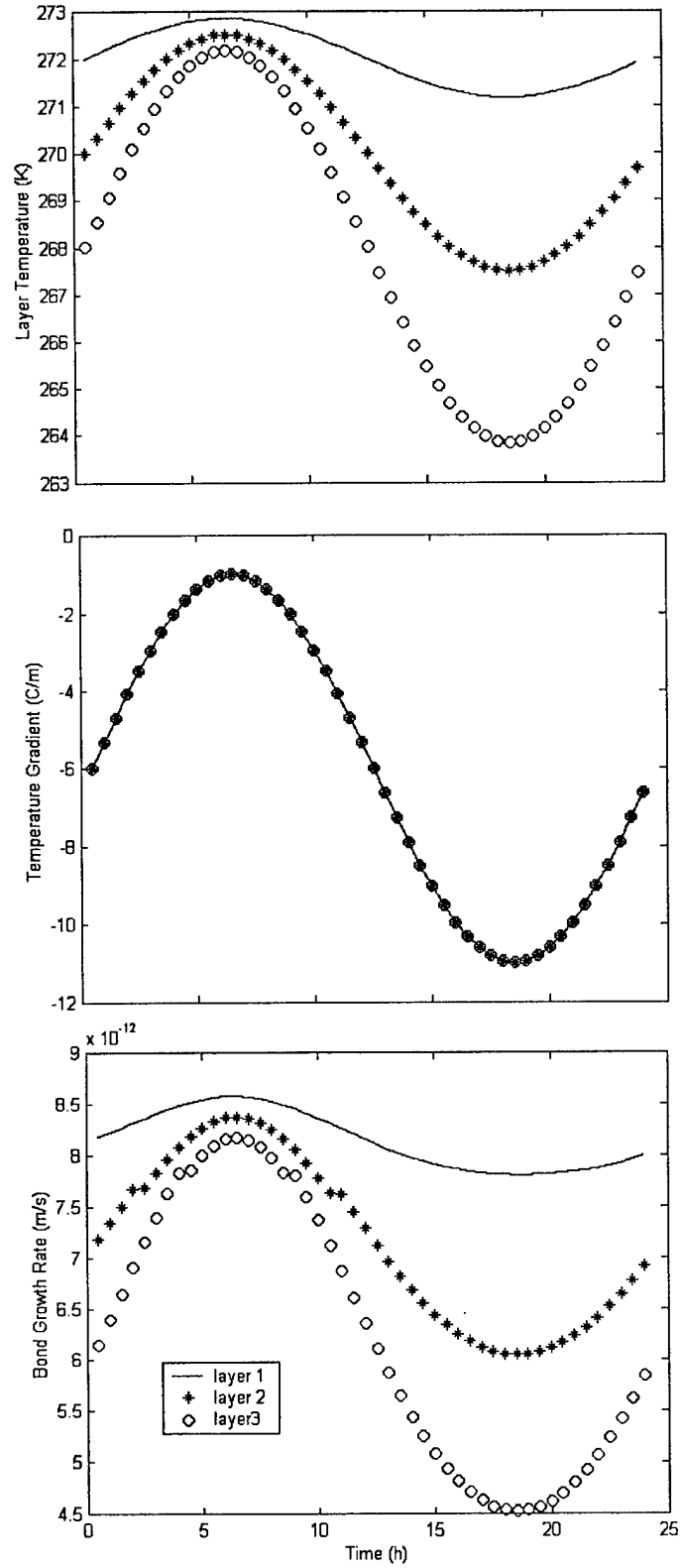
Figure 54. Case 1, equilibrium metamorphism snowpack simulation results.

Since the temperature gradients in each layer are identical, the variation in bond growth rates was a function of temperature differences only. As expected, the growth rate in the colder (upper) layers was lower than in the warmer regions. This example demonstrated the temperature dependence, but did not provide information on temperature gradient dependencies.

Case 2: Equilibrium Form Metamorphism with a Layered Snowpack

Next, variable density and thickness layers are introduced to a temperature gradient environment. In this case, the combined effects of temperature and temperature gradients were evident. The temperature distribution, temperature gradients, and bond growth rates are given in figure 55.

The temperature gradient was not sufficient for kinetic growth in any of the layers. The bond growth rates in figure 55 show both temperature dependence and the growth enhancements from a temperature gradient. The bond growth rate in the middle layer was greater than in the bottom layer, yet it was always colder. The enhanced growth rate resulted from the larger magnitude temperature gradient, offsetting the effect of lower temperature. Averaged over a 24 hour period, the top layer had the same growth rate as the bottom layer. In this case, the average temperature gradient offset the differences in average temperature. Of course, the temperature and temperature gradient fluctuations in the top layer manifested themselves in the variable bond growth rate of that layer. In each layer, the maximum bond growth rates coincided with the warmest temperatures although this was at the minimum magnitude temperature gradients, again reinforcing the strong temperature dependence of the metamorphic process.
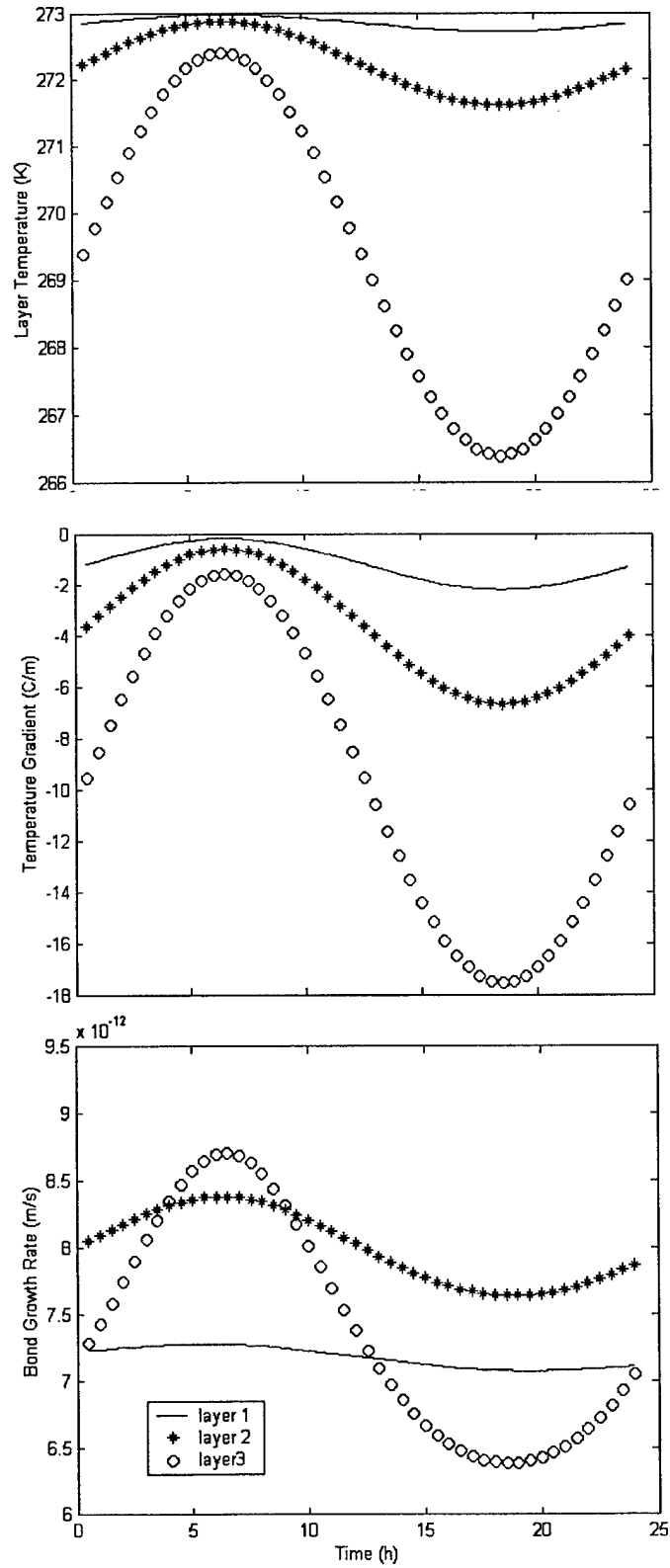
Figure 55. Case 2, equilibrium metamorphism with variable layers, snowpack simulation results.

Case 3: Depth Hoar

For the next case, a thin snowpack subjected to a large temperature gradient was examined. This scenario is very common in early winter when a thin snowpack bounded by a warm basal layer and cold surface develops depth hoar due to the large temperature gradients. This situation is normally of great concern since deep persistent snowpack instabilities may result. The temperatures, temperature gradients, and kinetic crystal growth rates are given in figure 56. Since kinetic growth takes place, only the dominant crystal orientation is presented. The growth rate, in this case, was larger near the bottom layer of the snowpack leading to the well-established depth hoar scenario.

The bottom two layers grew kinetically from the start. Although these layers had identical thickness and density, the kinetic growth rate of the bottom exceeded that of the other layers due to warmer temperatures. As the facets in the bottom layer grew, the growth rate was enhanced when the tip of the crystal reached into the warmer portions of the pore. The enhanced growth rate is evident in figure 56 as the average growth rate increased over the 24 hour evaluation period. This enhanced growth was discussed in chapter 3.

In the top layer, the temperature gradient was not sufficient for kinetic growth until hour 13 when the onset condition for kinetic growth was reached. Up to that point, the equilibrium forms sintered with enhancement from the temperature gradient. Since figure 56 depicts the kinetic growth rate, the top layer is not represented until the temperature gradient becomes sufficient for kinetic growth.
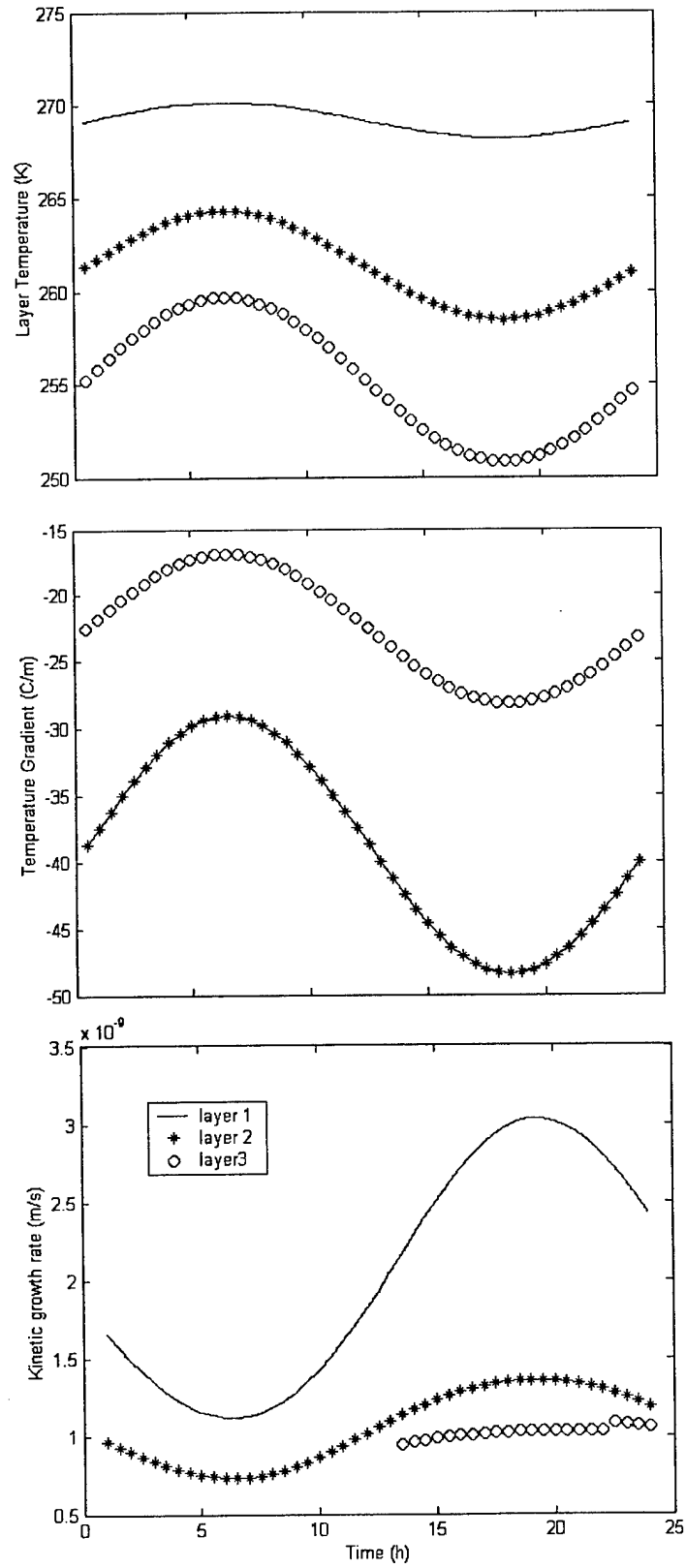
Figure 56. Case 3, depth hoar snowpack simulation results.
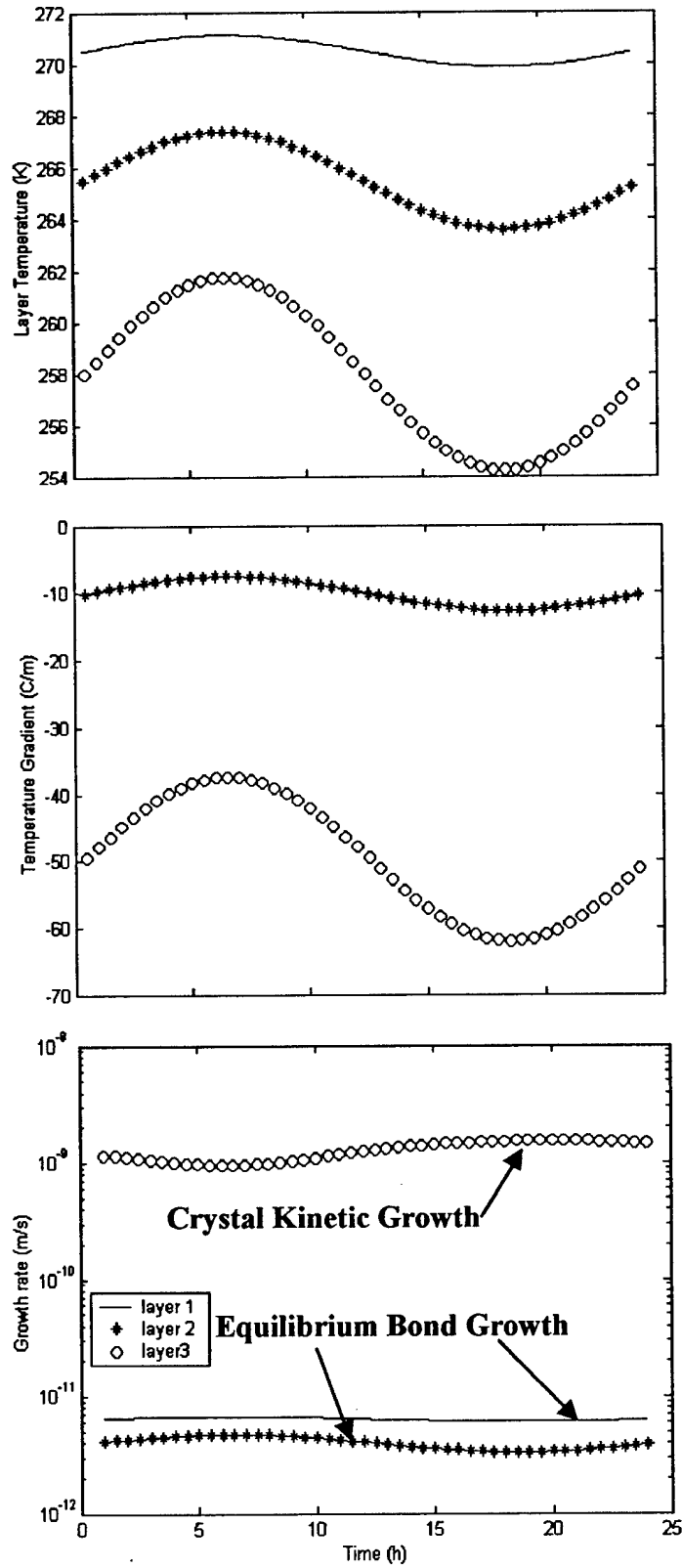
Figure 57. Case 4, near surface facet simulation results.

Case 4: Near Surface Faceting

The final example was composed of a relatively dense snowpack covered with a thin low density top layer. Cold diurnal conditions and low thermal conductivity of the top layer coupled with high thermal conductivity of dense layers ensured a large temperature gradient near the snow surface. Large temperature gradients can result in rapid kinetic growth of crystals just below the snow surface. Fukuzawa and Akitaya (1993) found this rapid growth when large temperature gradients within thin new snow was lying upon older, high density layers. They conducted laboratory growth experiments with gradients ranging between 100-300 °C/m to simulate this growth process. The rapid development of these faceted crystals (as quickly as overnight) has been the culprit in many avalanche accidents when buried by subsequent snow. Frequently, these crystals develop and may go unnoticed. As subsequent snowfalls bury these crystals, they can become the predominant weak layer. The identification of conditions under which this metamorphic process develops is critical to avalanche safety stability assessments.

The temperatures, temperature gradients, kinetic crystal growth rates, and equilibrium bond growth rates are given in figure 57. The temperature distributions show the large variation in temperature through the snow depth. The temperature gradients in the bottom layers were identical due to density and thickness parameters. The large temperature gradients within the top layer resulted in kinetic growth while the high density layers sintered in the equilibrium form.
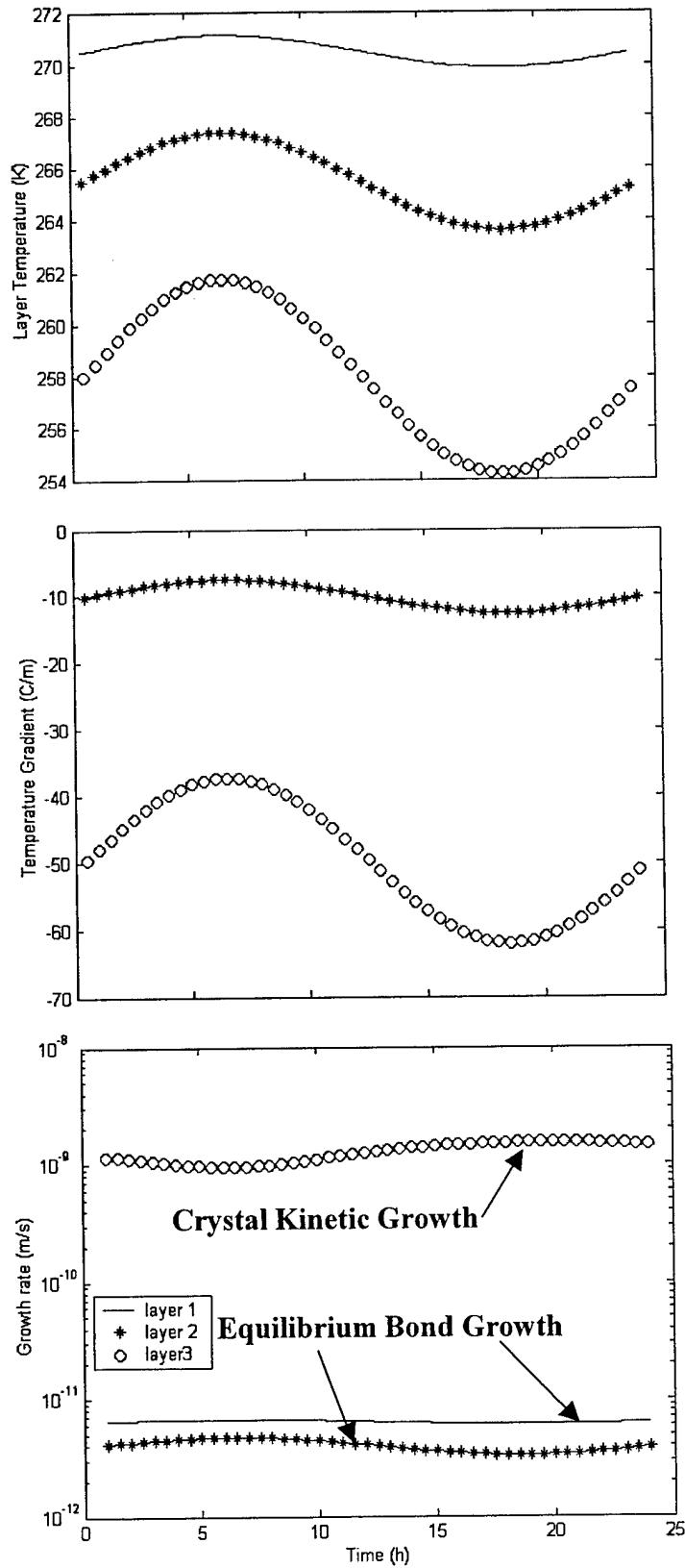
Figure 57. Case 4, near surface facet simulation results.

The growth rates are presented in figure 57 on a semi-log scale to demonstrate their relationship. The bond growth rates of the equilibrium forms are presented with the crystal growth rates of the kinetic form. Each of these growth rates is the primary metamorphism measure for the equilibrium or kinetic microstructure. The bond growth rate of the dense layers is several orders of magnitude smaller than the crystal growth rate in the top layer. The bond growth rate temperature dependence is evident in the high density layers. This example demonstrates the microstructural model's ability to predict multiple processes within the same snowpack.

Example Using Field Measured Data

The current approach is not restricted to use with other models. Remote instrumentation sites could also provide the required conditions to evaluate metamorphism of a snowpack. Montana State University maintains a meteorological station in the Wolverine Basin of the Bridger Range, MT. At that station, many measurements are made including snow surface and layer temperatures. Human snowpack observations are obtained weekly to document the snowpack, including general microstructural trends. Data from this station (or similar stations) could be used to monitor and predict snow metamorphism. To show how the current model could interface with such a station, one interesting scenario was analyzed from the 00-01 winter Wolverine Basin data. During the period from 2/16/01 to 2/28/01, Wolverine Basin experienced several cold clear nights. Snow pit observations on 2/26/01 noted the presence of near surface facets approximately 10cm below the snow surface. This

faceted layer was not noted during the 2/16/01 observations. This period was analyzed with the snowpack conduction and microstructural models in an attempt to predict the kinetic growth that was observed.

The snowpack was divided into three layers. These layers were determined from the 2/16/01 snow pit observations. Initial microstructure, density, and layer thicknesses were obtained from field notes and are summarized in table 7. The measured surface temperature (every 30 minutes) was used as the surface boundary condition for the snowpack conduction model. The temperatures, temperature gradients, and growth rates are given in figure 58.

Scenario	Density (kg/m^3)	Layer Thickness (m)	Grain Radius (mm)
Wolverine Basin			
Layer 1	365	0.8	0.5
Layer 2	300	0.3	0.4
Layer 3	215	0.2	0.5

Table 7. Wolverine Basin conditions on 2/16/01.

The top layer experienced large temperature gradients during the first day analyzed. In fact, the gradients were large enough to establish kinetic growth within that layer, predicting the appearance of near surface facets. The clear and cold conditions persisted throughout most of the 12 day evaluation period with very little new precipitation. While the top layer experienced kinetic growth, the bottom layers remained in the equilibrium form regime and sintered accordingly.
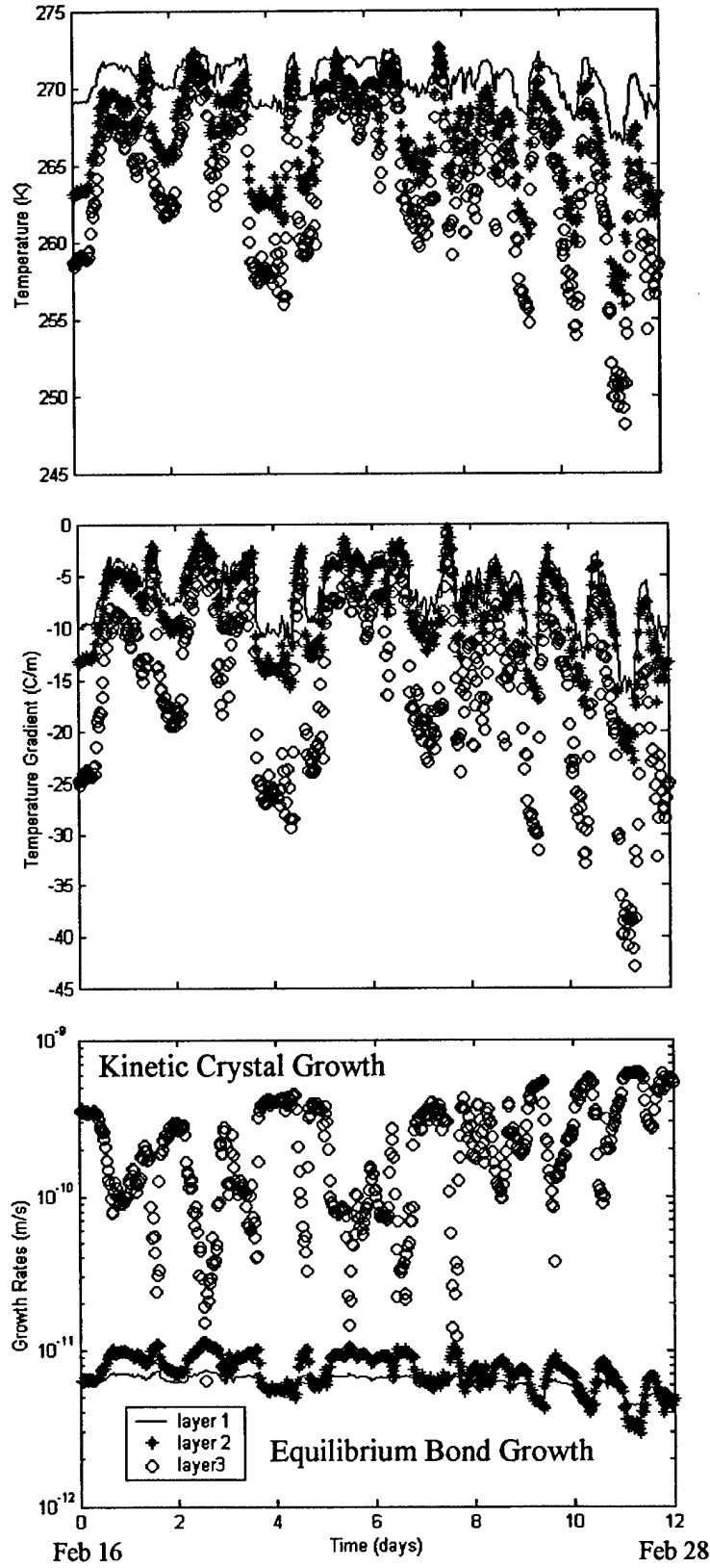
Figure 58. Wolverine Basin near surface facet development.

Although this analysis is very simple, it does provide another example of how the current research may be used in predicting metamorphism. In this case, there was not sufficient data to do a detailed microstructural comparison, but clearly the current effort was able to predict an observed trend using field data.

Summary

In this chapter, the application of the microstructural metamorphism model to a larger snowpack was examined. A very simple three layer heat conduction model was presented. Four common scenarios were evaluated using the layered conduction and metamorphism models. While the layered conduction model was not intended to suffice for a realistic snowpack model, it did demonstrate the process for using the microstructural model in a more sophisticated snow simulation. Temperature boundary conditions for the microstructural model were established using the layered conduction model. Data from a remote field weather station was also evaluated for a period where near surface facets developed. For more advanced techniques, the microstructural model could interface with other simulations that account for microstructure in thermal conductivity, radiation exchange, constitutive relationships, strength calculations, etc. As time progressed, a microstructural metamorphism module could provide feedback to these other physical models.

CHAPTER 6

CONCLUSIONS AND RECOMMENDATIONS

Conclusions

The literature review in chapter 1 identified the need for a realistic dry snow metamorphism model that could incorporate the important physical processes and microstructural geometry yet was applicable to a broad range of thermal environments. While many recent efforts have considered snow microstructure in metamorphism, the equi-temperature and temperature gradient thermal environments have traditionally been studied with different physical models. The current research developed a unified approach to snow metamorphism, independent of the thermal environment yet adequately considering the important physical processes and microstructure.

The theoretical development began with the definition of very simple spherical grains and intergranular connections. These grains and bonds were arranged relative to pore spaces, and pertinent physical interactions were discussed. Conservation of mass in the pore, conservation of energy in the ice network, and restrictions from heat and mass interactions during phase change were developed in detail. While the primary heat and mass flows were one dimensional, the phase interaction terms that coupled the equations

made the problem quasi-two dimensional. The three resulting nonlinear differential equations were coupled to each other through heat and mass exchanges during phase change.

The ice and pore networks were then discretized into elements and nodes. The appropriate finite difference equations were defined at each node. Due to the coupled nature of the equations, several iterative numerical techniques were used to solve the equations. The entire system was then iteratively solved until the mass and heat coupling terms converged. The ice and pore geometry was updated, time was incremented, and the process was begun again.

The first set of numerical studies involved macroscopically isothermal snow. The equilibrium geometry was analyzed for several scenarios. Very small microstructural temperature gradients developed to move heat and mass driven by differences in surface curvature. The existence of these gradients has been discussed in the literature, but this model was the first to show the development from physical principles. The equi-temperature studies found a strong metamorphic dependence on grain size, bond size, and temperature. Density was less of an influence on the sintering in an equi-temperature environment. This was attributed to the very short diffusion distance from the grain surface to a neighboring neck. A mass balance between the grains and necks found that the majority of the vapor leaving the grains arrived at neighboring necks, supporting the lack of density dependence.

The temperature gradient where crystals cease to grow in a smooth rounded form and begin to grow rapidly in large striated shapes has typically been defined between 10-25°C/m. This range of temperature gradients has been observed in the laboratory and

under field conditions. There has been little or no physical modeling or experiments to determine where this threshold may be and what parameters influence it. An onset of kinetic growth definition was proposed and evaluated using the current microstructural model. Unlike previous modeling efforts, the transition to kinetic growth was smooth and not based on a fixed numerical value. The numerical definitions appeared reasonable when compared with observed values, but also provided an important tool to analyze critical parameters influencing the transition. At the onset of kinetic growth, density, grain size, and bond size were the important parameters with temperature being less significant. While the kinetic growth onset was not significantly influenced by temperature, the growth rates at the onset were very temperature dependent.

After the onset of kinetic growth had been established, a crystal kinetic growth model was implemented. Results from several authors were integrated into one model. The approach considered crystal habit as well as crystallographic orientation in a screw dislocation growth model. Reasonable correlation with test data was demonstrated, but the need for standardized crystal geometric measurements was identified. The model led to a dominant grain theory whereby certain preferentially oriented crystals grow more rapidly than other crystals. The dominant grain theory demonstrated an increase in crystal size dispersion as metamorphism progressed. It was surmised that less preferentially oriented grains become buried in a complicated mass of ice. These masses may become faceted "bonds". SEM images of these regions were presented to support this supposition, but no direct evidence currently exists.

The dominant grain theory provided the basis for the first experiment. In order for the dominant grain theory to be valid, crystals grown from the vapor phase on existing

ice substrates must adopt the crystallographic orientation of the substrate. A simple experiment was described where new crystals were grown in the lab on existing ice with know crystallographic orientation. The experiment clearly showed that the new crystals grown from the vapor on existing ice adopted the orientation of the parent ice.

Faceted crystals were also grown in the lab. This experiment provided further validation of the model through periodic sampling and observation of the microstructure both optically and with a CT scanner. Samples showing the evolution of the snow microstructure were preserved and observed for a month. In addition, this experiment provided excellent examples of hoar crystals and bonds, which were used in formulating the dominant grain theory.

Avalanche debris was collected in the field and examined in the lab. The analysis of avalanche debris provided the microstructural model with an unusual field application. Analysis of the experiment pointed to sintering, rather than surface melt-freeze, as a primary mechanism for debris hardening.

Finally, the use of the microstructural model in a larger scale snowpack model was discussed. A simple layered heat conduction model was presented. Several scenarios were evaluated with the conduction model providing the thermal conditions for the microstructure model. While not intended to be an actual simulation, the layered model provided an example of how the microstructural model could be used in a more sophisticated approach.

The primary objective of developing a snow metamorphism theory that incorporates the important physical processes but is not limited by the thermal environment was achieved in this project. While many simplifications and assumptions

were necessary, the basic foundational approach has been established and is ready for further refinement and implementation.

Recommendations for Future Research

There are several areas where further research is required/desired. The microstructural model is ready to be used in an advanced snowpack model that accounts for microstructure using macroscopic conditions. A project where the microstructure is integrated into a sophisticated snowpack model, followed by a field or laboratory validation, is highly desirable. The Swiss model SNOWPACK is a candidate for this integration and this implementation may begin during the summer of 2002. An effort to use WINTHERM is also under consideration at Montana State University. Both of these programs can provide superior heat transfer analysis of a snowpack.

Within the microstructural model, there are several areas that could be improved. In the current configuration, facets are allowed to grow without bound. In reality, neighboring grains could interfere with growth. It would be desirable to provide size limits based on a physical parameter(s) such as pore size. In addition, grains that grow into neighboring grains would create a thermal short in the ice network. This too could be added to the existing model yielding attenuated growth rates as crystals became large.

Many of the envisioned enhancements to the current model would involve more complex, refined, or new microstructural parameters. Simple structures were defined for the current effort, but the theory is not limited to them. Complex grains and bonds could be easily added to the model. Not all observed bonds or grains are alike, but different

geometric classes could be added as further research identified them. It is envisioned that non-spherical grains, different classes of bonds, definable coordination numbers, etc could be added as new geometries are discovered or evaluated.

REFERENCES CITED

Adams, E.E. and R.L. Brown, 1982a, Further results on studies of temperature-gradient metamorphism, *Journal of Glaciology*, vol 28, no 98, 205-211.

Adams, E.E. and R.L. Brown, 1982b, A model for crystal development in dry snow, *Geophysical Research Letters*, vol 9, no 11, 1287-1289.

Adams, E.E. and R.L. Brown, 1983, Metamorphism of dry snow as a result of temperature gradient and vapor density differences, *Annals of Glaciology*, vol 4, 3-9.

Adams, E.E. and R.L. Brown, 1989, A constitutive theory for snow as a continuous multiphase mixture, *International Journal of Multiphase Flow*, vol 15, no 4, 553-572.

Adams, E.E. and R.L. Brown, 1990, A mixture theory for evaluating heat and mass transport processes in nonhomogeneous snow, *Continuum Mechanics and Thermodynamics*, vol 2, 31-62.

Adams, E.E. and A. Sato, 1993, Model for effective conductivity of a dry snow cover composed of uniform ice spheres, *Annals of Glaciology*, vol 18, 300-304.

Adams, E.E., Vanderroot, D.C., Edens, M.C., and R.M. Lang, 1994, Ice grain orientation of processed snow, *Proceedings of Snowsymp 94*, International Symposium on Snow & Related Manifestations, Manali, 96-102.

Adams, E.E. Priscu, J.C. and Sato, A., 1996, Some metamorphic processes in Antarctic lake ice, *Antarctic Journal of the United States*.

Adams, E.E, D.A. Miller and R.L. Brown, 2001, Grain boundary ridge on sintered bonds between ice crystals, *Journal of Applied Physics*, vol 90, no 11, 5782-5785.

Adams, E.E. and D.A. Miller, 2002, Ice crystals grown from the vapor phase onto an oriented substrate: application to snow depth hoar development and gas inclusions in lake ice, Submitted to *Journal of Glaciology*.

Akitaya, E., 1974a, Studies on depth hoar, *Contributions from the Institute of Low Temperature Science*, Series A, vol 26, 1-67.

Akitaya, E., 1974b, Studies on depth hoar, *Snow Mechanics Symposium: Proceedings of Grindelwald*, International Symposium on Snow Mechanics, Grindelwald, Switzerland, April, 42-48.

Armstrong, R.L., 1980, An analysis of compressive strain in adjacent temperature-gradient and equi-temperature layers in a natural snow cover, *Journal of Glaciology*, vol 26, no 94, 283-289.

Arons, E.M. and S. C. Colbeck, 1995, Geometry of heat and mass transfer in dry snow: a review of theory and experiment, *Reviews of Geophysics*, vol 33, no 4, 463-493.

Arons, E.M., 1994, Dependence of snow thermal conductivity on microstructure, Ph.D. Thesis, Dartmouth Coll, Hanover, N.H.

Ashby, M.F., 1974, [need title], *Acta Metall.*, vol 22, 275-?.

Bader, H. and Colleagues, 1939, *Der schnee und seine metamorphose*, Snow, Ice, and Permafrost Research Establishment, U.S. Army, 313pp.

Bader, H. P. and P. Weilenmann, 1992, Modeling temperature distribution, energy and mass flow in a (phase-changing) snowpack. I. Model and case studies, *Cold Regions Science and Technology*, vol 20, 157-181.

Baunach, T., C. Fierz, P.K. Satyawali, and M. Schneebeli, 2001, A model for kinetic grain growth, *Annals of Glaciology*, vol 32, in press.

Berry, M.O., 1981, Snow and Climate, *Handbook of Snow Principles, Processes, Management & Use*, Pergamon Press, Ontario, D. M. Gray and D.H. Male editors.

Bradley, C.C., R.L. Brown, and T. Williams, 1977a, On depth hoar and the strength of snow, *Journal of Glaciology*, vol 18, no 78, 145-147.

Bradley, C.C., R.L. Brown, and T. Williams, 1977b, Gradient metamorphism, zonal weakening of the snowpack, and avalanche initiation, *Journal of Glaciology*, vol 19, no 81, 335-342.

Brown, R.L., 1980, A volumetric constitutive law for snow based on a neck growth model, *Journal of Applied Physics*, vol 51, no 1, 161-165.

Brown, R.L. and M.Q. Edens, 1991, On the relationship between neck length and bond radius during compression of snow, *Journal of Glaciology*, vol 37, no 126, 203-208.

Brown, R.L., M.Q. Edens and M. Barber, 1999, Mixture theory of mass transfer based upon microstructure, *Defence Science Journal*, vol 49, no 5, 393-409.

Brown, R.L., P.K. Satyawali, M. Lehning, and P. Bartelt, 2000, Physical models for determining changes in microstructure of snow during metamorphism, *Proceedings 2000 International Snow Science Workshop*, Big Sky, MT, 240-246

Brun, E., E. Martin, V. Simon, C. Gendre, and C. Coleou, 1989, An energy and mass model of snow cover suitable for operational avalanche forecasting, *Journal of Glaciology*, vol 35, no 121, 333-342.

Brun, E. and E. Pahaut, 1991, An efficient method for a delayed and accurate characterization of snow grains from natural snowpacks, *Journal of Glaciology*, vol 37, no 127, 190-192.

Brun, E., P. David, M. Sudul, and G., Brugnot, 1992, A numerical model to simulate snowcover stratigraphy for operational avalanche forecasting, *Journal of Glaciology*, vol 38, no 128, 13-22.

Burden, R.L. and J.D. Faires, 1993, *Numerical Analysis* Fifth *Edition*, PWS-Kent Publishing Company, Boston.

Burton, W.K., N. Cabera, and F.C. Frank, 1951, The growth of crystals and the equilibrium structure of their surfaces, *Philosophical Transactions of the Royal Society of London, Series A, Mathematical and Physical Sciences*, vol 243, 299-358.

Christon, M., P.J. Burns, and R.A. Sommerfeld, 1990, A 2-D microscopic simulation of heat and mass transport in dry snow, *Chem. Eng. Commun.*, vol 87, 87-105.

Christon, M., P.J. Burns, and R.A. Sommerfeld, 1994, Quasi-steady temperature gradient metamorphism in idealized, dry snow, *Numerical Heat Transfer, Part A*, vol 25, 259-278.

Colbeck, S.C., 1980, Thermodynamics of snow metamorphism due to variations in curvature, *Journal of Glaciology*, vol 26, no 94, 291-301.

Colbeck, S.C., 1982, An overview of seasonal snow metamorphism, *Reviews of Geophysics and Space Physics*, vol 20, no 1, 45-61.

Colbeck, S.C., 1983a, Theory of metamorphism of dry snow, *Journal of Geophysical Research*, vol 88, no C9, 5475-5482.

Colbeck, S.C., 1983b, Ice crystal morphology and growth rates at low supersaturations and high temperatures, *Journal of Applied Physics*, vol 54, no 5, 2677-2682.

Colbeck, S.C., 1991, The layered characteristics of snow covers, *Reviews of Geophysics*, vol 29, no 1, 81-96.

Colbeck, S.C., 1997, A review of sintering in seasonal snow, *CRREL Report 97-10*, December.

Colbeck, S.C., 1998, Sintering in a dry snow cover, *Journal of Applied Physics*, vol 84, no 8, 4585-4589.

Colbeck, S.C., 2001, Sintering of unequal grains, *Journal of Applied Physics*, vol 89, no 8, 4612-4618.

Committee on Opportunities in the Hydrologic Sciences, and Water Science and Technology Board, 1991, *Opportunities in the Hydrologic Sciences*, National Academic Press, Washington D.C.

de Quervain, M.R., 1963, On the metamorphism of snow, *Ice and Snow Properties, Processes, and Applications*, The M.I.T. Press, Cambridge, MA, W.D. Kingery, editor.

de Quervain, 1972, Snow structure, heat, and mass flux through snow, *The Role of Snow and Ice in Hydrology, Proceedings of the Banff Symposia*, vol 1, September, 203-217.

Dozier, J., R.E. Davis and R. Perla, 1987, On the objective analysis of snow microstructure, *International Association of Hydrological Sciences Publication 162*, Symposium at Davos 1986-Avlanche Formation, Movement and Effects, 49-59.

Edens, M.Q. and R.L. Brown, 1991, Changes in microstructure of snow under large deformations, *Journal of Glaciology*, vol 37, no 126, 193-202.

Edens, M.Q., and R.L. Brown, 1994, Measurement of microstructure from surface sections, *Proceedings of Snowsymp 94*, International Symposium on Snow & Related Manifestations, Manali, 63-72.

Edens, M., 1997, An experimental investigation of metamorphism induced microstructure evolution in a "model" cohesive snow, Ph.D Thesis, Montana State University, Bozeman, MT.

Fukuzawa, T. and E. Akitaya, 1993, Depth-hoar crystal growth in the near surface layer under high temperature gradient, *Annals of Glaciology*, vol 18, 39-45.

Giddings, C.J. and E.R. LaChapelle, 1962, The formation rate of depth hoar, *Journal of Geophysical Research*, vol 67, 2377-2383.

Gray, J.M.N.T. and L.W. Morland, 1994, A dry snowpack model, *Cold Regions Science and Technology*, vol 22, 135-148.

Gubler, H., 1978a, Determination of the mean number of bonds per snow grain and of the dependence of the tensile strength of snow on stereological parameters, *Journal of Glaciology*, vol 20, no 83, 329-341.

Gubler, H., 1978b, An alternate statistical interpretation of the strength of snow, *Journal of Glaciology*, vol 20, no 83, 343-357.

Gubler, H., 1985, Model for dry snow metamorphism by interparticle vapor flux, *Journal of Geophysical Research*, vol 90, no D5, 8081-8092.

Hansen, A.C. and R.L. Brown, 1988, An internal state variable approach to constitutive theories for granular materials with snow as an example, *Mechanics of Materials*, vol 7, 109-119.

Hobbs, P.V. and B.J. Mason, 1964, The sintering and adhesion of ice, *Philosophy Magazine*, vol 9, 181-197.

Hobbs, P.V., 1965, The effect of time on the physical properties of deposited snow, *J.G.R.*, vol 70, no 15, August 15, 3903-3907.

Hobbs, P.V., 1974, *Ice Physics*, Clarendon Press, Oxford University Press, Bristol.

Incropera, F. and D. DeWitt, 1985, *Introduction to Heat Transfer*, John Wiley & Sons, New York.

Johnson, D.L., 1969, New method of obtaining volume, grain-boundary and surface diffusion coefficients from sintering data, *Journal of Applied Physics*, vol 40, no 1, 192-200.

Johnson, J.B. and M. Schneebeli, 1999, Characterizing the microstructural and micromechanical properties of snow, *Cold Regions Science and Technology*, vol 30, 91-100.

Jordan, R., 1991, A one-dimensional temperature model for a snow cover: technical documentation for SNTHERM. 89, *CRREL Special Report 91-16*, 1-49.

Kamata, Y., S. Sokratov, and A. Sato, 1999, Temperature and temperature gradient dependence of snow recrystallization in depth hoar snow, *Lecture Notes in Physics*, no 533, 395-402.

Keeler, C.M., 1969, The growth of bonds and the increase of mechanical strength in a dry seasonal snow-pack, *Journal of Glaciology*, vol 8, no 54, 441-450.

Kingery, W.D., 1960, Regelation, surface diffusion, and ice sintering, *Journal of Applied Physics*, vol 31, no 5, 833-838.

Kobayashi, T., 1956, Experimental researches on the snow crystal habit and growth by means of a diffusion cloud chamber (preliminary report), *Low Temperature Science*, A15, 1-11.

Kobayashi, T., 1957, Experimental researches on the snow crystal habit and growth by means of a diffusion cloud chamber, *J. met. Soc. Japan*, vol 75, 38-44.

Kobayashi, T, 1967, On the variation of ice crystal habit with temperature, *Physica of Snow and Ice*, 95-104.

Kry, P.R., 1975, The relationship between the viso-elastic and structural properties of fine-grained snow, *Journal of Glaciology*, vol 14, no 72, 479-500.

Kuczynski, J., 1949, *J. Met.*, 1, 169.

Kuroiwa, D., 1961, A study of ice sintering, *Tellus*, vol 13, 252-289.

Kuroiwa, D., 1974, Metamorphism of snow and ice sintering observed by time lapse cine-photography, *Snow Mechanics Symposium*, 82-88.

Lamb, D. and P.V. Hobbs, 1971, Growth rates and habits of ice crystals grown from the vapor phase, *Journal of Atmospheric Science*, vol 28, 1506-1509.

Lang, R.M., B.R. Leo, and R.L. Brown, 1984, Observations on the growth processes and strength characteristics of surface hoar, *Proceedings 1984 Snow Science Workshop*, Aspen, CO, 188-195.

Langham, E.J., 1981, *Handbook of Snow Principles, Processes, Management & Use*, Pergamon Press, Ontario, D. M. Gray and D.H. Male editors.

Langway, C. C., 1958, Ice Fabrics and the Universal Stage, *U.S. Army Snow Ice and Permafrost Research Establishment*, Technical Report 62.

Lehning, M., P. Bartelt, R.L. Brown, T. Russi, U. Stockli, and M. Zimmerli, 1999, SNOWPACK model calculations for avalanche warning based on a new network of weather and snow stations, *Cold Regions and Science Technology*, vol 30, 145-157.

Lindfield, G. and J. Penny, 1995, *Numerical Methods Using MATLAB*, Ellis Horwood, Hertfordshire, Great Britain.

Lock, G.S.H., 1990, *Studies in Polar Research: The Growth and Decay of Ice*, Cambridge University Press, Cambridge.

Lunardini, V. J., 1988, Heat conduction with freezing or thawing, *CRREL Monograph 88-1*, April.

Lundy, C.C., 2000, Statistical validation of a numerical snow cover model and preliminary experimental results to facilitate model improvement, Master's Thesis, Montana State University, Bozeman, MT.

Lundy, C.C., R.L. Brown, E.E. Adams, K.W. Birkeland, and M. Lehning, 2000, A statistical validation of the SNOWPACK model in a Montana climate, *Proceedings of 2000 International Snow Science Workshop*, Big Sky, Montana, 259-265.

Maeno, N. and Takao Eblnuma, 1983, Pressure sintering of ice and its implication to the densification of snow at polar glaciers and ice sheets, *The Journal of Physical Chemistry*, vol 87, no 21, 4103-4110.

Mahajan, P. and R.L. Brown, 1993, A microstructure-based constitutive law for snow, *Annals of Glaciology*, vol 18, 287-294.

Marbouty, D., 1980, An experimental study of temperature-gradient metamorphism, *Journal of Glaciology*, vol 26, no 94, 303-312.

MATLAB Version 6, 2000, *The Language of Technical Computing*, The Math Works Inc, Natick, MA.

McClung, D. and P. Schaerer, 1993, *The Avalanche Handbook*, The Mountaineers, Seattle, WA.

McElwaine, J., A. Hachikubo, M. Nemoto, T. Kaihara, T. Yamanda, and K. Nishimura, 2000, Observations and simulations of the formation of the faceted snow crystals in the weak-layer of the 1998 Niseko Haru no Taki avalanche, *Cold Regions Science and Technology*, vol 31, 235-247.

Michel, B and Ramseier, R.O., 1971, Classification of river and lake ice, *Canadian Geotechnical Journal*, vol 8, 36-451.

Morland, L.W., R.J. Kelly, and E.M. Morris, 1990, A mixture theory for a phase-changing snowpack, *Cold Regions Science and Technology*, vol 17, 271-285.

Nakaya, U., I. Sato, and Y. Sekido, 1938, Preliminary experiments on the artificial production of snow crystals, *J. Fac. Sci., Hokkaido University*, Ser II, no 2, 1-11.

Palm, E. and M. Tveitereid, 1979, On heat and mass flux through gry snow, *Journal of Geophysical Research*, vol 84, no C2, 745-749.

Paulke, W., 1934, Der Schnee und seine Diagenese. Z, *Gletscherkunde XXI*, 259-282.

Perla, R., 1978, Temperature-gradient and equi-temperature metamorphism of dry snow, *Proceedings International Meeting on Snow and Avalanches 12-13*, Grenoble, 43-48.

Perla, R., 1982, Preparation of section planes in snow specimens, *Journal of Applied Physics*, vol 28, no 98, 199-204.

Petrenko, V.F. and R.W. Whitworth, 1999, *Physics of Ice*, Oxford University Press.

Salm, B., 1982, Mechanical properties of snow, *Reviews of Geophysics and Space Physics*, vol 20, no 1, 1-19.

Satyawali, P.K., 1998, Temperature gradient metamorphism and its relation with avalanche release, *Norges Geotekniske Institutt*, Oslo, vol 203, 224-228.

Satyawali, P.K., 1999, Bond growth under temperature gradient, *Defence Science Journal*, vol 49, no 5, 363-370.

Shapiro, L.H., J.B. Johnson, M. Strum, and G.L. Blaisdell, 1997, Snow Mechanics: review of the state of knowledge and applications, *CRREL Report 97-3*, August.

Sommerfeld, R.A and E. LaChapelle, 1970, The classification of snow metamorphism, *Journal of Glaciology*, vol 9, no 55, 3-17.

Sommerfeld, R.A., 1983, A branch grain theory of temperature gradient metamorphism in snow, *Journal of Geophysical Research*, vol 88, no C2, 1484-1494.

Stefan, J., 1891, Ueber die theorie der eisbildung, inbesondere uber die eisbildung im polarmere, *Ann. Phys. Chem. Neue Folge*, vol 42, 269-286.

Stepphun, H., 1981, Snow and Agriculture, *Handbook of Snow Principles, Processes, Management & Use*, Pergamon Press, Ontario, D. M. Gray and D.H. Male editors.

St. Lawrence, W.F. and T.E. Lang, 1981, A constitutive relation for the deformation of snow, *Cold Regions Science and Technology*, vol 4, 3-14.

Sturm, M., 1991, The role of thermal convection in heat and mass transport in the subarctic snow cover, *CRREL Report 91-19*, October.

Sturm, M. and J.B. Johnson, 1991, Natural convection in the subarctic snow cover, *Journal of Geophysical Research*, vol 97, no B7, 11657-11671.

Sturm, M. and C.S. Benson, 1997, Vapor transport, grain growth and depth-hoar development in the subarctic snow, *Journal of Glaciology*, vol 43, no 143, 42-59.

Tannehill, J.C., D.A. Anderson, and R.H. Pletcher, 1997, *Computational Fluid Mechanics and Heat Transfer, Second Edition*, Taylor & Francis, Washington, DC.

Trabant, D. and C. Benson, 1972, Field experiments on the development of depth hoar, *Geological Society of America Memoir*, vol 135, 309-322.

Tremper, B., 2001, *Staying Alive in Avalanche Terrain*, The Mountaineers Books, Seattle, WA.

Warren, S.G., 1982, Optical properties of snow, *Reviews of Geophysics and Space Phusics*, vol 20, no 1, February, 67-89.

Weast, R.C., 1985, *CRC Handbook of Chemistry and Physics*, CRC Press Inc, Boca Raton, FL.

Wergin, W.P, A. Rango, E.F. Erbe, and C.A. Murphy, 1996, Low temperature SEM of precipitated and metamorphosed snow crystals collected and transported from remote sites, *Journal of Microscopy Society of America*, vol 2, no 3, 99-112.

Yen, Y.C., 1969, Recent studies on snow properties, *Advances in Hydroscience*, Academic Press, New York and London, Ven Te Chow, editor.

Yen, Y.C., 1981, Review of the thermal properties of snow, ice and sea ice, *CRREL Report 81-10.*

Yokoyama, E., 1993, Formation of patterns during growth of snow crystals, *Journal of Crystal Growth*, vol 128, part 1, 251-257.

Yosida, Z. and colleagues, 1955, Physical studies on deposited snow. Thermal properties, *Contributions from the Institute of Low Temperature Science*, vol 7, 19-74.

Yosida, Z., 1963, Physical properties of snow, *Ice and Snow Properties, Processes, and Applications*, The M.I.T. Press, Cambridge, MA, W.D. Kingery, editor.

Zhang, W. and J.H. Schneibel, 1995, The sintering of two particles by surface and grain boundary diffusion – a two-dimensional numerical study, *Acta Metallurgica Material*, vol 43, no 12, 4377-4386.

APPENDICES

APPENDIX A

LIST OF VARIABLES, CONSTANTS, AND PARAMETERS

List of variables, constants, and parameters

α - Absorption coefficient (0.01 from Yokoyama, 1993)

A - Cross sectional area for heat diffusion (m^2)

A_{ec} – Phase change area on ice surface (m^2)

A_{facet} – Surface area of a facet (m^2)

$A_{phase\ change}$ - Area at facet crystal tip available for step growth (m^2)

a_0 - Ice lattice parameter (4.519E-10m for a axis growth, 7.357E-10m for c axis growth)
       (Petrenko and Whitworth, 1999)

β - angle from dominant growth crystal axis and faceted crystal (deg)

C - Ice specific heat (J/kgK)

δ - Facet thickness (m)

ΔP - Excess vapor pressure during kinetic growth (Pa)

ΔP_1 - Critical excess vapor pressure during kinetic growth (Pa)

Δx – Phase change diffusion distance between the ice surface and pore (m)

D - Water vapor diffusion coefficient in air (2.02E-5 m^2/s)

γ - Crystal orientation, angle from dominant growth axis to temperature gradient (deg)

HS - Heat supply or sink from phase change (W/m)

J – Vapor mass flow from diffusion (kg/(sm^2))

J_{ec} – Vapor mass flow from phase change by evaporation or condensation (kg/(sm^2))

k – Ice thermal conductivity (2.2 W/(mK))

K - Boltzmann's constant (1.38E-23 J/Kmole)

L - Water latent heat of sublimation (2.838E6 J/kg)

l – Edge dimension on a faceted crystal (m)

MS - Mass supply or sink from phase change (kg/m^3s)

m – Ice molecular mass (2.989E-26 kg)

$\overline{m}_j$ - Grain mass average for a sieve (kg)

$\dot{m}$ is the mass flow from phase change (kg/s)

η - Ledge energy per unit step length for ice (2.0E-11 J/m from Yokoyama, 1993)

n – number of ice and pore elements (must be odd)

nl – Neck length (m)

NS - Number of facet surfaces present for a particular crystal (1-6)

P – Pore saturation vapor pressure (Pa)

P_0 - Reference vapor pressure (611 Pa) at reference temperature T_0

P_{ice} - Saturation vapor pressure over ice surface (Pa)

Q – Heat flow in the ice (W)

Q_{ec} – Heat flow associated with phase change by evaporation or condensation (W)

q_{ice} - Heat flux for phase change in the ice (W/m^2)

q_L - Latent heat flux for sublimation (W/m^2)

q_{pore} - Heat flux for phase change in the pore (W/m^2)

ρ - Density, vapor or snow depending upon context (kg/m^3)

ρ_{ice} - Ice density (917 kg/m^3)

ρ_s – Neck mean radius of curvature (m)

R - Water vapor gas constant (462 J/(kgK))

r_b – Bond radius (m)

r_g – Grain radius (m)

r_n – Neck surface radius of curvature (m)

σ - Ice surface tension (N/m)

ψ - Fit constant for faceted grain mass (126.6 kg/m^3) (Sturm and Benson, 1997)

θ - Ice temperature (K)

T - Pore temperature (K)

T_0 – Reference temperature (273 K)

T_s - Phase change temperature (K)

TG – Temperature gradient (K/m)

t - Time (s)

V - Vapor flow velocity (m/s)

$\dot{V}$ - Volumetric rate of change of ice element (m^3/s)

V_c and V_a - Respective linear growth velocities during kinetic growth (μm/s)

V_I - Facial velocity during kinetic growth (m/s)

$V_{crystal}$ – Facet crystal growth velocity (m/s)

V_{ice} - Total ice volume in the model (m^3)

V_{pore} - Pore volume (m^3)

V_{total} - Sum of ice and pore volumes (m^3)

w – Pore width, distance from ice surface to symmetry plane (m)

X_s - Mean absorption migration distance (m),

x – Symmetric pore distance (400a$_0$ m) (Yokoyama, 1993)

y – Vertical coordinate (m)

APPENDIX B

MATLAB CODE LISTING FOR MICROSTRUCTURAL MODEL

```
% main snow metamorphism program
%
% by Daniel A Miller
%
%*********************Functions called in METAMORPHISM****************
%
%GROWTHRATES - Finds the growth and decay of equilibrium ice grains and necks based on geometric
volume and mass
%transfer rates.
%
%INITGEOM - Sets the initial equilibrium form pore and ice geometry parameters.
%
%INITTEMP - Initialize the nodal temperatures of the pore and ice.
%
%LAYERS - Finds the temperatures at the boundaries of a three layer snowpack based on
%steady state conduction.
%
%NEWTEMP - Sets up and solves three systems of equations and iterates on their solutions until
%convergence.
%
%UPDATEFACETGEOM - Updates the L parameter of facet grains.
%
%UPDATEGEOM - Finds the new pore and ice geometries based on growth rates and time increment.
%Equilibrium form only.
%
%*********************************************************************
clear          %clear memory
%***********user defined input section********************************
%
n=101;  %set the number of elements (n).  Should be odd to have grain at each end.
          %There will be 2n+1 nodes
%
TG=0;        %The macroscopic temperature gradient (C/m).  Should be negative.
%
bctemp=263;    %Warm boundary temperature (K).  This will be temperature of node 1, others will be the
same (for TG=0)
          %or less than this value (TG<0).
          %
%If it is desired to use the LAYERS conduction program to define TG and boundary temperature
% then use the two lines below
%
%timetotal=0;i=1;
%[bctemp,TG]=layers(timetotal,i);
%
rhosample=150;  %Snow density (kg/m^3).
%
rinit=0.0004;  %initial grain radius for equilibrium form (m)
%
ratio=0.4;      %initial bond to grain radii ratio
%
deltat=3600/2; %time step (s).  This is the increment in time for each iteration.
%
totaltime=3600*50; %total time of simulation (s).  Number of iterations will be totaltime/deltat
%
%***********End of user defined input********************************
```

```
% ********************Initialize certain variables***********************
%
TGtrig=0;      % parameter that tells if TG has started yet.  =0 implies ET, anything else is TG
%
newdensity=rhosample;  %set updated density to initial sample density.  Will update after first iteration
%
timetotal=0;        %initialize the total elapsed time.  Will increase by deltat every iteration
%
%initalize array for facet location.  Will be updated and used in later calcs
wherefacets=zeros(n,1);    %array that tells where a facet is.  =0, no facet; =1, facet
facetL=zeros(n,1);         %length of facet side (in basal plane)(m)
beta=zeros(n,1);           %angle from dominant growth axis (c or a) to crystal.
                           %Based on relative growth of c vs a
gamma=zeros(n,1);          %angle from vertical to dominant growth axis (c or a) for facets
delta=zeros(n,1);       %grain thickness (m)
axisgrowth=zeros(n,1);     %this identifies the axis of growth.  If ==0 c axis down, if ==1, a axis down


%*****************************************************************************
%********************Constants************************************************
%
% D: diffusion coefficient of water vapor through air D=2.02E-5(kg/(sm^2)).  Could make temp dependent
%
% k: ice thermal conductivity k=2.2(W/(mK))
%
% L: latent heat of sublimation L=2.838e6(J/kg)
%
% R: water vapor gas constant R=462.(462 J/(kgK))
%
% rhoice: ice density rhoice=917(kg/m^3)
%
% sigma: ice surface tension, free energy sigma=.109(N/m)
%
%************* Problem initialization of geometry and temperatures********************
%
% Function that initializes the geometry of the ice and pore.
[r,rho,rb,A,Aec,w,vice,vpore,x]=initgeom(n,rhosample,rinit,ratio);
%
%
% Initialize the temperature distribution.  If TG=0, all the same temp
% otherwise, do linear distribution
%
[T,theta,Tinitial]=inittemp(n,TG,bctemp,r,w,Aec,vpore,rho,A,rb);
%
%**********************end of program initialization****************************
%
% Geometry and initial temps are done, now iterate in time and do the time varying calculations
%
% loop over all time
%
for i=1:round(totaltime/deltat)%
   timetotal=timetotal+deltat
   time(i)=timetotal;
   %disp('time is now (hours)'),disp(i*deltat/3600)%use to display elapsed time to screen
   %
   % set up and solve system of differential equations equations
```

```
% iterate inside each to find convergence at each time step
%This function will solve the differential equations iteratively until there is convergence
%
[T,theta,Jec,Ppore,facetL,wherefacets,beta,delta,vel,axisgrowth,massflow,TGtrig,gamma]=newtemp(deltat,
n,T,theta,r,rb,rho,Aec,A,w,vpore,Tinitial,TGtrig,wherefacets,facetL,beta,delta,axisgrowth,gamma,bctemp);
%
%After temperatures are converged for this step, find the grain and bond growth/decay rates
[rbdot]=growthrates(n,r,rb,Jec,Aec);
%total mass flow coming off grains.  If +, more mass is sublimating than condensing.
 %Use as a check only, not used directly
%totalmassflow=sum(massflow);
%
%***********************************************************************************
%save critical parameters at each step, can be used if every detail of microstructure needs to be saved.
%takes a lot of memory, not used frequently or for large models
%[rhist,rbhist,rbdothist,Thist,thetahist,densityhist]=savehistory(i,n,deltat,r,rb,rbdot,T,theta,newdensity);
%***********************************************************************************


%*************update the ice and pore geometry************************************
%
%Update equilibrium form geometry
%
[r,rho,rb,A,Aec,w,vice,vpore,newdensity]=updategeom(n,rbdot,deltat,x,r,rb,w,vpore,rhosample);
%
%Update kinetic growth geometry
if TGtrig~=0
 [facetL]=updatefacetgeom(deltat,n,TG,facetL,vel,wherefacets,axisgrowth,beta);
end


%reinitalize temps back to average values.  This can be done if desired, requires more iterations since
%starts with initial temp guess.
%Normally leave this out so the new temperatures can be used as the initial guess
%at the next iteration.
% [T,theta,Tinitial]=inittemp(n,TG,bctemp,r,w,Aec,vpore,rho,A,rb);
%
%If using a temperature input from another source that varies in time (such as LAYERS program),
% do it here
%
%[bctemp,TG]=layers(timetotal,i);


end  %end of loop for time integration
```

```
function [r,rho,rb,A,Aec,w,vice,vpore,x]=initgeom(n,rhosample,rinit,ratio)
%INITGEOM This function sets the initial equilibrium form pore and ice geometry parameters.
%
%*********************Inputs*************************
%n - number of elements in the model
%rhosample - snow density being evaluated
%rinit - equilibrium form inital grain radius
%ratio - inital bond to grain radii ratio
%*****************************************************
%
%*****************Outputs*************************
%r - vector of grain radii (odd elements) and neck length (even elements)(2n+1)
%rho - vector of ice element surface curvatures (n)
%rb - vector of distances from each node to ice surface (r for grain, rb for necks)(2n+1)
%A - vector or conduction areas for each ice node (2n+1)
%Aec - vector of surface areas of each ice element (n)
%w - vector of distances from symmetry plane to ice elements (n)
%vice - vector of ice element volumes (n)
%vpore - vector of pore element volumes (n)
%x - distance from ice centerline to symmetry plane
%*****************************************************


r=zeros(n,1);
rb=zeros(n,1);


% %*****this section uses average grain radius for each neck *****************
%
% set initial radii and geometry for grains
testcount=0;        %counter for setting different grain sizes every other grain
%set grain radius and surface curvature for round grains
for i=1:2:n          %round grains
        testcount=testcount+1;
        r(i)=rinit;                    %set grain radius to initial valued previously defined
        %r(((n+1)/2+1))=10*rinit;       %checkout only, large grain in the middle


        %******make every other grain large*********
%       if rem(testcount,2)==0
%           r(i)=4*rinit;
%       end
%       **********************************************


        %r(((n+1)/2)+3)=r(((n+1)/2)+1);
        %r(((n+1)/2)-1)=r(((n+1)/2)+1);

        rho(i)=r(i);    %surface radius of curvature for circular grain = grain radius
        rb(i)=r(i);     %distance from grain center too surface
end


    %now set neck length, bond radius, and surface curvature for bonds/necks
for i=2:2:n-1
        %make neck size for smaller neighboring grain
        if r(i-1)>r(i+1)
           aver=r(i+1);
        else
           aver=r(i-1);
```

```
      end
%
% %make neck size for larger neighboring grain
%      if r(i-1)<r(i+1)
%          aver=r(i+1);
%      else
%          aver=r(i-1);
%      end
       %aver=(r(i-1)+r(i+1))/2; %average r of 2 surrounding grains

       rb(i)=ratio*aver;  %bond radius, use average of surrounding grains if several sizes present

       %use average R for bond length
       r(i)=(aver*rb(i)^2)/(2*aver^2-2*rb(i)*aver+rb(i)^2);   %neck length

       %use average R for curvature
%      rho(i)=-(rb(i)^2)/(2*(aver-rb(i)));
       % average curvature.  Colbecks paper on curvature metamorphism.  Shuts off at rb/R > 2/3
       rho(i)=2/(1/rb(i)-2*(r(i-1)-rb(i))/rb(i)^2);   %average surface curvature, negative for concave

end
% % ***********************************************************************
r(n+1)=r(n-1);
rb(n+1)=rb(n-1);

%insert different sized grains

% r(((n+1)/2)+1)=8*rinit; %checkout only, large grain in the middle
% rb(((n+1)/2)+1)=r(((n+1)/2)+1); %grain radius
% rho(((n+1)/2)+1)=r(((n+1)/2)+1);
%
%********************3D geometry calcs************************

%  Calculate the ice conduction and phase change areas
%

for i=1:n
    if rem (i,2)~=0  %if i is odd, at a grain element
        A(2*i,1)=pi*r(i)^2; %3D conduction area in grain (at grain center).  For each ice node
        Aec(i,1)=4*pi*r(i)^2; %3D surface area of grain (surface area of sphere).  For each ice element

        %*********************************************************************
%       % 3D this is grain surface area minus neck contact area on each side of grain, could be used
%       if i==1
%          Aec(i,1)=4*pi*r(i)^2-2*pi*(rb(i+1)^2);
%       else
%          Aec(i,1)=4*pi*r(i)^2-pi*(rb(i+1)^2+rb(i-1)^2); % 3D this is grain surface area minus neck
contact area on each side of grain
%       end
%       %*********************************************************************

       %Aec(i,1)=r(i); %cylinder check out
    else    %if at even element it is a bond

        %A(i,1)=pi*(rb(i)^2)/2; %cylindrical bond conduction area 3D
```

```
    A(2*i+1)=pi*rb(i)^2; %3D conduction through the necks, same value at all three neck nodes
    A(2*i-1)=pi*rb(i)^2;
    A(2*i)=pi*rb(i)^2;

    %Aec(i,1)=pi*rb(i)*2*r(i); % area of one side of a cylinder 3D
    Aec(i,1)=pi^2*rb(i)^3/(2*r(i-1)); %3D neck surface area from Hobbs Ice Physics. For ice elements
    %Aec(i,1)=4*pi*r(i)*rb(i); %3D surface area of neck cylindrical
  end

end

A(2*n+1)=A(2*n-1); % this gives a conduction area out of the top of the last grain
A(1)=A(3);
Aec(n+1)=Aec(n-1);


%*********************************find the pore volumes**********************
%
%first we need the volume of the ice elements
%
icevol=0;  %total volume of ice in the model


%find the volume of circular grains
%
for i=1:2:n
   vice(i)=4*pi*r(i)^3/3; %3D ice piece volume
   %vice(i)=2*r(i)^2 %cylinder check out
   icevol=icevol+vice(i);
end

%find the volume of necks, treat as 3D cylinders

for i =2:2:n-1
   vice(i)=pi*rb(i)^2*2*r(i); %3D cylinder volume
   %vice(i)=2*r(i)^2; % cylinder checkout
   icevol=icevol+vice(i); %cylindrical neck volume
end

%we have the volume for each grain and bond plus the total ice volume
%can now find the total volume of the combined pore and ice for the model
%


%
% ice density
%
rhoice=917;

vtotal=rhoice*icevol/rhosample; %total volume of ice and pore in the model

%now find total pore volume for the model

%icevol

porevol=vtotal-icevol; %total pore volume
```

```
%

%***** this section is for original pore volume *********************
temp=0;
for i=1:n
    temp=temp+r(i)*rb(i)^2;
end
%*************This is from 5/8/01 3D pore size development. *****************
%find distance x from grain/bond centers to pore centers

x=((porevol+2*pi*temp)/(2*pi*sum(r)))^0.5;

% %find the individual pore widths and pore volumes
%
% for i=1:n
%     w(i)=x-rb(i);
%     vpore(i)=2*pi*r(i)*w(i)*(rb(i)+x);%3D pore volume for each element
%     %need to put in a check for negative pore volumes.  If pore volume is negative, make it the same as
another one
%     if vpore(i) < 0
%         vpore(i)=vpore(i-2);
%     end
%
% end
% %***********************************************
%******An alternative approach, simpler for pore volume*********
%this conserves mass better for ET analysis

for i=1:n
    w(i)=x-rb(i);
    vpore(i)=r(i)/sum(r)*porevol;
end

%sum(vice)*917/(sum(vice)+sum(vpore)); %should give back density here
%*******************end of 3D calcs***********************
```

```
function [T,theta,Tinitial]=inittemp(n,TG,bctemp,r,w,Aec,vpore,rho,A,rb)
%INITTEMP Initialize the nodal temperatures of the pore and ice.
%
%***************Inputs********************
%n - the number of elements
%TG - macroscopic temperature gradient
%bctemp - the warm boundary temperature
%r - vector of grain radii and bond lengths for equilibrium form
%w - vector of pore widths
%Aec - vector of surface areas available for evaporation/condensation
%vpore - vector of pore element volumes
%rho - vector of ice element surface curvatures
%A - vector of heat diffusion areas in ice
%rb - vector of distances from ice center nodes to ice surface (=r for grains, =rb for bonds)
%********************Outputs*******************
%T - vector of pore nodal temperatures
%theta - vector of ice nodal temperatures
%Tinitial- vector of initial pore nodal temperatures
%********************************************
% zero out initial arrays
%
T=zeros(2*n+1,1);
theta=zeros(2*n+1,1);
x=0;
% check to see if temp gradient is present
%
if TG==0
    for i=1:2*n+1 % if no TG, set all temps the same
        T(i)=bctemp;
        theta(i)=bctemp;
    end
else   %if TG present, linear distribution of temps
    T(1)=bctemp;
    theta(1)=bctemp;
    for i=1:n
        x=x+2*r(i); % this is the current location of the boundary node
        T(2*i)=(x-r(i))*TG+bctemp; % pore temp of center node
        T(2*i+1)=x*TG+bctemp; %pore temp of boundary node
        theta(2*i)=(x-r(i))*TG+bctemp; %ice temp of center node
        theta(2*i+1)=x*TG+bctemp; %ice temp of boundary node

    end
end
Tinitial=T;

%now do the conduction part to get real initial temps

% %*****************************************************************************
%  this is solving conduction problem first


%do first conduction problem using direct method

for jj=1:n
    Ts(jj)=theta(2*jj);
```

```
    HS(jj)=0;

end

[coefice,rhsice]=coef(n,A,r,HS,theta);%for first try at solving ice eqns
icenew=coefice\rhsice;

%update ice temps
for s=2:2*n;

    theta(s)=icenew(s-1);
end;
%
%*******************************************************************************
```

```
function
[T,theta,Jec,Ppore,facetL,wherefacets,beta,delta,vel,axisgrowth,massflow,TGtrig,gamma]=newtemp(deltat,
n,T,theta,r,rb,rho,Aec,A,w,vpore,Tinitial,TGtrig,wherefacets,facetL,beta,delta,axisgrowth,gamma,bctemp)
%NEWTEMP This function sets up the system of equations and solves them.
%It will iterate until reaching convergence with heat and mass source interaction terms
%
%****************Outputs*****************************************
%T - pore nodal temperatures (2n+1)
%theta - ice nodal temperatures (2n+1)
%Jec - phase change flux for each element (n)
%Ppore - vapor pressure at each pore node (2n+1)
%facetL - L dimension of each facet
%wherefacets - location of grains where facets are allowed to grow, if =0, no facet. if =1, facet there
%beta - angle from dominant growth axis to crystal, defines habit for each crystal
%delta - facet thickness
%vel - velocity of dominant growth axis
%axisgrowth - defines which axis is dominant for kinetic growth. =0 is c axis, =1 is a axis
%massflow - the mass flow rate for each element. + is sublimation, - is condensation.
%TGtrig - defines if entered kinetic growth =0 is no kinetic growth, >0 is kinetic growth
%gamma - angle from temperature gradient to dominant growth axis for each facet
%****************************************************************
%
%***************Functions called********************************
%
%SURFACETEMP - Newton's method to find the ice surface temps used in vapor pressure calculations
%
%FACET - Does the growth calculations for the temperature gradient facet grains
%
%NEWTONSOLVE - Forms the system and solves the nonlinear vapor equations using newton's method
%
%SOURCE - Finds the mass and heat source interaction terms applied to the ice and pore
%
%COEF - Forms the coefficient matrices and right hand side of equations for ice conduction
%
%****************************************************************
MSerror=.9; %set inital error for mass source terms to get through first iteration
MScount=0; %initalize counter for the number of attempts at convergence
while MSerror>.02 & MScount<155 &MSerror<1e3    %iterate until the interaction error is small, error is
very large, or large number of attempts
    %display message if iteration count getting large
    if MScount>150
        disp('iteration count exceeded, non convergence')
    end
    MScount=MScount+1; %counter for the number of iterations

    %set convergence tolerance
    tol=1e-7*sqrt(2*n+1); %can put other number in here, 1e-7 seemed to work well. Smaller numbers
possible for stable problems
    %set initial value for error
    %
    newcount=0;
    error=1;
    %
    %*******************Newton's method to find the ice surface temperatures*****************
    %
```

```
[Ts]=surfacetemp(n,T,theta,w,rb,rho,r);
% %make initial surface temps the same as ice temp, not generally needed
%  for jj=1:n
%   Ts(jj)=theta(2*jj);
%  end
```

%***

```
    %check to see if growing any facets or if Tg transition

    if TGtrig~=0

        %then we grow some facets for a temp gradient
        disp('did go to facet')

[facetMS,facetHS,facetjacobian,facetL,wherefacets,beta,delta,vel,axisgrowth,gamma]=facet(TGtrig,n,r,T,th
eta,deltat,vpore,wherefacets,facetL,beta,delta,axisgrowth,gamma,bctemp);

        %facetMS=zeros(n,1); %use this for checkout only
    else
        facetMS=zeros(n,1); %mass sources for facet grains
        facetHS=zeros(n,1); %heat sources for facet grains
        facetjacobian=zeros(n,1);%jacobian terms from facets for vapor eqns
        disp('did not go into facet')
    end
```

```
%
%************************Solve vapor equations*********************************
    error=1;
    newcount=0;
    %loop on vapor equations until converged.  Use Newton's method to solve vapor eqns
    while error > tol & newcount < 151
        %now use newton method to solve system of equations
        %the function returns y, a change in the temp for a particular iteration
        %
        [y]=newtonsolve(n,r,T,Aec,vpore,w,Ts,rho,rb,facetMS,facetjacobian);

        %check the norm of y to see if converged
        error=norm(y); %set error to L2 norm of increment
        %Update temps
        for k=2:2*n
            T(k)=T(k)+y(k-1);
        end
        newcount=newcount+1;
    end
%******end of vapor solution ***************************************
```

```
%*****ice conduction problem*****************************************
    %Now solve the ice conduction problem.  Direct solution method assuming source terms are constant

    %Heat source terms for ice conduction problem
    [HS,MS,Jec,Ppore,Pice,massflow]=source(n,T,theta,r,rb,rho,Aec,w,vpore,Ts,facetMS,facetHS);
    % Direct solution of ice eqns
    [coefice,rhsice]=coef(n,A,r,HS,theta);%for first try at solving ice eqns

    icenew=coefice\rhsice;
```

```
%update ice temps
for s=2:2*n;

    theta(s)=icenew(s-1);
end;


%******end of ice conduction problem*******************************
%
%**************update surface temps*********************************
    [Ts]=surfacetemp(n,T,theta,w,rb,rho,r);
%*****************************************************************
    %****Find new MS terms to compare with old to see if converged******

[nothing2,MSnew,nothing1,nothing3,nothing4,nothing5]=source(n,T,theta,r,rb,rho,Aec,w,vpore,Ts,facetM
S,facetHS);
    %compare new and old MS terms
    MSerror=abs((sum(MS)-sum(MSnew))/sum(MS))
end
%end of iteration on temps for this time step




%***now check to see if transitioned to TG metamorphism using MS terms********
%if all MS terms (usually in middle of model) are negative, everything is growing
    percentcheck=.30;  % determines how much of the model will be checked for on set of TG
                %it will be centered about the center element
    lowerlimit=round((n+1)/2-percentcheck/2*n);%lower ice number for TG check
    upperlimit=round((n+1)/2+percentcheck/2*n);%upper ice piece number for TG check
    if MS(lowerlimit:upperlimit)<0
        TGtrig=TGtrig+1;%if all MS terms checked are negative, TG is turned on
%        TGtrig=0;%turn off facet growth for checkout, comment out to get facet working
    end
%*******************************************************************************
```

```
function [Ts]=surfacetemp(n,T,theta,w,rb,rho,r)
%SURFACETEMP This function uses Newton's method to find the ice surface temps used
%in vapor pressure calculations
%
%***********************Outputs************************
%
%Ts - ice element surface temperatures (n)
%
%**********************************************************
%****** Define constants ******************************
%
% Diffusivity
%
D=2.02e-5;
%
% Latent heat of sublimation
%
L=2.838e6;
%
% ice density
%
rhoice=917;
%
% water vapor ideal gas constant
%
R=462;
%
% surface tension (free energy)
%
sigma=.109;
%
% reference pressure and temperature
%
T0=273;
P0=611.3;

%thermal conductivities
kice=2;
kpore=.0182;
%kpore=0; %turn off the pore conduction
%***********************************************************
%
tol=1e-8;   %convergence tolerance for newton's method
for i = 1:n %find the surface temp at each ice element
    count=0;
    error=1;
    Told=T(2*i); % initial guess at surface temp, central node temp
    %define the diffusion distance
%can use different diffusion distances
%       DD=w(i);%use pore width as diffusion distance
        DD=r(i); %ice radius as diffusion distance
%       DD=4e-6; %Colbeck diffusion distance
%
    while error > tol & count < 101 %loop until converged or exceed user defined number of iterations
        %
```

%f for flux dependent upon temp and curvature. uses pore temp for pressure calcs

```
f=(kice/rb(i))*(Told-theta(2*i))+(kpore/DD)*(Told-T(2*i))-...
    (D*P0*L/(R*T(2*i)*DD))*(exp((L/R)*(1/T0-1/T(2*i)))-exp((2*sigma/(rhoice*R*T0*rho(i)))+...
    (L/R)*(1/T0-1/Told)));
```

%fprime with flux for temp and curvature dependence. uses pore temp in pressure gradient calcs

```
fprime=kice/rb(i)+kpore/DD+(L/R)*(D*P0*L/(R*Told^2*T(2*i)*DD))*...
    exp((2*sigma/(rhoice*R*T0*rho(i)))+(L/R)*(1/T0-1/Told));
Tnew=Told-f/fprime;
error=abs(Tnew-Told);
Told=Tnew;
count=count+1;
end
%update surface temperature after convergence
Ts(i)=Tnew;
end
```

```
function [y]=newtonsolve(n,r,T,Aec,vpore,w,Ts,rho,rb,facetMS,facetjacobian)
%NEWTONSOLVE Forms the system and solves the nonlinear vapor equations using newton's method
%This version is for 4/16/01 development that includes all source terms in Jacobian.  Other
%version found in Matlab2 directory
%
%****************************Outputs*****************************
%
%y - vector of pore temperature changes (2n+1)
%
%*********************************************************************
%
%****** Define constants ***********************************
%
% Diffusivity
%
D=2.02e-5;
%
% Latent heat of sublimation
%
L=2.838e6;
%
% ice density
%
rhoice=917;
%
% water vapor ideal gas constant
%
R=462;
%
%thermal conductivity of ice
%
k=2.2;
%
%
% surface tension (free energy)
%
sigma=.109;
%
% reference pressure and temperature
%
T0=273;
P0=611;
%*****************************************************************************
%
%
%find the jacobian values at each node
%
%do the F(x) part first (RHS), then Jacobian terms
%
for i=2:2*n
    %Ppore(i)=P0*exp((L/R)*(1/T0-1/T(i))); %pore vapor pressure at each node
    if rem (i,2)~=0  %if i odd,
        %find even f entries (boundary nodes)
        aver=r((i+1)/2)+r((i-1)/2);
```

```
    f(i-1,1)=(L/R)*exp((L/R)*(1/T0-1/T(i)))*((2*T(i+1)/(aver*r((i+1)/2)*T(i)^2))-
2/(aver*r((i+1)/2)*T(i))+...
        2*T(i-1)/(aver*r((i-1)/2)*T(i)^2)-2/(aver*r((i-1)/2)*T(i))+(L/(R*aver^2*T(i)^4))*(T(i+1)^2-...
        2*T(i+1)*T(i-1)+T(i-1)^2)-(3/(aver*T(i)^3))*(T(i+1)-T(i-1)));

%this is from MAPLE as a check

%f(i-1,1)=L/R*exp(L/R*(1/T0-1/T(i)))*(2.0*T(i+1)/aver/r((i+1)/2)/(T(i)*T(i))-
2.0/aver/r((i+1)/2)/T(i)+2.0*T(i-1)/aver/r((i-1)/2)/(T(i)*T(i))-2.0/aver/r((i-1)/2)/T(i)+L/R/(aver*aver)/...
    %(T(i)*T(i)*T(i)*T(i))*(T(i+1)*T(i+1)-2.0*T(i-1)*T(i+1)+T(i-1)*T(i-1))-
3.0/aver/(T(i)*T(i)*T(i))*(T(i+1)-T(i-1)));


%find the odd numbered jacobian terms (boundary nodes)
    JB(i)=(L/R)*exp((L/R)*(1/T0-1/T(i)))*(2/(aver*r((i-1)/2)*T(i)^2)+2*L*T(i-1)/(R*aver^2*T(i)^4)-...
        2*L*T(i+1)/(R*aver^2*T(i)^4)+3/(aver*T(i)^3));%partial deriv wrt T(i-1) boundary node
    JA(i)=(L^2/(R^2*T(i)^2))*exp((L/R)*(1/T0-1/T(i)))*((2*T(i+1)/(aver*r((i+1)/2)*T(i)^2))-
2/(aver*r((i+1)/2)*T(i))+...
        2*T(i-1)/(aver*r((i-1)/2)*T(i)^2)-2/(aver*r((i-1)/2)*T(i))+(L/(R*aver^2*T(i)^4))*(T(i+1)^2-...
        2*T(i+1)*T(i-1)+T(i-1)^2)-(3/(aver*T(i)^3))*(T(i+1)-T(i-1)))+...
        (L/R)*exp((L/R)*(1/T0-1/T(i)))*(-4*T(i+1)/(aver*r((i+1)/2)*T(i)^3)+2/(aver*r((i+1)/2)*T(i)^2)-...
        4*T(i-1)/(aver*r((i-1)/2)*T(i)^3)+2/(aver*r((i-1)/2)*T(i)^2)-...
        4*L/(R*aver^2*T(i)^5)*(T(i+1)^2-2*T(i+1)*T(i-1)+T(i-1)^2)+...
        9*(T(i+1)-T(i-1))/(aver*T(i)^4));%partial deriv wrt T(i) boundary node
    JF(i)=(L/R)*exp((L/R)*(1/T0-1/T(i)))*(2/(aver*r((i+1)/2)*T(i)^2)+2*L*T(i+1)/(R*aver^2*T(i)^4)-...
        2*L*T(i-1)/(R*aver^2*T(i)^4)-3/(aver*T(i)^3));%partial deriv wrt T(i+1) boundary node


%these are generated by MAPLE as a check

%JB(i)=L/R*exp(L/R*(1/T0-1/T(i)))*(2.0/aver/r((i-
1)/2)/(T(i)*T(i))+L/R/(aver*aver)/(T(i)*T(i)*T(i)*T(i))*(-2.0*T(i+1)+2.0*T(i-
1))+3.0/aver/(T(i)*T(i)*T(i)));

%JA(i)=L*L/(R*R)/(T(i)*T(i))*exp(L/R*(1/T0-1/T(i)))*(2.0*T(i+1)/aver/r((i+1)/2)/(T(i)*T(i))-
2.0/aver/r((i+1)/2)/T(i)+2.0*T(i-1)/aver/r((i-1)/2)/(T(i)*T(i))-2.0/aver/r((i-1)/2)/T(i)+L/R/...
    %(aver*aver)/(T(i)*T(i)*T(i)*T(i))*(T(i+1)*T(i+1)-2.0*T(i-1)*T(i+1)+T(i-1)*T(i-1))-
3.0/aver/(T(i)*T(i)*T(i))*(T(i+1)-T(i-1)))+L/R*exp(L/R*(1/T0-1/T(i)))*(...
    %-4.0*T(i+1)/aver/r((i+1)/2)/(T(i)*T(i)*T(i))+2.0/aver/r((i+1)/2)/(T(i)*T(i))-4.0*T(i-1)/aver/r((i-
1)/2)/(T(i)*T(i)*T(i))+2.0/aver/r((i-1)/2)/(T(i)*T(i))-4.0*L/R/...
    %(aver*aver)/(T(i)*T(i)*T(i)*T(i)*T(i))*(T(i+1)*T(i+1)-2.0*T(i-1)*T(i+1)+T(i-1)*T(i-
1))+9.0/aver/(T(i)*T(i)*T(i)*T(i))*(T(i+1)-T(i-1)));


%JF(i)=L/R*exp(L/R*(1/T0-
1/T(i)))*(2.0/aver/r((i+1)/2)/(T(i)*T(i))+L/R/(aver*aver)/(T(i)*T(i)*T(i)*T(i))*(2.0*T(i+1)-2.0*T(i-1))-
3.0/aver/(T(i)*T(i)*T(i)));


else   %even i,
    %odd f, even nodes (center)

    %can use different diffusion distances for phase change
%       DD=w(i/2);%use pore width as diffusion distance
    DD=r(i/2); %ice radius as diffusion distance
```

```
%       DD=4e-6; %Colbeck diffusion distance
%       %use Hobbs book (Ice Physics) p403 for diffusion distance
%       if rem(i,4)~=0 %if at grain center
%           DD=rb((i/2)+1)^2/(2*r(i/2));
%       else  %neck center
%           DD=rb(i/2)^3/(2*r((i/2)-1));
%       end
        %use DD as diffision distance.  Change to desired value above
        %
        f(i-1,1)=(L/(R*r(i/2)^2))*exp((L/R)*(1/T0-1/T(i)))*(T(i-1)/T(i)^2-2/T(i)+T(i+1)/T(i)^2+...
            (L/(4*R*T(i)^4))*(T(i+1)^2-2*T(i-1)*T(i+1)+T(i-1)^2)-3*r(i/2)*(T(i+1)-T(i-1))/(2*T(i)^3))+...
            Aec(i/2)/(DD*vpore(i/2))*(exp((L/R)*(1/T0-1/Ts(i/2))+2*sigma/(rhoice*R*Ts(i/2)*rho(i/2)))-...
            exp((L/R)*(1/T0-1/T(i))))-facetMS(i/2)*T(i)*R/(D*P0);


%
        %this is the one generated by MAPLE as a check

        %f(i-1,1)=L/R/(r(i/2)*r(i/2))*exp(L/R*(1/T0-1/T(i)))*(T(i-1)/(T(i)*T(i))-
2.0/T(i)+T(i+1)/(T(i)*T(i))+L/R/(T(i)*T(i)*T(i)*T(i))*(T(i+1)*T(i+1)-2.0*T(i-1)*T(i+1)+T(i-1)*T(i-
1))/4.0-3.0/2.0*r(i/2)/(T(i)*T(i)*T(i))*(T(i+1)-...
        %T(i-1)))+Aec(i/2)/w(i/2)/vpore(i/2)*(exp(L/R*(1/T0-1/Ts(i/2))+2.0*sigma/rhoice/R/Ts(i/2)/rho(i/2))-
exp(L/R*(1/T0-1/T(i))));
        %
        %find the even numbered Jacobian terms (center nodes)
        %
        JB(i)=(L/(R*r(i/2)^2))*exp((L/R)*(1/T0-1/T(i)))*(1/T(i)^2+L*T(i-1)/(2*R*T(i)^4)-
L*T(i+1)/(2*R*T(i)^4)+...
            3*r(i/2)/(2*T(i)^3)); %partial deriv for previous node temp wrt T(i-1)
        %
        JA(i)=(L^2/(R^2*r(i/2)^2*T(i)^2))*exp((L/R)*(1/T0-1/T(i)))*(T(i-1)/T(i)^2-
2/T(i)+T(i+1)/T(i)^2+...
            (L/(4*R*T(i)^4))*(T(i+1)^2-2*T(i-1)*T(i+1)+T(i-1)^2)-3*r(i/2)*(T(i+1)-T(i-1))/(2*T(i)^3))+...
            L/(R*r(i/2)^2)*exp((L/R)*(1/T0-1/T(i)))*(-2*T(i-1)/T(i)^3+2/T(i)^2-2*T(i+1)/T(i)^3-...
            (L/(R*T(i)^5))*(T(i+1)^2-2*T(i+1)*T(i-1)+T(i-1)^2)+9*r(i/2)*(T(i+1)-T(i-1))/(2*T(i)^4))-...
            (Aec(i/2)/(DD*vpore(i/2)))*((L/(R*T(i)^2))*exp((L/R)*(1/T0-1/T(i))))+...
            facetjacobian(i/2);%partial deriv wrt T(i)

        JF(i)=(L/(R*r(i/2)^2))*exp((L/R)*(1/T0-1/T(i)))*(1/T(i)^2+L*T(i+1)/(2*R*T(i)^4)-L*T(i-
1)/(2*R*T(i)^4)-...
            3*r(i/2)/(2*T(i)^3));%partial deriv wrt T(i+1)


        %these are the terms generated by MAPLE as a check

        %JB(i)=L/R/(r(i/2)*r(i/2))*exp(L/R*(1/T0-1/T(i)))*(1/(T(i)*T(i))+L/R/(T(i)*T(i)*T(i)*T(i))*(-
2.0*T(i+1)+2.0*T(i-1))/4.0+3.0/2.0*r(i/2)/(T(i)*T(i)*T(i)));

        %JA(i)=L*L/(R*R)/(r(i/2)*r(i/2))/(T(i)*T(i))*exp(L/R*(1/T0-1/T(i)))*(T(i-1)/(T(i)*T(i))-
2.0/T(i)+T(i+1)/(T(i)*T(i))+L/R/(T(i)*T(i)*T(i)*T(i))*(T(i+1)*T(i+1)-2.0*T(i-1)*T(i+1)+T(i-1)*T(i-
1))/4.0-3.0/2.0*r(i/2)/...
        %(T(i)*T(i)*T(i))*(T(i+1)-T(i-1)))+L/R/(r(i/2)*r(i/2))*exp(L/R*(1/T0-1/T(i)))*(-2.0*T(i-
1)/(T(i)*T(i)*T(i))+2.0/(T(i)*T(i))-2.0*T(i+1)/(T(i)*T(i)*T(i))-L/R/(T(i)*T(i)*T(i)*T(i)*T(i))*...
        %(T(i+1)*T(i+1)-2.0*T(i-1)*T(i+1)+T(i-1)*T(i-1))+9.0/2.0*r(i/2)/(T(i)*T(i)*T(i)*T(i))*(T(i+1)-T(i-
1)))-Aec(i/2)/w(i/2)/vpore(i/2)*L*R/(T(i)*T(i))*exp(L/R*(1/T0-1/T(i)));
```

```
    %JF(i)=L/R/(r(i/2)*r(i/2))*exp(L/R*(1/T0-
1/T(i)))*(1/(T(i)*T(i)))+L/R/(T(i)*T(i)*T(i)*T(i))*(2.0*T(i+1)-2.0*T(i-1))/4.0-
3.0/2.0*r(i/2)/(T(i)*T(i)*T(i)));



    end
end
JB(2*n+1)=0;
JF(1)=0;
%only store the nonzero elements of jacobian
for i= 1:2*n-1  % B matrix columns become diagonals of Jacobian matrix

    B(i,1)=JB(i+2);
    B(i,2)=JA(i+1);
    B(i,3)=JF(i);
end

%this locates what diagonal the vectors defined above
d=[-1;0;1];
%form the jacobian using diagonal vectors stored in B
J=spdiags(B,d,(2*n-1),(2*n-1)); %find the sparse jacobian matrix
%full(J) %will display full matrix

condest(J);%condition numder of J since it needs to be inverted.  Good thing to check if having
convergence problems

%
%NOW FIND THE PORE TEMP INCREMENT
%
%invert the jacobian and multiply by RHS to get temperature increment
y=-J\f;
```

```
function
[facetMS,facetHS,facetjacobian,facetL,wherefacets,beta,delta,vel,axisgrowth,gamma]=facet(TGtrig,n,r,T,th
eta,deltat,vpore,wherefacets,facetL,beta,delta,axisgrowth,gamma,bctemp)
%FACET Does the growth calculations for the temperature gradient facet grains
%
%***************************Outputs*********************
%facetMS - mass source terms for kinetic growth
%facetHS - heat source terms for kinetic growth
%facetjacobian - jacobian terms for vapor eqns
%facetL - L dimension of facets
%wherefacets - location of grains where facets are allowed to grow, if =0, no facet.  if =1, facet can grow
there
%beta - angle from dominant growth axis to crystal, defines habit for each crystal
%delta - facet thickness
%vel - velocity of dominant growth axis
%axisgrowth - defines which axis is dominant for kinetic growth. =0 is c axis, =1 is a axis
%gamma - angle from temperature gradient to dominant growth axis for each facet
%*************************************************************
%***********Define constants**************************
rhoice=917; %ice density
alpha=.01;  %absorption coef a axis
alpha2=126.6; %constant for grain mass calcs from Sturm and Benson 1997
k=1.38e-23;  %Boltzman const(J/Kmole)
m=2.989e-26; %molecular mass (kg)
aa=4.519e-10; %lattice parameter for a axis growth
ac=7.357e-10; %lattice parameter for c axis growth
xsa=400*aa; %mean migration distamce of absorption for a axis
xsc=400*ac; %mean migration distance of absorption for c axis
eta=2e-11; %ledge energy/length (J/m)
D=2.02e-5;  %water vapor diffusivity
L=2.838e6;  % Latent heat of sublimation
R=462;  % water vapor ideal gas constant
% reference pressure and temperature
T0=273;
P0=611.3;
%**********************************************************
%need to define the number of faces that the grains will have grow.  Ranges 1-6, usually 2 or 3
NS=3;

%these need to be zeroed at each iteration
facetMS=zeros(n,1); %mass sources for facet grains
facetHS=zeros(n,1);%heat sources for facet grains
facetjacobian=zeros(n,1);%jacobian terms for the vapor eqns
vel=zeros(n,1);%a axis velocities
%
%first time through (first time step) initialize facets

if TGtrig==1
%************************define facet location(s)**************
    %initialize one facet in the center.


%     wherefacets((n+1)/2)=1; %middle grain

%     %******make all odd ice pieces (grains) facets******
```

```
%      for g=7:2:n-6  % avoid end elements so grains don't grow out of model
%          wherefacets(g)=1;
%      end
    %********

%      gamma(51)=60*pi/180;
%      gamma((n+1)/2)=pi/2*0;
%*********this next section makes all grains facets from n=21 to n=89*******
%      for pp=21:10:81
%          pp=41;%start at 41
%          wherefacets(pp)=1;
%          gamma(pp)=0;
%          wherefacets(pp+2)=1;
%          gamma(pp+2)=30*pi/180;
%          wherefacets(pp+4)=1;
%          gamma(pp+4)=60*pi/180;
%          wherefacets(pp+6)=1;
%          gamma(pp+6)=-30*pi/180;
%          wherefacets(pp+8)=1;
%          gamma(pp+8)=-60*pi/180;
%      end
    %***********************************
    wherefacets(61)=1;
    gamma(61)=-30*pi/180;
     wherefacets(71)=1;
     gamma(71)=-60*pi/180;
     wherefacets(51)=1;
     gamma(51)=60*pi/180;
    wherefacets(41)=1;
    gamma(41)=30*pi/180;
    wherefacets(31)=1;
    gamma(31)=0;
    wherefacets(71)=1;
    gamma(71)=-60*pi/180;
%*****************************************************************

%***********find growth angle beta********************************
    %now find the a vs c axis growth rates based on linear curves of experimental data (Lamb and Hobbs)
    for j=1:n
        if wherefacets(j)~=0  %if there is a facet at the current location

            %aveT=theta(2*j)-273;  %set temp to grain temp at that location
            aveT=bctemp-273; %based on boundary temp
            %aveT=mean(theta)-273; %average temp


            %start by finding c axis growth rate

            if aveT>-3.6% & aveT<=-2
                vc=0.5*aveT+2.05;
            elseif aveT<=-3.6 &aveT>-5
                vc=0.26;
            elseif aveT<=-5 & aveT>-5.7
                vc=-.5833*aveT-2.6165;
            elseif aveT<=-5.7 & aveT>-7.5
```

```
            vc=.2388*aveT+2.06;
        else
            vc=.0210784*aveT+.4215686;
        end


    %now find growth rate for a axis

        if aveT>-7.6% & aveT<=-2
            va=0.17555*aveT+1.444;
        elseif aveT<=-7.6 &aveT>-9.2
            va=0.11;
        elseif aveT<=-9.2 & aveT>-11
            va=-.2*aveT-1.72;
        elseif aveT<=-11 & aveT>-14.3
            va=.48;
        else
            va=.1432836*aveT+2.528955;
        end
        %now find the growth angle based on relative growth rates.  which axis is dominant?
        if vc>va  %then c axis dominant growth
            beta(j)=atan2(va,vc);  %angle from c axis to growth direction (radians)
            betadeg=beta*180/pi;  %angle from c axis to growth direction in deg
        else  %a axis dominat growth
            axisgrowth(j)=1;  %identifies this as a axis growth
            beta(j)=atan2(vc,va);  %angle from c axis to growth direction (radians)
            betadeg=beta*180/pi;  %angle from c axis to growth direction in deg
        end
%           beta(j)=20*pi/180;%this is to fix beta at 20 deg for studies
    end
end
%*********************************************************************************
***


    %set the inital crystal side length equal to grain radius.  Calculate grain thickness
    for j=1:n
        if wherefacets(j)~=0
            length=1.5*r(j);  %starting length of the crystal, usually 1.25 - 1.5
            facetL(j)=length*sin(beta(j));%the L dimension of crystal.  This is main parameter tracked
            %delta(j)=alpha2*facetL(j)/(rhoice*NS*4*sin(beta(j))^2);  %crystal thickness
            delta(j)=alpha2*r(j)/(rhoice*4*NS*sin(beta(j)));%thickness based on r(i)
        end
    end

end
%*******end of initialization section************************************

%*******next section done at every iteration*************************
%find which pore the end of the grain is currently resides in
for j=1:n
    if wherefacets(j)~=0  %if there is a facet at the current location
        locate=1;
        counter=0;
        while locate>0
            dist=0;
            for kk = 0:counter
```

```
        if kk==0
            dist=r(j);  %finds a distance kk radii from current grain
        else
            dist=dist+2*r(j-kk);
        end
    end
    counter=counter+1;
    locate=abs(facetL(j)*cos(gamma(j)+beta(j))/sin(beta(j)))-dist; %when this goes <0, it is the distance
it is short
    end
    %*****check to see if above horizontal*****************
    if facetL(j)*cos(gamma(j)+beta(j))/sin(beta(j))>0
        porenum=j-kk;  %gives the pore number where the end of the grain is located
%        elseif abs(facetL(j)*cos(gamma(j)+beta(j))/sin(beta(j)))<r(j)
%            porenum=j
%            locate=abs(facetL(j)*cos(gamma(j)+beta(j))/sin(beta(j)))+r(porenum);
    else
        porenum=j;
        locate=r(porenum);
    end
    %*******************************************************

    %we want vapor coming from pores with odd (grains)
    if rem(porenum,2)==0
        porenum=porenum-1;
        locate=2*r(porenum);
    end




    %now find the growth rates for each faceted grain

    pice=P0*exp((L/R)*(1/T0-1/theta(2*j)));  %no curvature considerations, use the ice temp where the
grain is attached
    if j==porenum  %if in first pore associated with the grain
    %*******interpolate for pore pressures*****
        pcold=P0*exp((L/R)*(1/T0-1/T(porenum*2)));
        phot=P0*exp((L/R)*(1/T0-1/T(porenum*2-4)));
        ppore=pcold+(phot-pcold)*(r(porenum)-abs(locate))/(r(porenum));

    else
        pcold=P0*exp((L/R)*(1/T0-1/T(porenum*2)));
        phot=P0*exp((L/R)*(1/T0-1/T(porenum*2-4)));
        ppore=pcold+(phot-pcold)*(2*r(porenum)-abs(locate))/(2*r(porenum));
    end
%*********end pore pressure interpolation*********
%***********find facial growth velocity************
    if axisgrowth(j)==0  %then c axis growth

        deltaP1=2*2^0.5*(pi*eta*ac^2*pice)/(k*xsc*theta(j*2));  %critical excess vapor pressure c axis
    else
        deltaP1=2*2^0.5*(pi*eta*aa^2*pice)/(k*xsa*theta(j*2));  %critical excess vapor pressure a axis
    end

    deltaP=ppore-pice;  %excess vapor pressure
```

```
%***************don't allow negative velocities********************
if deltaP<0
    vel(j)=0;
else
    vel(j)=(alpha/rhoice)*(m/(2*pi*k*theta(2*j)))^.5*deltaP^2/deltaP1*tanh(deltaP1/deltaP);% axis
growth velocity
end
%***********************************
deltaold=delta(j);
    newL=facetL(j)+vel(j)*deltat*tan(beta(j));%new L for a axis growth
%heat and mass source terms based on crystal volume change
%       facetMS2(porenum)=alpha2/8*((facetL(j)/sin(beta(j)))^3-
(newL/sin(beta(j)))^3)/(deltat*vpore(porenum));%original mass source
%
%       facetHS2(j)=L*alpha2/8*((facetL(j)/sin(beta(j)))^3-
(newL/sin(beta(j)))^3)/(deltat*newL/sin(beta(j)));%original heat sources


%heat and mass source terms based on crystal growth rate


%       facetMS3(porenum)=-
alpha2*vel(j)*(facetL(j)/sin(beta(j)))^2*cos(beta(j))/(4*vpore(porenum));%variable thickness
    facetMS(porenum)=facetMS(porenum)+-
delta(j)*facetL(j)*NS*vel(j)/cos(beta(j))*rhoice/vpore(porenum);%const thickness facet


%       facetjacobian(porenum)=alpha2*(facetL(j)/sin(beta(j)))^2*cos(beta(j))/4/vpore(porenum)*...
%       (2*alpha/rhoice)*(m/(2*pi*k*theta(2*j)))^.5*deltaP/deltaP1*tanh(deltaP1/deltaP)*...
%       P0*exp((L/R)*(1/T0-1/T(2*porenum)))*L/R/T(2*porenum)^2;  %facet jacobian terms


%       facetHS3(j)=-L*vel(j)*alpha2*facetL(j)/sin(beta(j))*cos(beta(j))/4; %variable thickness facet
    facetHS(j)=-L*delta(j)*NS*vel(j)/cos(beta(j))*rhoice*facetL(j)/(facetL(j)/sin(beta(j)));%const
thickness



    end
end
```

```
function [HS,MS,Jec,Ppore,Pice,massflow]=source(n,T,theta,r,rb,rho,Aec,w,vpore,Ts,facetMS,facetHS)
%SOURCE Finds the mass and heat source terms applied to the ice and pore
%
%*********************Outputs************************
%HS - heat source term for each ice element (n)
%MS - mass source term for each pore element (n)
%Jec - the phase change flux for each element (n)
%Ppore - vapor pressure at each pore node (2n+1)
%Pice - vapor pressure over each ice element (n)
%massflow - the mass flow rate at each element (n)
%****************************************************
%****** Define constants ***************************
%
% Diffusivity
%
D=2.02e-5;
%
% Latent heat of sublimation
%
L=2.838e6;
%
% ice density
%
rhoice=917;
%
% water vapor ideal gas constant
%
R=462;
%
% surface tension (free energy)
%
sigma=.109;
%
% reference pressure and temperature
%
T0=273;
P0=611.3;
%
%*********************************************************
%
% Find the vapor flux terms for this time step
%
%find the nodal pore vapor pressures
for i=1:2*n+1

    if rem (i,2)~=0  %if i is odd at grain

      Ppore(i)=P0*exp((L/R)*(1/T0-1/T(i))); %pore vapor pressure at each node

    else   %if at even element it is a bond

      Ppore(i)=P0*exp((L/R)*(1/T0-1/T(i))); %pore vapor pressure at each node (even)

    end
```

```
end
%
%find the vapore pressure over the surface of each ice element, then find phase change flux
for i=1:n  % each element (ice or pore) has flux associated with it

    %can use different diffusion distances
%        DD=w(i);%use pore width as diffusion distance
        DD=r(i); %ice radius as diffusion distance
%        DD=4e-6; %Colbeck diffusion distance
        %use Hobbs book p403
%        if rem(i,2)~=0 %if at grain center
%            DD=rb(i+1)^2/(2*r(i));
%        else   %neck center
%            DD=rb(i)^3/(2*r(i-1));
%        end

    % vapor pressure over the element ice surfaces, based on surface temperature
    Pice(i)=P0*exp((2*sigma/(rhoice*R*Ts(i)*rho(i)))+(L/R)*(1/T0-1/Ts(i)));
    %
    %find the phase change flux, use variable diffusion distance defined above
    Jec(i)=-D*(Ppore(2*i)-Pice(i))/(R*Ts(i)*DD);    %Notice pore pressure at each node, ice pressure at
each element
    %
    % mass source term for vapor equation, must include source from facet growth on that grain
    MS(i)=Jec(i)*Aec(i)/vpore(i)+facetMS(i);
    massflow(i)=Jec(i)*Aec(i);  %total massflow for that element
    %
    %heat source term for conduction equation
    HS(i)=Jec(i)*L*Aec(i)/(2*r(i))+facetHS(i);
    %
end
```

```matlab
function [coefice,rhsice]=coef(n,A,r,HS,theta)
%COEF Forms the coefficient matrices and right hand side of equations for ice conduction
%
%***************************Outputs***********************
%coefice - coeficient matrix for heat conduction problem
%rhsice - right hand side of ice conduction equation
%************************************************************
%****** Define constants ******************************
%
% Diffusivity
%
D=2.02e-5;
%
% Latent heat of sublimation
%
L=2.838e6;
%
% ice density
%
rhoice=917;
%
% water vapor ideal gas constant
%
R=462;
%
%thermal conductivity of ice
%
k=2.2;
%************************************************************
%Find all the coefficient entries
%
%the first loop is for even numbered nodes (located at the pore and ice centers)
for i=2:2:(2*n) % first and last nodes have predefined temps
    %
%central difference for all derivatives

    HH(i)=(1+(A(i-1)-A(i+1))/(4*A(i)))/r(i/2)^2;
    II(i)=-2/r(i/2)^2;
    JJ(i)=(1+(A(i+1)-A(i-1))/(4*A(i)))/r(i/2)^2;
    KK(i)=HS(i/2)/(k*A(i));
end
%
% get quantities for boundary (odd) nodes
%
for i=3:2:(2*n-1)
    %
%    %center differenced
    aver=r((i+1)/2)+r((i-1)/2);
    LL(i)=2/(aver*r((i-1)/2))+(A(i-1)-A(i+1))/(A(i)*aver^2);
    MM(i)=-2/(r((i+1)/2)*r((i-1)/2));
    NN(i)=2/(aver*r((i+1)/2))+(A(i+1)-A(i-1))/(A(i)*aver^2);
end
LL(2*n+1)=0;
NN(1)=0;
%set up coefficient matrices
```

```
%use sparse matrix notation
%B matrix has columns that become diagonals in coef matrix
for i=1:2:(2*n-1)%start with odd (every other) along diagonals
    B(i,1)=LL(i+2);
    B(i,2)=II(i+1);
    B(i,3)=NN(i);
end
for i=2:2:(2*n-2);
    B(i,1)=HH(i+2);
    B(i,2)=MM(i+1);
    B(i,3)=JJ(i);
end
%determines where diagonals are located
d=[-1;0;1];
%form the coef matrix with only nonzero entries
coefice=spdiags(B,d,(2*n-1),(2*n-1));
%condest(coefice)   %condition number, good to check for stability

% Now find the right hand side of each set of equations
 %apply boundary conditions
rhsice(1,1)=KK(2)-HH(2)*theta(1);
rhsice((2*n-1),1)=KK(2*n)-JJ(2*n)*theta(2*n+1);
%
%do the even numbered entries

for i=2:2:(2*n-2)
   rhsice(i,1)=0;
end

%do the odd numbered entries

for i=3:2:(2*n-3)
   rhsice(i,1)=KK(i+1);
end
%rhsice %to examine the rhs of ice conduction equations
```

```
function [rbdot]=growthrates(n,r,rb,Jec,Aec)
%GROWTHRATES Finds the growth and decay of equilibrium ice grains and necks based on geometric
volume and mass
%transfer rates.
%
%*********************Outputs********************
%rbdot - rate of change of grain radius or bond radius
%*************************************************
%
% ice density
%
rhoice=917;
%
%

%loop over even n, these are the bonds (necks)

for i=1:n
    if rem (i,2)~=0  %if i is odd, at a grain element
        vdot=-Jec(i)*Aec(i)/rhoice; %volumetric flow rate (m^3/s)
        rbdot(i)=vdot/(4*pi*rb(i)^2); %grain radius growth rate (m/s)
    else  %i is even, at a bond
        vdot=-Jec(i)*Aec(i)/rhoice; %volumetric flow rate (m^3/s)
        rbdot(i)=vdot*r(i-1)/(pi^2*rb(i)^3);  %neck growth rate (m/s) using n-1 grain radius for R
    end
end
```

```
function [facetL]=updatefacetgeom(deltat,n,TG,facetL,vel,wherefacets,axisgrowth,beta)
%UPDATEFACETGEOM This function updates the L parameter of facet grains

if TG==0
    return  %if ET, don't do any calcs
else
    for j=1:n
        if wherefacets(j)~=0  %if there is a facet at the current location
%           if axisgrowth(j)==0
%               facetL(j)=facetL(j)+vela(j)*deltat; %this is new L grain parameter after delta t c axis growth
%           else
            facetL(j)=facetL(j)+vel(j)*deltat*tan(beta(j));% axis growth based on either c or a
%           end

        end
    end
end
```

```
function [r,rho,rb,A,Aec,w,vice,vpore,newdensity]=updategeom(n,rbdot,deltat,x,r,rb,w,vpore,rhosample)
%UPDATEGEOM Finds the new pore and ice geometries based on growth rates and time increment.
Equilibrium form only.
%
%************************Outputs**************************
%r - grain radii and neck lengths for each element (updated)(n)
%rho - ice surface curvatures (updated) for each ice element(n)
%rb - distance from ice nodes and ice surface (n)
%A - ice heat conduction area at each node(2n+1)
%Aec - ice surface area for each ice element (n)
%w - vector of distances from symmetry plane to ice elements (n)
%vice - vector of ice element volumes (n)
%vpore - vector of pore element volumes (n)
%newdensity - updated density
%*****************************************************************
%Ice density
rhoice=917;
%update geometry based on rbdot
%
for i=1:n
    if rem (i,2)~=0  %if i is odd get grain radius
        r(i)=r(i)+rbdot(i)*deltat;
        rho(i)=r(i);%surface radius of curvature for circular grain = grain radius
        rb(i)=r(i); %this is the dimension perpendicular to model centerline (for pore calcs)
                %for circular grain = grain radius
    else    %if at even element it is a bond
        rb(i)=rb(i)+rbdot(i)*deltat;  % bond radius (use this)
        %r(i) is bond length (use this)
        r(i)=(r(i-1)*rb(i)^2)/(2*r(i-1)^2-2*rb(i)*r(i-1)+rb(i)^2);
        %bond surface curvature.  Negative for concave.
%       rho(i)=-(rb(i)^2)/(2*(r(i-1)-rb(i)));
        %could use average curvature.  Colbecks paper on curvature metamorphism.  Shuts off at rb/R > 2/3
        rho(i)=2/(1/rb(i)-2*(r(i-1)-rb(i))/rb(i)^2);
    end
end
%set the end radii the same as last bond
r(n+1)=r(n-1);
rb(n+1)=rb(n-1);


%*******************3D geometry calcs*************************
%  Calculate the ice conduction and phase change areas
%
for i=1:n
    if rem (i,2)~=0  %if i is odd, at a grain element
        A(2*i,1)=pi*r(i)^2; %3D conduction area in grain (at grain center)
        Aec(i,1)=4*pi*r(i)^2;  %3D surface area of grain (surface area of sphere)
%       Aec(i,1)=0;%turn off et stuff

        %****************************************************************************
%       % 3D this is grain surface area minus neck contact area on each side of grain
%       if i==1
%           Aec(i,1)=4*pi*r(i)^2-2*pi*(rb(i+1)^2);
%       else
%           Aec(i,1)=4*pi*r(i)^2-pi*(rb(i+1)^2+rb(i-1)^2); % 3D this is grain surface area minus neck
contact area on each side of grain
```

```
%      end
%*********************************************************************

       else    %if at even element it is a bond

          A(2*i+1)=pi*rb(i)^2; %3D conduction through the necks
          A(2*i-1)=pi*rb(i)^2;
          A(2*i)=pi*rb(i)^2;
          Aec(i,1)=pi^2*rb(i)^3/(2*r(i-1));  %3D neck surface area from Hobbs book Page
          %Aec(i,1)=4*pi*r(i)*rb(i); %3D surface area of neck cylinder
       end
end
%define end points
A(2*n+1)=A(2*n-1); % this gives a conduction area out of the top of the last grain
A(1)=A(3);
Aec(n+1)=Aec(n-1);
%now find the pore volumes.
%assume the pore width changed by the same amount as grain radius but different direction (keeps x
constant
for i=1:n
    w(i)=w(i)-rbdot(i)*deltat;
end;
% we can now find a new density based on new geometry
%find the volume of circular grains
%
icevol=0;
for i=1:2:n
    vice(i)=4*pi*r(i)^3/3;  %3D ice piece volume
    %vice(i)=2*r(i)^2 %cylinder check out
    icevol=icevol+vice(i);
end

%find the volume of necks, treat as 3D cylinders
for i =2:2:n-1
    vice(i)=pi*rb(i)^2*2*r(i); %3D cylinder volume
    %vice(i)=2*r(i)^2;  % cylinder checkout
    icevol=icevol+vice(i); %cylindrical neck volume
end

%find pore volumes
%find the individual pore volumes
porevol=0;
vtotal=rhoice*icevol/rhosample;

%now find total pore volume for the model
porevol=vtotal-icevol; %total pore volume
%
%******An alternative approach, simpler for pore volume*********
%this conserves mass better for ET analysis

for i=1:n
    vpore(i)=r(i)/sum(r)*porevol;
end
porevol=sum(vpore);
newdensity=icevol*rhoice/(icevol+porevol)
```

```
function [bctemp,TG]=layers(timetotal,i)
%LAYERS This function finds the temperatures at the boundaries of a three layer snowpack based on
%steady state conduction.  Surface temperature is a sinusoid in time.
%
%Define layer properties.
%
%layer densities
rho1=365;
rho2=300;
rho3=215;
%layer thermal conductivity.  Based on density for this effort
k1=2.22326*(rho1/1000)^1.885;
k2=2.22326*(rho2/1000)^1.885;
k3=2.22326*(rho3/1000)^1.885;

%layer thicknesses (m)
d1=.8;
d2=.3;
d3=.2;
%
%Define surface temperature mean and temp fluctuations
avesurfacetemp=253;
tempfluctuations=5;
%Define ground temperature
T1=273;
%surface temperature as a function of total time.  timetotal is in seconds.  24 hour cycle on temps
T4=avesurfacetemp+tempfluctuations*sin(timetotal*pi/(12*3600))
%can read temps from metstation from file
%fid=fopen('tempdata.txt','r');
%surfacetemp=dlmread('tempdata.txt','\t');
%fclose(fid);
%T4=surfacetemp(i)+273;
%

%find other temps based on conduction
T2=(k2*d3*k1*T1+k3*d2*k1*T1+k3*T4*k2*d1)/(k2*d3*k1+k3*d2*k1+k3*k2*d1)
T3=(k1*d2*k3*T4+k2*d3*k1*T1+k3*T4*k2*d1)/(k2*d3*k1+k3*d2*k1+k3*k2*d1)
%find average temperature gradients and temperatures for each layer
avetemp1=(T1+T2)/2 %layer 1 ave temp
avetemp2=(T2+T3)/2 %layer 2 ave temp
avetemp3=(T3+T4)/2 %layer 3 ave temp
TG1=(T2-T1)/d1 %TG layer 1
TG2=(T3-T2)/d2 %Tg layer 2
TG3=(T4-T3)/d3 %TG layer 3
%now it is time to designate which temperature and temperature gradient will be placed back into the
analysis
%this depends upon which layer is currently analyzed

TG=TG2;
bctemp=avetemp2;
```